Durham University

Department of Chemistry

Paramagnetic Probes for Magnetic Resonance

Peter Harvey

A thesis submitted for the degree of Doctor of Philosophy

December 2012

Abstract

Novel paramagnetic lanthanide complexes have been synthesised for use as probes for magnetic resonance imaging and spectroscopy. Initially, complexes containing a trifluoromethyl group were examined for ^{19}F MRI/S, due to the large chemical shift range, favourable NMR properties, and the absence of a background signal *in vivo*. The use of paramagnetic lanthanide ions increases relaxation rates, allowing faster acquisition times and increased signal intensity per unit time. In addition, chemical shift non-equivalence is enhanced, which is important for the development of responsive probes. Examples are presented that report selectively on changes to citrate concentration levels in the presence of other anions or signal enzyme hydrolysis.

To improve signal intensity for *in vivo* applications, conjugate systems have been developed containing a number of fluorinated lanthanide complexes covalently bound to high molecular weight adducts (glycol chitosan, PAMAM dendrimer). These systems resulted in one major species being observed in solution, despite the broad molecular weight ranges exhibited by these polymeric entities. Preliminary i*n vivo* MRI studies in animal models were undertaken with the glycol chitosan conjugate.

In order to enhance the signal further, a set of fluorinated complexes was synthesised containing a pyridyl moiety designed to increase the rigidity of the overall system, thereby reducing dynamic exchange broadening. Additionally, the ^{19}F NMR spectra of these complexes displayed much larger lanthanide induced shifts than observed for the previous systems. By substituting the CF_3 group for a *tert*-butyl moiety, the corresponding ^{1}H NMR signal was shifted well beyond the standard diamagnetic range, leading to the development of a new series of complexes for use as ^{1}H MRI and MRS probes. These complexes have been applied to preliminary *in vivo* MRI studies. A further system has been developed that displays pH-dependent behaviour, observed by both ^{1}H NMR spectroscopy and in phantom imaging studies.

Declaration

The research described herein was undertaken at the Department of Chemistry, Durham University between October 2009 and December 2012. All of the work is my own, except where specifically stated otherwise. No part has been previously submitted for a degree at this, or any other, university.

Statement of Copyright

Acknowledgements

I would like to first thank my supervisor, Prof. David Parker, for his inspiration, guidance, and patience over the last three years, which has been greatly appreciated.

The analytical services at Durham University have been invaluable, in particular Dr. Alan Kenwright, Catherine Hefferman, and Ian McKeag for their advice and assistance with NMR spectroscopy, and Dr. Dmitry Yufit for analysis of crystals. Thanks also to Prof. Andrew Blamire, Dr. Ross Maxwell, and Dr. Ian Wilson, at the Newcastle Magnetic Resonance Centre, for *in vivo* and phantom imaging. Additionally, Dr. Phil Dyer, for his support during my fourth year and throughout my PhD.

I thank Kirsten, for her patience when I started and friendship ever since; Robert Pal, for help with cell studies and for playing the drums very loudly; Alex, for help running high field NMR spectra and fitting of relaxation data; and Anurag, who worked closely with me on the responsive systems, despite his strong aversion to fluorine chemistry.

The rest of CG27, thanks for making the last three years so enjoyable, in particular Dave, James, and Brad for many good memories. Additionally to Rachel, Martina, Steve, Nick, Brian, Katie, Emily, Neil, Kat, Stuart, and Elena for making the lab such a fun place to work. A special thanks to Kanthi, for her guidance, friendship, and chats over the years. I would also like to thank other friends from Durham, especially Jo, Andy Henderson, Andy Illot, Dan Smith, Graeme, Ffion, and Sam. A particular thanks must go to Katharine, for managing to live with me for five years and for motivating me through my undergraduate studies, without which I may never have started a PhD.

A very special thanks to Mum and Dad, for their continued love and support throughout my life that have given me the opportunity to achieve so much. Finally, thanks to Jess, for her love and encouragement.

For Mum and Dad

& in memory of my great aunties; Irene and Iris

Abbreviations

5-FU	5-fluorouracil
Ar	aromatic
BOC	*tert*-butoxycarbonyl
br	broad
CSI	chemical shift imaging
cyclen	1,4,7,10-tetraazacyclododecane
d	doublet
DCM	dichloromethane
DIPEA	*N*,*N*-Diisopropylethylamine
DMF	*N*,*N*-dimethylformamide
DMSO	dimethyl sulphoxide
DO2A	1,7-bis(carboxymethyl)-1,4,7,10-tetraazacyclododecane
DO3A	1,4,7-tris(carboxymethyl)-1,4,7,10-tetraazacyclododecane
DOTA	1,4,7,10- tetraazacyclododecane-1,4,7,10-tetraacetic acid
DOTP	1,4,7,10- tetraazacyclododecane-1,4,7,10-tetrakis(methylene phosphinate)
DTPA	diethylenetriaminepentaacetic acid
EDC	*N*-(3-dimethylaminopropyl)-*N*'-ethylcarbodiimide hydrochloride
EPR	enhanced permeability and retention
ESI/MS$^+$	electrospray ionisation with positive ion detection
ESI/MS$^-$	electrospray ionisation with negative ion detection
FBAL	α-fluoro-β-alanine
FDG	2-fluorodeoxyglucose
FSB	(E,E)-1-fluoro-2,5-bis(3-hydroxycarbonyl-4-hydroxy)styrylbenzene
GPC	gel permeation chromatography
HATU	1-[bis(dimethylamino)methylene]-1*H*-1,2,3-triazolo[4,5-*b*]pyridinium 3-oxid hexafluorophosphate
HEPES	4-(2-hydroxyethyl)-1-piperazineethanesulphonic acid
HOBt	hydroxybenzotriazole
HPLC	high pressure liquid chromatography
HRMS	high resolution mass spectrometry

LIS	lanthanide induced shift
Ln	lanthanide
m	multiplet
MR	magnetic resonance
MRI	magnetic resonance imaging
MRS	magnetic resonance spectroscopy
MW	molecular weight
MWCO	molecular weight cut-off
NBS	*N*-bromosuccinimide
NMM	4-methylmorpholine
NMR	nuclear magnetic resonance
PAMAM	polyamidoamine
PBS	phosphate buffered saline
PCS	pseudocontact shift
PET	positron emission tomography
PFC	perfluorocarbon
ppm	parts per million
q	quartet
RF	radiofrequency
RP	reverse phase
s	singlet
SAP	square-antiprismatic
SNR	signal-to-noise ratio
t	triplet
TBTU	*O*-(benzotriazol-1-yl)-*N,N,N',N*'-tetramethyluronium tetrafluoroborate
TFA	trifluoroacetic acid
THF	tetrahydrofuran
TLC	thin layer chromatography
tri-Boc	1,4,7-tris-*tert*-butoxycarbonyl-1,4,7,10-tetraazacyclododecane
TSAP	twisted square-antiprismatic
UV	ultra-violet

Contents

3. Strategies to Enhance Signal Intensity; Increasing Fluorine Density

4. Strategies to Enhance Signal Intensity; Reducing Dynamic Motion

5. Strategies to Enhance Signal Intensity; A New Approach

6. Experimental

1. Introduction

1.1 Magnetic Resonance Imaging

Magnetic resonance imaging (MRI) is a widely employed imaging method and is acknowledged as one of the essential tools of clinical diagnostics, with over 46 MRI exams being carried out per 1000 population every year, according to the OECD (Organisation for Economic Co-operation and Development) Health Data 2011.[1,2] It is a powerful, non-invasive technique that utilises the strong ^{1}H NMR signal of water molecules *in vivo* to generate highly detailed, anatomical three-dimensional images with impressive (sub mm) spatial resolution, without the need for harmful ionising radiation.[3,4] This has been applied to countless human and animal studies, with some examples shown in *Figure 1.1*. The global importance of this imaging technique was highlighted by the award of the 2003 Nobel Prize in Medicine to Paul Lauterbur and Sir Peter Mansfield for their efforts into the development of MRI, which can be placed with 12 other Nobel Prizes directly and indirectly linked to the advance of MRI.[5]

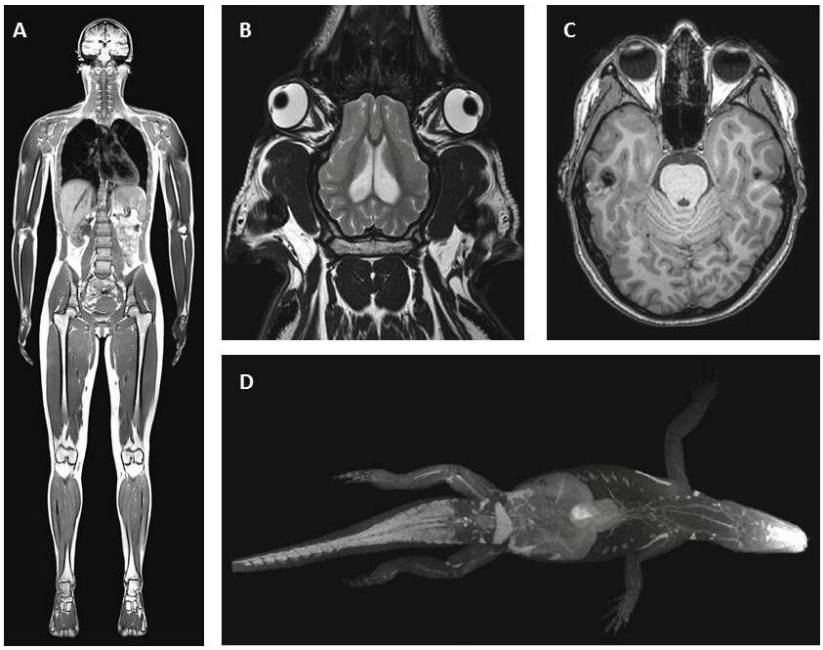

Figure 1.1 *^{1}H MRI images displaying the anatomical details and powerful resolution possible. A) Vertical section through a human; B) horizontal section through the head of a mini pig; C) horizontal section through the head of a human; D) horizontal image through an entire alligator.*[6,7]

Proton MRI can be used to determine the distribution of water *in vivo* by taking advantage of the differing longitudinal (T_1) and transverse (T_2) relaxation times of the water proton signal. It is possible to utilise the variation in these relaxation times to help distinguish between different tissue types. For example, malignant breast tissue has a significantly longer T_1 value (1.080 s) than healthy tissue (0.367 s), giving rise to differential image contrast in a T_1-weighted scan.[8] As well as being an important tool in medical diagnosis, MRI is also starting to find applications in reporting certain chemical reactions.[9] This has been utilised by numerous groups to image a variety of processes, such as flow systems,[10] corrosion effects,[11] and tracking temperature changes during reactions.[12]

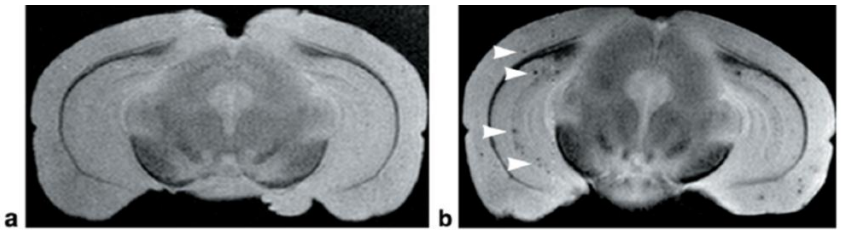

Figure 1.2 *Ex vivo T_2-weighted coronal MR images of a) control and b) APP-transgenic mouse brains after injection of iron-oxide nanoparticles (MION) with 15% mannitol to transiently open the blood-brain barrier. Arrowheads indicate dark spots caused by accumulation of MION, corresponding to location of amyloid-β plaques, demonstrating the 'negative contrast' image*[13]

MRI signal intensity increases with increasing longitudinal relaxation rate, R_1 ($R_1 = T_1^{-1}$), and decreases with increasing transverse relaxation rate, R_2 ($R_2 = T_2^{-1}$). This allows two common methods of enhancing the contrast of an image to be devised. The first method, and the one that will be focussed on more in this work, utilises paramagnetic gadolinium(III)[14] or manganese(II)[15] contrast agents, which significantly increase both the R_1 and R_2 of nearby water protons. However, the relative change of R_1 is much larger than that of R_2 and, therefore, they are best visualised using T_1 weighted images, which utilise pulse sequences that accentuate changes in R_1.[14] The second class of contrast agent are mainly based on polysaccharide iron oxide particles that work by increasing the transverse relaxation rate, producing a 'negative contrast' image (*Figure 1.2*). Each of these systems results in an increased contrast between healthy and

malignant tissue. Both are in clinical practice, although the majority of those used are those containing gadolinium, and they will be discussed in further detail. Another, more recent class of MRI contrast agents are based on the use of paramagnetic lanthanide complexes that utilise the chemical exchange saturation transfer (CEST) mechanism. These so called PARACEST agents increase the frequency difference between two pools under chemical exchange and have been shown to be capable of reporting on changes in temperature and pH. The theory behind this mechanism is too complex to be discussed in detail here, but can be found elsewhere.[16,17]

The first paramagnetic compounds used to increase relaxation rates of water protons were simple salts of manganese(II),[18] but research quickly progressed into the use of gadolinium(III). The choice of Gd(III) could be predicted, due to the fact that it is the only stable ion with seven unpaired electrons. There is more than this to its success, however, as two other lanthanide ions, dysprosium(III) and holmium(III), actually have larger magnetic moments than Gd(III) due to orbital contributions to electron angular momentum. The asymmetry of the electronic states of Dy(III) and Ho(III) causes very rapid electron spin relaxation, whereas the near symmetrical Gd(III) allows for slower electronic relaxation rates more closely in tune with the proton frequency of water, leading to much greater increases in relaxation rates.[14]

The free Gd(III) ion, however, is toxic (LD_{50} ≈ 0.2 mmol/kg in mice) and so multidentate ligands must be employed in order to form stable chelates to ensure that the paramagnetic metal complex is well tolerated *in vivo* (LD_{50} ≈ 10 mmol/kg).[19] Countless examples of these coordinating ligands have been published in the literature. Gd(DTPA)(H_2O), commercially marketed as Magnevist®, was introduced in 1988 and became the first contrast agent to be used in clinical MRI.[2] By the turn of the century, it was estimated over 30 metric tons of gadolinium had been administered to patients worldwide. There are now eight gadolinium-based contrast agents that have been FDA approved for clinical use, and these are employed in around 30 % of current MRI scans.[2,14]

The ability of a compound to enhance the relaxation of nearby nuclei per unit concentration is termed the relaxivity (r_1), which is often given in units of $mM^{-1}\ s^{-1}$. It is used when determining the ability of a contrast agent to increase the relaxation rate of bulk water, defined as the increase in $1/T_1$ and $1/T_2$, and is proportional to the concentration of the paramagnetic species, [Gd] (*Equation 1.1*). Three different terms must be taken into account when analysing the relaxivity of water protons in the presence of a contrast agent, depending on how the water molecules interact with the paramagnetic species. The first is the inner-sphere contribution, r_i^{IS} (where *i*=1 for longitudinal and *i*=2 for transverse relaxation), and results from water molecules directly bound to the Gd(III) ion.[14] The second term is the outer-sphere contribution, r_i^{OS}. This arises from the fact that bulk solvent molecules diffusing around the paramagnetic complex also experience an increase in relaxivity. Finally, when hydrogen bonding or other similar interactions occur, a loose layer of water molecules between the inner- and outer-sphere can arise. This is the second-sphere contribution, r_i^{SS}. The total relaxivity of the system is a sum of these three terms (*Equation 1.2*). An illustration of these contributions is shown in *Figure 1.3*.

$$\frac{1}{T_{1,obs}} = \frac{1}{T_{1,d}} + r_1[\mathrm{Gd}] \qquad (1.1)$$

$$r_i = r_i^{\mathrm{IS}} + r_i^{\mathrm{OS}} + r_i^{\mathrm{SS}} \qquad (1.2)$$

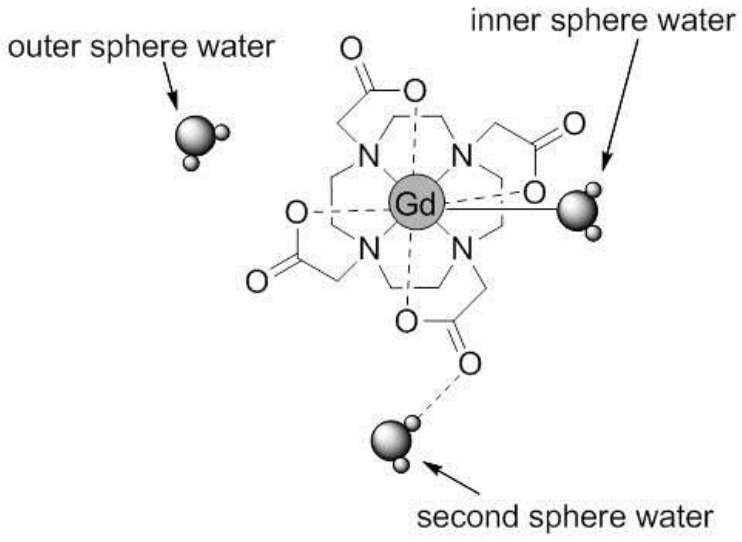

Figure 1.3 *Illustration of inner-, outer-, and second-sphere water molecules around a gadolinium(III) complex.*

The practicality of the current system is also its major drawback, i.e. the intense background of the water signal. Due to this severe background signal, differentiation between tissue types can be extremely challenging. The ability to distinguish easily between healthy and tumourous tissues is crucial in the early detection of cancer and related illnesses. The detection of metabolites other than water can also be of vital importance in the detection of disease, for example low levels of citrate in prostate and seminal fluid can be indicative of prostate cancer.[20,21] However, *in vivo* such metabolites generally suffer from unmanageable spectral overlap, or are not present in sufficient concentrations to allow direct observation by standard ^{1}H MRI against the strong background signal, although more complicated *in vivo* NMR spectroscopic techniques (e.g. two-dimensional methods) can be attempted.[22]

In an effort to overcome this issue, and increase the applicability of MRI, a variety of Gd(III) contrast agents have been described that respond to changes in pH,[23] selectively signal the presence of certain metal ions in a competitive media,[24,25] and report on various chemical processes, such as enzyme cleavage[26] (for further details, see *Section 1.5*). The major drawback with these systems is that the behaviour being investigated is signalled by a change in relaxivity. However, relaxivity is also dependent on concentration. Therefore, in order for these systems to be applicable towards *in vivo* studies, it is necessary to be able to determine the local concentration of the contrast agent. Whilst some methods have been designed to overcome this problem, such as combining MRI with alternative techniques (optical emission, PET, CT, etc.),[24] in most cases calculation of the local concentration is highly problematic, if at all possible.

1.2 ^{19}F MRI/MRS

1.2.1 Advantages of Heteronuclear MRI/MRS

A potential solution to some of the issues discussed in the previous section is to move away from using ^{1}H as the imaging nucleus. Therefore, the use of heteronuclear magnetic resonance has been investigated as a tool in order to overcome the difficulty

caused by the intense water signal present in the body.[27–30] Of particular interest are heteronuclei that are not biologically prevalent, the most promising of these being ^{19}F (see *Table 1.1*).[31] The attractive properties of ^{19}F are its 100 % natural abundance, its nuclear spin (I = ½), and its high NMR sensitivity (0.83 relative to ^{1}H). The large gyromagnetic ratio is only 6 % lower than that of ^{1}H, which should allow spectral acquisition on existing instrumentation, with relatively straightforward tuning of the RF coil.

Table 1.1 *Selection of nuclear isotopes and their properties*[31,32]

Isotope	Spin state	Natural abundance / %	Magnetogyric ratio γ / 10^6 rad s^{-1} T^{-1}	Atomic abundance in humans [(a)] / %
^{1}H	$^{1}/_{2}$	~ 100	267.522	63
^{2}H	$^{3}/_{2}$	0.015	41.066	0.0095
^{11}B	$^{3}/_{2}$	80.1	85.847	3 x 10^{-6}
^{12}C	0	98.9	N/A	12
^{13}C	$^{1}/_{2}$	1.1	67.283	0.13
^{15}N	$^{1}/_{2}$	0.37	-27.126	0.58
^{16}O	0	~ 100	N/A	24
^{17}O	$^{5}/_{2}$	0.04	-36.281	0.0096
^{19}F	$^{1}/_{2}$	~ 100	251.815	0.0012
^{23}Na	$^{3}/_{2}$	~ 100	70.808	0.037
^{29}Si	$^{1}/_{2}$	4.7	-53.190	0.0058
^{31}P	$^{1}/_{2}$	~ 100	108.394	0.14
^{129}Xe	$^{1}/_{2}$	24.4	-74.521	N/A

(a) As percentage of total atoms[33,34]

Other than its excellent properties for NMR spectroscopy, the main advantage of ^{19}F from an imaging perspective is its scarcity in biological systems. Whilst fluorine is present in low quantities in the body, the physiological concentrations of detectable fluorine are below the detection limit (<10^{-3} µmol/g wet tissue weight).[35] Fluorine does exist at higher concentrations in the bone matrix and teeth, but displays a very short transverse relaxation time due to the immobilised form, making them invisible by standard NMR methods.[36] This results in an almost complete lack of endogenous

background signal and so, in theory, it should be possible to utilise ^{19}F MRI to observe directly an exogenous fluorine-containing compound administered to a patient. The large chemical shift range of ^{19}F NMR, with respect to ^{1}H, also allows the development of chemical shift reporters. This would alleviate the problem of calculating local probe concentration in responsive systems, as variation in environment could be reported by changes in the chemical shift, which is a parameter that is independent of concentration. However, in order for this to be a practicable method, it is imperative that any chemical shift non-equivalence is amplified as much as possible.

1.2.2 The Advent of ^{19}F MRI and the development of perfluorocarbons

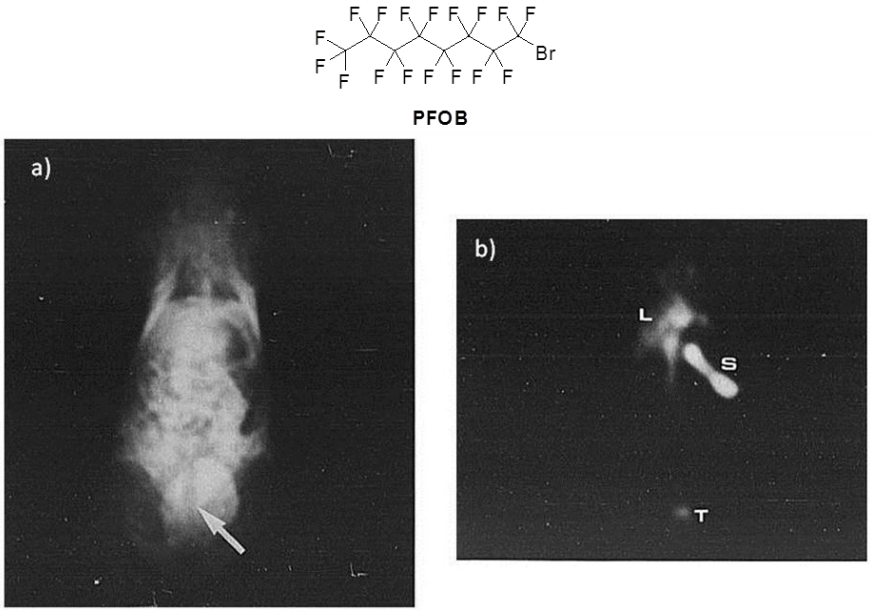

Figure 1.4 *First example of the detection of tumours using ^{19}F MRI; a) ^{1}H coronal image of a mouse with implanted tumour indicated by the arrow, b) corresponding ^{19}F image with identical orientation after intravenous injection of 10g/kg of PFOB emulsion. ^{19}F signal is observed in the liver (L), spleen (S), and in the centre of the tumour (T). Chemical structure of PFOB is shown above.*[37]

The use of ^{19}F as an imaging nucleus was suggested in the late 1970s,[38] only a few years after ^{1}H MRI was developed by Lauterbur in 1973.[39] The first detection of tumours utilising ^{19}F MRI was achieved around a decade later, utilising perfluorooctyl bromide (PFOB) as the imaging probe (*Figure 1.4*).[37] A PFOB emulsion is known to

localise in the reticuloendothelial system and it is a successful agent in the imaging of tumours. When it is intravenously injected, it leaks through the gaps in the tumour vascular endothelium and collects in the extracellular space. The concentration of PFOB builds up in this region and the fluorine signal can be detected. It should be noted that the ^{19}F NMR spectrum of PFOB contains numerous peaks, due to the chemical inequivalence of the fluorine groups in the molecule. Only selective imaging of one set of peaks is possible in an imaging experiment, otherwise chemical shift artefacts would be observed if all peaks were attempted to be imaged simultaneously. More recent examples have focussed on perfluoropolyethers, for example containing 12-, 15-, or 18-crown ethers, as they display a single sharp resonance, thereby eliminating this problem.[35]

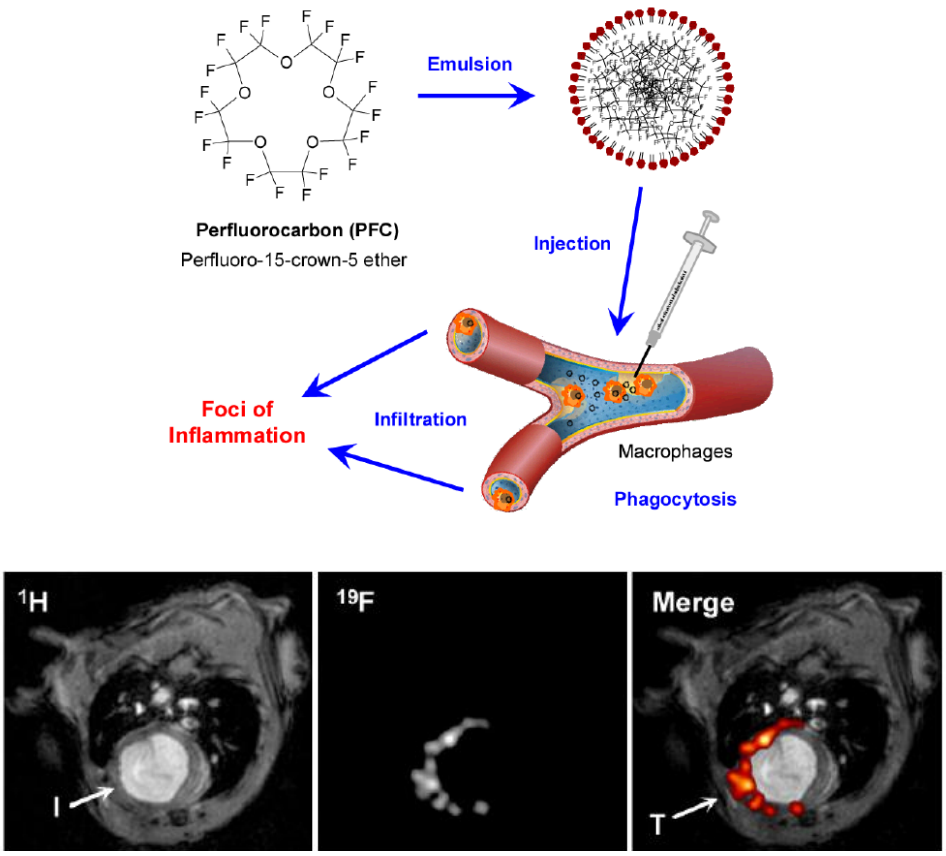

Figure 1.5 *Above; schematic illustration of the use of PFCs for monitoring inflammatory processes. Emulsified PFC is taken up by the monocyte-macrophage system and transported to areas of inflammation. Below; corresponding ^{1}H and ^{19}F images and overlay (^{19}F in red) from the mouse thorax recorded 4 days after ligation of the left anterior descending coronary artery showing an accumulation of ^{19}F signal near the infarcted region (I) and at location of surgery, where the thorax was opened (T).* [40]

Since then, many examples of the use of perfluorocarbons (PFCs) in imaging have been published, due to the strong ^{19}F NMR signal present and their interesting biological properties. For example, the high oxygen affinity of PFCs was first recognised in the 1960s, when mice and cats were shown to survive complete immersion in oxygenated PFCs, followed by long-term survival post-treatment without ill-effects.[41] This has led to the development of PFCs as blood substitutes and aerosols, including applications in drug delivery during liquid ventilation.[42] One issue regarding the use of PFCs for biological applications is their poor water solubility, although this can be overcome by preparing them as water emulsions.[43] This inherent poor water solubility can result in the benefit of slow diffusion, causing a long retention time at the target site of the compound.[35] PFCs have also shown good uptake by the monocyte/macrophage system, resulting in transportation to areas of inflammation. This has been used to visualise macrophage infiltration in the infarcted myocardium (heart muscle after cardiac arrest) by the *in vivo* ^{19}F MRI of perfluoro-15-crown-ether (*Figure 1.5*).[40]

1.2.3 Fluorinated gases

Fluorinated gases have also been suggested as potential imaging agents, in particular for imaging lung function, due to the possibility of direct imaging and their unique properties. For example, various fluorinated gases (SF_6, C_2F_6, CF_4, C_3F_8) can be mixed with 20 % oxygen and allow continuous breathing with simultaneous imaging of the lungs.[35] They were first reported for use in MRI in the early 1980s,[44] and have since been employed in both experimental and clinical applications, with SF_6 being one of the more widely used fluorinated molecules.[35] However, unfavourable relaxation rates and the poor diffusivity of this gas has led to the use of fluoroethane (C_2F_6) and fluoropropane (C_3F_8) gases, which are more suitable and promising for measurements of diffusion in human lungs by ^{19}F MRI.[45,46] Fluoropropane is in fact currently used clinically for ultrasound imaging of internal organs in humans, under the trade name Optison®. Hyperpolarised noble gases have been suggested as a viable alternative to fluorinated gases due to their much improved SNR. However, this benefit is somewhat offset by the increase in cost, associated with the hyperpolarisation apparatus required. A direct comparison of imaging capabilities of both fluoroethane and hyperpolarised helium is displayed in *Figure 1.6*.

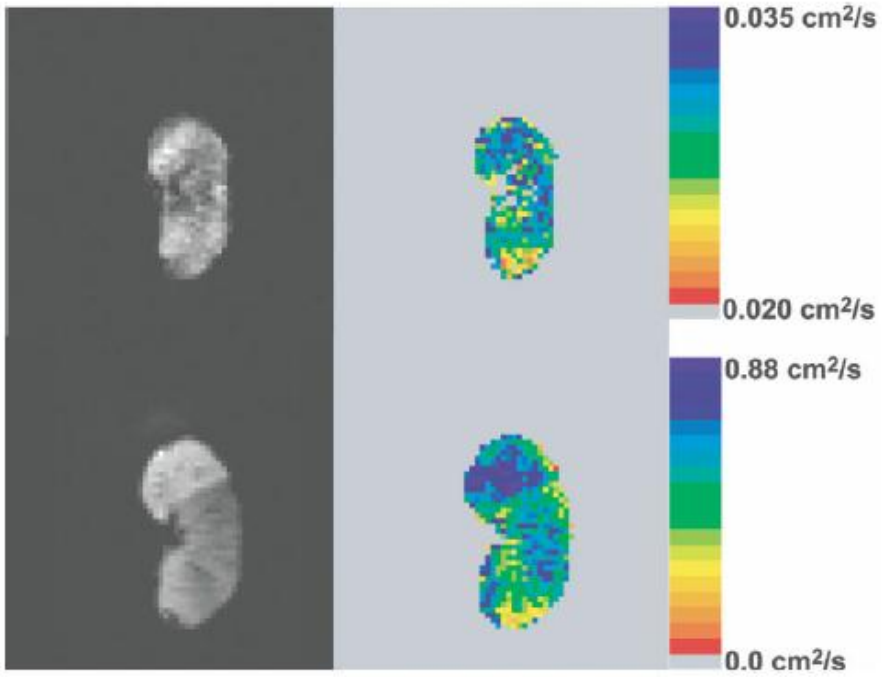

Figure 1.6 *Comparison of C_2F_6 (top row) and hyperpolarised ^3He (bottom row) gradient-echo spin density images (left) and apparent diffusion coefficient maps (right) of a formalin-fixed emphysematous lung.*[45]

1.2.4 Fluorinated drugs and biomarkers

Fluorine is also a very attractive element from a biological perspective, as substitution of hydrogen for fluorine often has little effect on the biological activity of a molecule. Traditional medicinal chemistry was based almost entirely on the use of natural compounds or closely related derivatives, and so did not contain fluorinated compounds. Hence, fluorinated drugs were extremely rare before the 1970s. This has changed quite dramatically in the last 20 years and fluorine is becoming an increasingly important element in drug design.[47] There are now many examples where fluorine has effectively replaced hydrogen or oxygen (the size and electronegativity of fluorine is much closer to oxygen than hydrogen) in a molecule whilst retaining or increasing the compound's biological activity, albeit often with different properties.[48] According to the World Drug Index, as of 2004 there were 128 fluorinated compounds with US trade names and of the 31 molecules approved in 2002, nine contained fluorine.[47] ^{19}F MRS is therefore becoming an increasingly attractive method for the investigation of fluorinated drugs and their metabolic by-products, generally focussing on their

chemical structure, anabolism, catabolism, distribution, and pharmacokinetics *in vivo*.[35] It is also relatively simple to create new tracers by the fluorination of biologically active compounds[49] and this can also be combined with ^{18}F positron emission tomography to lend further diagnostic detail.[50,51]

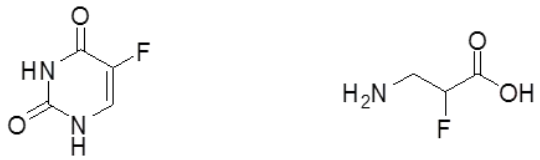

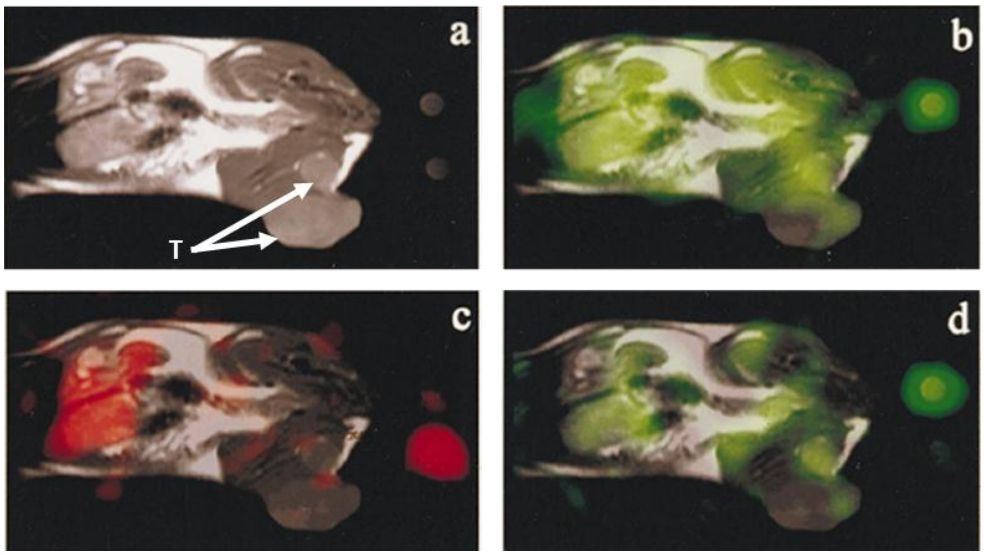

Figure 1.7 *Coronal MR images of a rat with transplanted Morris hepatoma; (a) ^{1}H MRI, (b-d) ^{19}F MR images superimposed onto ^{1}H MRI (green = 5-FU, red = FBAL). T = tumour and its position is the same in each image. Early 5-FU image (b) 5-37 min after injection shows transport of the drug into body tissue, the FBAL image (c) 40-72 min after injection indicates catabolic conversion of 5-FU to FBAL in the liver, and the late 5-FU image (d) 75-107 min after injection displays the retention of the active drug in areas that showed a strong uptake in the transport phase, including the tumour. Vials on right-hand side of images indicate complete suppression of the ^{19}F MR signal of either 5-FU (upper vial) or FBAL (lower vial) when imaging one selectively. Chemical structures of 5-FU and FBAL are shown above.*[52]

One of the most exploited uses of ^{19}F MRS in the pharmaceutical field has been the investigation of the pharmacokinetic behaviour of the fluorinated anticancer drug 5-FU, with the first MRS studies carried out in the late 1970s and early 1980s.[53,54] The mode of action of this drug involves inhibition of RNA function and interference with DNA synthesis via anabolites of 5-FU; 5-fluorouridine-5'-triphosphate and 5-fluoro-2'-deoxyuridine-5'-monophosphate. However, in the competing catabolic pathway, 5-FU is converted within the liver to the amino acid analogue α-fluoro-β-alanine (FBAL), which displays low toxicity and minimal activity, reducing the overall bioavailability of the drug.[55] It is possible to independently monitor the biodistribution of the two compounds *in vivo*, as shown in *Figure 1.7*.[52] Investigations such as this have developed the understanding of the metabolic pathway of 5-FU and aided in the design of pro-drugs that display higher activity and improved selectivity.

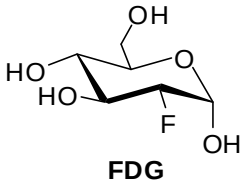

FDG

2-Fluorodeoxyglucose (FDG) is one of the most commonly employed compounds for ^{18}F positron emission tomography (PET). As FDG is an analogue of glucose, it exploits glucose transporters to enter highly metabolically active cells (tumours, brain, heart, etc.). Once inside these cells, it is converted to FDG-6-phosphate and is no longer recognised as a substrate, so does not undergo further metabolism, causing it to accumulate inside the cells. Regional uptake can then be monitored with great sensitivity by PET. However, it cannot differentiate between FDG and its metabolites, severely limiting the information that can be gathered from *in vivo* studies. ^{19}F MRS has therefore been applied in order to investigate the metabolic pathway of FDG in more detail. This has led to the identification of further, previously unidentified metabolites of FDG, highlighting the need to consider multiple imaging approaches when investigating the behaviour of drugs and other biologically relevant compounds.[56]

The concept of adding a fluorine atom to a compound that is known to target biological sites has recently been utilised for potential early diagnosis of Alzheimer's disease by *in vivo* ^{19}F NMR. ^{19}F-containing (E,E)-1-fluoro-2,5-bis(3-hydroxycarbonyl-4-hydroxy)styrylbenzene (FSB) has been shown to cross the blood-brain barrier and display high selectivity for β-amyloid plaques, which are one of the earliest indicators for the onset of Alzheimer's disease.[57] Intravenous injection of FSB, followed by ^{19}F MRI analysis, showed specific and definitive identification of β-amyloid plaques, when overlaid with the non-specific ^{1}H MRI image (*Figure 1.8*). This was confirmed by fluorescence studies on frozen brain sections.[58]

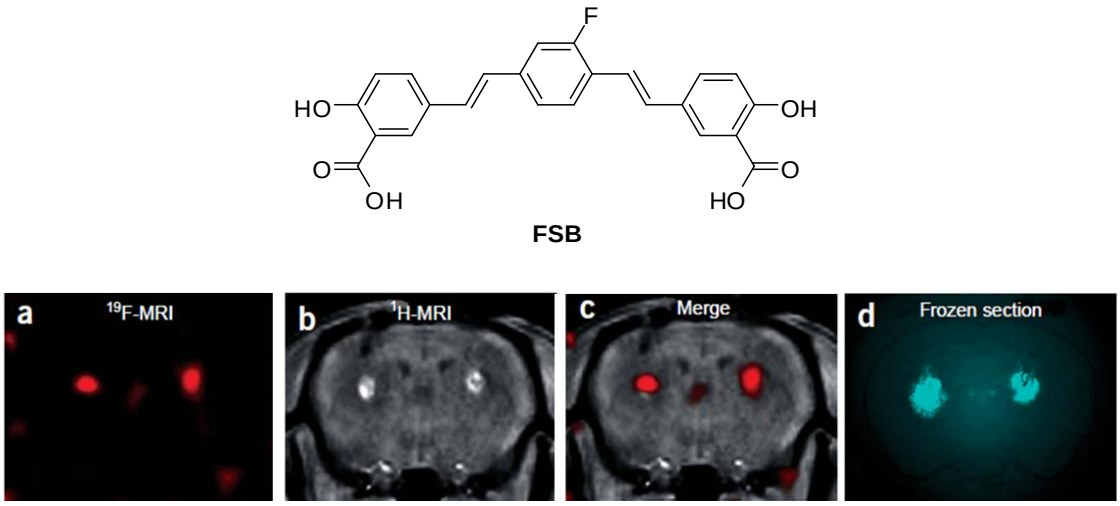

Figure 1.8 *Coronal MR images after injection of FSB into bilateral basal ganglia of 6-month-old wild-type mice; (a) ^{19}F MRI, (b) T_1-weighted gradient echo ^{1}H MRI, (c) overlay of ^{19}F and ^{1}H MR images, (d) fluorescence image of corresponding frozen brain section. Chemical structure of FSB shown above.*[58]

1.2.5 Limitations of ^{19}F MRI

The signal in ^{1}H MRI derives from nearly two thirds of all nuclei present in the body. In order for ^{19}F MRI to produce an image of similar quality, it is essential to significantly improve the sensitivity of the resulting signal. That is why, for the majority of published examples, perfluorinated probes have proved so attractive.[35] One of the reasons these agents require such a high density of ^{19}F nuclei on the molecule, in addition to a very high tissue concentration *in vivo*, is due to the intrinsically slow relaxation rates of the ^{19}F nucleus. The longitudinal relaxation rate for a ^{19}F nucleus in

a diamagnetic solution is generally of the order of 1 Hz, resulting in a relaxation time of around 1 s. For a MRS experiment, it is necessary to wait at least four times the magnitude of the relaxation time per scan in order to allow for sufficient relaxation of the NMR active nuclei of interest. This results in extremely long acquisition times, making most MRS experiments clinically unsuitable without the use of perfluorinated compounds, which still suffer from slow acquisition times, as well as added drawbacks and limited applications.

This presents a method of increasing the sensitivity in MR studies by increasing the longitudinal relaxation rate of the ^{19}F nucleus, which can be achieved by introducing a lanthanide ion, or other paramagnetic centre, in close proximity to the fluorine nucleus of interest. This is the technique that will be concentrated on for the remainder of this work. By increasing the relaxation rates, acquisition times are significantly reduced and hence a much greater number of scans may be carried out in a given length of time. There is an added benefit in that chemical shift non-equivalence may also be increased, improving the possibility of resulting probes to act as chemical shift reporters. Before discussing applications further, the theory behind these phenomena should first be considered.

1.3 Lanthanide Relaxation Theory

The most stable oxidation state of the lanthanides is +3, resulting in an electronic configuration of [Xe]4f^n, where *n* varies from 0 to 14 (*Table 1.2*). There are exceptions to this, such as when the ion can achieve an empty (f^0), half-filled (f^7), or filled (f^{14}) f orbital, for example Eu(II). When a Ln(III) ion interacts with a Lewis base, the unpaired 4*f* electrons of the lanthanide influence any NMR active nuclei that are within close proximity. This leads to perturbations of NMR parameters, such as increased relaxation, linewidth broadening, and change in chemical shift. Gadolinium(III) is unique amongst the lanthanides, in that it has an isotropic spatial distribution of unpaired *f* electrons. The remaining Ln(III) ions have an anisotropic spatial distribution

of unpaired *f* electrons and so are able to instigate a dipolar lanthanide induced shift (LIS) in solution.

The first major use for paramagnetic compounds in NMR spectroscopy was as shift and relaxation agents. The ability of lanthanide containing compounds to act as shift agents derives from the LIS,[59] the origins of which are described in further detail below. Due to the effects of this LIS, the chemical shift range for a ^{1}H NMR spectrum can be increased from the standard diamagnetic 0 to 12 ppm range up to -500 to 500 ppm, depending on the Ln(III) ion chosen. This phenomenon was employed to investigate complicated, overlapping NMR spectra of protein samples, for example.[60] This technique has become less popular in recent times, due to the introduction of high field superconducting magnets and the increasing availability of high resolution NMR spectrometers.[61]

As discussed above, another potentially advantageous property of paramagnetic NMR spectroscopy is the significant increase in relaxation rates of paramagnetic over diamagnetic compounds. In the past, this behaviour has been exploited as a mapping device. The closer a nucleus is to the paramagnetic centre, the quicker its T_2 relaxation time will be, and so, the broader its resonance will be. This allows estimations of the distance between the lanthanide ion and certain nuclei within the compound, resulting in structural information and mapping of the molecule.[62] However, the advent of 2D NMR spectroscopy (COSY, NOESY, etc.) has lessened the demand for such paramagnetic techniques. Again, further details on the basis of this relaxation enhancement effect are given below.

1.3.1 Chemical Shift

The LIS for a nucleus within a ligand that is coordinated to a Ln(III) ion can be expressed as the sum of three terms; the diamagnetic (Δ_d), the contact (Δ_c), and the pseudocontact shift (Δ_p) (*Equation 1.3*).

$$\Delta = \Delta_d + \Delta_c + \Delta_p \qquad (1.3)$$

The diamagnetic shift mainly derives from effects such as conformational changes, and is generally negligible, unless the nucleus is directly coordinated to the Ln(III) ion.[63] The contact shift stems from through-bond transmission of unpaired electron spin density to the nucleus from the 4*f* orbital. This is expressed in *Equation 1.4*. The magnitude of this contact shift decreases significantly as the number of bonds between the Ln(III) ion and the nucleus under investigation increases. This allows the identification of the nuclei directly bound to the metal:[64]

$$\Delta_c = < S_Z > F = < S_Z > \frac{-A}{\hbar \gamma_1 B_0} 10^6 \qquad (1.4)$$

where $<S_Z>$ is the expectation value of the time-average electron spin polarisation for a given paramagnetic ion (*Table 1.2*), B_0 is the magnetic field strength, γ_1 the gyromagnetic ratio, and $A/\hbar$ the hyperfine coupling constant of the nucleus under investigation.

The pseudocontact shift (PCS) is the rotationally invariant component of the dipolar interaction between the nuclei and the Curie magnetisation induced on the unpaired electrons by the applied magnetic field.[65] The electron magnetisation supplements the applied magnetic field, which leads to additional chemical shielding of the nuclei. PCS has been derived elsewhere,[66] but it can be expressed in a simplified form if the principal magnetic axes system is used. The resulting expression displays strong directional dependence (*Equation 1.5*):[65,67]

$$\Delta_p = \frac{C_J {\mu_B}^2}{60(kT)^2}\left[\frac{(3\cos^2\theta - 1)}{r^3} B_0^2 + \frac{(sin^2\theta \cos 2\varphi)}{r^3} B_2^2\right] \qquad (1.5)$$

where C_J is the Bleaney constant characteristic of the particular Ln(III) ion (*Table 1.2*), μ_B is the Bohr magneton, Θ is the angle between the nucleus under consideration and the principal axis of the lanthanide ion, and B_0^2 and B_2^2 are second order crystal field terms determined by local symmetry and donor polarisability.

For a given probe nucleus, PCS may be viewed as a 3D scalar field. *Figure 1.9* displays a typical distribution of PCS, along with an example of the effect it induces on the ^1H NMR spectrum of a given Eu(III) complex, in this case $[Eu(DOTA)H_2O]^-$. If the nucleus

under investigation resides in an area of strong positive PCS (red), the NMR shift relating to this nucleus will be shifted in the opposite direction to a nucleus located in an area of strong negative PCS (blue). In the case of $[Eu(DOTA)H_2O]^-$, any nuclei that experience positive PCS are shifted to a value of positive ppm, whereas those experiencing negative PCS are shifted to a value of negative ppm.

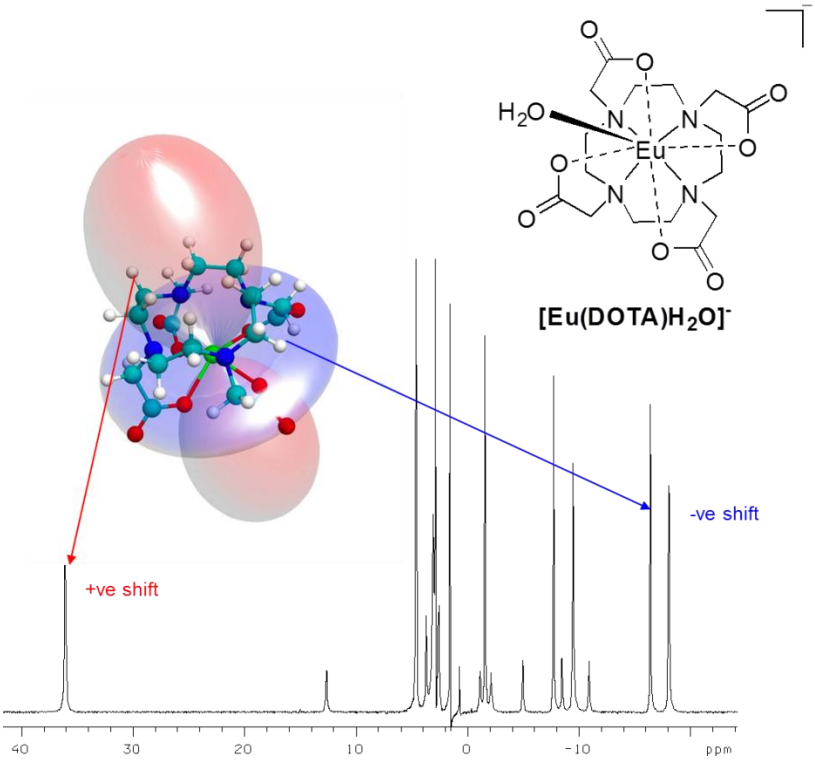

Figure 1.9 *Schematic stereodrawing of the pseudocontact shift field around a typical lanthanide complex, $[Eu(DOTA)H_2O]^-$, with an axial magnetic susceptibility tensor and the effect this has on the shifts in the ^1H NMR spectrum.*

For a given series of isostructural complexes, it is generally assumed that the ligand field coefficients are invariant amongst the lanthanides, although it has been shown that there is a general contraction across the series.[68] However, the different Ln(III) ions possess Bleaney coefficients (*Table 1.2*) of varying magnitude and sign, and it is largely this contribution that can lead to dramatically different pseudocontact shifts for common resonances in a given complex. The strong dependence of the PCS on the nuclear coordinates can be exploited in order to enhance chemical shift non-equivalence. For example, this is important in the development of chemical shift reporters that respond to changes in environmental parameters, such as pH.

Table 1.2. *Selected magnetic and relaxation properties of lanthanide(III) ions*

Ln(III)	Electronic configuration	Ground state term	μeff/μB [(a)]	Electronic relaxation time [(b)] (aqua ion, 2.1 T) / 10^{-13} s	$\langle S_z \rangle$ [(c)]	C_J [(d)]
Ce	[Xe] $4f^1$	$^2F_{5/2}$	2.56	0.90	-0.97	-6.5
Pr	[Xe] $4f^2$	$^3H_4$	3.62	0.57	-2.96	-11.4
Nd	[Xe] $4f^3$	$^4I_{9/2}$	3.68	1.15	-4.45	-4.5
Pm	[Xe] $4f^4$	$^5I_4$	2.68	unknown	-3.94	2.4
Sm	[Xe] $4f^5$	$^6H_{5/2}$	1.55-1.65	0.45	0.22	-0.5
Eu	[Xe] $4f^6$	$^7F_0$	3.40-3.51	0.09	7.57	4.0
Gd	[Xe] $4f^7$	$^8S_{7/2}$	7.94	10^4-10^5	31.5	0
Tb	[Xe] $4f^8$	$^7F_6$	9.7	2.03	31.9	-87
Dy	[Xe] $4f^9$	$^6H_{15/2}$	10.6	2.99	28.6	-100
Ho	[Xe] $4f^{10}$	$^5I_8$	10.6	1.94	22.6	-39
Er	[Xe] $4f^{11}$	$^4I_{15/2}$	9.6	2.38	15.4	32
Tm	[Xe] $4f^{12}$	$^3H_6$	7.6	3.69	8.21	53
Yb	[Xe] $4f^{13}$	$^2F_{7/2}$	4.5	1.37	2.59	22

(a) Ref.[69] (b) Refs.[70–72] (c) Ref.[73] (d) Ref.[65]

1.3.2 Relaxation Theory

In a standard NMR experiment, the nucleus of interest is excited by a radiofrequency pulse that tips the magnetisation vector from the z-axis to the transverse plane. The magnetisation processes around the direction of the magnetic field and recovers to the state of equilibrium. This process is recorded as a free-induction decay (FID), which is then converted by Fourier transform to obtain the final NMR spectrum. The speed of this process is defined by the relaxation rates.[74]

The longitudinal relaxation time, T_1, is so-called as it is related to the time it takes for the magnetisation to relax back to the thermal equilibrium, along the direction of the magnetic field, i.e. along the z-axis. Likewise, the transverse relaxation time (T_2) describes the relaxation of the x and y components. The corresponding longitudinal

and transverse relaxation rates (R_1 and R_2 respectively) are simply the reciprocal of these relaxation times, as shown in *Equation 1.6*.

$$R_1 = \frac{1}{T_1} \qquad R_2 = \frac{1}{T_2} \qquad (1.6)$$

Relaxation processes are driven by fluctuations in the local field experienced by the nucleus of interest.[31] In paramagnetic NMR spectroscopy, the unpaired electron(s) present provide additional pathways for relaxation back to the ground-state, thereby increasing relaxation rates significantly. Further details into this relaxation enhancement are discussed below, with a particular emphasis on Ln(III) paramagnetic relaxation rate enhancement on ^{19}F NMR spectroscopy.

1.3.2.1 Fluorine relaxation in lanthanide-based systems

As discussed, the coordination of a ligand to a paramagnetic lanthanide ion enhances both the longitudinal and transverse relaxation rates. For ^{19}F nuclei in non-viscous solutions of paramagnetic ions, there are five important spin relaxation processes that contribute to this increase in relaxation rates. The first two of these processes, chemical shift anisotropy (CSA) and inter-nuclear dipole-dipole (DD) relaxation, can largely be ignored. This is due to the fact that they are diamagnetic relaxation processes and so are negligible in comparison to the much larger paramagnetic terms. For example, experimentally observed ^{19}F T_1 values are generally of the order of 1 s. This means that CSA and inter-nuclear DD interactions cannot contribute more than 1 Hz to the paramagnetic relaxation rates, which may be of the order of 100 Hz. The third process, the contact mechanism, can also be ruled out due to its strong distance dependence. DFT calculations have shown that a ^{19}F nucleus positioned over 5 Å away from an f-type unpaired electron gives a zero value for this term.[75–77]

The remaining two processes (electron-nucleus DD and the Curie relaxation) do contribute significantly to paramagnetic relaxation rates and so have to be taken into consideration. Combination of their independent contributions to the relaxation rates result in *Equations 1.7* and *1.8*, with the first term in each equation relating to

modulation of the electron-nucleus dipolar interactions and the second term arising from the Curie relaxation:[75]

$$R_1 = \frac{2}{15}\left(\frac{\mu_0}{4\pi}\right)^2 \frac{\gamma_F^2 \mu_{eff}^2}{r^6}\left(\frac{7\tau_{R+e}}{1+\omega_e^2\tau_{R+e}^2} + \frac{3\tau_{r+e}}{1+\omega_F^2\tau_{R+e}^2}\right) + \frac{2}{5}\left(\frac{\mu_0}{4\pi}\right)^2 \frac{\omega_F^2 \mu_{eff}^4}{(3kT)^2 r^6}\left(\frac{3\tau_R}{1+\omega_F^2\tau_R^2}\right) \quad (1.7)$$

$$R_2 = \frac{1}{15}\left(\frac{\mu_0}{4\pi}\right)^2 \frac{\gamma_F^2 \mu_{eff}^2}{r^6}\left(4\tau_{R+e} + \frac{3}{1+\omega_e^2\tau_{R+e}^2} + \frac{13\tau_{r+e}}{1+\omega_F^2\tau_{R+e}^2}\right) + \frac{1}{5}\left(\frac{\mu_0}{4\pi}\right)^2 \frac{\omega_F^2 \mu_{eff}^4}{(3kT)^2 r^6}\left(4\tau_R + \frac{3\tau_R}{1+\omega_F^2\tau_R^2}\right) \quad (1.8)$$

where μ_0 is the vacuum permeability, γ_N is the magnetogyric ratio of the nucleus (i.e. ^{19}F), r is the electron-nuclear distance, τ_R is the rotational correlation time, ω_N is the nuclear Larmor frequency, T is the absolute temperature, k is the Boltzmann constant, and the remaining symbols are defined as below:

$$\mu_{\text{eff}}^2 = g_j^2 \mu_B^2 J(J+1), \qquad \tau_{R+e} = (\tau_R^{-1} + T_{1e}^{-1})^{-1}, \qquad \omega_e = \left(\frac{g_J \mu_B}{\hbar}\right) B_0$$

in which g_J is the effective electron g-factor, μ_B is Bohr magneton, $J(J + 1)$ is the effective electron angular momentum, and T_{1e} is the longitudinal relaxation time of the electron spin.

The behaviour of the relaxation rates can be plotted as a function of the effective magnetic moment, μ_{eff}, and the electron-nuclear separation, r. This is represented in *Figure 1.10*. The dependence on the electron-nuclear separation is to the reciprocal sixth power in both the dipolar and Curie mechanism, while the effective magnetic moment is quadratic. It is important to note that the relaxation rates are strongly temperature dependent, with the effective magnetic moment, electron relaxation rate, rotational correlation time, and the Curie term all affected by changes in temperature. It is therefore imperative to keep the temperature at a constant value during experimental measurements. As the longitudinal relaxation rate can be measured with very high precision, it is possible to extract the electron-nucleus distances, rotational correlation times, and effective magnetic moments by fitting to these equations.[75]

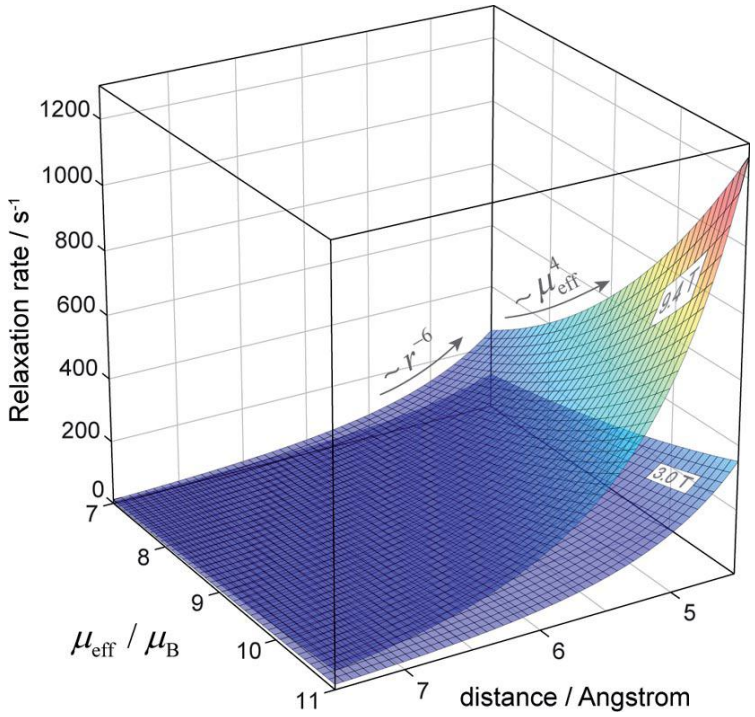

Figure 1.10 *Longitudinal ^{19}F spin relaxation rate as a function of Ln-F distance (r) and the effective magnetic moments of the electron (μ_{eff}) at two different magnetic fields (3.0 and 9.4 T). T_{1e} = 0.2 ps, τ_r = 250 ps, and T = 298 K.*[67]

While an increase in the longitudinal relaxation rate will allow faster acquisition times and increase sensitivity in imaging experiments, an increase in the transverse relaxation rate will lead to increased line broadening and so decrease sensitivity. Therefore, a balance needs to be struck between increasing R_1 while keeping R_2 as relatively low as possible when designing a suitable probe. Volumetric plots (*Figure 1.11*) have been generated that display the dependence of both R_1 and R_2 on the magnetic field (B_0), the internuclear distance (r), and the rotational correlation time (τ_r).[75] Analysis of these plots allows a good estimation of the ideal Ln-F distance to be extracted. To achieve two-orders of magnitude increases in both relaxation rates (ca. 100 Hz) at 3.0 T, a Ln-F distance of between 5.5 and 7 Å would be expected for a general macrocyclic lanthanide (Ln = Tb, Dy, Ho, Er, Tm) complex, with rotational correlation times for such complexes being in the region of 10^2-10^3 ps. It is also important to note that chemical exchange processes may also contribute to an increase in R_2, so it is also essential to keep exchange processes at a minimum.[67]

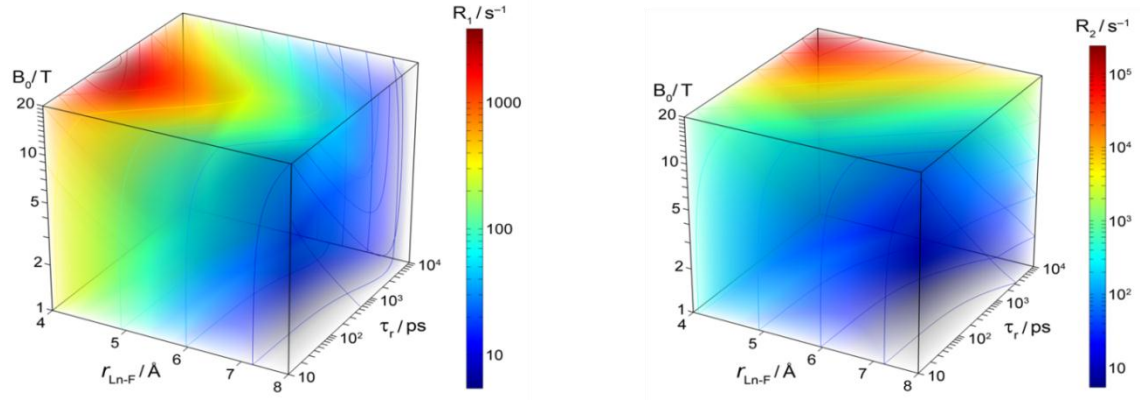

Figure 1.11 *Volumetric plots showing the variations in the longitudinal (left) and transverse (right) relaxation rates with applied field (B_0), mean distance from paramagnetic centre (r), and effective rotational correlation time (τ_r). Analysis is based upon Equations 1.7 and 1.8 with the assumptions μ_{eff} = 10 BM and τ_e = 0.2 ps.*[75]

1.4 Responsive Systems for MRI applications

MRI contrast provides excellent sensitivity for detecting subtle changes in anatomy and function, but poor specificity when assigning image contrast to pathologies.[23] A good example is in the diagnosis of breast cancer lesions, where MRI is in fact better than X-ray mammography in its ability to detect such tumour tissues. However, many non-cancerous lesions are also detected by MRI, leading to false-positive diagnosis and so MRI is only recommended for women with a high cancer risk in this case.[78] Also, the changes in anatomy and function that are detected by standard MRI techniques are often caused by mid- to late- stage developments of a disease, which may be too late for early-stage intervention.[23] In order to overcome this limitation, a large amount of research has been undertaken into the development of responsive MRI contrast agents whose relaxivity can signal a specific parameter of the microenvironment in which they localise. However, a large amount of the work published has so far concentrated on *in vitro* examples, with very few applications of systems that work *in vivo*.[79] It is also important to note that relaxivity is concentration dependent. Therefore, in order for such a system to be applicable there must be some method of examining the concentration of the probe *in vivo*, which is extremely challenging. A selection of examples will now be discussed, covering a number of diagnostically

relevant physiochemical variables that have been successfully reported by changes in the relaxivity of Gd(III) complexes.

1.4.1 pH-responsive systems

Changes in pH often accompany the development of various pathologies, such as stroke, infection, and renal failure. Therefore, mapping pH *in vivo* is an important task in medical imaging and can also be vital for developing therapies that remain effective in regions of altered pH.[80] Assessment of *in vivo* pH levels can be particularly important when diagnosing cancer, as poor perfusion, reduced bicarbonate levels, and increased lactic acid secretion within cancerous tissue often leads to acidic conditions.[81] The high spatial resolution of MRI is particularly well suited for evaluation of pH variations over small tissue volumes.[23] The pK_a of any pH-dependent modulation should ideally be in the physiologically relevant pH range of 6.5 to 7.5.

One method of reporting changes in pH is to develop pH-dependent ligands that alter water accessibility to the Gd(III) ion. Gillies, Sherry, and co-workers have developed a dual injection technique for measuring the extracellular pH (pH_e) in kidney and tumour models, involving the use of two different Gd(III) contrast agents; pH-insensitive $[Gd(DOTP)]^{5-}$ and pH-sensitive $[Gd(DOTA\text{-}4AmP)]^{5-}$ (*Figure 1.12*).[82,83] The pH-dependent behaviour of $[Gd(DOTA\text{-}4AmP)]^{5-}$ is believed to arise from the hydrogen-bonding network created by the protonated phosphonates aiding exchange of the bound water protons with the protons of the bulk water, resulting in a two-fold increase in T_1 relaxation time from pH 6.0 to 8.5. The idea behind this dual contrast agent strategy is that the distribution of the pH-insensitive agent can be used to infer the local concentration of the pH-sensitive agent, removing the issue of monitoring the concentration directly. Despite being structurally dissimilar, the two complexes were found to have similar renal pharmokinetics due to similarities in their structure and charge and so were assumed to have identical local concentrations. This may not be entirely accurate, as minor structural differences can have large effects on biodistribution kinetics. The system did generate the expected pH profile images with mice kidney studies. With more difficult tumour models (C6 glioma, *Figure 1.12*), the

pharmokinetics of the two contrast agents were well correlated over the whole tumour model, but this correlation was substantially reduced when the tumours were examined on a pixel-by-pixel basis. It is also important to note that the two contrast agents cannot be applied simultaneously in this example. An *in vivo* experiment would require a long delay between administrations of the two contrast agents, in order to allow for full body clearance of the first probe before addition of the second. During this time, physiopathological changes may occur, further endangering the assumption of identical biodistribution.[79]

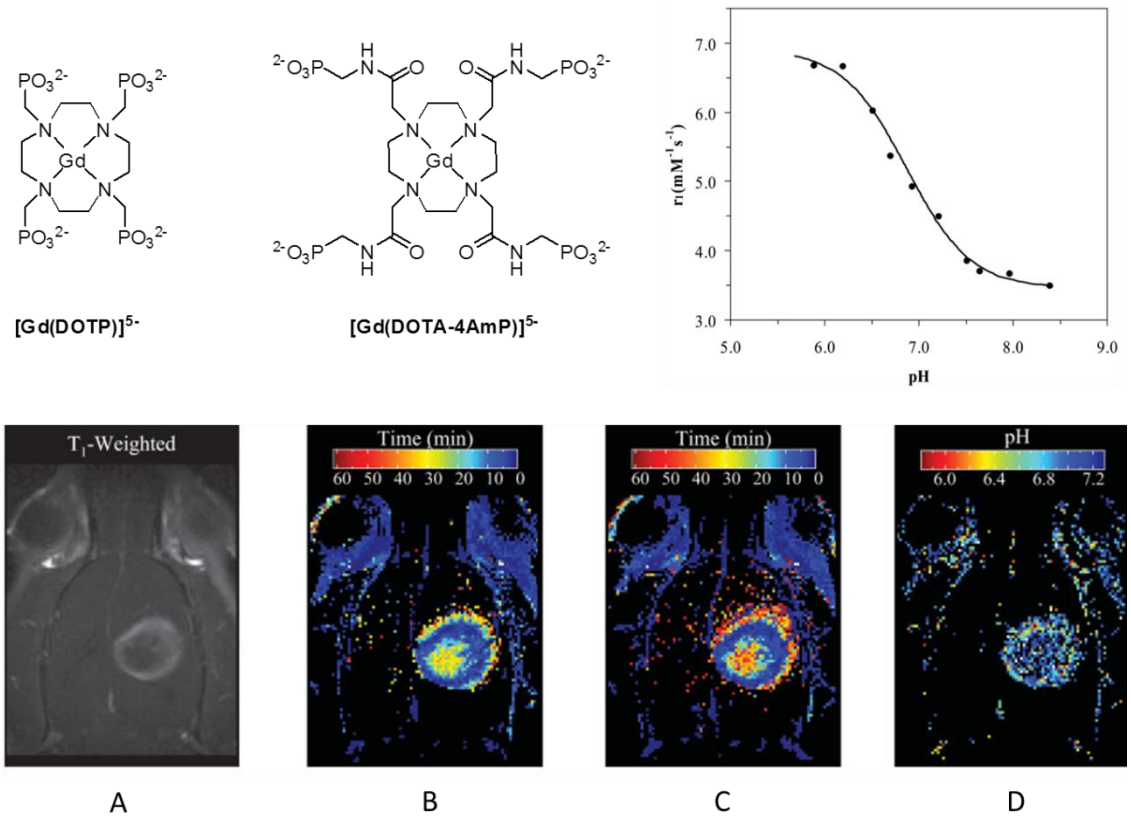

Figure 1.12 *Top; chemical structures of $[Gd(DOTP)]^{5-}$ and $[Gd(DOTA\text{-}4AmP)]^{5-}$ with dependence of $[Gd(DOTA\text{-}4AmP)]^{5-}$ relaxivity on pH (37°C, 4.7 T). Bottom; representative time-to-maximal intensity (TMI) images and calculated pH_e map of a C6 glioma in the brain of a live rat. (A) T_1-weighted ^1H MRI of the brain prior to administration of either contrast agent, (B) TMI image after administration of pH-insensitive $[Gd(DOTP)]^{5-}$, (C) TMI image after administration of pH-sensitive $[Gd(DOTA\text{-}4AmP)]^{5-}$, (D) resulting calculated pH_e image.*[83]

A further example utilising the pH-dependent nature of $[Gd(DOTA\text{-}4AmP)]^{5-}$ has been published that negates the need to measure an absolute value of the tissue pH by only aiming to image areas of abnormally low pH, therefore not requiring knowledge of the probe concentration. For example, when the complex was administered to control hearts, there were no regions with observable differences in their contrast enhancement, whereas ischemic hearts display distinctly brighter areas that are attributable to areas with low pH values. This complex has also been applied to rat pancreatic islets embedded in alginate beads, which showed considerable contrast enhancement only upon exposure to high levels of glucose. This is due to glucose-mediated insulin secretion being accompanied by the release of protons and the resulting increase in local proton concentration is detected by increase in relaxivity of $[Gd(DOTA\text{-}4AmP)]^{5-}$.[84] Another recent *in vitro* example from Caravan and co-workers has involved the use of a derivative of $[Gd(DOTA\text{-}4AmP)]^{5-}$ with an incorporated ^{18}F atom to form a bimodal MR/PET agent.[85] This allows the concentration of the complex to be calculated from the total PET signal, which is independent of pH, but does require the use of ionising radiation and the associated increase in cost.

Early work in Durham and Italy led to the development of a sulphonamide-based system that displays pH-dependent modulation of relaxivity due to a change in hydration state (q) associated with the on/off ligation of a sulphonamide nitrogen donor (*Figure 1.13*).[86] Control over the pK_a of the protonation can be exerted by variation of the electron density of the nitrogen, which can be tuned by altering the identity of the *para*-substituent, R. Variation of this substituent led to the determination of protonation constants of 5.7, 6.4, and 6.7 for the $-CF_3$, -Me, and -OMe moieties respectively.

It was expected that intermolecular binding of endogenous anions (lactate, bicarbonate, etc.) or protein might displace bound water, thereby suppressing the change in relaxivity. In order to combat this, a related series of ligands were designed with carboxyalkyl substituents on the carboxylate pendant arms. However, from the related europium(III) emission studies it was found that competitive intramolecular

carboxylate coordination was occurring. This could be minimised by either enhancing electron density at the sulphonamide nitrogen or by enlargement of the chelate ring from 7 to 8. Therefore, the most successful system was found to be that with the para-CF_3 substituent and a longer carboxyalkyl arm (3-CF_3, *Figure 1.13*), which displayed a 48 % change in relaxivity over the pH range 7.4-6.8 (298 K, 65.6 MHz, 50 % human serum solution). This system also displays significant amplification of relaxivity changes upon protein binding. This amplification derives from the non-covalent interaction of the gadolinium complex undergoing relatively fast water exchange with a more slowly tumbling macromolecule.[86] In order to allow the concentration of this system to be mapped *in vivo*, a proof of concept dual MRI/SPECT agent has recently been developed that utilises a gadolinium(III) sulphonamide compound (1-OMe, *Figure 1.13*) in combination with the equivalent holmium(III) complex as a concentration reporting SPECT tracer.[87] Another recent example has taken the same idea of alteration of hydration state with varying pH, but with an aminoethyl substituent in place of the sulphonamide.[88] However, unlike the sulphonamide compounds, the pK_a for this system is not in the ideal physiological range, although there is scope to improve this by variation of the amino-substituents.

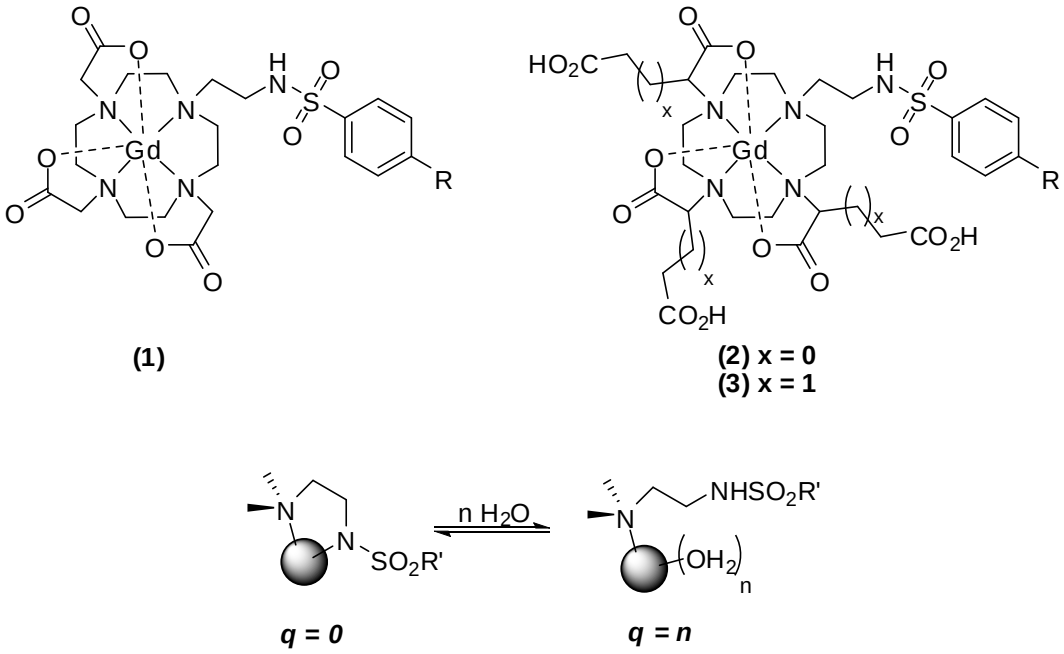

Figure 1.13 *Chemical structure of sulphonamide-based pH responsive systems (R = CF_3, Me, OMe) and the variation in coordination environment of the lanthanide ion as a function of pH.*

An alternative approach is to design contrast agents that experience a change in rotational tumbling time as a function of pH. For example, in the phospholipid mimetic structure [Gd($(C_{18})_2$-DTPAGlu)], high pH causes deprotonation resulting in higher lipophilicity, driving the formation of colloidal aggregates and causing an increase in relaxivity (*Figure 1.14*).[89] This has also been reported with an analogous DO3A-derivative,[90] as well as gadofullerene derivatives that behave in the opposite manner, i.e. increased relaxivity at low pH.[91] A related PAMAM dendritic contrast agent has been shown to display an increase in rigidity as pH decreases from 11 to 6, resulting in a relaxivity increase of 60 %.[92]

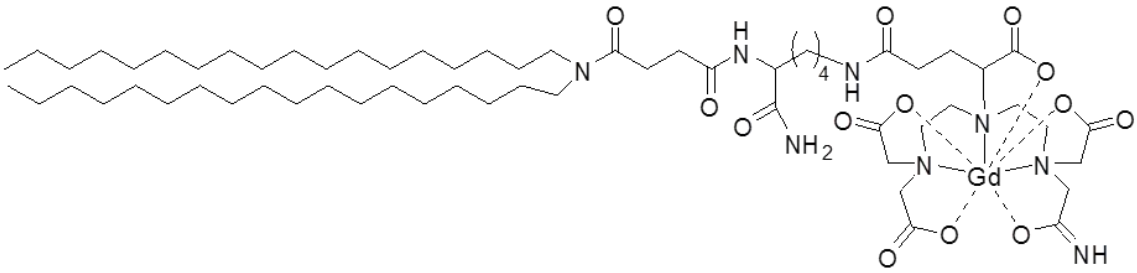

[Gd($(C_{18})_2$-DTPAGlu]

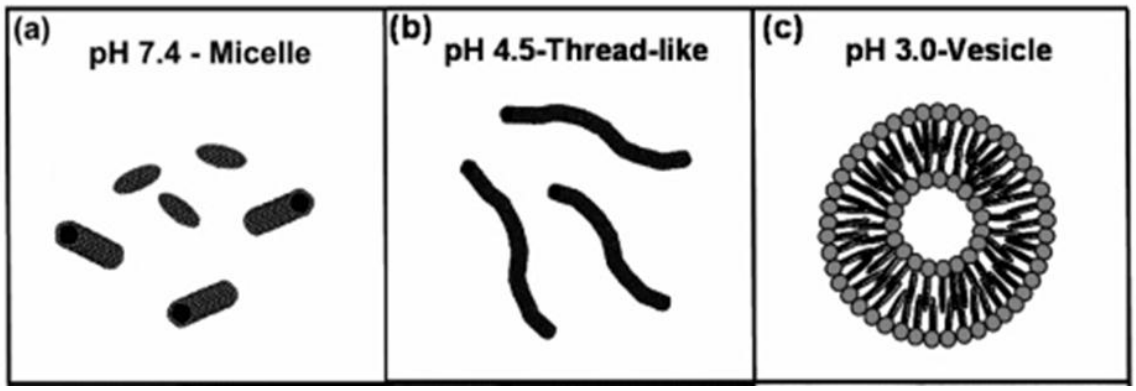

Figure 1.14 *Chemical structure of [Gd($(C_{18})_2$-DTPAGlu)] pH responsive system and illustration of the different structural forms the ligand takes at varying pH.*[89]

1.4.2 Molecular imaging of cations, anions, and other metabolites

MRI contrast agents are relatively insensitive, requiring a minimum threshold of around 0.01-10 mM for adequate *in vivo* detection (for comparison PET, SPECT, and fluorescence imaging typically have pM detection sensitivity thresholds). This means that endogenous metabolites present at higher concentrations than this detection threshold are suitable targets for responsive MRI.[23] It is vital that the specificity of any

non-covalent metabolite binding targets only the particular molecule of interest in a competitive medium, otherwise interpretation of any relaxivity changes is almost impossible. Ideally, any responsive behaviour should also be reversible.

Metal ions are associated with numerous biological signalling pathways and pathologies and the rapid flux of metal ions on a sub-second timescale can require rapid measurements, posing difficulty for accurate quantitative investigation by MRI.[23] For example, intracellular calcium plays an important role in muscular contraction, neuronal transduction, and hormonal secretion, leading to a number of gadolinium(III) compounds being proposed to signal variation in Ca(II) concentration by changes in relaxivity.[93] One example of a system developed in Durham, involves the use of an eight-coordinate pyro-EGTA-based moiety that is attached to the Gd(III)-containing macrocycle via an amide bond (*Scheme 1.1, A)*.[25] In the absence of Ca(II), the amide carbonyl oxygen binds to the Gd(III) ion resulting in a 7-ring chelate. However, when Ca(II) is added the amide carbonyl preferentially coordinates to the added metal, resulting in a vacant site at the Gd(III) that can be occupied with water. This is accompanied by an increase in relaxivity. Ca(II) levels in cerebrospinal fluid may drop by up to 90 % in a traumatic event and this should be reflected by a 22 % variation in r_{1p} with this system at 1.4 T, provided that the timescale for MRI data acquisition is faster than the time it takes for the Ca(II) levels to return to equilibrium and that the local concentration of contrast agent does not change over this time.

Minor alteration to the structure of this compound (6-coordinate pyro-EGTA instead of 8-coordinate) allows selective binding of Zn(II) (*Scheme 1.1, B)*. A similar example based on the same principle but with a di-2-picolylamine chelator containing a naphthylamine-derivative moiety has recently been proposed as a bimodal probe for detection of copper(II), with the addition of Cu(II) signalled by both an increase in relaxivity and quenching of the naphthylamine fluorescence signal (*Scheme 1.1, C)*.[94] Examples of systems that exhibit an increase in relaxation rates due to an increase in rotational correlation times in the presence of iron(II) and iron(III) have also been reported.[95–97]

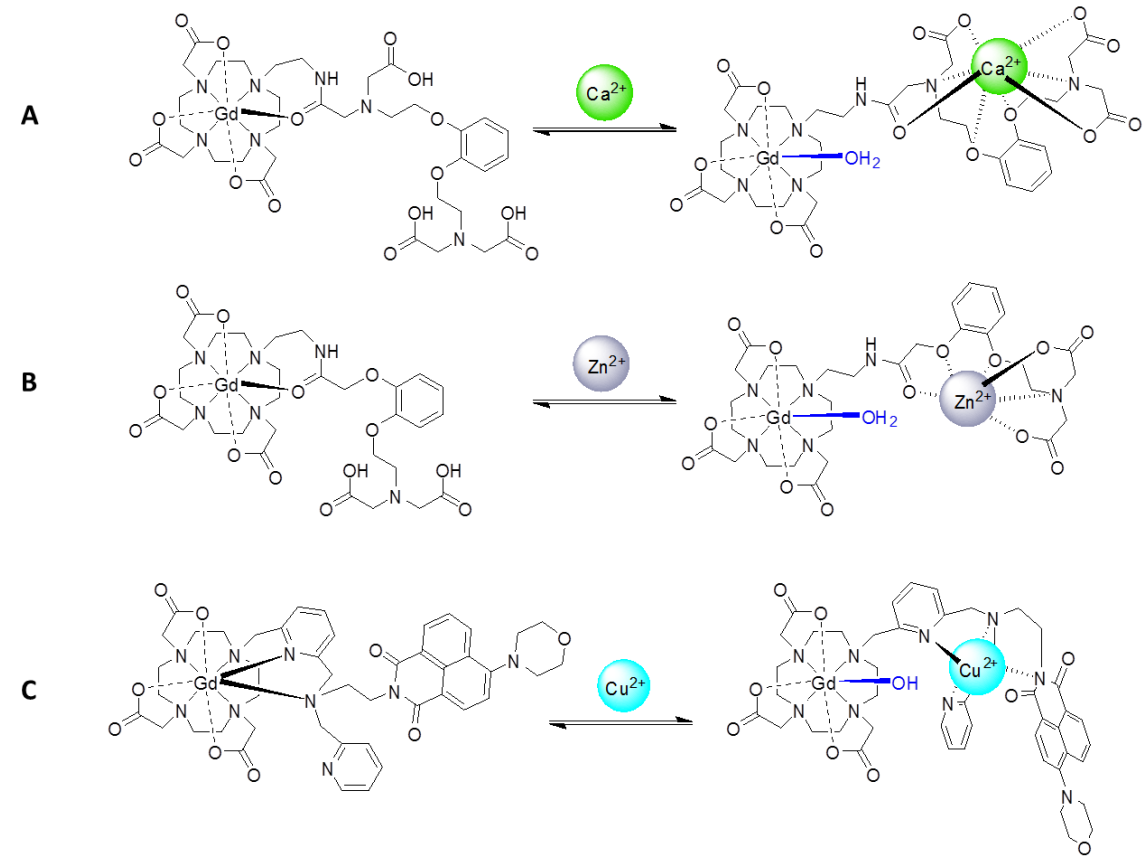

Scheme 1.1 *Mode of action of cation-responsive Gd(III) complexes discussed.*[25,94]

As mentioned previously, variation in levels of endogenous anions can be indicative of serious health issues. However, unlike the numerous examples of metal-responsive MRI systems, contrast agents that report on anionic analytes are much rarer, mainly due to the intrinsic difficulty in binding anions selectively in aqueous media.[98] There have been some studies into the behaviour of Gd(III) complexes with biologically significant anions (acetate, lactate, citrate, etc.)[99,100] and systems have been developed that show changes in luminescence for selective anions,[21,101,102] but there are very few examples of systems that selectively report on the presence of anions by modulation of relaxivity. Recently, Vilar and co-workers did report a pyrophosphate-responsive system that utilises two phosphate-binding zinc(II)-dipicolylamine moieties attached to a Gd(III)-DTPA-bis-amide complex (*Figure 1.15*).[98] Addition of pyrophosphate initially causes a decrease in relaxivity until one equivalent of pyrophosphate (PPi) had been added, which is suggested to be due to the formation of a more spherical overall species, reducing the rotational correlation time, as the hydration state of the complex remains unchanged. Upon addition of further equivalents of PPi, the binding mode

changes, resulting in an increase in τ_R and a corresponding increase in r_{1p}. While this system does show good specificity for PPi over mono-phosphates and other similar anions, addition of other polyphosphates (e.g. ATP) is likely to be competitive. Also, the dual-mechanism of relaxivity modulation that results in an initial decrease in r_{1p} followed by a significant increase is likely to prove too complicated to be directly applicable in an *in vivo* situation.

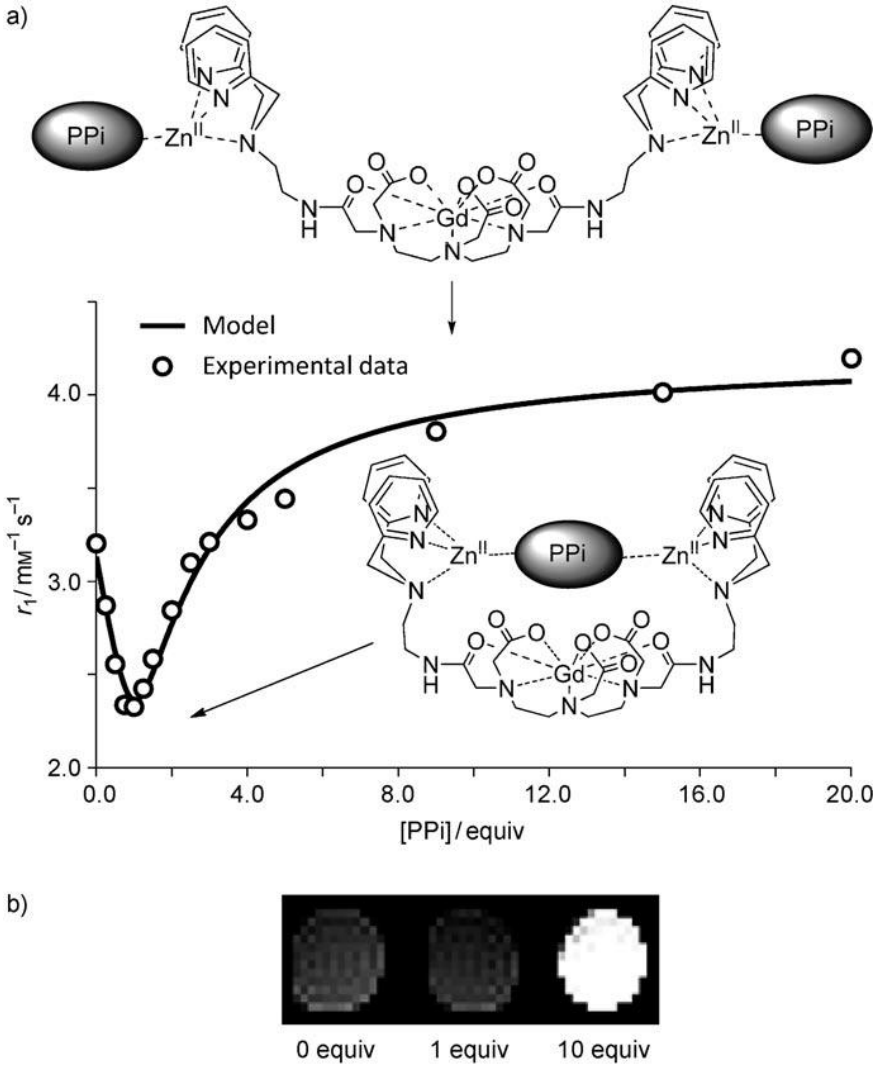

Figure 1.15 *(a) Relaxivity plot displaying suggested binding modes with initial formation of the 1:1 complex accompanied by a decrease in relaxivity, followed by conversion to the 1:2 complex that displays a marked increase in r_{1p}; (b) Phantom images of increasing equivalents of PPi with respect to concentration of Gd(III) complex.*[98]

1.5 Potential Molecular Adducts for Contrast Enhanced MRI

Conjugation of multiple paramagnetic MRI contrast agents to a macromolecular adduct can have a number of advantages. By dramatically increasing the molecular weight and steric bulk of the system, the rate of clearance from the body is markedly reduced with *in vivo* experiments, increasing the retention time and reducing the concentration of contrast agent that needs to be administered. Macromolecular adducts can also be employed to target specific areas of the body. Of particular interest is the potential to target tumour cells by the enhanced permeability retention effect,[103] which is detailed further below. There are a wide range of adducts that have so far been investigated, with a far from exhaustive selection chosen to be discussed here.

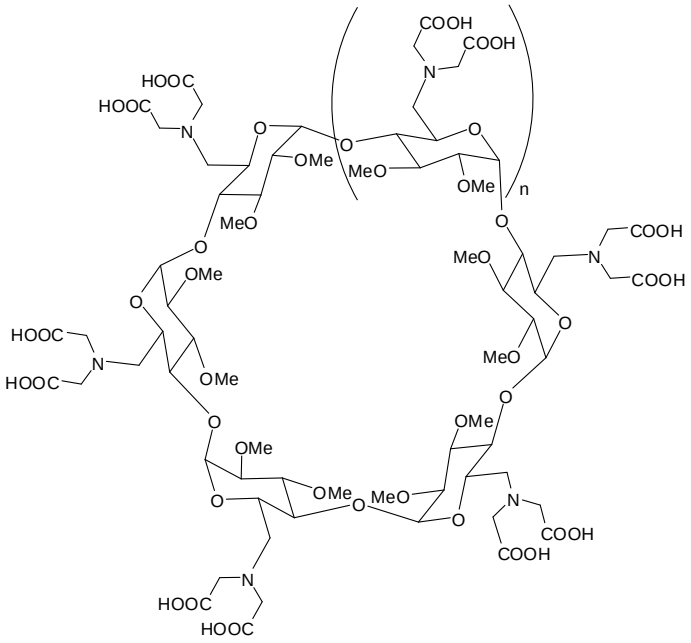

Figure 1.16 *Chemical structure of polycarboxylated EDTA-type cyclodextrin (CD) ligand reported by Yannakopoulou and co-workers (n = 0, AEDTA; n = 1, BEDTA; n = 2, GEDTA).*[104]

A potential Gd(III) contrast agent had been developed by Yannakopoulou and co-workers based on a polycarboxylated EDTA-type cyclodextrin (CD) ligand, which contained an α-, β-, or γ-CD core (AEDTA, BEDTA, and GEDTA respectively) with bis(carboxymethyl)amino groups on all the primary hydroxyl CD sites (*Figure 1.16*).[104] Mass spectrometry and luminescence emission analysis showed the formation of

multimetallic complexes upon addition of a lanthanide(III) ion (2-3 for AEDTA, mainly 3 for BEDTA, and 4 for GEDTA), with DFT calculations predicting each Ln(III) ion binding *via* four carboxylate oxygen atoms, two nitrogen atoms, and a glucopyranose oxygen. They show some potential for use as contrast agents as they display relaxivity values up to 12 times larger than commercial probes (Magnevist® and Dotarem®) in human blood plasma at 100 MHz and show no sign of toxicity in preliminary cytotoxicity studies in human skin fibroblasts. However, the kinetic stability of these systems with respect to loss of gadolinium has not been evaluated in detail and it is likely that significant loss of the Ln(III) ion from the adduct would occur *in vivo*.

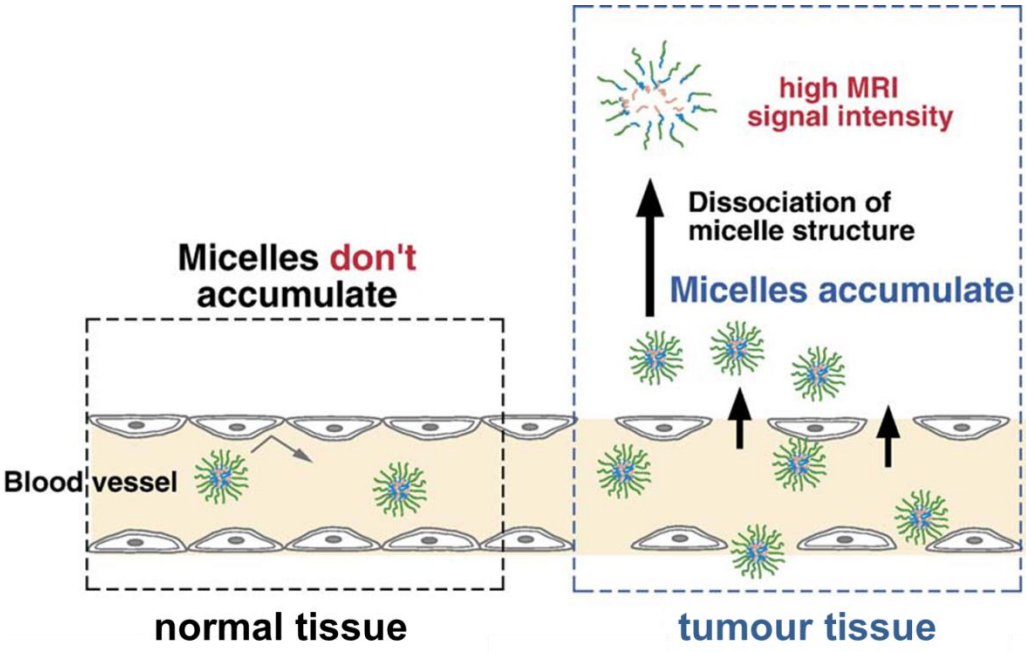

Figure 1.17 *Schematic representation of the polymeric micelle MRI probe developed by Yokoyama and co-workers displaying the concept of the enhanced permeability retention effect (EPR).*[105]

Yokoyama and co-workers have developed a polymeric micelle MRI probe based on anionic block co-polymers. As the polymeric micelle is an associate of many block copolymer chains, when dissociated the individual chains can be easily excreted through the kidneys, lowering chronic toxicity and keeping the signal intensity in vascular space low. However, the pharmacokinetics of this system is suitable for the targeting of tumours, where the micelle can enter into the tumour vasculature. The micelle is then dissociated to its individual block co-polymers and they are retained for

a relatively long time due to the poor lymphatic drainage at the tumours site (EPR effect, *Figure 1.17*).[105] This system works particularly well for MRI purposes as the dissociated block co-polymers display a much greater relaxivity than the polymeric micelle, due to the Gd(III) being situated in the inner core of the micelle, hindering access to the bulk water. The block copolymers only accumulate in tumour tissue, as they are rapidly excreted from the rest of the body, and hence the only major increase in signal intensity should be within the tumour. This principle was proved *in vivo* with colon 26-bearing CDF_1 female mice. A two-fold increase in signal intensity was observed following selective accumulation of the polymeric micelle 24 hours after injection (*Figure 1.18*).[106]

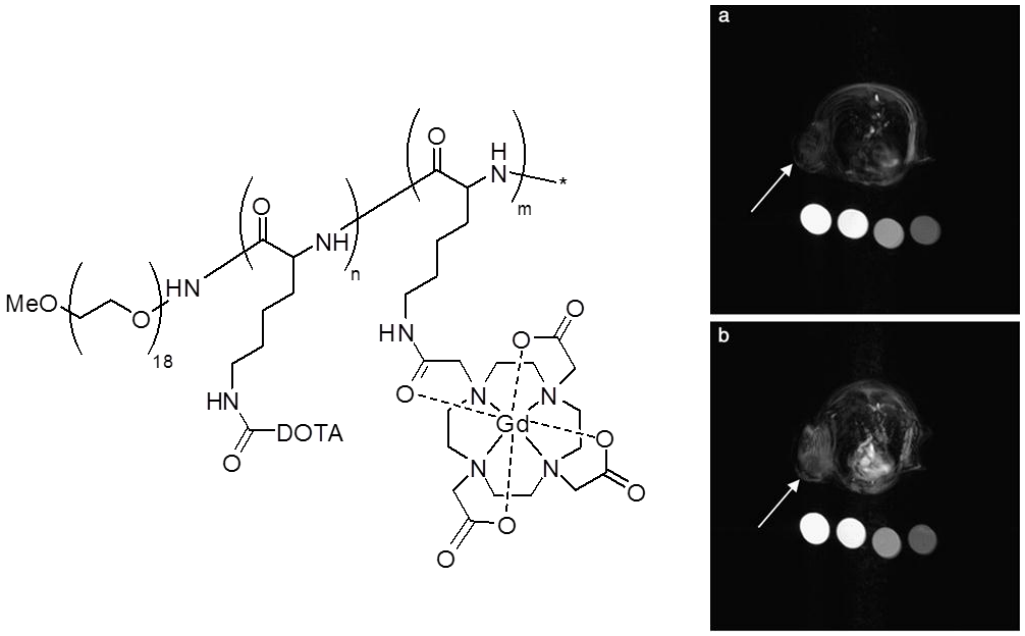

Figure 1.18 *Chemical structure of anionic block copolymer reported by Yokoyama and co-workers and T_1-weighted MR images of axial slices (a) before and (b) 24 h after injection at dose of 0.05 mmol Gd/kg. Arrow indicates the tumour and circles are stock solutions of (left to right) 1.0 mM, 0.5 mM, 0.1 mM, and 0 mM Gd(III) ion in agarose gel.*[106]

Dendrimers are becoming an increasingly important class of high molecular weight adducts and have found multiple applications in drug delivery, transfection, and tissue engineering. This is due to the highly branched nature of these systems with a defined number of end-groups and the possibility of tuning the structural elements to affect both the surface and core properties of the macromolecule.[107,108] Numerous ideas

have been suggested for developing dendrimer-based MRI contrast agents. For example, Sherry and co-workers have designed a system based on an ethylenediamine core Generation 5-PAMAM dendrimer (128 terminal amines) coupled to a pH-responsive Gd(III) probe, with around a 75 % coverage of complexes on the macromolecule, i.e. 96 of the 128 sites per dendrimer.[109] This succeeded in both increasing the relaxivity, r_{1p}, and enhancing the difference in relaxivity, Δr_{1p}, between the low and high pH states by more than a factor of 2, as shown in *Figure 1.19*. This clearly shows great potential, but further work needs to be done to see if such a system could be applied *in vivo*, and whether such a large macromolecule would be well tolerated by the body. There also needs to be a method for analysing the local concentration of the probe as discussed in *Section 1.4*.

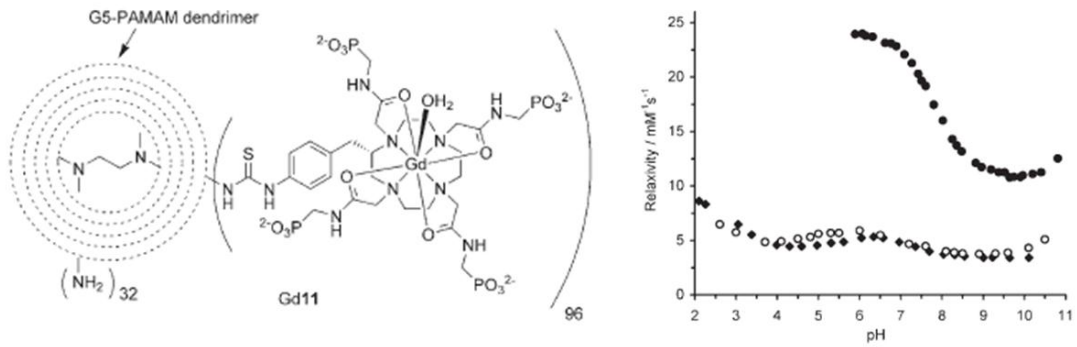

Figure 1.19 *Left) Representation of G5-PAMAM dendrimer coupled to pH-responsive Gd(III) complexes; Right) Variation of relaxivity with pH (upper line is generated from dendrimer-based Gd(III) complexes while lower lines are from analogous monomer units of the Gd(III) complex).*[109]

1.6 Paramagnetic Enhanced Heteronuclear MRI/MRS

As discussed in *Section 1.3*, relaxation rates of NMR active nuclei can be dramatically increased by the introduction of a proximate paramagnetic ion, resulting in an increase in signal intensity for a given time. It can also have the added benefit of increased chemical shift non-equivalence, depending on the paramagnetic ion chosen. While a large amount of research has been carried out in the area of paramagnetic MRI contrast agents that enhance the relaxation rates of water molecules, comparatively

little work has been published in the area of paramagnetic enhanced heteronuclear MRI/MRS, despite the enormous potential of imaging nuclei such as ^{19}F. Interest has started to increase in the last few years and a brief overview of some of the more recent studies carried out in paramagnetic enhanced ^{19}F MRI/MRS and related areas will now be detailed, followed by the work conducted previously within our research group that laid the foundations for the research reported in this thesis. Alternative methods not discussed here have also been suggested for enhancing ^{19}F MRI signal intensity, such as the use of hyperpolarisation.[110]

1.6.1 Enhancing signal intensity

One of the earliest examples of ^{19}F MRI paramagnetic relaxation enhancement was reported in the mid-1990s, utilising Gd(DTPA) to enhance the *in vivo* signal observed from previously administered trifluoromethylsulphonate to image a rabbit brain abscess. An approximate signal enhancement factor of around 4 was calculated upon addition of the paramagnetic Gd(III) complex, with imaging times generally less than 5 mins.[111] Studies have also looked at the paramagnetic relaxation enhancement in fluorinated derivatives of biological substrates, such as fluoroacetate and trifluorolactate.[112,113] An illustrative example of the increase in signal intensity achieved by utilising the paramagnetic enhancement effect is shown in *Figure 1.20*, where the ^{19}F NMR signal for trifluoro-L-lactate is shown both with (B) and without (A) the addition of Gd(DO3A).[113]

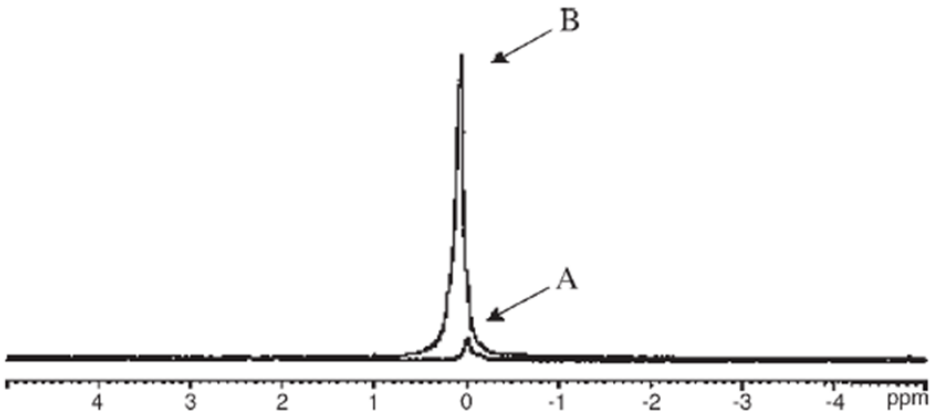

Figure 1.20 *^{19}F NMR T_1-weighted spin echo spectra of a 10 mM solution of trifluoro-L-lactate with (B, 0.9 mM) and without (A) Gd(DO3A).*[113]

However, with systems that rely on an intermolecular interaction between the fluorinated probe and the paramagnetic ion, the encounter probability is inherently low, resulting in modest relaxation enhancements.[67] This can be increased if both moieties are contained within the same molecule. An early example from Sherry and co-workers focussed on a series of [Ln(F-DOTPME)]$^-$ complexes (*Figure 1.21*), which were observed to exist as a mixture of diastereoisomers in solution.[114] Due to the sensitivity of ^{19}F NMR spectroscopy to minor structural changes, it was possible to assign several of the shifted fluorine resonances to specific isomers. Addition of ionic detergents was then monitored by variations in shift and/or population of individual stereoisomers. While this is an interesting example of using the intrinsic sensitivity of ^{19}F NMR spectroscopy to probe the structural forms of a Ln(III) complex, for imaging applications it is important to promote the formation of one species in solution to maximise the signal intensity obtained.

A more recent example involved the use of a perfluoro-*tert*-butyl group coupled to a DO3A-based ligand *via* a short helical oxyethylene chain to aid with water solubility ([Ln(FC)], *Figure 1.21*).[115] As could be expected, introduction of a variety of di- and tri-valent paramagnetic metal ions caused increases in relaxation rates and resulted in distinct ^{19}F NMR shifts for each metal complex. This has led to the system being described as a multi-chromic ^{19}F tracer, whereby different therapeutic agents could be labelled with individual metal complexes of FC allowing them to be tracked independently *in vivo* by the different ^{19}F NMR frequencies. However, it is debatable whether the chemical shift non-equivalence between the different species is large enough for this application, with only 7-8 ppm variation across the entire series tested. This may be improved by positioning the fluorine containing moiety in closer proximity to the metal ion, which would likewise improve upon the fairly modest increases in relaxation rates reported (e.g. for [Tb(FC)] $R_1 \approx 14$ Hz). Further work also needs to be done into investigating why this system does not follow the patterns set out by the Bleaney coefficients. For example, the ^{19}F signal for the Er(III) complex should be shifted in an opposite direction to the corresponding Dy(III), Ho(III), and Tb(III) complexes compared to the diamagnetic analogue, yet this is not the case. Similarly, the Gd(III) complex shows the largest relaxation rate enhancement as would be

expected, but it also displays a significant shift in the ^{19}F NMR signal in comparison to the diamagnetic Y(III) complex, which should not occur due to the isotropic nature of the Gd(III) ion (see *Section 1.3.1* for further details of chemical shift behaviour in paramagnetic lanthanide systems).

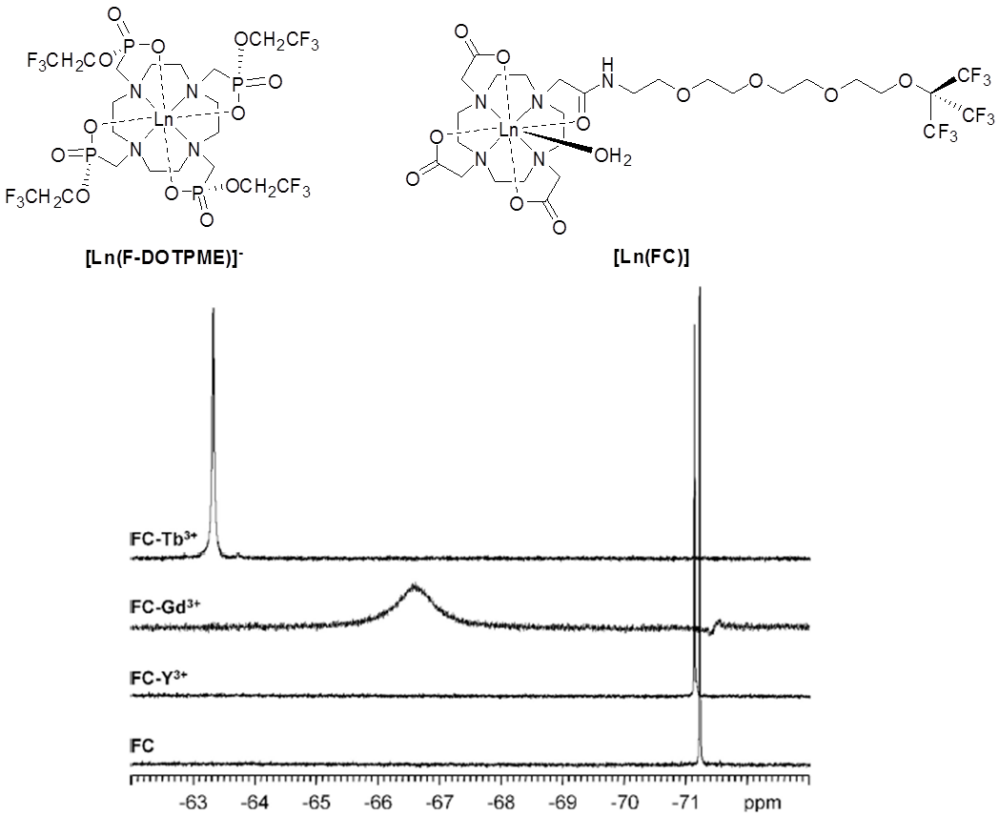

Figure 1.21 *Top) Chemical structures of [Ln(F-DOTPME)]*$^{-}$ [114] *and [Ln(FC)]; Bottom) Example of chemical shift differences noted when FC ligand is complexed with a variety of metals.*[115]

While not technically heteronuclear imaging, an interesting example of a ^{1}H chemical shift magnetic resonance probe has been reported by Caravan and co-workers.[116] This utilises the four magnetically equivalent cyclen ring protons on a simple ytterbium(III) complex, $[Yb(DOTA)]^{-}$. Due to the presence of the paramagnetic Yb(III) ion, the resonance for this set of protons is shifted to 19.9 ppm, out of the typical biological range of ^{1}H NMR spectroscopy. This was imaged simultaneously with sodium 3-(trimethylsilyl)-1-propanesulphonate (DSS) and 3-(2-hydroxyethyl)thiazolium bromide (HETB), which display shifts on the limits of the standard 'biological window' at 0 ppm and 9.8 ppm respectively. To investigate the possibility for multiplex

detection of these probes, they were imaged separately and as a mixture at the three different resonances, which indicated that simultaneous detection of all the investigated compounds was possible (*Figure 1.22*). An experiment was also run that successfully incorporated DSS within a liposome to improve the *in vivo* applicability, with a commercial Gd(III) compound added to increase the relaxation rates. These are promising preliminary results and it would be interesting to see the effect that changing the lanthanide ion in the DOTA complex would have on the shift observed, in addition to whether this concept could be applied to *in vitro* and/or *in vivo* studies.

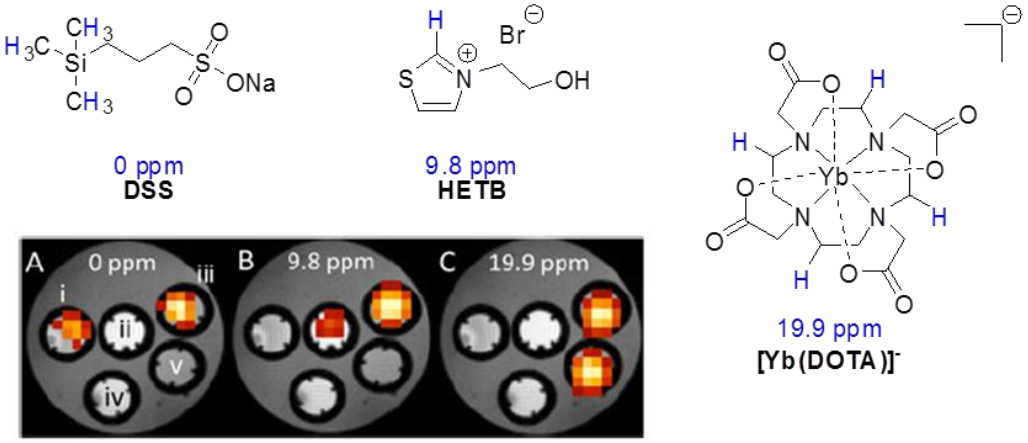

Figure 1.22 *^{1}H Chemical shift imaging agents (protons with relevant chemical shifts highlighted in blue) and colour overlays showing the chemical shift images at (A) 0 ppm (DSS resonance), (B) 9.8 ppm (HETB resonance), and (C) 19.9 ppm ([Yb(DOTA)]$^{-}$ resonance). Five phantoms contain equimolar proton concentrations of (i) DSS, (ii) HETB, (iii) DSS, HETB, [Yb(DOTA)]$^{-}$, (iv) blank, (v) [Yb(DOTA)]$^{-}$; $YbCl_3$ was added to samples not containing [Yb(DOTA)]$^{-}$ to compensate for the bulk magnetic susceptibility effect of Yb(III).*[116]

1.6.2 Responsive systems

A gadolinium-based probe has recently been developed for the *in vitro* imaging of protease activity, utilising variable transverse relaxation rates of ^{19}F nuclei to signal enzyme cleavage. The probe consists of three sections; a Gd(III) complex, a ^{19}F-containing label, and a peptide to link the two together (*Figure 1.23*).[117] This peptide is designed as a substrate for caspase-3, which is of interest as it is an effective marker for cell apoptosis. In its intact state, the ^{19}F signal of the probe experiences large enhancement of the transverse relaxation rate, resulting in significant line broadening

and a weak signal. However, addition of caspase-3 causes cleavage of the peptide bond, releasing the fluorine containing moiety. As the fluorine is no longer in close proximity to the Gd(III) ion, the paramagnetic transverse relaxation enhancement is reduced and the ^{19}F NMR signal intensity increases in a time-dependent manner. However, there are some severe limitations to this design, in that the process is irreversible and the longitudinal relaxation rate of the ^{19}F signal after cleavage is slow, presenting the usual problem of long acquisition times in diamagnetic systems. A related example has recently been reported whereby a ^{19}F-containing aglycone derivative is cleaved in the presence of β-galactosidase, inducing a large ^{19}F NMR chemical shift response.[118] The released diamagnetic aglycone spontaneously traps ferric ions, rendering the ^{19}F NMR signal invisible due to line broadening and generating intense proton MRI T_2 contrast, allowing a dual modality approach to imaging. This system has been applied to preliminary *in vivo* experiments.

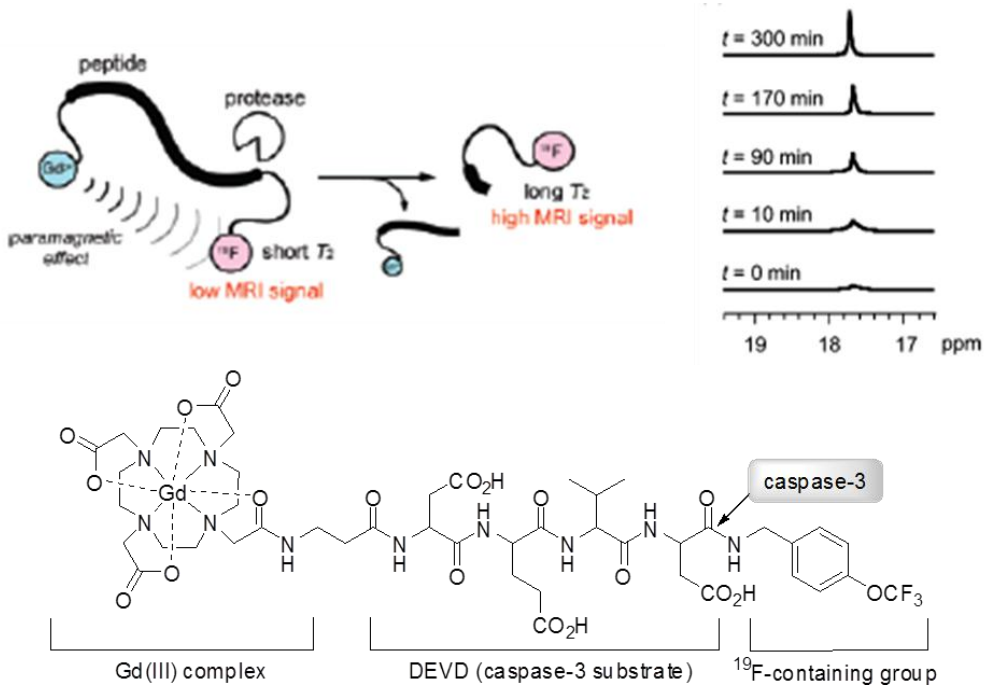

Figure 1.23 *Design principle of probe to detect protease activity (top) and structure of probe used (bottom). Time-dependent ^{19}F NMR spectral change of probe after addition of caspase-3 at 37°C (top right).*[117]

An interesting system has been suggested by Aime and co-workers that utilises a fluorine- containing probe to allow local concentration of a pH-responsive Gd(III)

complex to be monitored, resulting in the possibility of ratiometric pH mapping.[119] The probe consists of a poly-β-cyclodextrin (poly-β-CD) carrier comprising of 8-10 β-CD units, to which the separate Gd(III) and fluorine-containing molecules are non-covalently bound *via* adamantane moieties (*Figure 1.24*). The Gd(III) compound displays pH-sensitive modulation of relaxivity in the range of 6 to 9, with the variation in relaxivity increased by conjugation to the higher molecular adduct due to an increase in rotational correlation time. The ^{19}F signal, however, is not affected by changes in pH and so will be proportional to the fluorine density, allowing the local probe concentration to be calculated. To avoid line broadening and resulting loss of signal, the system has been designed so that the fluorine-containing molecules are sufficiently far enough away from the Gd(III) ion that they do not experience significant transverse relaxation rate enhancement. While this system has been successfully applied *in vitro*, major modifications would be necessary for *in vivo* application due to the competition effect that proteins, oxy-anions, and endogenous molecules would exhibit on both the adamantane to β-CD binding (e.g. K_A = 1300 M^{-1} for Gd complex to β-CD and 13000 M^{-1} for Gd complex to HSA) and on the availability of water molecules to the gadolinium probe.

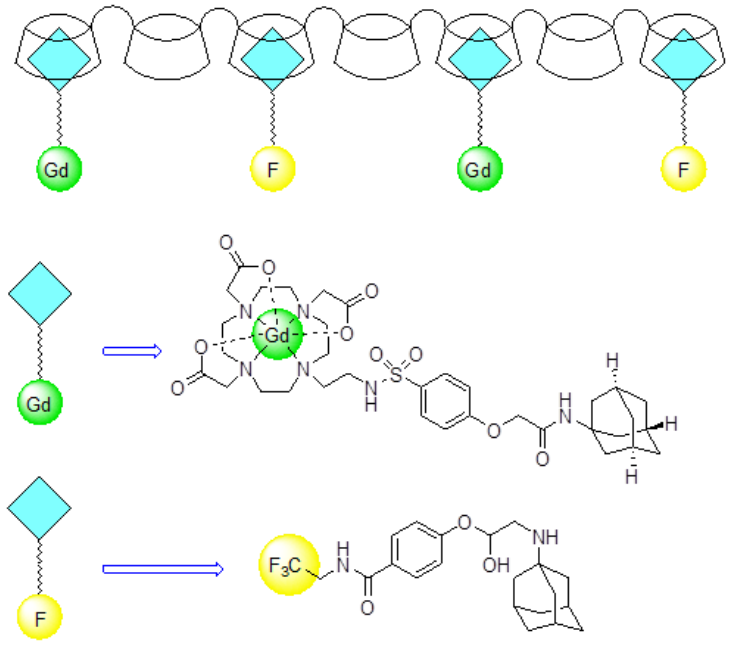

Figure 1.24 *Schematic representation of potential ratiometric pH mapping probe containing a pH-responsive Gd(III) complex, a concentration reporting fluorinated molecule, and a poly-β-CD adduct.*[119]

1.6.3 Previous work in the group

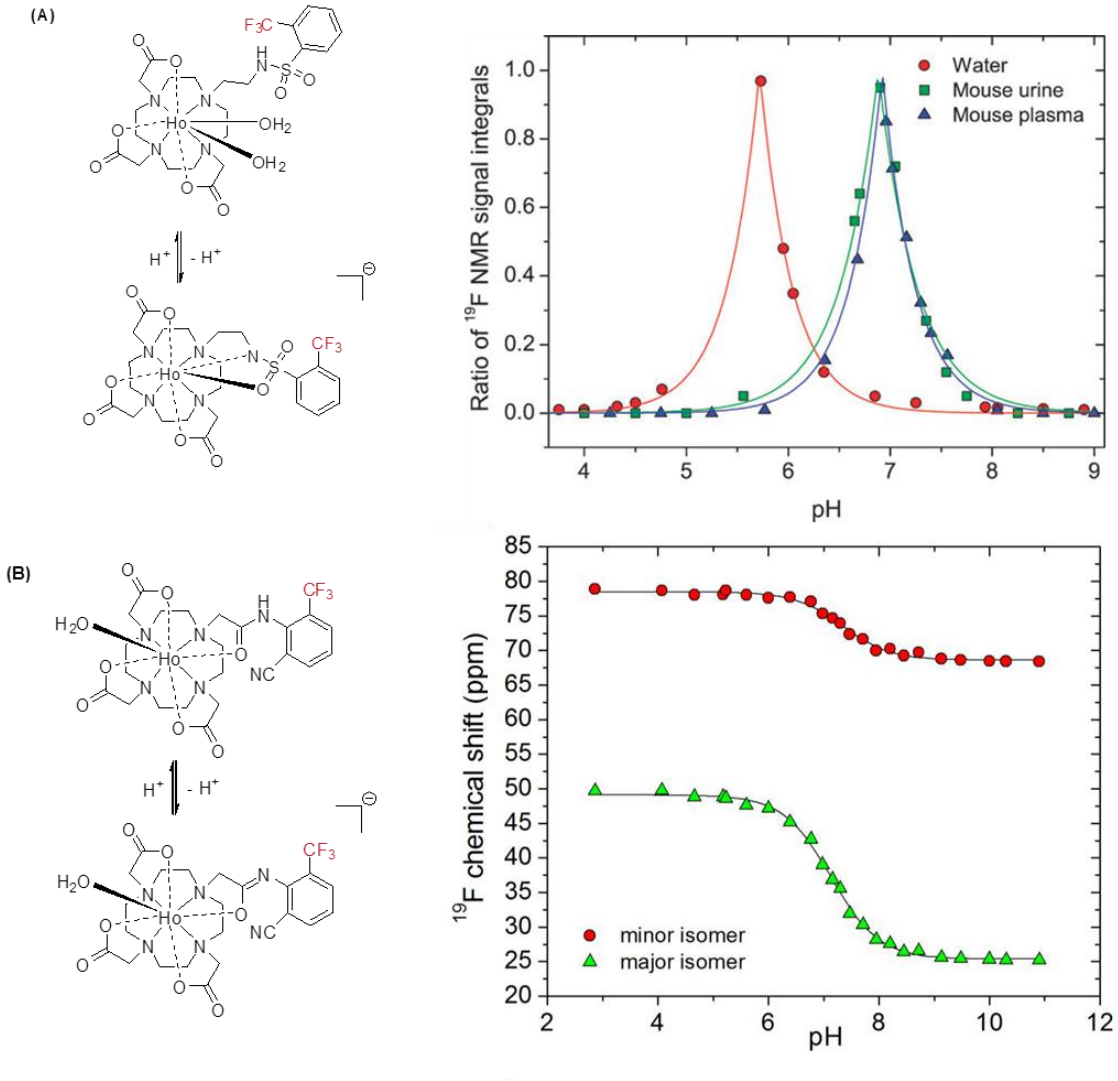

Figure 1.25 *(A) pH Dependence of the ^{19}F chemical shift for the holmium sulphonamide complex in water, urine, and plasma; (B) the variation of chemical shift for the two isomers of the holmium ortho-cyano amide complex.*[75,120,121]

Research in Durham over the last five years has led to the development of a number of novel fluorinated paramagnetic lanthanide(III) complexes with interesting ^{19}F magnetic resonance behaviour. From the theory outlined in *Section 1.3*, these have been based on tetraazacyclododecane (cyclen) derivatives, in which a homotopic CF_3 group has been incorporated in the region of 4.5 – 7.5 Å from the paramagnetic centre, in order

to increase the ^{19}F relaxation rate by around two orders of magnitude. The first examples were designed as ^{19}F NMR chemical shift pH probes, with two different designs of complex investigated whereby variation in pseudocontact shifts result in dramatic amplification of shift non-equivalence between the acid and base forms in each case. The first was based on a fluorinated sulphonamide system and displayed reversible slow exchange between the low and high pH forms, resulting in a ^{19}F signal for each form whose relative ratio varied with pH.[120,121] The associated pK_a of this process was 5.71 in 0.1 M NaCl solution, however this rose to 6.92 in serum or urine due to competitive hydrogen carbonate binding shifting the process in favour of the acid form (*Figure 1.25.A*). The ^{19}F chemical shift difference between the two forms was 40 ppm, with the basic species observed as two diastereoisomers.

The second pH responsive system was based on fluorine-containing mono-amide derivatives, with protonation/deprotonation of the amide nitrogen occurring with varying pH. A range of substituents was investigated, with the most promising results being displayed by the *ortho*-cyano system (pK_a = 7.1, *Figure 1.25.B*).[121,75] Unlike the sulphonamide example, the exchange between the acid and base forms is fast on the NMR timescale, resulting in the observation of an averaged signal that varies in shift as the pH is altered. This system exists as two major isomers due to restricted rotation about the aryl carbon-nitrogen bond. Each isomer exhibited a large chemical shift non-equivalence in addition to differing pH-dependent shifts, allowing the shift separation between the two isomers ($\Delta\delta_F$ = 14 ppm) to be used to calculate the pH. In both cases, this alleviates the requirement for calibration of chemical shift, as in this case pH can be measured as a chemical shift separation and in the previous sulphonamide example it relies upon measuring the ratio of two signals.

The limitations to the examples discussed above were numerous isomeric species in solution and linewidths greater than anticipated, due to prototropic exchange or dynamic intramolecular conformational exchange processes. For *in vivo* applications, it is necessary to maximise any signal observed, therefore promotion of one major isomer and reduction of any chemical exchange line broadening in solution is vital.

Therefore a number of systems were investigated in an attempt to improve the signal intensity obtained.[122] The most promising system studied involved mono-amide triphosphinate complexes, as they possessed increased longitudinal relaxation rates over their carboxylate analogues (CF_3 around 0.3 Å closer to Ln(III) in phosphinates compared to carboxylates) yet displayed narrower linewidths due to the bulkier phosphinate groups suppressing dynamic motion of the complex. They also give rise to one major isomer (>85%) in solution, as shown in *Figure 1.26*. In order to maximise signal intensity with this system, phantom experiments were run with the series of Ln(III) ions of this complex (*Figure 1.26.c*).[123] From this it was determined that dysprosium(III) complex gave the highest signal intensity at 7 T, with an overall lower limit for detection by imaging of 20 µM. Ultrafast imaging sequences can also be employed to increase signal intensity further.[124] However, despite all the advances in these systems, an *in vivo* ^{19}F magnetic resonance signal has so far proved elusive, necessitating the need for further improvements in signal intensity.

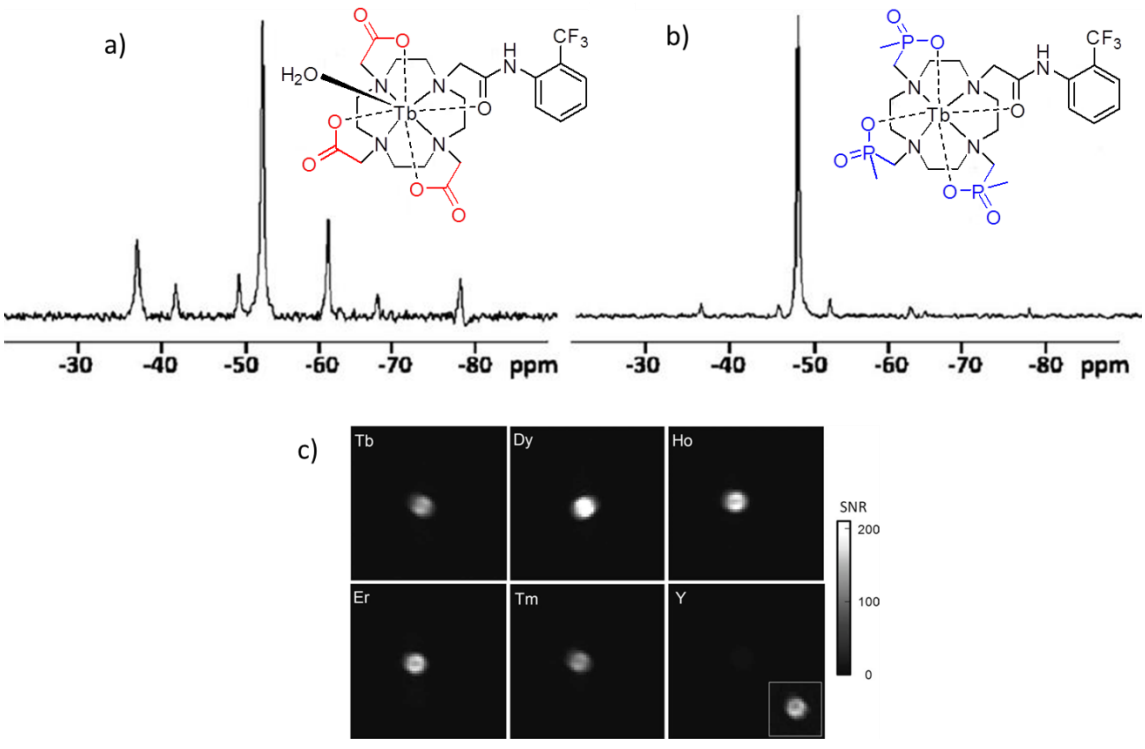

Figure 1.26 *^{19}F NMR spectra of the monoamide carboxylate (a) and phosphinate analogue (b) indicating greatly reduced isomerisation in the phosphinate complex. (c) Phantom imaging data acquired for the phosphinate complex with different Ln(III) ions at 7.0 T with image intensities scaled to the same value; Inset Y image scaled in intensity by a factor of 10.*[122,123]

1.7 Project Aims

The aim of this work is to continue the advancement of fluorinated paramagnetic lanthanide complexes as probes for ^{19}F magnetic resonance imaging and spectroscopy by the synthesis and evaluation of novel systems, with the main goal to develop a system that is applicable for *in vivo* studies. Therefore, it is imperative to improve on the signal intensity that has been observed in previous examples. There are two main methods that will be investigated in order to do this. The first is to incorporate numerous complexes into high molecular weight adducts, examples of which were discussed in *Section 1.5*. This should have two significant benefits for *in vivo* use; the overall fluorine signal density per unit concentration should be dramatically increased by having a number of complexes bound to one conjugate, and the clearance rate from the body should be greatly reduced. Other forms of complex will also be examined with a view to improving the signal intensity by further reducing dynamic motion and increasing the rigidity of the compound. It is also important that any new systems developed are present as one major isomer in solution and any fluorine signals present display one main resonance in their ^{19}F NMR spectra.

Further investigations will also be carried out into the development of responsive probes, the importance of which was detailed in *Section 1.4*. A particular emphasis will be placed on designing systems that are sensitive to variation in pH and/or signal the presence of biologically significant anions, with any changes ideally reported by significant modulations in the ^{19}F chemical shift. Any sensitivity discovered will also be analysed by a second method (variations in relaxivity, emission, etc.) to validate the results.

1.8 References

1. *OECD/European Union (2010)*, "Medical Technologies: CT Scanners and MRI Units", in Health at a Glance: Europe 2010, OECD Publishing. http://dx.doi.org/10.1787/9789264090316-33-en.

2. M. Botta, *Eur. J. Inorg. Chem.*, 2012, 1873–1874.

3. E. J. Werner, A. Datta, C. J. Jocher, and K. N. Raymond, *Angew. Chem. Int. Ed.*, 2008, **47**, 8568–8580.

4. J. Yu, V. D. Kodibagkar, W. Cui, and R. P. Mason, *Curr. Med. Chem.*, 2005, **12**, 819–848.

5. C. Partain, *J. Magn. Reson. Imaging*, 2004, **19**, 515–526.

6. C. Cofield, *Symmetry*, 2008, **5**, 340.

7. A. Ziegler, M. Kunth, S. Mueller, C. Bock, R. Pohmann, L. Schroder, C. Faber, and G. Giribet, *Zoomorphology*, 2011, **130**, 227–254.

8. R. Damadian, K. Zaner, D. Hor, and T. DrMaio, *Proc. Nat. Acad. Sci. USA*, 1974, **71**, 1471–1473.

9. M. M. Britton, *Chem. Soc. Rev.*, 2010, **39**, 4036–4043.

10. E. Yuen, A. Sederman, and L. Gladden, *Appl. Catal. A-Gen.*, 2002, **232**, 29–38.

11. A. Davenport, M. Forsyth, and M. Britton, *Electrochem. Commun.*, 2010, **12**, 44–47.

12. I. Koptyug, A. Khomichev, A. Lysova, and R. Sagdeev, *J. Am. Chem. Soc.*, 2008, **130**, 10452–10453.

13. Y. Z. Wadghiri, E. M. Sigurdsson, M. Sadowski, J. I. Elliott, Y. Li, H. Scholtzova, C. Y. Tang, G. Aguinaldo, M. Pappolla, K. Duff, T. Wisniewski, and D. H. Turnbull, *Magn. Reson. Med.*, 2003, **50**, 293–302.

14. P. Caravan, J. Ellison, T. McMurry, and R. Lauffer, *Chem. Rev.*, 1999, **99**, 2293–2352.

15. D. Pan, S. D. Caruthers, A. Senpan, A. H. Schmieder, S. A. Wickline, and G. M. Lanza, *WIREs Nanomed. Nanobiotechnol.*, 2011, **3**, 162–173.

16. M. Woods, D. E. Woessner, and A. D. Sherry, *Chem. Soc. Rev.*, 2006, **35**, 500–511.

17. S. Zhang, M. Merritt, D. E. Woessner, R. E. Lenkinski, and A. D. Sherry, *Acc. Chem. Res.*, 2003, **36**, 783–790.

18. M. R. Goldman, T. J. Brady, I. L. Pykett, C. T. Burt, F. S. Buonanno, J. P. Kistler, J. H. Newhouse, W. S. Hinshaw, and G. M. Pohost, *Circulation*, 1982, **66**, 1012–1016.

19. R. S. Ranganathan, N. Raju, H. Fan, X. Zhang, M. F. Tweedle, J. F. Desreux, and V. Jacques, *Inorg. Chem.*, 2002, **41**, 6856–6866.

20. L. C. Costello, R. B. Franklin, and P. Narayan, *Prostate*, 1999, **38**, 237–245.

21. R. Pal, A. Beeby, and D. Parker, *J Pharmaceut. Biomed.*, 2011, **56**, 352–358.

22. P. S. Allen, R. B. Thompson, and A. H. Wilman, *NMR Biomed.*, 1997, **10**, 435–444.

23. B. Yoo and M. D. Pagel, *Front. Biosci.*, 2008, **13**, 1733–1752.

24. E. Que and C. Chang, *Chem. Soc. Rev.*, 2010, **39**, 51–60.

25. A. Mishra, N. K. Logothetis, and D. Parker, *Chem. Eur. J.*, 2011, **17**, 1529–1537.

26. J. L. Major and T. J. Meade, *Acc. Chem. Res.*, 2009, **42**, 893–903.

27. P. F. Daly, R. C. Lyon, P. J. Faustino, and J. S. Cohen, *J. Biol. Chem.*, 1987, **262**, 14875–14878.

28. X.-H. Zhu, N. Zhang, Y. Zhang, X. Zhang, K. Ugurbil, and W. Chen, *NMR Biomed.*, 2005, **18**, 83–103.

29. R. Gruetter, G. Adriany, I.-Y. Choi, P.-G. Henry, H. Lei, and G. Oz, *NMR Biomed.*, 2003, **16**, 313–338.

30. M. Kitamura, T. Suzuki, R. Abe, T. Ueno, and S. Aoki, *Inorg. Chem.*, 2011, **50**, 11568–11580.

31. M. H. Levitt, *Spin Dynamics: Basics of Nuclear Magnetic Resonance*, John Wiley & Sons, 2001.

32. J. Selbin, *J. Chem. Educ.*, 1973, **50**, 306–310.

33. H. J. M. Bowen, *Environmental chemistry of the elements*, Academic Press, 1979.

34. A. M. James and M. P. Lord, *Macmillan's chemical and physical data*, Macmillan, 1992.

35. J. Ruiz-Cabello, B. P. Barnett, P. A. Bottomley, and J. W. M. Bulte, *NMR Biomed.*, 2011, **24**, 114–129.

36. R. F. Code, J. E. Harrison, K. G. McNeill, and M. Szyjkowski, *Magn. Reson. Med.*, 1990, **13**, 358–369.

37. A. Ratner, H. Muller, and B. Bradley-Simpson, *Invest. Radiol.*, 1988, **23**, 361–364.

38. G. N. Holland, P. A. Bottomley, and W. S. Hinshaw, *J. Magn. Reson.*, 1977, **28**, 133–136.

39. P. Lauterbur, *Nature*, 1973, **242**, 190–191.

40. U. Flögel, Z. Ding, H. Hardung, S. Jander, G. Reichmann, C. Jacoby, R. Schubert, and J. Schrader, *Circulation*, 2008, **118**, 140–148.

41. L. C. Clark and F. Gollan, *Science*, 1966, **152**, 1755–1756.

42. M. Wolfson, *ASAIO J.*, 2006, **52**, 490.

43. L. Clark, J. Ackerman, S. Thomas, R. Millard, R. Hoffman, R. Pratt, H. Raglecole, R. Kinsey, and R. Janakiraman, *Adv. Exp. Med. Biol.*, 1984, **180**, 835–845.

44. P. Rinck, S. Petersen, and P. Lauterbur, *Fortschr. Rontg. Neuen.*, 1984, **140**, 239–243.

45. R. E. Jacob, Y. V. Chang, C. K. Choong, A. Bierhals, D. Zheng Hu, J. Zheng, D. A. Yablonskiy, J. C. Woods, D. S. Gierada, and M. S. Conradi, *Magn. Reson. Med.*, 2005, **54**, 577–585.

46. U. Wolf, A. Scholz, C. P. Heussel, K. Markstaller, and W. G. Schreiber, *Magn. Reson. Med.*, 2006, **55**, 948–951.

47. H.-J. Böhm, D. Banner, S. Bendels, M. Kansy, B. Kuhn, K. Müller, U. Obst-Sander, and M. Stahl, *Chem. Bio. Chem.*, 2004, **5**, 637–643.

48. W. Hagmann, *J. Med. Chem.*, 2008, **51**, 4359–4369.

49. J. Knight, P. Edwards, and S. Paisey, *RSC Adv.*, 2011, **1**, 1415–1425.

50. M. Adam and D. Wilbur, *Chem. Soc. Rev.*, 2005, **34**, 153–163.

51. O. Couturier, A. Luxen, J.-F. Chatal, J.-P. Vuillez, P. Rigo, and R. Hustinx, *Eur. J. Nucl. Med. Mol. I.*, 2004, **31**, 1182–1206.

52. G. Brix, M. E. Bellemann, L. Gerlach, and U. Haberkorn, *Magn. Reson. Imaging*, 1999, **17**, 151–155.

53. J. Shani and W. Wolf, *Cancer Res.*, 1977, **37**, 2306–2308.

54. A. N. Stevens, P. G. Morris, R. A. Iles, P. W. Sheldon, and J. R. Griffiths, *Brit. J. Cancer*, 1984, **50**, 113–117.

55. R. Martino, V. Gilard, F. Desmoulin, and M. Malet-Martino, *J. Pharm. Biomed. Anal.*, 2005, **38**, 871–891.

56. T. Nakada, I. L. Kwee, and C. B. Conboy, *J. Neurochem.*, 1986, **46**, 198–201.

57. K. Sato, M. Higuchi, N. Iwata, T. C. Saido, and K. Sasamoto, *Eur. J. Med. Chem.*, 2004, **39**, 573–578.

58. M. Higuchi, N. Iwata, Y. Matsuba, K. Sato, K. Sasamoto, and T. C. Saido, *Nat. Neurosci.*, 2005, **8**, 527–533.

59. I. Bertini, C. Luchinat, and G. Parigi, *Solution NMR of Paramagnetic Molecules: Applications to metallobiomolecules and models*, Elsevier, 2001.

60. A. Sigel, *Metal Ions in Biological Systems, Volume 40*, M. Dekker, 2003.

61. J. D. Satterlee, *Concepts Magn. Reson.*, 1990, **2**, 69–79.

62. J. D. Satterlee, *Concepts Magn. Reson.*, 1990, **2**, 119–129.

63. J. Ren and A. D. Sherry, *J. Magn. Reson., Ser. B*, 1996, **111**, 178–182.

64. C. C. Bryden, C. N. Reilley, and J. F. Desreux, *Anal. Chem.*, 1981, **53**, 1418–1425.

65. B. Bleaney, *J. Magn. Reson.*, 1972, **8**, 91–100.

66. J. A. Peters, J. Huskens, and D. J. Raber, *Prog. Nucl. Magn. Reson. Spectrosc.*, 1996, **28**, 283–350.

67. P. Harvey, I. Kuprov, and D. Parker, *Eur. J. Inorg. Chem.*, 2012, 2015–2022.

68. J. B. Gruber, R. P. Leavitt, C. A. Morrison, and N. C. Chang, *J. Chem. Phys.*, 1985, **82**, 5373–5378.

69. H. Gysling and M. Tsutsui, *Adv. Organomet. Chem.*, 1971, **9**, 361–395.

70. B. Alsaadi, F. Rossotti, and R. Williams, *J. Chem. Soc., Dalton Trans.*, 1980, 2151–2154.

71. S. Aime, L. Barbero, M. Botta, and G. Ermondi, *J. Chem. Soc., Dalton Trans.*, 1992, 225–228.

72. I. Bertini, P. Turano, and A. Vila, *Chem. Rev.*, 1993, **93**, 2833–2932.

73. A. Pinkerton, M. Rossier, and S. Spiliadis, *J. Magn. Reson.*, 1985, **64**, 420–425.

74. J. Keeler, *Understanding NMR Spectroscopy*, John Wiley & Sons, 2005.

75. K. H. Chalmers, E. De Luca, N. H. M. Hogg, A. M. Kenwright, I. Kuprov, D. Parker, M. Botta, J. I. Wilson, and A. M. Blamire, *Chem. Eur. J.*, 2010, **16**, 134–148.

76. S. L. Grage, U. H. N. Dürr, S. Afonin, P. K. Mikhailiuk, I. V. Komarov, and A. S. Ulrich, *J. Magn. Reson.*, 2008, **191**, 16–23.

77. L. Helm, *Prog. Nucl. Magn. Reson. Spectrosc.*, 2006, **49**, 45–64.

78. D. A. Bluemke, C. A. Gatsonis, M. H. Chen, G. A. DeAngelis, N. DeBruhl, S. Harms, S. H. Heywang-Köbrunner, N. Hylton, C. K. Kuhl, C. Lehman, E. D. Pisano, P. Causer, S. J. Schnitt, S. F. Smazal, C. B. Stelling, P. T. Weatherall, and M. D. Schnall, *J. Amer. Med. Assoc.*, 2004, **292**, 2735–2742.

79. E. Terreno, D. D. Castelli, A. Viale, and S. Aime, *Chem. Rev.*, 2010, **110**, 3019–3042.

80. H. Adrogué and N. Madias, *N. Engl. J. Med.*, 1998, **338**, 26–34.

81. R. A. Gatenby and R. J. Gillies, *Nat. Rev. Cancer*, 2004, **4**, 891–899.

82. N. Raghunand, C. Howison, A. D. Sherry, S. Zhang, and R. J. Gillies, *Magn. Reson. Med.*, 2003, **49**, 249–257.

83. M. L. Garcia-Martin, G. V. Martinez, N. Raghunand, A. D. Sherry, S. Zhang, and R. J. Gillies, *Magn. Reson. Med.*, 2006, **55**, 309–315.

84. L. M. De Leon-Rodriguez, A. J. M. Lubag, C. R. Malloy, G. V. Martinez, R. J. Gillies, and A. D. Sherry, *Acc. Chem. Res.*, 2009, **42**, 948–957.

85. L. Frullano, C. Catana, T. Benner, A. D. Sherry, and P. Caravan, *Angew. Chem. Int. Ed.*, 2010, **49**, 2382–2384.

86. M. P. Lowe, D. Parker, O. Reany, S. Aime, M. Botta, G. Castellano, E. Gianolio, and R. Pagliarin, *J. Am. Chem. Soc.*, 2001, **123**, 7601–7609.

87. E. Gianolio, L. Maciocco, D. Imperio, G. B. Giovenzana, F. Simonelli, K. Abbas, G. Bisi, and S. Aime, *Chem. Commun.*, 2011, **47**, 1539–1541.

88. G. B. Giovenzana, R. Negri, G. A. Rolla, and L. Tei, *Eur. J. Inorg. Chem.*, 2012, 2035–2039.

89. M. Vaccaro, A. Accardo, D. Tesauro, G. Mangiapia, D. Löf, K. Schillén, O. Söderman, G. Morelli, and L. Paduano, *Langmuir*, 2006, **22**, 6635–6643.

90. R. Hovland, C. Gløgård, A. J. Aasen, and J. Klaveness, *J. Chem. Soc., Perkin Trans. 2*, 2001, 929–933.

91. E. Tóth, R. D. Bolskar, A. Borel, G. González, L. Helm, A. E. Merbach, B. Sitharaman, and L. J. Wilson, *J. Am. Chem. Soc.*, 2005, **127**, 799–805.

92. S. Laus, A. Sour, R. Ruloff, E. Tóth, and A. E. Merbach, *Chem. Eur. J.*, 2005, **11**, 3064–3076.

93. C. F. G. C. Geraldes and S. Laurent, *Contrast Media Mol. I.*, 2009, **4**, 1–23.

94. X. Zhang, X. Jing, T. Liu, G. Han, H. Li, and C. Duan, *Inorg. Chem.*, 2012, **51**, 2325–2331.

95. V. Comblin, D. Gilsoul, M. Hermann, V. Humblet, V. Jacques, M. Mesbahi, C. Sauvage, and J. F. Desreux, *Coord. Chem. Rev.*, 1999, **185-186**, 451–470.

96. J. Costa, R. Ruloff, L. Burai, L. Helm, and A. E. Merbach, *J. Am. Chem. Soc.*, 2005, **127**, 5147–5157.

97. S. Aime, M. Botta, M. Fasano, and E. Terreno, *Spectrochim. Acta, Part A*, 1993, **49**, 1315–1322.

98. A. J. Surman, C. S. Bonnet, M. P. Lowe, G. D. Kenny, J. D. Bell, E. Tóth, and R. Vilar, *Chem. Eur. J.*, 2011, **17**, 223–230.

99. R. S. Dickins, S. Aime, A. S. Batsanov, A. Beeby, M. Botta, J. I. Bruce, J. A. K. Howard, C. S. Love, D. Parker, R. D. Peacock, and H. Puschmann, *J. Am. Chem. Soc.*, 2002, **124**, 12697–12705.

100. E. Terreno, M. Botta, P. Boniforte, C. Bracco, L. Milone, B. Mondino, F. Uggeri, and S. Aime, *Chem. Eur. J.*, 2005, **11**, 5531–5537.

101. R. S. Dickins, T. Gunnlaugsson, D. Parker, and R. D. Peacock, *Chem. Commun.*, 1998, 1643–1644.

102. P. Atkinson, Y. Bretonniere, and D. Parker, *Chem. Commun.*, 2004, 438–439.

103. H. Maeda, *Adv. Enzyme Regul.*, 2001, **41**, 189–207.

104. D. Maffeo, M. Lampropoulou, M. Fardis, Y. G. Lazarou, I. M. Mavridis, D. A. I. Mavridou, E. Urso, H. Pratsinis, D. Kletsas, and K. Yannakopoulou, *Org. Biomol. Chem.*, 2010, **8**, 1910–1921.

105. E. Nakamura, K. Makino, T. Okano, T. Yamamoto, and M. Yokoyama, *J. Controlled Release*, 2006, **114**, 325–333.

106. K. Shiraishi, K. Kawano, T. Minowa, Y. Maitani, and M. Yokoyama, *J. Controlled Release*, 2009, **136**, 14–20.

107. M. A. Mintzer and M. W. Grinstaff, *Chem. Soc. Rev.*, 2011, **40**, 173–190.

108. S. Langereis, A. Dirksen, T. M. Hackeng, M. H. P. van Genderen, and E. W. Meijer, *New J. Chem.*, 2007, **31**, 1152–1160.

109. M. M. Ali, M. Woods, P. Caravan, A. C. L. Opina, M. Spiller, J. C. Fettinger, and A. D. Sherry, *Chem. Eur. J.*, 2008, **14**, 7250–7258.

110. U. Bommerich, T. Trantzschel, S. Mulla-Osman, G. Buntkowsky, J. Bargon, and J. Bernarding, *Phys. Chem. Chem. Phys*, 2010, **12**, 10309–10312.

111. H. Lee, R. R. Price, G. E. Holburn, C. L. Partain, M. D. Adams, and W. P. Cacheris, *J. Magn. Reson. Imaging*, 1994, **4**, 609–613.

112. C. S. Bonnet and P. H. Fries, *ChemPhysChem*, 2010, **11**, 3474–3484.

113. E. Terreno, M. Botta, W. Dastrù, and S. Aime, *Contrast Media Mol. I.*, 2006, **1**, 101–105.

114. W. D. Kim, G. E. Kiefer, J. Huskens, and A. D. Sherry, *Inorg. Chem.*, 1997, **36**, 4128–4134.

115. Z.-X. Jiang, Y. Feng, and Y. B. Yu, *Chem. Commun.*, 2011, **47**, 7233–7235.

116. Y. Yang, D. T. Schühle, G. Dai, J. K. Alford, and P. Caravan, *Contrast Media Mol. I.*, 2012, **7**, 276–279.

117. S. Mizukami, R. Takikawa, F. Sugihara, Y. Hori, H. Tochio, M. Wälchli, M. Shirakawa, and K. Kikuchi, *J. Am. Chem. Soc.*, 2008, **130**, 794–795.

118. J.-X. Yu, V. D. Kodibagkar, R. R. Hallac, L. Liu, and R. P. Mason, *Bioconjugate Chem.*, 2012, **23**, 596–603.

119. E. Gianolio, R. Napolitano, F. Fedeli, F. Arena, and S. Aime, *Chem. Commun.*, 2009, 6044–6046.

120. P. K. Senanayake, A. M. Kenwright, D. Parker, and S. K. Van Der Hoorn, *Chem. Commun.*, 2007, 2923–2925.

121. A. M. Kenwright, I. Kuprov, E. De Luca, D. Parker, S. U. Pandya, P. K. Senanayake, and D. G. Smith, *Chem. Commun.*, 2008, 2514–2516.

122. K. H. Chalmers, M. Botta, and D. Parker, *Dalton Trans.*, 2011, **40**, 904–913.

123. K. H. Chalmers, A. M. Kenwright, D. Parker, and A. M. Blamire, *Magn. Reson. Med.*, 2011, **66**, 931–936.

124. F. Schmid, C. Höltke, D. Parker, and C. Faber, *Magn. Reson. Med.*, 2012, in press.

2. Development of Responsive Probes

2.1 Introduction

As introduced in Chapter 1, ^{19}F NMR spectroscopy studies with fluorinated probes offer substantial opportunity, due to the favourable properties (high receptivity and Larmor frequency) of the nucleus. In addition, the large chemical shift range is generally an order of magnitude greater than for ^{1}H NMR spectroscopy. As has been previously demonstrated, the long acquisition times of ^{19}F MRS studies can be alleviated somewhat by the introduction of a paramagnetic lanthanide centre in close proximity to the observed fluorine nucleus.[1,2] The introduction of a Ln(III) ion can also have the added benefit of amplifying chemical shift non-equivalence, *via* the pseudo-contact shift mechanism (see *Section 1.3.1*), allowing a general means of tracking changes in probe geometry by using NMR spectroscopy or chemical shift imaging. This concept has been applied previously in Durham, by positioning a CF_3 group within 6 to 6.5 Å of a lanthanide ion linked by an amide bond.[1,3,4] As the pH passes through the amide bond pK_a, this is signalled by the CF_3 group as a shift in δ_F. The presence of the Ln(III) ion accentuates the difference in chemical shift between the acid and base forms of the complex. This value is up to 36 ppm over the physiological pH range, offering a vast improvement over systems currently in use ($\Delta\delta_H \approx 1$ ppm).[5,6]

This principle will be employed here in the development of new responsive probes. Two different strategies for probe design can be envisioned, depending on whether the process under investigation leads to either a reversible change in structure or an irreversible alteration of the probe. In each case, in order for the relaxation rates of the CF_3 group to remain unaltered, it is preferable that the distance between the Ln(III) ion and the fluorinated label should stay fixed. These concepts have led to the development of two different probe designs reported here. The first involves the reversible interaction of anions with the probe at the metal centre by displacement of weakly coordinated water molecules. This is accompanied by a change in the local ligand field, and is reported as variation in δ_F. The second example exploits an

irreversible amide hydrolysis that is enzyme activated. Careful positioning of the CF_3 label allows the perturbation in local electron density to be signalled by a shift of δ_F.

2.2 An Anion Responsive System

There is a range of illnesses associated with abnormal levels of anions in the body. Therefore, it is of great importance to develop probes that can report on relative levels of specific analytes. In order to be applicable, the key properties for a probe that responds to a certain analyte are as follows;

- The probe must be sensitive to a specific analyte in competitive media
- There must be an easy and direct method for monitoring analyte levels
- Any changes should be accompanied by large variations in the parameter being monitored, i.e. large shift changes in the ^{19}F NMR spectrum
- The probe should be water soluble and fully functional in aqueous solution
- Binding should be fully reversible

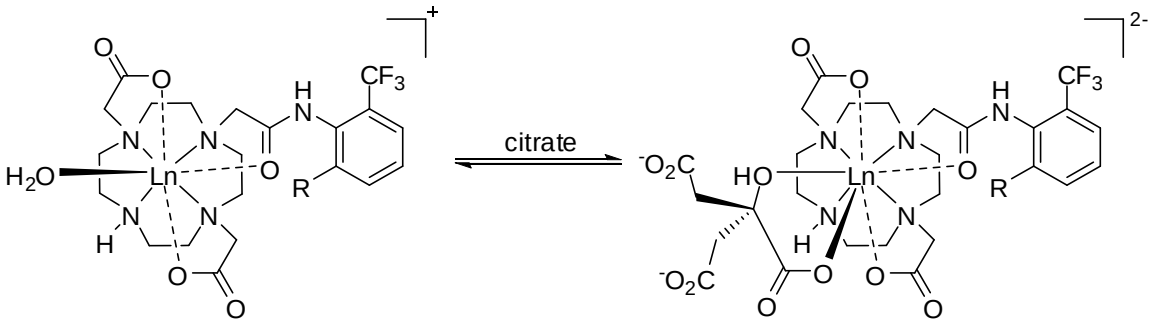

Scheme 2.1 *Variation in lanthanide ion speciation following reversible anion binding (citrate in this example).*

For the detection of anions, most reported lanthanide probes have been based on the displacement of water at the metal centre in a coordinatively unsaturated heptadentate complex. The majority of cases use modulation of lanthanide luminescence as the signalling method.[7–9] This concept has been incorporated in the design of the cationic monoamide complexes investigated here, **[Ln.L^1]$^+$** and **[Ln.L^2]$^+$**, in

which the coordinated water is displaced by an anion, while the CF_3 label remains in a constant relative position (*Scheme 2.1*). **[Ln.L^2]$^+$** contains a cyano-group (*Scheme 2.2*), which should significantly reduce the pK_a of the amide nitrogen, and it will be of interest to investigate how this affects the behaviour of the complex. The ability of the two complexes to report on the concentration of biologically significant anions by variations in δ_F is discussed below, along with full synthetic details and spectroscopic properties.

2.2.1 Synthetic details

The syntheses of **[Ln.L^1]$^+$** and **[Ln.L^2]$^+$** are fairly straightforward, requiring only a few steps and resulting in relatively high overall yields (*Scheme 2.2*). Firstly, the α-chloroamides (**1** and **9**) were made from the relevant amines by stirring with sodium hydride to deprotonate the amine, followed by the addition of chloroacetyl chloride. These were then purified over silica gel. Controlled alkylation of the tertiary butyl ester of 1,7-bis(carboxymethyl)-1,4,7,10-tetraazacyclododecane (DO2A, synthesised by published methods[10,11]) by mild heating with the α-chloroamides and sodium carbonate resulted in the formation of the corresponding mono-amides, **5** and **10**, which were purified by column chromatography. The *tert*-butyl ester protecting groups were removed by stirring overnight with trifluoroacetic acid in dichloromethane, to generate the di-acid ligands as the triflate salts. Metal complexation was achieved using an aqueous solution of the appropriate metal chloride at pH 5.5 and 60°C overnight, before the pH was raised to 10 in order to precipitate any excess Ln(III) ions as the metal hydroxide. The free metal was removed by centrifugation before the pH was lowered back to 5.5 and the water removed by lyophilisation. The resulting solid was extracted into a mixture of methanol and dichloromethane and insoluble material again removed by centrifugation. Pre-treated anion exchange resin was used to prepare the chloride salts of **[Ln.L^1]$^+$** and **[Ln.L^2]$^+$**.

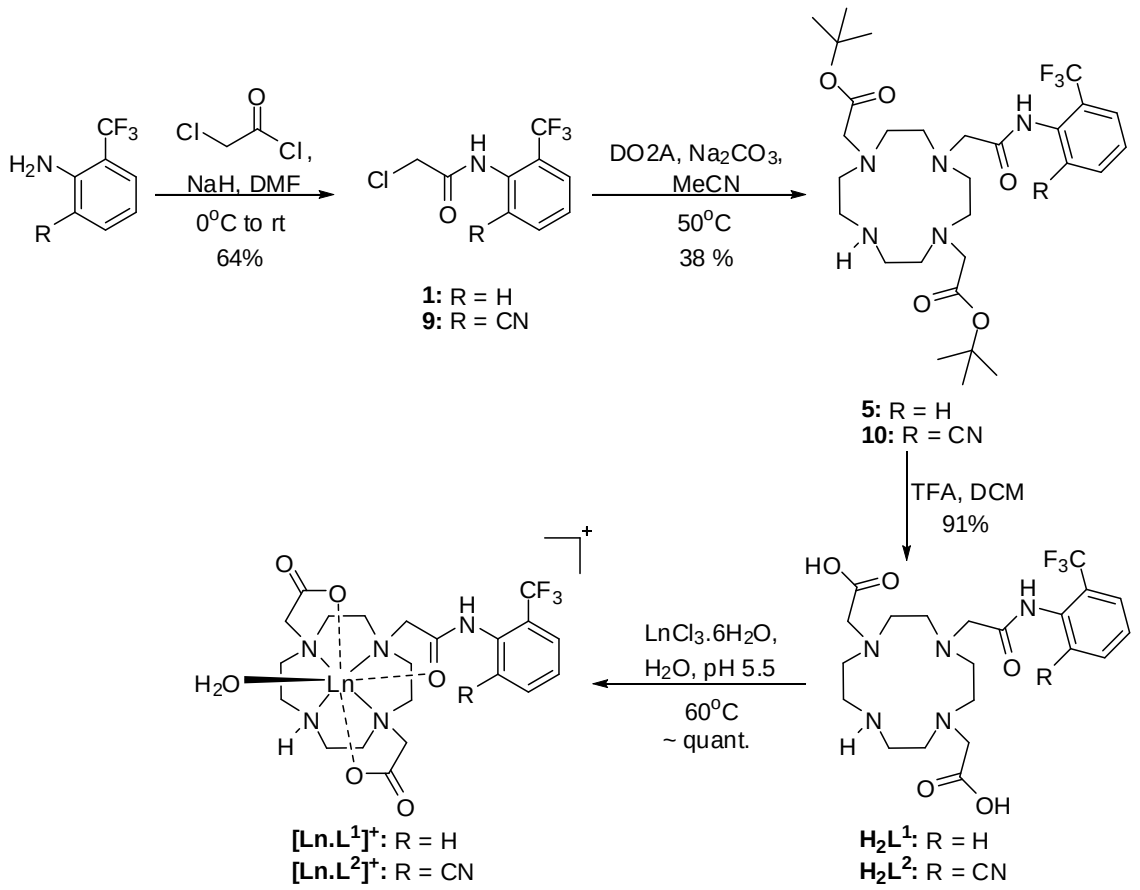

Scheme 2.2 *General procedure for the synthesis of* ***[Ln.L^1]$^+$*** *and* ***[Ln.L^2]$^+$*** *(yields stated for R=CN; yields for R=H are comparable).*

2.2.2 Characterisation of complexes

Low resolution electrospray and high resolution accurate mass spectrometry was carried out to confirm the constitution of each complex. A characteristic isotope pattern was observed in each case, showing good correlation with the calculated spectrum. An example is shown in *Figure 2.1*. ^{19}F NMR spectroscopic data were also collected for each complex. In all cases, one major isomer appeared to form in solution (>85 %) with the appearance of a number of small, minor isomers. For the following discussion, the chemical shift values quoted refer to the dominant isomer.

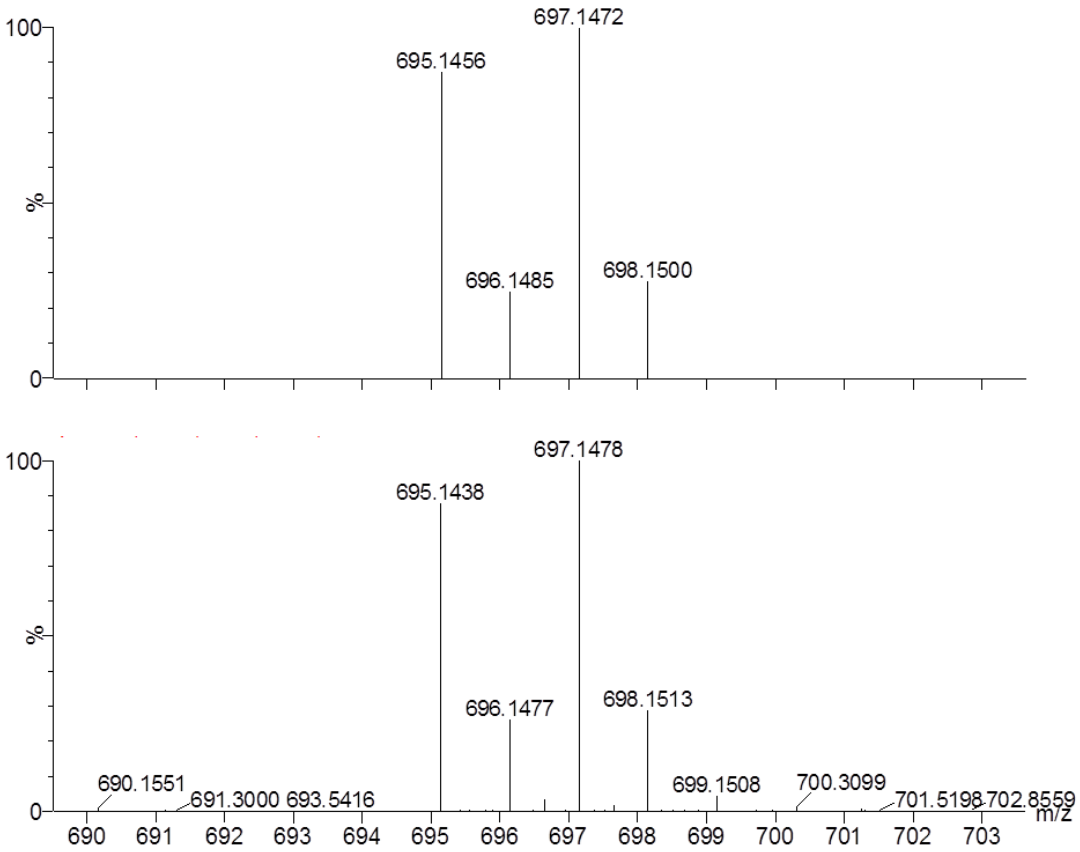

Figure 2.1 *Theoretical (top) and experimental (bottom) high resolution electrospray mass spectrum of* ***[Eu.L^2]$^+$*** *showing characteristic isotope pattern.*

Crystals of **[Tm.L^2]$^+$** were grown from aqueous solution, from which the X-ray structure was determined (*Figure 2.2*). These were the first molecular structures generated for such fluorinated lanthanide complexes, and revealed the geometry of the charge neutral conjugate base, which is formed following deprotonation of the amide NH proton. Analysis of this molecular structure divulges several interesting features. There is a single coordinated water molecule, which is located 0.55 Å out of the plane defined by the other three coordinated oxygen molecules. The twist angle between the N4 and O4 planes (38.4^o) is typical of related square anti-prismatic eight coordinate complexes.[12,13] The individual fluorine atoms have Tm-F distances of 5.34, 6.78, and 7.33 Å, with an average distance of 6.48 Å. This average distance is likely to be more relevant when comparing behaviour in the solution state as fast rotation about the C-CF_3 bond occurs in solution. The amide carbon-nitrogen bond is relatively short (1.30 Å), consistent with its double bond character resulting from deprotonation of the amide group and charge delocalisation into the *o*-cyano moiety.

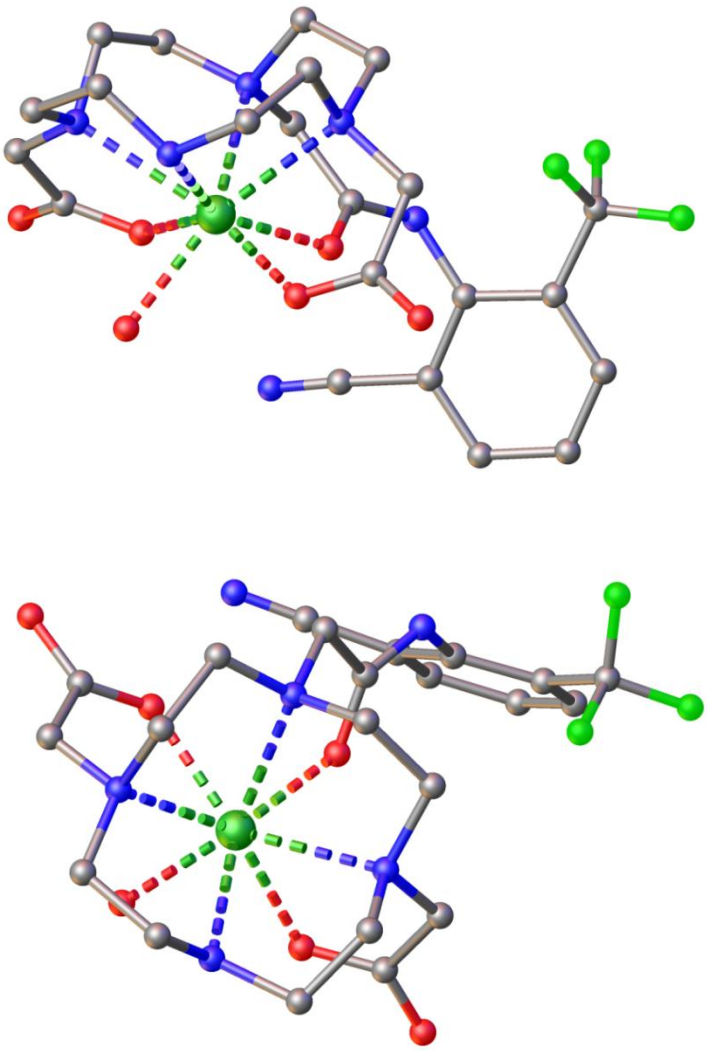

Figure 2.2 *Views of the molecular structure of* ***[Tm.L^2]$^+$*** *from the X-ray analysis viewed from the side (top) and down the z-axis (bottom) showing the bound water molecule that can be displaced upon addition of anions. Atoms shown are C (grey), N (blue), O (red), F (light green), and Tm (dark green). H atoms are omitted for clarity. Further data for the molecular structure above are included in Section 6.1.6.*

2.2.3 Anion responsive behaviour of the R=H system, [Ln.L^1]$^+$

Changes in the ^{19}F NMR parameters for the Ho(III) and Tm(III) complexes of **L^1** were investigated, upon addition of up to a ten-fold excess of the sodium salts of bicarbonate, citrate, lactate, and hydrogen phosphate at pD 7.4 in HEPES buffer (*Table 2.1*). Addition of the anions resulted in a characteristic ^{19}F chemical shift for each adduct formed. The large shift non-equivalence between the different ternary adducts

and the aqua species were promising, with around a 20 ppm range in resonance values exhibited by both complexes.

Table 2.1 *^{19}F NMR spectroscopy data for **[Ln.L^1]$^+$** and their anion adducts (D_2O, 188 MHz, 295 K, pD 7.4, 2 mM complex, 50 mM HEPES, 20 mM anion).*

Complex	Anion	δ_F / ppm	R_1 / Hz	Linewidth, ω_f / Hz
[Ho.L^1]$^+$	aqua species	-76.8	45	67
	bicarbonate	-66		broad[(a)]
	lactate	-64.6		214
	phosphate	-53.6		230
	citrate	-66.5	48	208
[Tm.L^1]$^+$	aqua species	-67.6	23	120
	bicarbonate	-63.2		189
	lactate	-70.2		99
	phosphate	-83.0		198
	citrate	-72.3[(b)]	25	175

(a) Linewidth > 1500 Hz; (b) Significant decomplexation of the Ln ion from the ligand was observed over a period of 24 h.

Linewidth broadening was not too severe in the resulting ternary adducts, in comparison with the aqua species, with the exception of the bicarbonate adduct of **[Ho.L^1]$^+$**. Chemical exchange broadening was apparent with some of the other adducts, but to manageable levels. Unfortunately, with an equimolar mixture of the anions, no significant preference for binding to a given anion was observed for either complex. Instead, single resonances corresponding to all the individual adduct species were observed, with increased linewidth broadening attributed to chemical exchange between the free and bound anion adducts that is fast on the NMR timescale.

Another major limiting feature of this system is the modest stability of the compounds to decomplexation of the Ln(III) ion by the added anions. This was most apparent with

[Tm.L^1]$^+$, in particular upon the addition of citrate. *Figure 2.3* shows the ^{19}F NMR spectra for the aqua species, the ternary adducts for each anion, and the ligand, L^1. As well as the major signals corresponding to the anion bound complexes, there is a significant signal observed that corresponds to the decomplexed ligand at -61.7 ppm. This is most noticeable for the citrate bound species, which undergoes substantial decomplexation almost immediately following addition of 20 equivalents of citrate. Smaller additions of citrate do allow the citrate bound ternary adduct to be observed independently without significant decomplexation occurring. However, leaving the complexes in solution with any of the anions for a longer period of time (>1 week for citrate, >1 month for the other species) led to almost complete decomplexation occurring. This made this system impractical for applications and so it was not studied further.

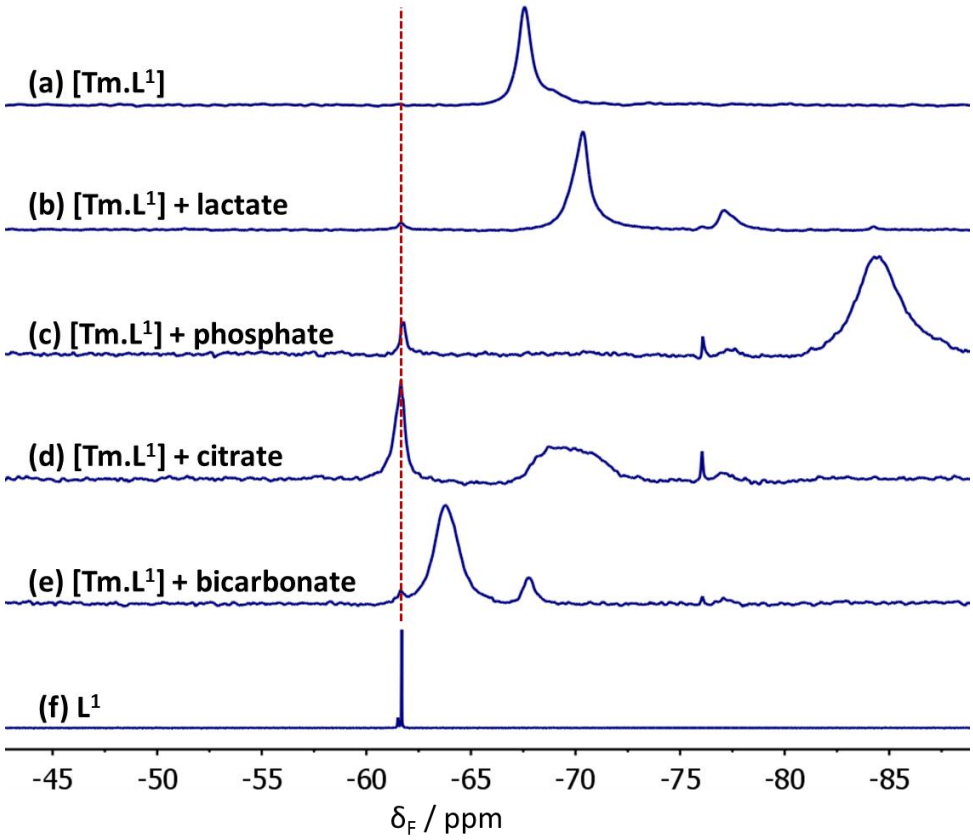

Figure 2.3 *^{19}F NMR spectra for **[Tm.L^1]$^+$** before and after the addition of anions; (a) aqua species, (b) 20 equivalents lactate, (c) 20 equivalents phosphate, (d) 20 equivalents citrate, (e) 20 equivalents bicarbonate, (f) L^1 before the addition of any Ln(III) ion, with dotted line indicating position of signal relating to the ligand at -61.7 ppm (9.4 T, 2 mM complex, 50 mM HEPES, D_2O, 295 K, pD 7.4).*

2.2.4 Anion responsive behaviour of the R=CN system, $[Ln.L^2]^+$

2.2.4.1 pH dependent behaviour

For the previous compound, where R=H, the pK_a associated with the amide nitrogen is > 8.5 and, hence, lies outside the biological pH range that is of interest with these studies. However, the introduction of a cyano-group at the *ortho*-position of the aromatic ring has been shown to significantly increase the acidity of the amide moiety.[1] Therefore, before any investigation into potential anion binding behaviour, it was imperative to understand how the ^{19}F NMR chemical shift varied with pH.

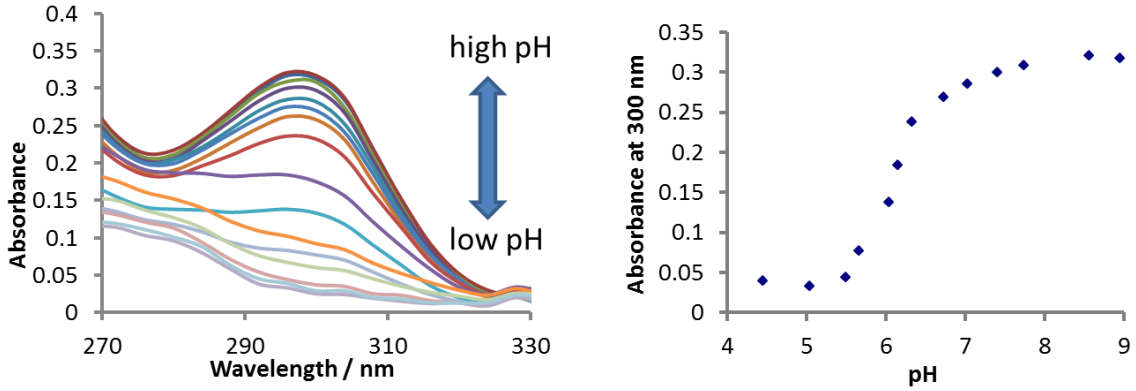

Figure 2.4 *Partial UV absorption spectrum (left) and pH profile (right) generated by monitoring the change in intensity of the absorbance at 300 nm for* ***$[Tm.L^2]^+$****.*

The protonation/deprotonation of the amide group can be followed by changes in the UV absorption spectral profile, due to charge delocalisation from the amide carbonyl bond into the *o*-cyano moiety of the aromatic ring upon formation of the conjugate base. In particular, a significant decrease in the absorbance band at 300 nm was observed as the pH was lowered (*Figure 2.4*). By plotting the intensity of this band as a function of pH and fitting the resulting curves, the pK_a of the amide was measured. The values obtained for the different complexes are shown in *Table 2.2*.

Table 2.2 *pK_a values for $[Ln.L^2]^+$ calculated by measuring changes in intensity of the UV absorbance band at 300 nm as a function of pH.*

Complex	pK_a
$[Ho.L^2]^+$	7.01 (± 0.03)
$[Tm.L^2]^+$	6.57 (± 0.06)
$[Eu.L^2]^+$	6.10 (± 0.04)

For **$[Ho.L^2]^+$**, the deprotonation of the amide nitrogen was also followed by ^{19}F NMR spectroscopy by monitoring changes of δ_F as a function of pH (*Figure 2.5*). A 7 ppm difference in the shifts was found for the protonated and deprotonated forms. For intermediate pH values only one signal is observed, corresponding to the weighted average of the chemical shifts of the individual forms. This behaviour is consistent with an acid-base equilibrium that is fast on the NMR timescale and is accompanied by an increase in chemical exchange line-broadening, as was observed for related systems.[1,4] The resulting pH profile generated is in good agreement with the curve obtained from the UV absorbance study (*Figure 2.6*). For **$[Tm.L^2]$**, the exchange broadening was so severe that a fluorine NMR signal could only be observed under acidic conditions (at pD 4, 9.4 T, and 295 K; δ_F = -61.4 ppm, R_1 = 67 Hz). As the pH increased, exchange between the acid and base forms caused linewidth broadening and the peak was barely discernible (linewidth > 1500 Hz). Therefore, a similar plot of pH versus δ_F for the thulium compound was not generated.

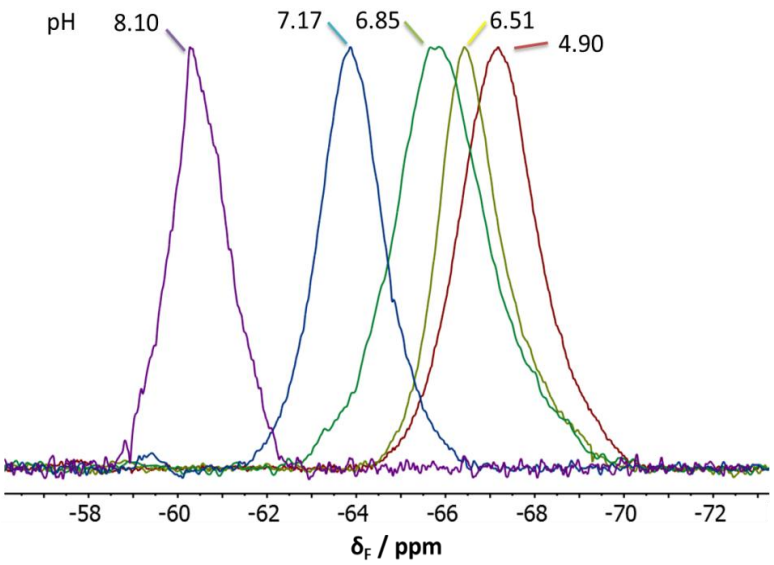

Figure 2.5 *^{19}F NMR spectra of $[Ho.L^2]^+$ at selected pH values.*

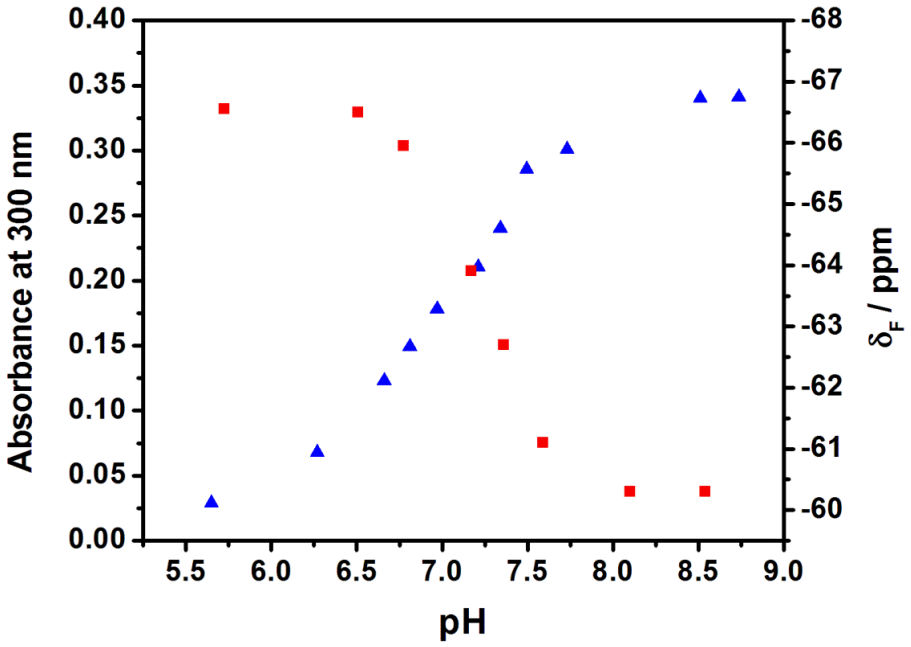

Figure 2.6 *pH profile for* ***[Ho.L^2]$^+$*** *generated by monitoring changes in intensity of the UV absorbance band at 300 nm (blue) and the change in the chemical shift of the ^{19}F NMR signal (red).*

2.2.4.2 Anion responsive behaviour

After carrying out promising preliminary ^{19}F NMR spectroscopy studies, it was decided to first investigate the anion affinities of the emissive europium complex, **[Eu.L^2]$^+$**, as the emission spectra of Eu(III) complexes are amenable to examination and have been frequently studied in the literature.[7] Ideally, the complex would contain a sensitising chromophore to absorb light energy and transfer this to the europium $^5D_1$ or $^5D_0$ excited states. However, due to the lack of such 'antennae', the Eu(III) ion had to be directly excited at 397 nm, which led to weak but interpretable spectra being recorded (*Figure 2.7*). Incremental addition of anions could be observed by monitoring the changes in the form and intensity of the europium emission bands, in particular variations in the ΔJ = 1 and ΔJ = 2 bands. The addition of lactate, citrate, and bicarbonate led to significant increases in the intensity of the ΔJ = 2 band. However, with added phosphate, the ΔJ = 2 band remained relatively unchanged. Instead, a change in the form of the ΔJ = 1 band is observed. This suggests a difference in binding modes between the carboxy anions and phosphate.

Table 2.3 *Apparent binding constants for* ***[Eu.L^2]$^+$*** *with selected anions, calculated from changes in the ratio of the ΔJ = 2 to ΔJ = 1 emission bands (H_2O, pH 7.4, 50 mM HEPES, 2 mM complex, 0 to 100 mM anion, 295 K, λ_{exc} = 397 nm).*

Anion	log *K* (±0.05)
citrate	2.71
lactate	1.98
phosphate	1.93
bicarbonate	0.81
citrate in anion mixture[(a)]	1.95

(a) Citrate competition experiment involved incremental addition of sodium citrate to a solution containing complex (2 mM), HEPES (50 mM), sodium bicarbonate (20 mM), sodium dihydrogenphosphate (1 mM), and sodium lactate (2 mM).

In each case, by plotting the change in the intensity ratio of the Eu(III) Δ*J* = 2 to Δ*J* = 1 emission band areas as a function of added anion concentration, relative binding affinities were calculated using reported methods (*Table 2.3*).[7,14–16] At pH 7.4, these calculated binding affinities suggest selectivity for citrate over the other anions tested. A 'competition' experiment was run, incrementally adding citrate to the complex in a fixed background of the other anions at biologically relevant concentrations. It was observed that citrate bound selectively, but with a reduced apparent affinity, associated with a K_d value of the order of 10 mM.

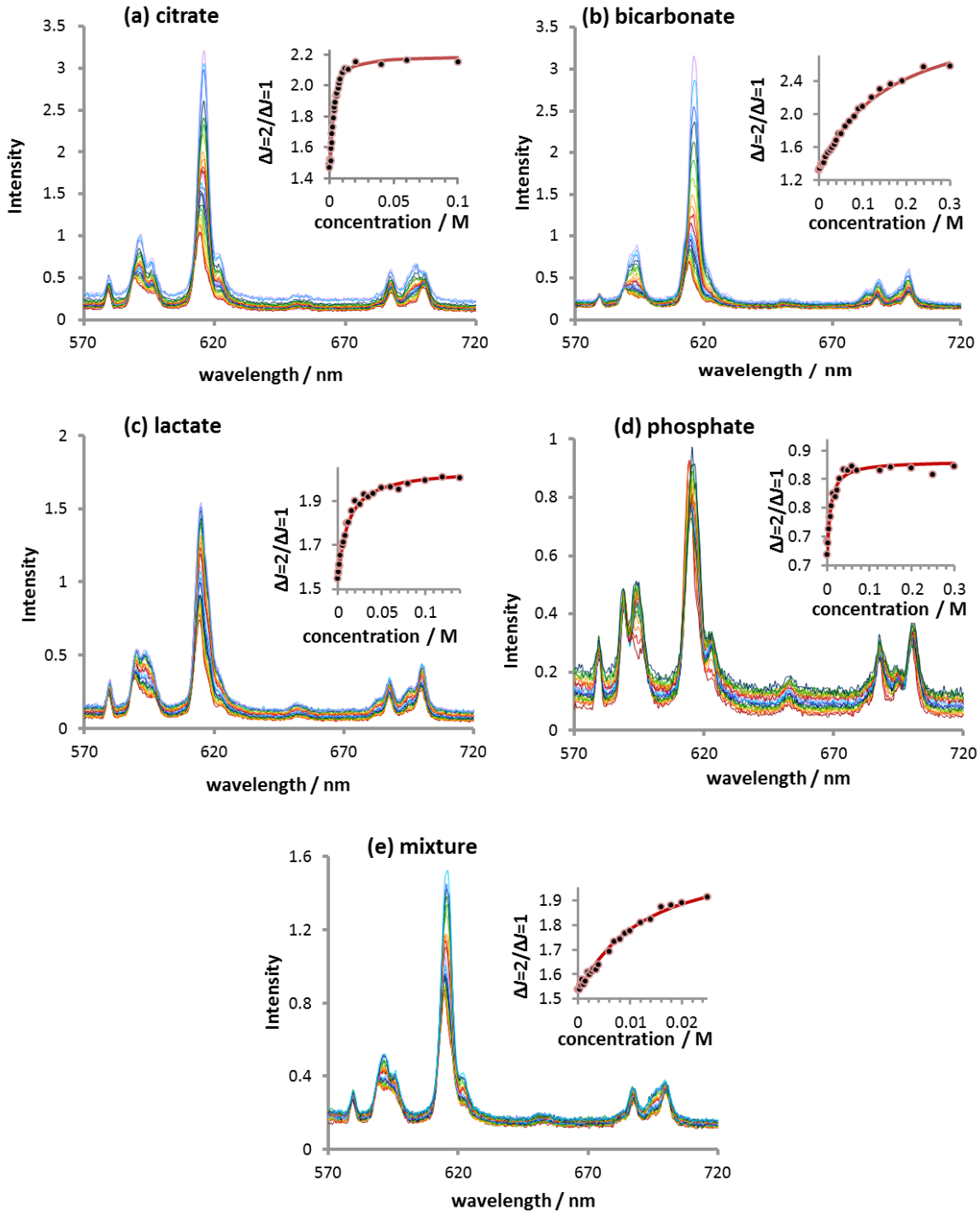

Figure 2.7 *Eu(III) emission spectra and accompanying fits of the ΔJ = 2/ΔJ = 1 intensity ratio against anion concentration for* ***[Eu.L^2]$^+$*** *with incremental addition of; (a) citrate, (b) bicarbonate, (c) lactate, (d) phosphate, and (e) citrate in a fixed background of 20 mM bicarbonate, 2 mM lactate, and 1 mM phosphate (H_2O, pH 7.4, 2 mM complex, 50 mM HEPES, 295 K, λ_{exc} = 397 nm).*

These results, in particular the selectivity displayed for citrate over the other analytes tested, were extremely promising. Accordingly, the ^{19}F NMR spectra of **[Ho.L^2]$^+$** and **[Tm.L^2]$^+$** were measured before and after the addition of a ten-fold excess of the sodium salts of bicarbonate, citrate, lactate, and hydrogen phosphate at pD 7.4 in HEPES buffer. In the case of the holmium species, addition of the anions again resulted in shifted resonances with a characteristic ^{19}F chemical shift for each adduct formed (*Table 2.4*), as was observed with **[Ln.L^1]$^+$**. Chemical shift values for the citrate and lactate bound species were most similar, suggesting a common coordination mode to the Ln(III) ion, involving chelation of the α-hydroxy and carboxylate groups. This is consistent with the similar europium emission profiles of the two complexes, in addition to reported crystallographic analyses of related compounds.[17] For the thulium complex, however, exchange broadening remained so extreme that no signal was observed for any species, except the citrate bound adduct.

While the chemical shift non-equivalence for the different ternary adducts of **[Ln.L^2]$^+$** was not as high as for **[Ln.L^1]$^+$**, they did not display any evidence of decomplexation upon addition of anions, even over relatively long periods of time, which was the major drawback in the earlier experiments with **[Ln.L^1]$^+$**. For a given field, the R_1 values for the complexes of **L^2** were also significantly faster than for the corresponding **L^1** compounds. For example, at 4.7 T the R_1 values for **[Ho.L^1]$^+$** and **[Ho.L^2]$^+$** were 45 and 83 Hz respectively. Utilising knowledge gained from the X-ray analysis of **[Tm.L^2]$^+$**, and given the r^{-6} dependence of R_1 (see *Section 1.3*), it can be estimated that the CF_3 group is around 0.6 Å closer to the lanthanide ion in complexes of **L^2** compared to those of **L^1**. In each case, R_1 values were not significantly altered upon binding of anions, suggesting that the Ln-F distance does not change upon anion binding, as surmised in the design of the probe.

Table 2.4 *^{19}F NMR spectroscopic data for **[Ln.L^2]$^+$** and their anion adducts (D_2O, 188 MHz, 295 K, pD 7.4, 2 mM complex, 50 mM HEPES, 20 mM anion).*

Complex	Anion	δ_F / ppm	R_1 / Hz	Linewidth, ω_f / Hz
[Ho.L^2]	aqua species	-66.3	83	420
	bicarbonate	-64.6		400
	lactate	-68.6		1200
	phosphate	-64.8		700
	citrate	-68.0	91	260
	mixture[(a)]	-68.1	92	250
[Tm.L^2][(b)]	aqua species	No signal observed		
	bicarbonate	No signal observed		
	lactate	No signal observed		
	phosphate	No signal observed		
	citrate	-61.1	54	134

(a) Mixture consists of 10 equivalents each of phosphate, bicarbonate, lactate, and citrate; (b) only addition of citrate gave rise to an observable signal at pD 7.4.

As before, introduction of the anions led to a general exchange broadening of the observed signals of the corresponding ternary adducts, dramatically so in the case **[Tm.L^2]**. With **[Ho.L^2]**, an exception occurred for addition of citrate, when a significant reduction in linewidth was observed from 420 Hz for the aqua species to 260 Hz for the citrate adduct. This behaviour suggested a slower rate of exchange between anion and aqua species than for the other anions, consistent with a higher affinity constant. Earlier, the binding constants generated by analysis of europium emission spectra had also indicated selectivity for citrate over the other anions tested. For a mixture of the holmium complex and ten equivalents each of citrate, lactate, phosphate, and bicarbonate, the only signal observed in the resulting ^{19}F NMR spectrum correlates to the signal observed for the citrate adduct, confirming the selectivity of this system.

Now that the selectivity of the system for citrate had been determined, it was decided to investigate the binding of this anion in more detail. Citrate (0 to 30 mM) was

incrementally added to a fixed concentration of the complex (2 mM) and HEPES (50 mM), with the ^{19}F NMR spectrum obtained after each addition. This allowed free and bound species to be observed simultaneously (*Figure 2.8*), consistent with chemical exchange between the aqua species and the citrate adduct that is slow on the NMR timescale. Following addition of half an equivalent of citrate, each species was observed in around a 50:50 ratio. By measuring the ratio of the areas of each peak as a function of [citrate], a rough binding curve could be generated. However, due to the broad and overlapping nature of the peaks, the data obtained was not accurate enough to determine an affinity constant.

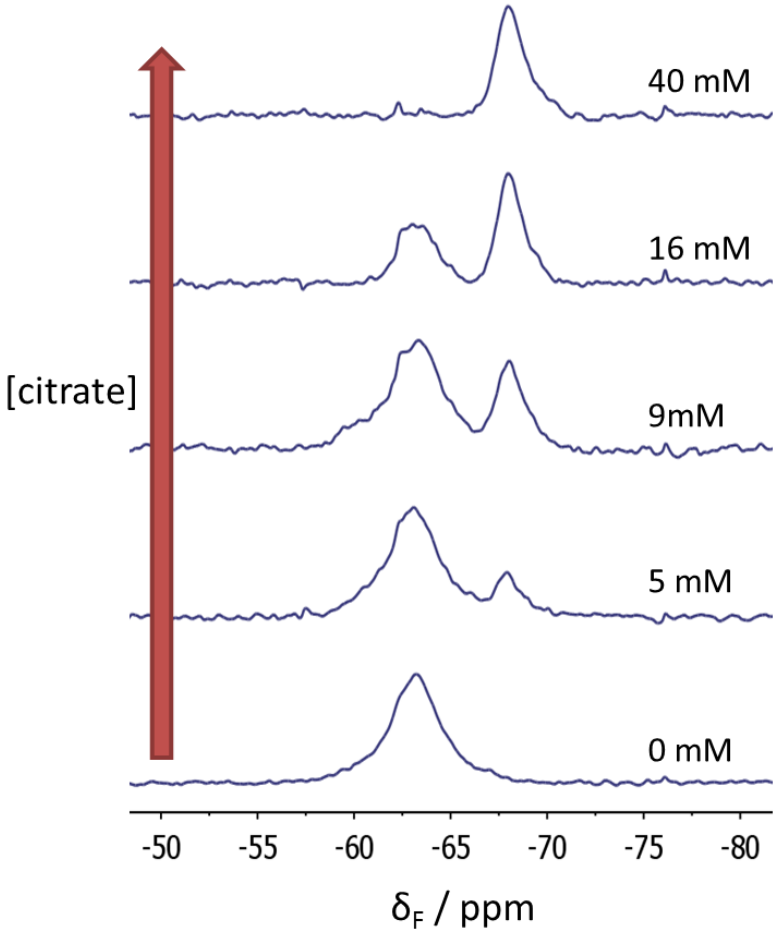

Figure 2.8 *^{19}F NMR spectra of **[Ho.L^2]** (4.7 T, 4 min spectral acquisition time, 2 mM complex, 50 mM HEPES, D_2O, 295 K, pD 7.4) following addition of increasing amounts of citrate. Bottom spectrum shows signal for complex before addition of citrate. Top spectrum after addition of twenty equivalents of citrate; only the signal corresponding to the citrate adduct was observed.*

For **[Tm.L^2]**, the case was complicated somewhat by the extreme exchange broadening apparent in the system. However, the fact that the signal was observed only for the citrate species, and that it was present as a relatively sharp resonance, suggests that the thulium compound is also selective for citrate. Addition of a mixture of the other anions to this citrate adduct did not result in any change in the ^{19}F NMR spectrum, confirming this hypothesis. As there was no other signal to which to compare the intensity of the signal, and in order to analyse the binding behaviour, it was necessary to employ an internal, fixed reference. Using trifluoroethanol as the reference compound, this procedure allowed incremental addition of citrate at pD 7.4 to be monitored by ^{19}F NMR spectroscopy (*Figure 2.9.a*). The ratio of the two signals was compared as a function of [citrate]. In this case, the two signals are sufficiently far apart ($\Delta\delta_F \approx 16$ ppm) and narrow that an affinity constant could be measured from the resulting binding curve (*Figure 2.9.b*). This generated a value (log K = 2.79 (± 0.03)), corresponding well to that defined by monitoring the emission spectral changes for **[Eu.L^2]** (log K = 2.71 (± 0.05)).

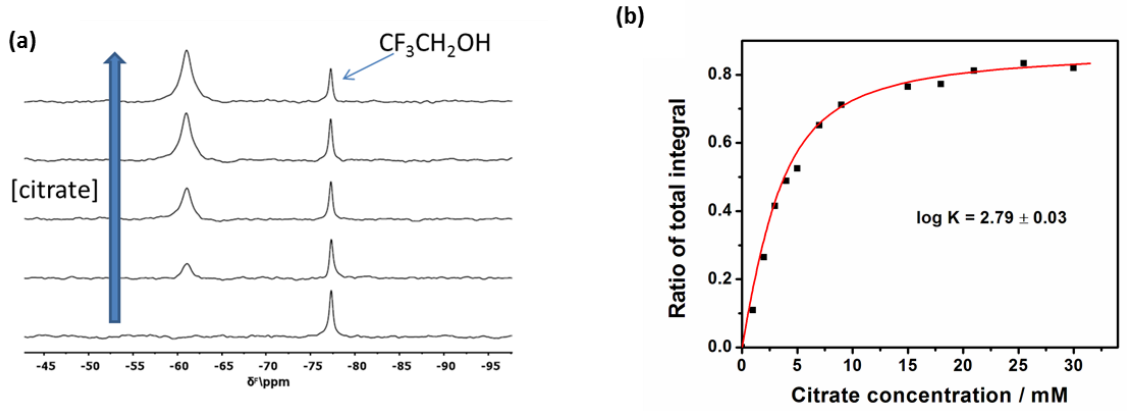

Figure 2.9 *(a) ^{19}F NMR spectra of **[Tm.L^2]** (4.7 T, 4 min spectral acquisition time, 3 mM complex, 50 mM HEPES, 0.2 mM CF_3CH_2OH, D_2O, 298 K, pD 7.4) following addition of increasing amounts of citrate. Bottom spectrum shows the signal for the complex before addition of citrate. Top spectrum was obtained after addition of excess citrate; only the signal corresponding to the citrate adduct is observed. (b) Resulting binding curve, showing the fit (line) to the experimental data, following the increase in relative intensity of the **[Tm.L^2(citrate)]** signal at -61.1 ppm as the ratio of total signal area with respect to added trifluoroethanol at -77.3 ppm. Integrals normalised so that maximum ratio = 1.*

2.3 A Probe for Signalling Ester Hydrolysis

Fluorinated lanthanide probes have previously been utilised for the signalling of enzyme-activated cleavage, but have been mainly based on an 'on/off' mode of action with dramatic changes in relaxation rates upon cleavage.[18,19] However, it is more desirable for the fluorine containing moiety to remain a fixed distance from the Ln(III) ion, so that R_1 and R_2 are minimally perturbed, allowing standard pulse sequences to be employed throughout the monitoring process. Accordingly, such a probe was developed by De Luca that contained an integral CF_3 group in an amide bound subunit (*Scheme 2.3*).[20,21]

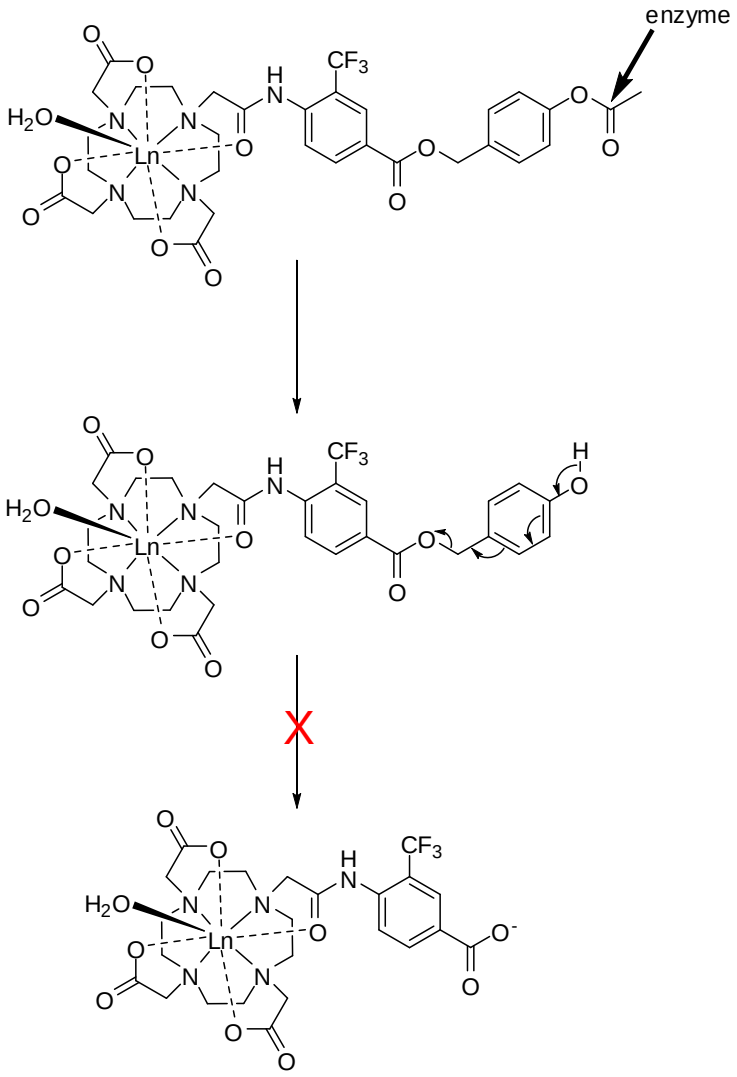

Scheme 2.3 *Envisaged stepwise cleavage induced by pig-liver esterase. Second step is not observed experimentally without the use of elevated pH.*[20,21]

The distal ester group was designed to undergo irreversible cleavage in the presence of pig-liver esterase, followed by relayed self-immolative hydrolysis of the *para*-substituted aryl ester group. This process was expected to lead to a change in the chemical shift of the reporting CF_3 group, amplified by the presence of the paramagnetic lanthanide ion. However, it was found that whilst the initial ester hydrolysis did occur, following the addition of pig-liver esterase, very little change was observed by ^{19}F NMR spectroscopy. Reaction progress had to be followed by mass spectrometry. At physiological pH, complete hydrolysis *via* the self-immolative pathway was not observed, and could only be triggered by raising the pH to 10. The ^{19}F NMR spectra for this system were also rather complex, owing to the presence of several isomers in solution.

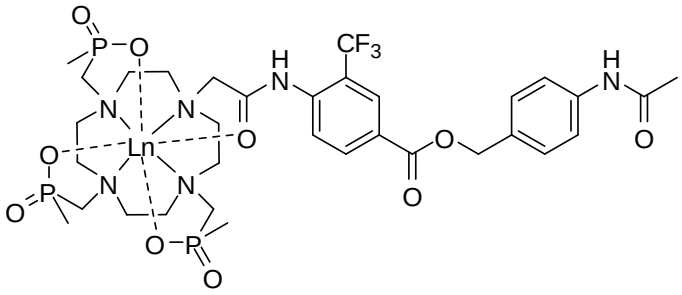

Figure 2.10 *Chemical structure of* ***[Ln.L^4]***

With this previous work in mind, we set out to improve the behaviour of this system. In order to reduce the number of isomers present in solution, the carboxylate pendant arms were replaced by phosphinate groups, increasing the rigidity of the complex and reducing the number of observed isomers, as shown previously.[22] In an attempt to coerce the self-immolative behaviour, the distal ester group was replaced by an amide, creating a substrate for α-chymotrypsin. The resulting target molecule, **[Ln.L^4]**, is shown in *Figure 2.10*. The ability of this complex to signal ester hydrolysis by variations in δ_F is discussed below.

2.3.1 Synthetic details

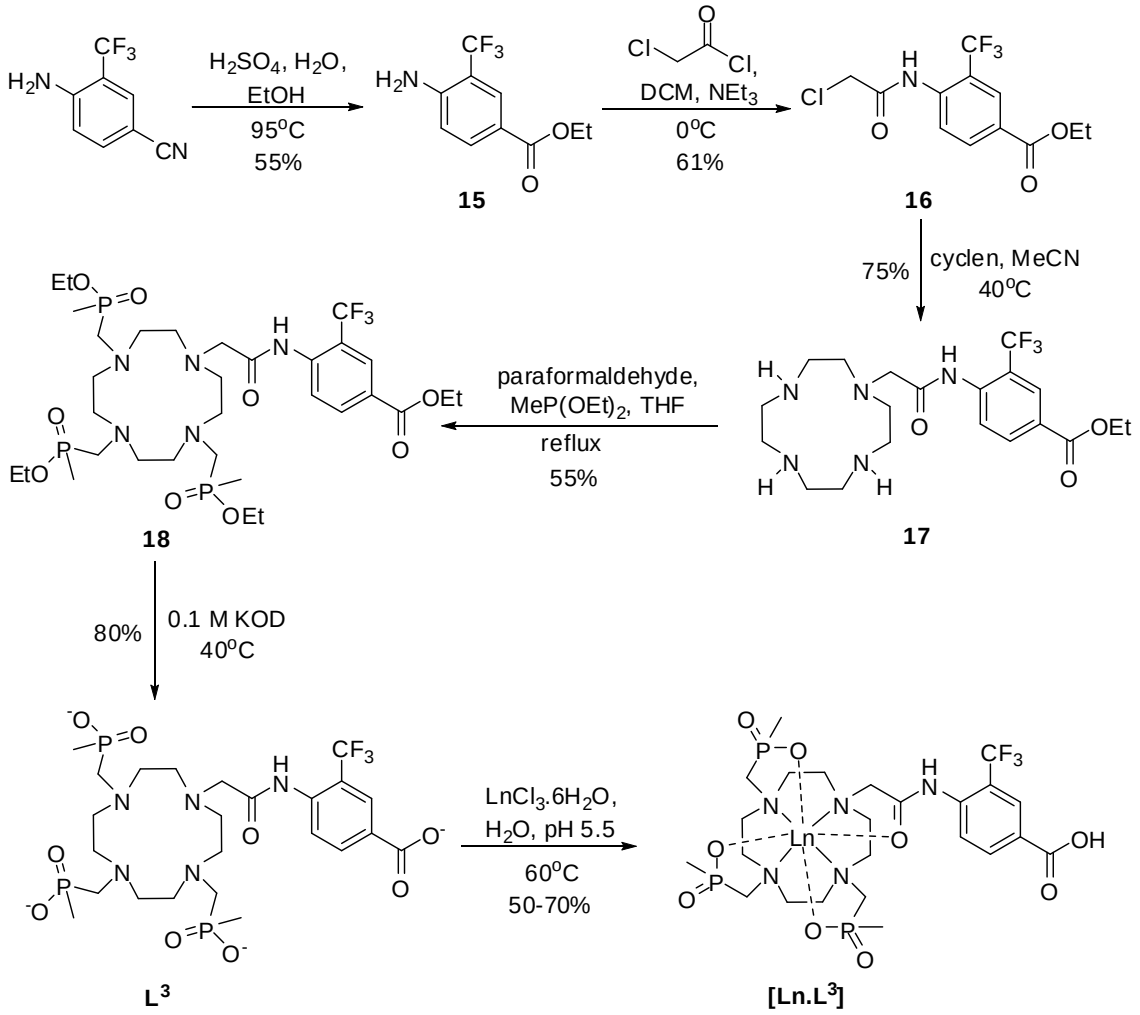

Scheme 2.4 *General procedure for the synthesis of the intermediate complex,* ***[Ln.L^3]****.*

For the synthesis of **[Ln.L^4]**, the ester bond was formed from the corresponding *p*-carboxylic acid complex, **[Ln.L^3]**, in the final step (*Scheme 2.4*). The synthesis of the intermediate triphosphinate complex, **[Ln.L^3]**, began with oxidation and esterification of the nitrile compound, followed by alkylation to generate the previously reported α-chloroamide, **16**.[1] Monoalkylation of cyclen in acetonitrile gave **17**, using an excess of the macrocycle to prevent over-alkylation and to act as the base in the reaction. Soxhlet equipment was used in a one-pot synthesis involving a co-condensation of the mono-alkylated macrocycle with paraformaldehyde and diethyl methylphosphonite. An Arbusov rearrangement yielded the desired triethylphosphinate ester, **18**, which was formed as a mixture of stereoisomers differing in configuration at each stereogenic phosphorus centre. Alumina gel column chromatography was initially

used to purify this compound. However, improved separation was achieved utilising a 3:1 mixture of alumina and silica respectively.

Ideally, acid hydrolysis would have been performed to remove the ester protecting groups, due to the simple work-up required and faster reaction times. However, such conditions can also lead to cleavage of the amide bond, and so base hydrolysis was employed instead, using 0.1 M KOD solution at 40°C, with the reaction being monitored by ^{1}H, ^{19}F, and ^{31}P NMR spectroscopy. Under these conditions, no cleavage of the amide bond was observed, and hydrolysis of all of the ester groups generally took 2-3 days to complete. After this time, the pH was lowered and the solvent removed before the ligand, **L^3**, was extracted with ethanol. Metal complexation was achieved using an aqueous solution of the appropriate metal chloride at pH 5.5 and 60°C, before the pH was raised to 10 in order to precipitate any excess Ln(III) ions as the metal hydroxide. The free metal was removed by centrifugation before the pH was lowered back to 5.5 and the intermediate complex, **[Ln.L^3]**, was purified by preparative reverse phase HPLC.

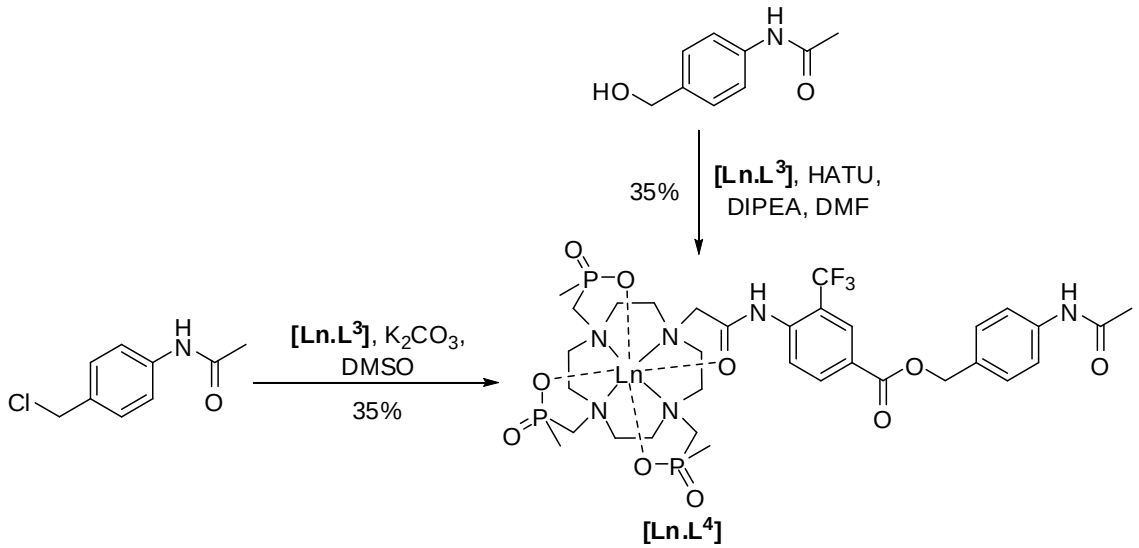

Scheme 2.5 *Alternative pathways for the synthesis of* ***[Ln.L^4]***

The ester, **[Ln.L^4]**, was then prepared *via* two different methods (*Scheme 2.5*). The first method involved O-alkylation with *N*-(4-(chloromethyl)phenyl)acetamide and

potassium carbonate as the base. The second proceeded by a coupling reaction with *N*-(4-(hydroxymethyl)phenyl)acetamide, mediated by HATU. Crude products from both reactions were purified by reverse phase HPLC and each resulted in a 35 % yield.

2.3.2 Characterisation of complexes

Low resolution electrospray and high resolution accurate mass spectra were obtained to confirm the constitution of the complexes. Characteristic isotope patterns were observed in each case that showed a good correlation with the calculated spectra. ^{19} F NMR spectroscopic data was collected for each complex, revealing the presence of one observable signal in solution, consistent with the formation of one major isomeric species in solution.

2.3.3 Signalling a remote functional group transformation

In order to test the ability of these probes to report enzyme hydrolysis, α-chymotrypsin was added to solutions of **[Dy.L^4]** and **[Tm.L^4]**, and the resulting mixtures stirred at 25°C in water at pH 7.4. The ^{19}F NMR spectra were acquired periodically to follow the reaction as a function of time. In each case, a negative control was applied by simultaneously monitoring a sample containing the complex without the presence of the enzyme.

For **[Dy.L^4]**, the paramagnetic enhanced ^{19}F chemical shift non-equivalence was 4.9 ppm between **[Dy.L^4]** (- 69.4 ppm) and the product carboxylate complex, **[Dy.L^3]** (- 64.5 ppm). This allowed straightforward monitoring of the cleavage reaction. However, the ^{19}F NMR signal for **[Dy.L^4]** suffers from increased exchange broadening at pH 7.4, due to the associated lower pK_a of the internal amide group with a *para*-ester substituent, in comparison to the acid functionality found in **[Dy.L^3]**. This behaviour had been previously observed with related systems.[1,4] Therefore, in order to reduce this exchange broadening, the pH was temporarily lowered to 6.5 during spectral data acquisition, before being increased back to pH 7.4 for the reaction to proceed. The

series of ^{19}F NMR spectra for **[Dy.L^4]** over time after the addition of α-chymotrypsin are shown in *Figure 2.11*.

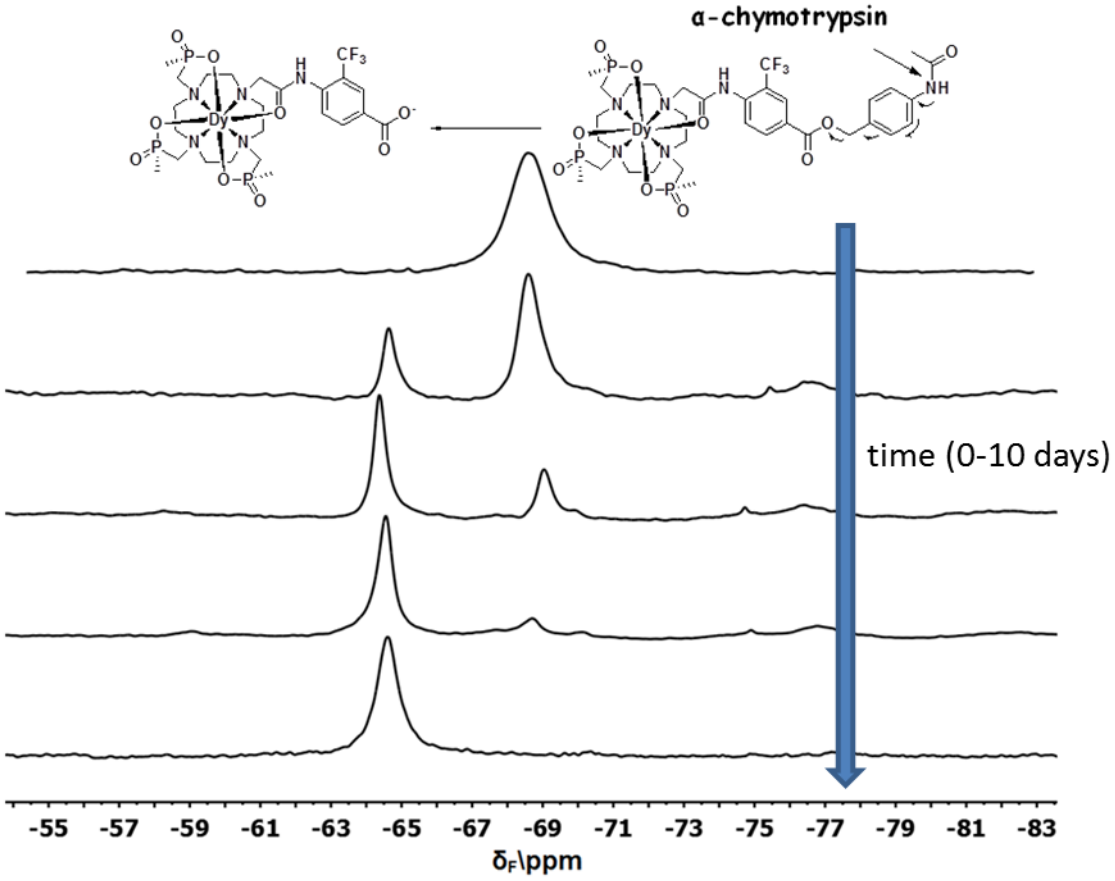

Figure 2.11 *Change in the ^{19}F NMR spectrum of **[Dy.L^4]** as a function of time, following cleavage of the remote amide bond induced by α-chymotrypsin (H_2O, pH 7.4, 9.4 T, 295 K); spectra above measured at pH 6.5 with a D_2O coaxial insert to lock the NMR instrument; substrate spectrum is at the top, product at the bottom.*

As can be seen from the ^{19}F NMR spectra, upon enzymatic cleavage the reaction proceeds directly to the product acid complex, **[Dy.L^3]**, with no signal observed for the intermediate amino compound. The above spectra show the ease of interpretation of this system, as the relative intensities of the two clearly defined peaks can be readily measured as a function of time after addition of the enzyme. However, the major drawback was the very slow rate of reaction, taking around 10 days to reach completion. After this time, an HPLC chromatogram was acquired of the reaction

mixture, showing >95 % conversion of the substrate, **[Dy.L^4]**, into the product, **[Dy.L^3]** (*Figure 2.12*).

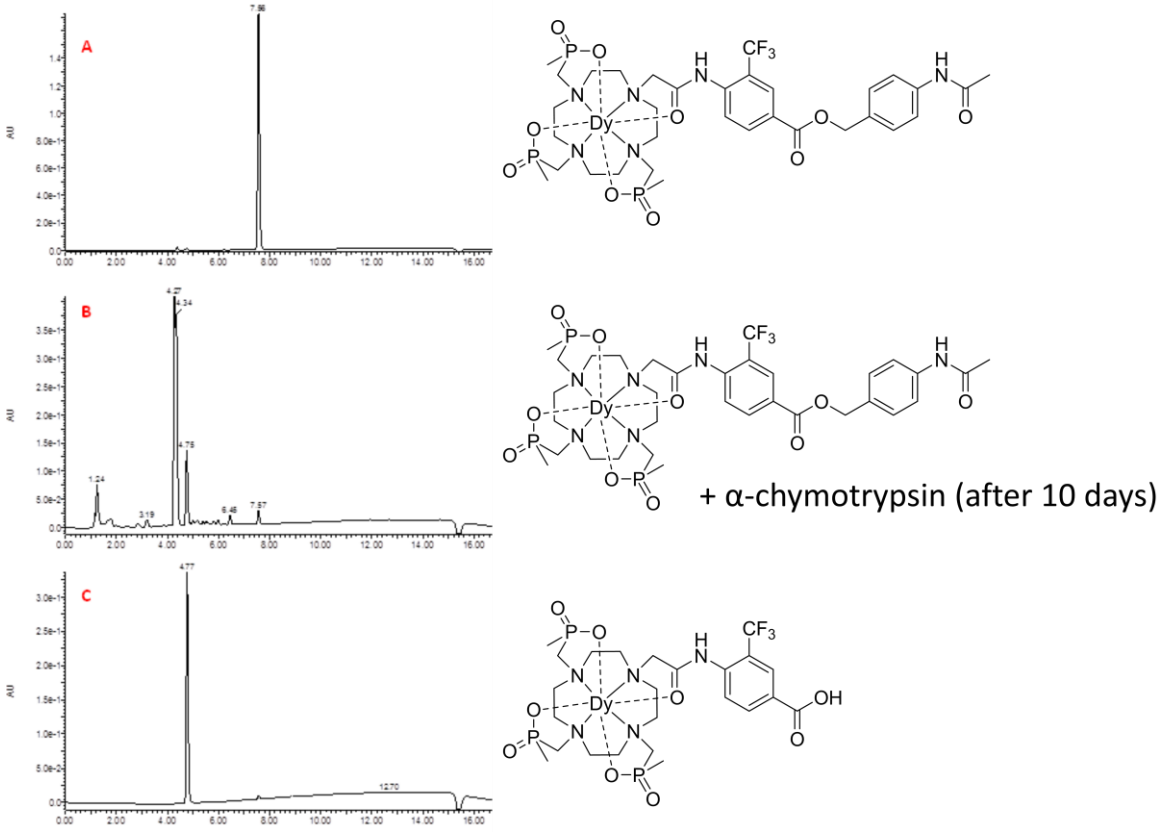

Figure 2.12 *HPLC chromatograms of: (a)* ***[Dy.L^4]****, (b)* ***[Dy.L^4]*** *+ α-chymotrypsin after 10 days, and (c)* ***[Dy.L^3]****.*

For **[Tm.L^4]**, the behaviour was more complex. The ^{19}F chemical shift non-equivalence was even larger for this system, at 12.1 ppm between the ester **[Tm.L^4]** (δ_F = -102.4 ppm) and the product carboxylate complex, **[Tm.L^3]** (δ_F = -90.3 ppm). However, when α-chymotrypsin was added to **[Tm.L^4]**, only a weak signal was apparent in the region expected for **[Tm.L^3]**. Indeed, this was barely discernible above the baseline noise and did not get stronger over time. A new, exchange broadened shift appeared at -77 ppm (*Figure 2.13*). This may be due to the formation of an adduct between the enzyme and the cleaved product, **[Tm.L^3]**, which is in chemical exchange and leads to linewidth broadening. In order to confirm this, α-chymotrypsin was added to a separate sample of **[Tm.L^3]** and the ^{19}F NMR spectrum recorded. The

same signal at -77 ppm was observed, albeit to a much lesser extent. This behaviour suggests there is some interaction occurring between this complex and the enzyme that was not apparent with the dysprosium analogue. More analyses would have to be carried out in order to fully understand the behaviour of this system with α-chymotrypsin, although separate mass spectral analysis revealed the presence of **[Tm.L^4]**, **[Tm.L^3]**, and the intermediate amine, suggesting that the reaction process was proceeding.

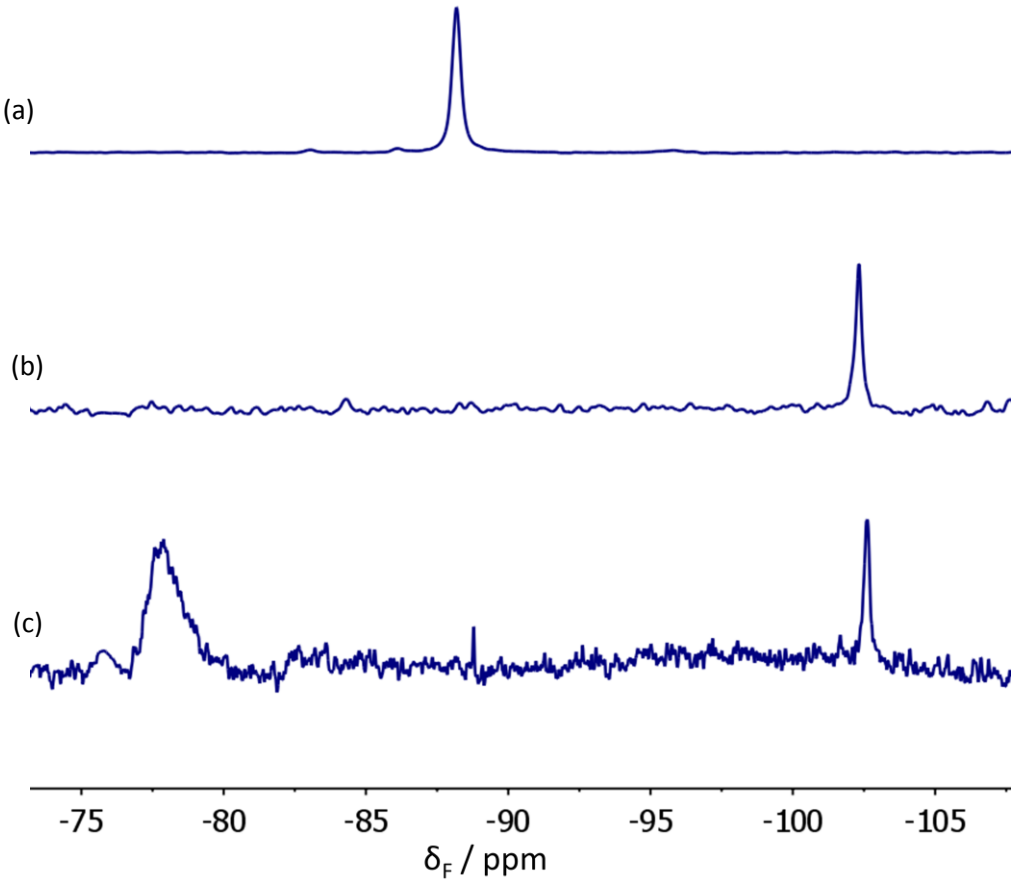

Figure 2.13 *^{19}F NMR spectra for; (a) **[Tm.L^3]**, (b) **[Tm.L^4]**, and (c) **[Tm.L^4]** + α-chymotrypsin after 1 week showing the emergence of a new, broad peak at -77 ppm (H_2O, pH 7.4, 9.4 T, 295 K; D_2O coaxial insert to lock the NMR instrument).*

2.4 Conclusions

These examples demonstrate how amplified chemical shift non-equivalence can be combined with decreased spectral acquisition times in the development of novel paramagnetic MR probes that allow the signalling of both reversible and irreversible reactions by ^{19}F NMR spectroscopy. In the first case, reversible anion binding at a lanthanide centre in aqueous solution resulted in a dipolar shift of the ligand probe resonance, induced by changing the local coordination environment. Characteristic chemical shifts were observed in the ^{19}F NMR spectra for the adducts formed with each anion. For the first complex, **[Ln.L^1]$^+$**, no anion selectivity was observed, with a combination of exchange broadened peaks observed upon the addition of an equimolar mixture of the anions. This system also suffered from poor complex stability in the presence of anions, with considerable leaching of the lanthanide ion observed. However, the second complex tested, **[Ln.L^2]$^+$**, showed considerable improvement, both in terms of selectivity and stability. Citrate selectivity was demonstrated by NMR spectroscopy for Ho(III) and Tm(III) complexes. With the related Eu(III) complex, emission spectral changes allowed a quantification of anion binding constants. The inherently large linewidths observed are the major drawback of these systems, and need to be minimised in order to make the probes more applicable. However, a proof-of-principle has been demonstrated, correlating well with previous emission-based studies using related lanthanide complexes.

In the second example, it was demonstrated that ester cleavage can be signalled by a ^{19}F NMR shift change of a remote CF_3 reporter, with chemical shift non-equivalence up to 12 ppm depending on the lanthanide chosen. This is an order of magnitude greater than differences typically found with diamagnetic systems.[23] There are, however, a number of issues that would need to be overcome to proceed with such a system. The major drawback is the slow reaction time, taking over 10 days to reach completion. It is necessary to find a better substrate for the hydrolytic enzyme, in order to reduce the reaction time significantly. However, this work does establish the feasibility of such systems and sets the groundwork in place for further investigations.

2.5 References

1. K. H. Chalmers, E. De Luca, N. H. M. Hogg, A. M. Kenwright, I. Kuprov, D. Parker, M. Botta, J. I. Wilson, and A. M. Blamire, *Chem. Eur. J.*, 2010, **16**, 134–148.

2. P. Harvey, I. Kuprov, and D. Parker, *Eur. J. Inorg. Chem.*, 2012, 2015–2022.

3. P. K. Senanayake, A. M. Kenwright, D. Parker, and S. K. Van Der Hoorn, *Chem. Commun.*, 2007, 2923–2925.

4. A. M. Kenwright, I. Kuprov, E. De Luca, D. Parker, S. U. Pandya, P. K. Senanayake, and D. G. Smith, *Chem. Commun.*, 2008, 2514–2516.

5. E. Pérez-Mayoral, V. Negri, J. Soler-Padrós, S. Cerdán, and P. Ballesteros, *Eur. J. Radiol.*, 2008, **67**, 453–458.

6. P. Provent, M. Benito, B. Hiba, R. Farion, P. López-Larrubia, P. Ballesteros, C. Rémy, C. Segebarth, S. Cerdán, J. A. Coles, and M. L. García-Martín, *Cancer Res.*, 2007, **67**, 7638–7645.

7. D. Parker, *Chem. Soc. Rev.*, 2004, **33**, 156–165.

8. R. Pal, A. Beeby, and D. Parker, *J Pharmaceut. Biomed.*, 2011, **56**, 352–358.

9. D. G. Smith, B. K. McMahon, R. Pal, and D. Parker, *Chem. Commun.*, 2012, **48**, 8520–8522.

10. Z. Kovacs and A. D. Sherry, *J. Chem. Soc., Chem. Commun.*, 1995, 185–186.

11. Z. Kovacs and A. D. Sherry, *Synthesis-Stuttgart*, 1997, 759–763.

12. D. Parker, R. S. Dickins, H. Puschmann, C. Crossland, and J. A. K. Howard, *Chem. Rev.*, 2002, **102**, 1977–2010.

13. P. Caravan, J. Ellison, T. McMurry, and R. Lauffer, *Chem. Rev.*, 1999, **99**, 2293–2352.

14. D. Parker and J. Yu, *Chem. Commun.*, 2005, 3141–3143.

15. J. Yu, D. Parker, R. Pal, R. A. Poole, and M. J. Cann, *J. Am. Chem. Soc.*, 2006, **128**, 2294–2299.

16. R. Pal, D. Parker, and L. C. Costello, *Org. Biomol. Chem.*, 2009, **7**, 1525–1528.

17. R. S. Dickins, S. Aime, A. S. Batsanov, A. Beeby, M. Botta, J. I. Bruce, J. A. K. Howard, C. S. Love, D. Parker, R. D. Peacock, and H. Puschmann, *J. Am. Chem. Soc.*, 2002, **124**, 12697–12705.

18. S. Mizukami, R. Takikawa, F. Sugihara, Y. Hori, H. Tochio, M. Wälchli, M. Shirakawa, and K. Kikuchi, *J. Am. Chem. Soc.*, 2008, **130**, 794–795.

19. S. Mizukami, H. Matsushita, R. Takikawa, F. Sugihara, M. Shirakawa, and K. Kikuchi, *Chem. Sci.*, 2011, **2**, 1151–1155.

20. E. De-Luca, PhD Thesis, Durham University, 2010.

21. P. Harvey, K. H. Chalmers, E. De Luca, A. Mishra, and D. Parker, *Chem. Eur. J.*, 2012, **18**, 8748–8757.

22. K. H. Chalmers, M. Botta, and D. Parker, *Dalton Trans.*, 2011, **40**, 904–913.

23. J. Yu, L. Liu, V. D. Kodibagkar, W. Cui, and R. P. Mason, *Bioorg. Med. Chem.*, 2006, **14**, 326–333.

3. Strategies to Enhance Signal Intensity; Increasing Fluorine Density

3.1 Introduction

As discussed in *Chapter 1*, one of the major drawbacks of ^{19}F MRI is the low sensitivity of the technique. The incorporation of a paramagnetic lanthanide ion alleviates this somewhat by increasing relaxation rates and dramatically reducing acquisition times. Unfortunately, this approach has yet to be demonstrated for *in vivo* studies, showing the need for further improvements to be developed that increase the sensitivity of any imaging experiment. One method to do this is to increase the fluorine density per unit concentration, something that has been commonly applied in diamagnetic systems through the use of perfluorocarbon compounds. However, there are limitations with the strategy of perfluorination, especially with cyclen-based lanthanide complexes. It is imperative that all of the fluorine atoms are magnetically equivalent, and so give rise to one major signal in solution, otherwise any potential signal intensity gains would be lost. It is also essential that biocompatibility is maintained, i.e. good water solubility and low toxicity.

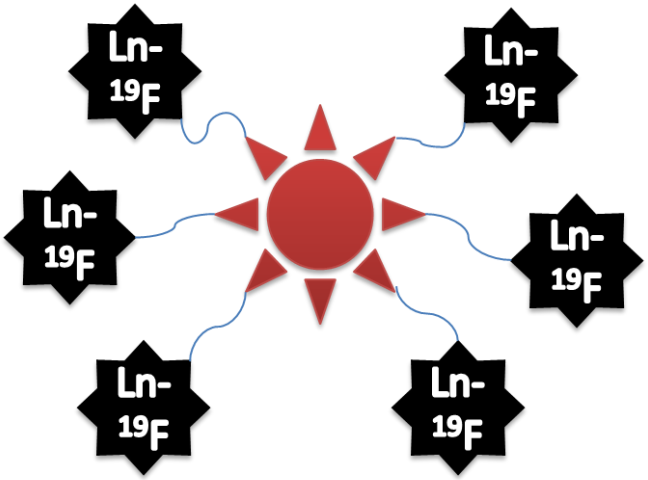

Figure 3.1 *Schematic of conjugate principle: red centre represents high molecular weight vector, Ln-^{19}F represents fluorinated lanthanide complex, and blue line represents covalent bond linker.*

A potential solution to increase the fluorine density per unit concentration, without the need for perfluorinated compounds, is to covalently link a number of fluorine containing lanthanide complexes to a central, higher molecular weight adduct (*Figure 3.1*). This would retain the benefits of the individual complexes, which should all be equivalent in the resulting conjugate, resulting in one signal in the ^{19}F NMR spectrum. In addition to increasing the signal per unit concentration, medium to high molecular weight conjugates should possess relatively slow rates of clearance in the body.[1–3] This increase in retention time should result in an accompanied rise in the local signal density *in vivo*. In order to assess the behaviour and potential benefits of such compounds, two different adducts were investigated: chitosan, a naturally derived linear polysaccharide; and PAMAM, a polyamidoamine-based dendrimer.

3.2 Glycol chitosan based system

3.2.1 Previous work

Previous, unpublished work has demonstrated the feasibility of forming medium to high molecular weight conjugates using glycol chitosan as the vector.[4,5] These studies used both commercially available glycol chitosan (≈ 195,000 D) and a modified form that results from acidic digestion of the commercial sample with 4 M HCl at 50°C over 24 h. This procedure results in a significantly reduced molecular weight (≈ 6,500 D), in addition to complete de-acetylation being observed (*Scheme 3.1*). The latter, lower average molecular weight compound displayed greatly improved solubility, and was studied in further detail. A conjugate was formed using this chitosan compound with a carboxylate lanthanide complex, **[Ln.3^1]** (*Scheme 3.1*).

Firstly, the gadolinium compound, **[Gd.3^1-chitosan]**, was investigated to determine biodistribution and tumour uptake. Nude mice bearing HT29 colorectal tumour xenografts were injected with the conjugate complex at a dose of 0.017 mmol kg^{-1} and analysed by dynamic contrast enhanced ^{1}H MRI. Almost immediately, contrast enhancement (< 1 min) was observed after tail vein injection in both the tumour area and the bladder. The conjugate was well tolerated by the animals and the presence of

the compound in the bladder is desirable, as it is indicative of renal excretion eliminating it from the system. The longer retention time in the tumour offered an improvement on analogous low molecular weight complexes that had previously been investigated.

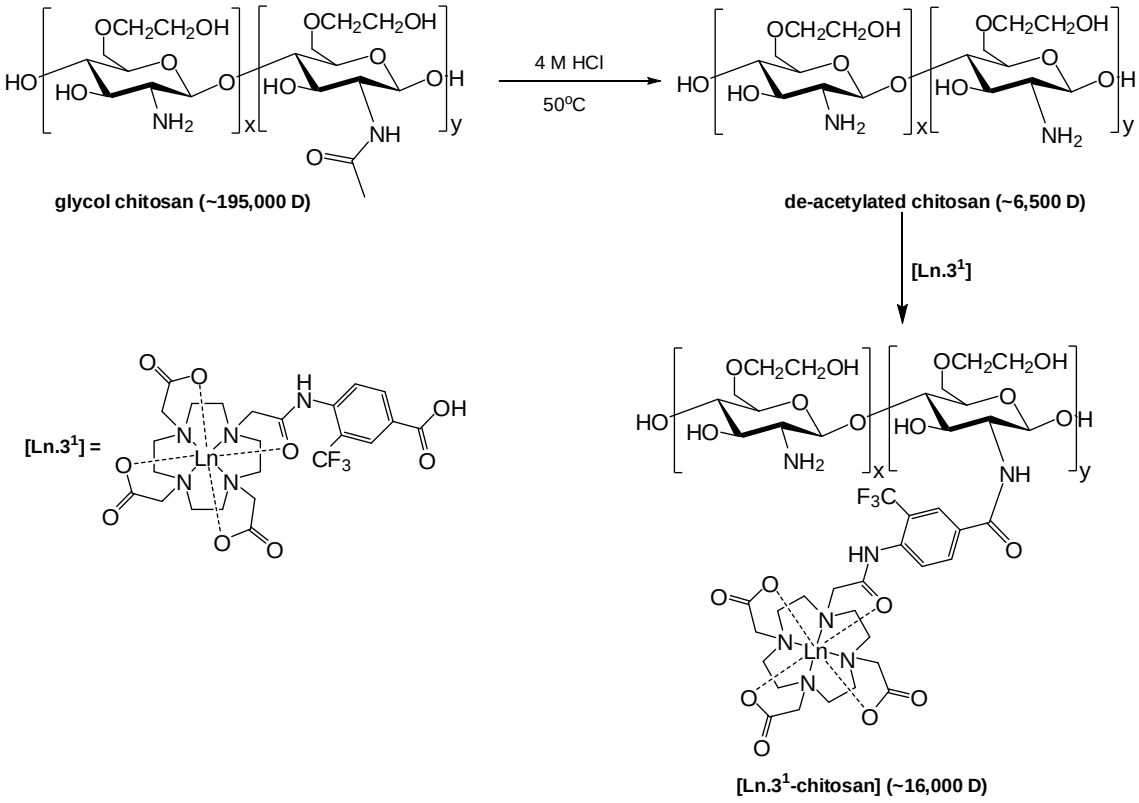

Scheme 3.1 *Synthesis of previously investigated chitosan conjugate,* ***[Ln.3^1-chitosan]***.[4]

Unfortunately, when a similar ^{19}F MRI dynamic experiment was undertaken using the holmium complex, **[Ho.3^1-chitosan]**, no fluorine signal was detected over one hour following administration, even with an increase in dose (0.034 mmol kg^{-1}). This lack of observable signal was most likely due to the rather broad linewidth of the fluorine resonance, leading to inadequate signal intensity for observation. Therefore, in an effort to overcome this issue, the analogous phosphinate complex is investigated here. It possesses a narrower linewidth and exists as predominantly one isomeric species in solution. Each of these factors have been attributed to the presence of the more bulky

phosphinate groups, that favour one main species and inhibit intramolecular chemical exchange.[6]

3.2.2 Synthesis and characterisation of the complex

The synthesis of the complex, **[Ln.L^3]**, is detailed in *Chapter 2*. For potential *in vivo* applications, as discussed here, the only change necessary in the synthetic procedure was for the deprotection of the ethyl protecting groups to form the ligand, **L^3**. Previously, aqueous potassium hydroxide had been used to hydrolyse the ethyl groups. However, in this case it was more ideal to employ NaOD as the agent for base hydrolysis, due to the lower relative toxicity of sodium in comparison to potassium salts; hydrolysis took around twice as long to reach completion. In all other aspects, the synthetic route followed that described previously.

The complex was purified by preparative scale reverse-phase HPLC. As previously described, low resolution electrospray and high resolution accurate mass spectrometry were carried out to confirm the presence of the complex, with characteristic isotope patterns observed showing good correlation with calculated spectra. A ^{19}F NMR spectrum showed the presence of one signal in solution, indicating the formation of one major isomer (>90 %) in solution.

3.2.3 Conjugate synthesis

The synthesis of the conjugate, **[Dy.L^3-chitosan]** is outlined in *Scheme 3.2*. The carboxylic acid group of **[Dy.L^3]** was first converted to an active ester, by reacting with *o*-(benzotriazol-1-yl)-*N,N,N′,N′*-tetramethyluronium tetrafluoroborate (TBTU) and 4-methylmorpholine (NMM) in DMF. After stirring for 1 h, to allow formation of the active ester, a concentrated aqueous solution of glycol chitosan was added and the mixture stirred for a further 36 h. Purification of **[Dy.L^3-chitosan]** was achieved by extensive dialysis, using dialysis tubing and Float-A-Lyzer G2 filters with 5000 molecular weight cut-offs (MWCO) to remove unreacted coupling reagents and excess complex.

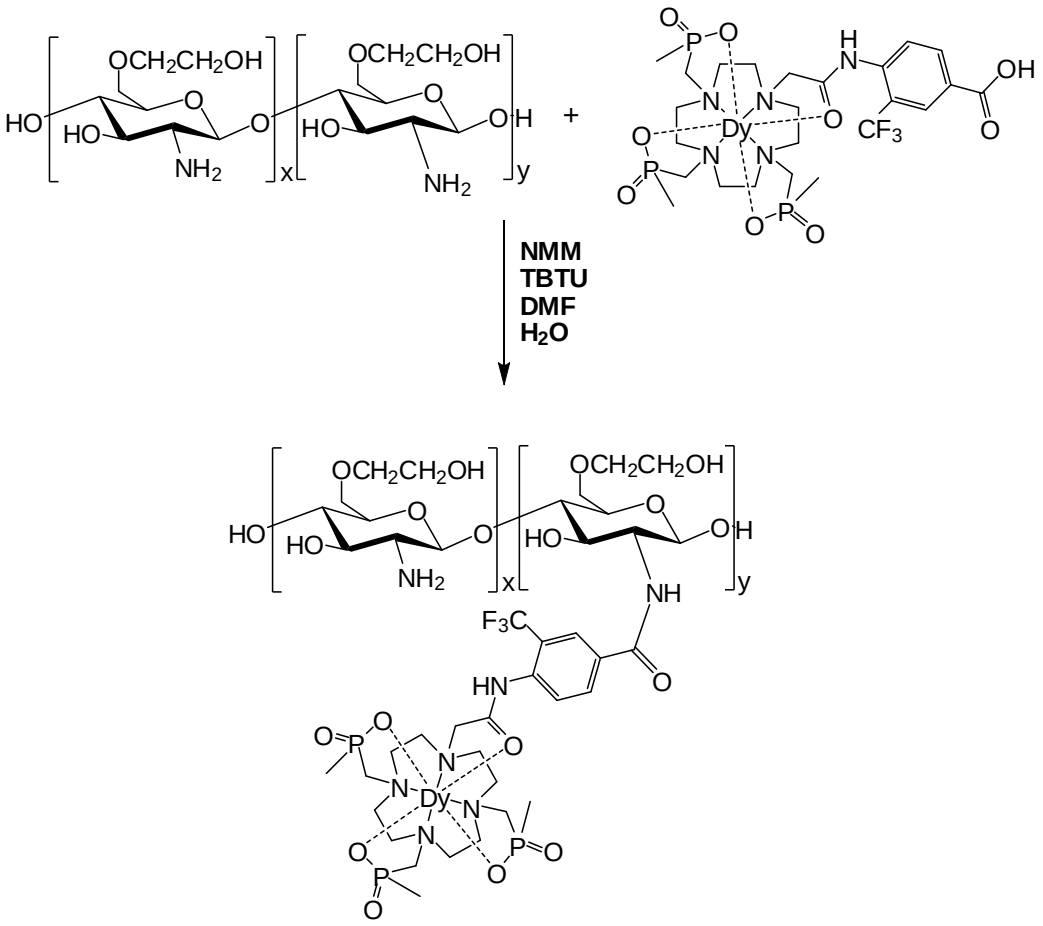

Scheme 3.2 *Synthesis of the chitosan conjugate complex,* ***[Dy.L^3-chitosan]****.*

3.2.4 Characterisation of the conjugate

Table 3.1 *Gel permeation chromatography (GPC) data for the starting glycol chitosan compound and the corresponding conjugate,* ***[Dy.L^3-chitosan]****.*

Sample	M_w [(a)]	M_n [(b)]	PDI [(c)]
Glycol chitosan	6700	3150	2.1
[Dy.L^3-chitosan]	10900	5590	1.9

For corresponding unreacted complex, **[Dy.L^3]**, M_w = 852. (a) Calibrated using Pullulan polysaccharides and calculated molecular weight averages are expressed as the polysaccharide equivalent molecular weights. (b) Number average molecular weights. (c) Polydispersity (M_w/M_n).

To determine the average size and mean number of complexes conjugated to chitosan, the complex was analysed by aqueous gel permeation chromatography (GPC). The results indicated an increase in the molecular weights of the conjugates (*Table 3.1*), with respect to the unreacted glycol chitosan, confirming the formation of covalently

bound complex conjugates. By comparing the molecular weights of the unreacted complex and glycol chitosan with that of **[Dy.L^3-chitosan]**, it can be calculated that there are around 5 complexes bound to each molecule of glycol chitosan. As glycol chitosan is a polydisperse system, such values are averages for the whole system. Poor solubility in water had been observed for some previous chitosan-based systems studied, but no issues were seen with the conjugate reported here, at the concentrations employed (2-5 mM).

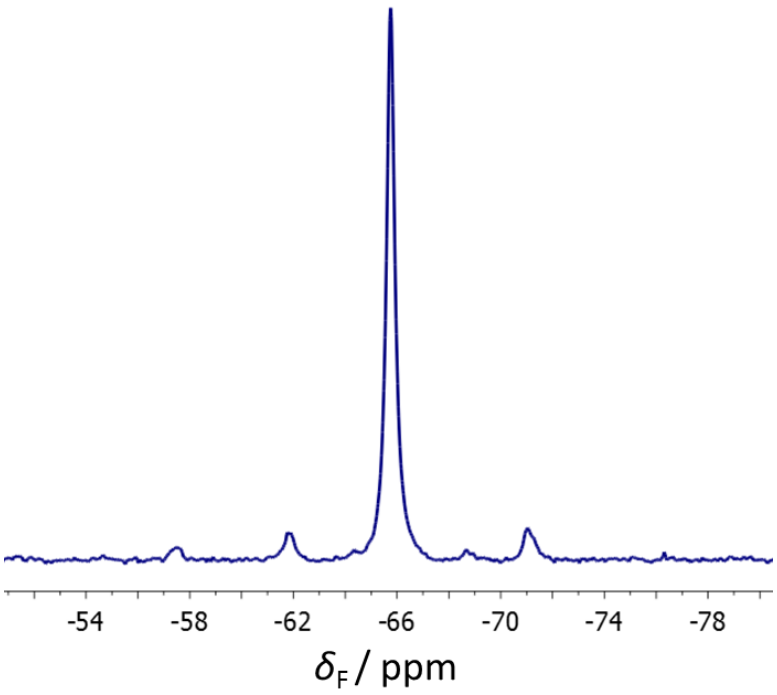

Figure 3.2 *^{19}F NMR spectra of **[Dy.L^3-chitosan]** (D_2O, 9.4 T, pD 7.4, 0.1 M NaCl, 298 K).*

The ^{19}F NMR spectrum of **[Dy.L^3-chitosan]** displayed one principal resonance (> 90 %), indicating equivalence of each complex in the conjugated adduct (*Figure 3.2*). Promotion of one major signal is necessary for any potential *in vivo* applications, to ensure that signal intensity is maximised. The next area to consider is the relaxation rates, which are shown in *Table 3.2*, along with the data for the unreacted complex, **[Dy.L^3]**, and a previous chitosan-based system, **[Ho.3^1-chitosan]**.

Table 3.2 *^{19}F NMR longitudinal and transverse relaxation rates at two magnetic fields (4.7 and 9.4 T) for **[Dy.L^3]**, its glycol chitosan adduct, **[Dy.L^3-chitosan]**, and comparison with the previously analysed **[Ho.3^1-chitosan]**.*

Complex	δ_F / ppm	4.7 T		9.4 T	
		R_1 / Hz	R_2 / Hz [(a)]	R_1 / Hz	R_2 / Hz [(a)]
[Dy.L^3]	-64.5	110	217	186	440
[Dy.L^3-chitosan]	-65.7	108	176	183	367
[Ho.3^1-chitosan] [(b)]	-56.8	56	741	100	807

(a) R_2 values were estimated as ($\pi\omega_{1/2}$) for a Lorentzian line fit. (b) Values taken from unpublished work.[4]

There is a substantial improvement in relaxation rates for the phosphinate conjugate, **[Dy.L^3-chitosan]**, over the previously studied carboxylate based system, **[Ho.3^1-chitosan]**. The longitudinal relaxation rate, R_1, is almost twice as large for the dysprosium system, coupled with a sizeable reduction in the transverse relaxation rate, R_2, calculated from the linewidths. Both of these factors will serve to improve signal intensity and the combination of the improvement in both relaxation rates suggested considerable scope for acquisition of a ^{19}F MR image with **[Dy.L^3-chitosan]**, in comparison with the work previously done with **[Ho.3^1-chitosan]**. The only potential drawback with the dysprosium system is that the conjugate formed possessed fewer complexes per molecule of chitosan than was found for the previous system (**[Dy.L^3-chitosan]** ≈ 5 complexes/chitosan, **[Ho.3^1-chitosan]** ≈ 11 complexes/chitosan).

3.2.5 Preliminary MRI studies

Preliminary imaging studies of **[Dy.L^3-chitosan]** were carried out at 7 T by Prof. Andrew Blamire at the Newcastle Magnetic Resonance Centre using a 3D gradient echo sequence (*Figure 3.3*) with a 4 turn solenoid coil (20 mm diameter, 20 mm coil length). The R_1 and R_2 values were estimated to be 145 and 270 Hz, respectively, leading to a calculated Ernst angle of 60.7^o for a repetition rate, T_R, of 25 ms. With a total scan duration of 131 s, good quality images were acquired at a resolution of 1x1x1 mm^3, which was a significant improvement over the 1x1x25 mm^3 resolution obtained with previous systems. Shorter echo times, T_E (2.07 ms), were applied in order to minimise

R_2 loss. The resulting mean signal-to-noise ratio (SNR) from 1x1x1 mm^3 was calculated to be 9.1, which was a significant improvement on previously studied compounds when scaled for comparison. These results were highly promising for further investigation, leading to an *in vivo* experiment being undertaken.

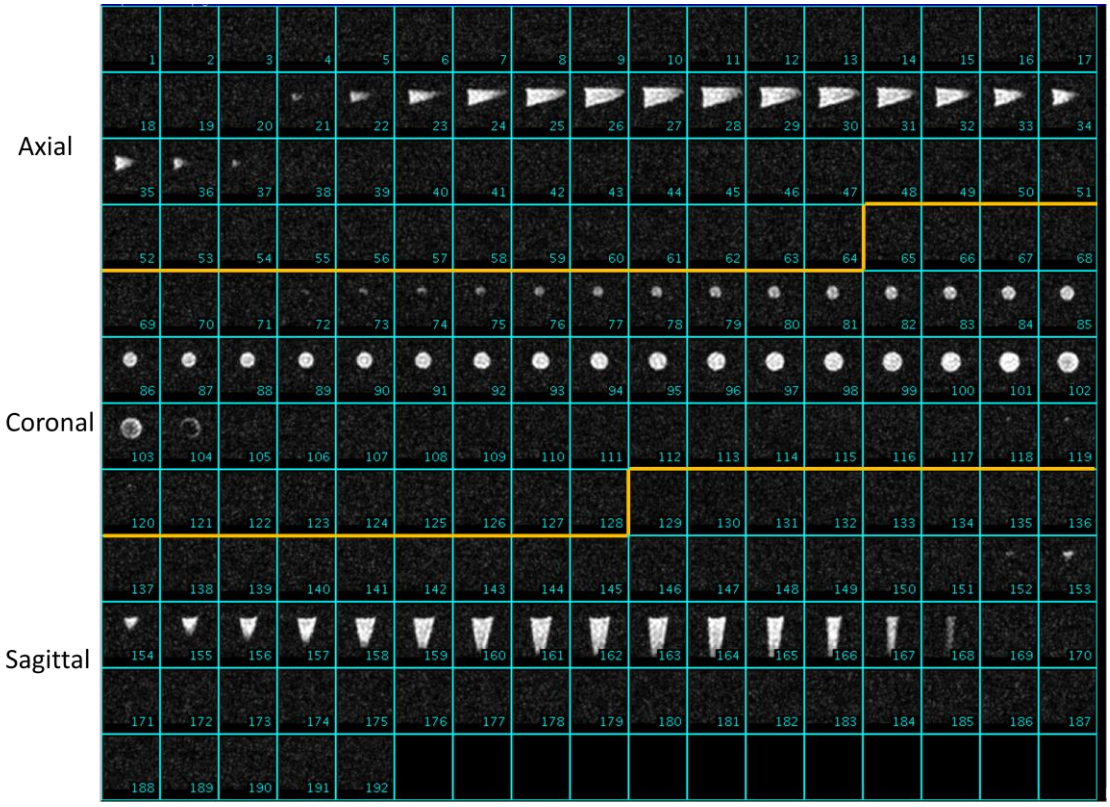

Figure 3.3 *^{19}F MR phantom images of **[Dy.L^3-chitosan]** contained in an Eppendorf tube (2 mM complex, H_2O, 0.1 M NaCl, 7 T, 295 K, 3D gradient echo sequence, 1x1x1 mm^3 resolution, T_R = 4.91 ms, T_E = 2.07 ms, flip angle = 60.7^o, 26 averages, scan duration = 131 s, mean SNR from 1x1x1 mm^3 = 9.1).*

Preliminary *in vivo* studies were carried out by Prof. Andrew Blamire and Dr. Ian Wilson, at the Newcastle Magnetic Resonance Centre, on SCID male mice (25 g) with HT29 tumours (human colorectal carcinoma). Measurements were taken 10-14 days after inoculation when tumours were around 10 mm in diameter, with the mouse anaesthetised with a mixture of ketamine (0.75 mg/kg) and medetomidine (0.5-1.0 mg/kg). A solution (5 mM) of **[Dy.L^3-chitosan]** was administered by intravenous injection in the tail. The mouse received 200 µL of the solution,

corresponding to a dose of 0.04 mmol kg^{-1}. The results were obtained with a ^{19}F tuned square surface coil (30 mm coil length), onto which the animal was laid, and are shown in *Figure 3.4*.

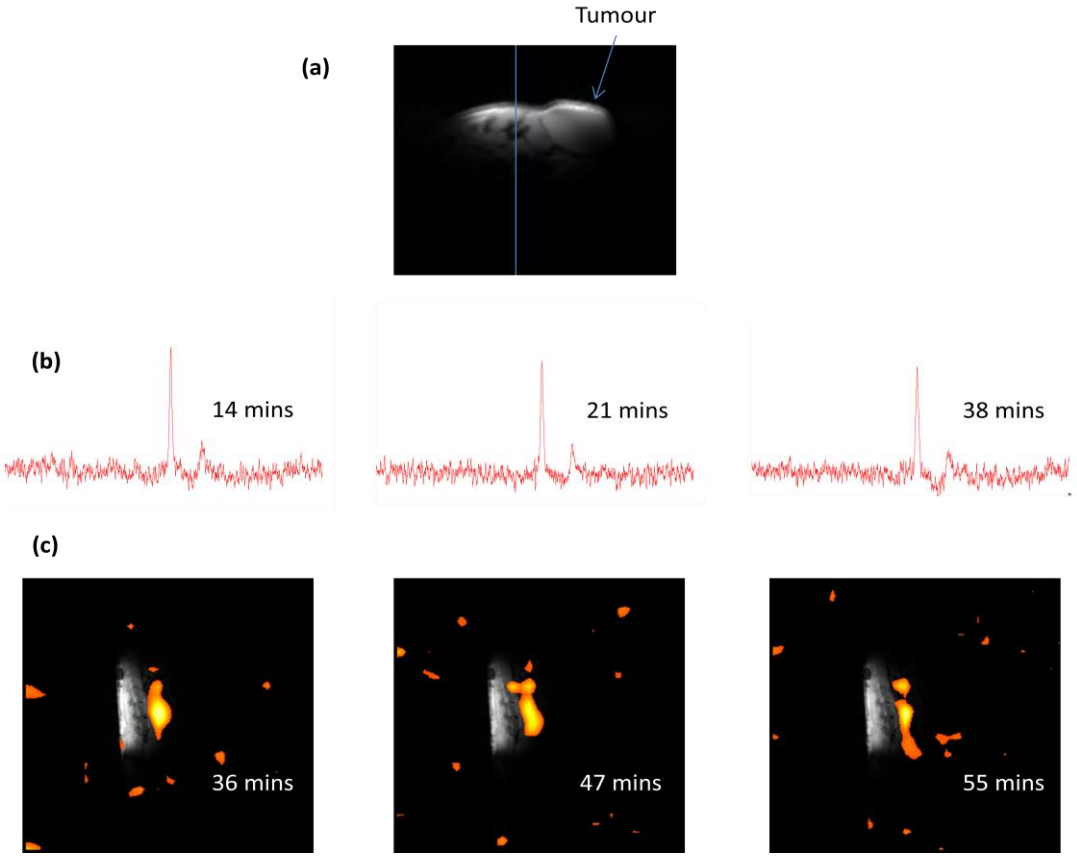

Figure 3.4 *MR images obtained of a HT29 tumour-bearing SCID male mouse showing: (a) ^{1}H MR image (tumour indicated by arrow, blue line indicates approximate location of slice with maximal ^{19}F signal observed); (b) in vivo ^{19}F NMR resonances and (c) ^{19}F MR images observed at indicated times after administration.*

A fluorine resonance was observed in the tissue in an unlocalised data collection during infusion. The image could then be refined and ^{19}F 3D gradient echo scans were obtained, which were overlaid onto the basic anatomical ^{1}H MR image and indicated a build-up of the compound in one of the major arteries of the mouse. Unfortunately, the mouse expired at some stage in the experiment. Due to the set up required for this imaging method, the life signs of the mouse could not be monitored during the experiment and so it is not known when, or why, the mouse expired. It is likely that the mouse was alive when intravenously injected, and expired shortly afterwards,

which would explain why the compound was present in an artery and why very little change in distribution was observed over the time scale of the experiment (≈ 1 h).

While the death of the animal was disappointing and limited the data that could be obtained from the experiment, the fact that a signal has been observed is promising and is the first *in vivo* ^{19}F MR signal obtained for such compounds. These results indicate that the system works in principle, although the experiment needs to be repeated in order to fully understand the behaviour of the compound. Further *in vivo* investigations are on-going, utilising both the gadolinium and dysprosium analogues of **[Ln.L^3-chitosan]**, in order to establish biodistribution, toxicity, and imaging behaviour of the compound.

3.3 Dendrimer based system

3.3.1 Design of probe

While the chitosan based system showed considerable potential, a drawback of this system is the polydisperse nature of the compounds. This polydispersity has limitations for clinical practice, both in terms of reproducibility and the variability in the rate of clearance. Therefore, it was decided to attempt to form a well-defined system, with a known number of complexes and molecular weight. A class of medium-to-high molecular weight adducts that stand out as suitable for such a purpose are dendrimers, as they possess branched three-dimensional structures with elements that can control both the surface and internal properties of the macromolecules.[7] Dendrimers have been previously investigated for use with Gd(III)-based contrast agents,[8–10] in addition to applications as drug transporters, tissue engineering, and as drugs themsleves.[11–13] There are a number of commercially available dendrimers that could be used, but the system chosen here was PAMAM generation 2.0, with an ethylenediamine core (*Figure 3.5*). This dendrimer was chosen for a number of reasons: the favourable size and molecular weight (1430 g mol^{-1}); the well-defined,

functionable end groups (eight primary amine surface groups); and its relatively low cost.

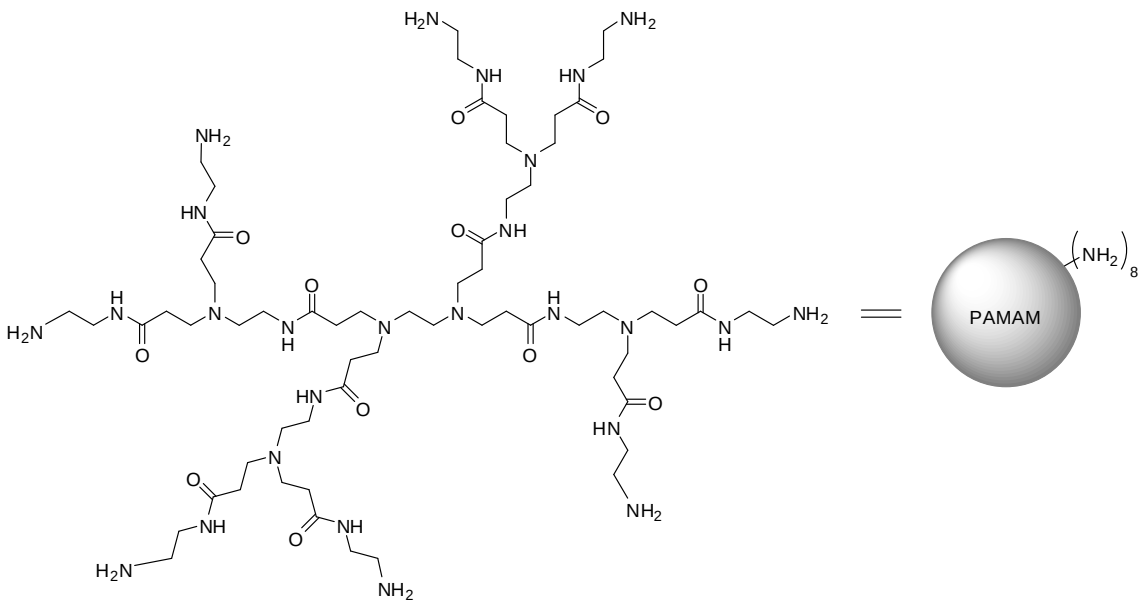

Figure 3.5 *Structure of* PAMAM dendrimer, ethylenediamine core, generation 2.0, and abbreviated form to be used for the rest of this work.

3.3.2 Trial studies

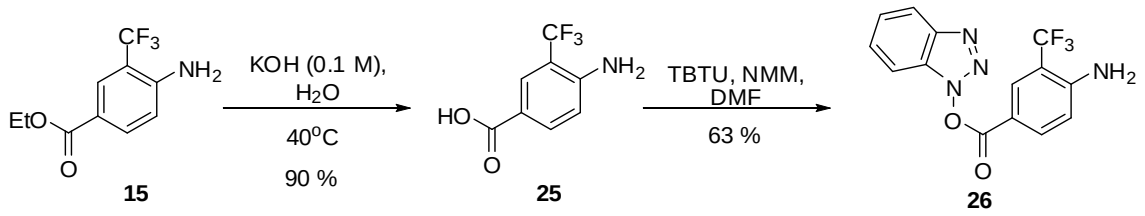

Scheme 3.3 *Procedure for the synthesis of the active ester compound.*

In order to determine the feasibility of functionalising all eight terminal amine groups of the dendrimer, a preliminary study was first undertaken on a model CF_3 containing compound. The active ester of 4-amino-3-(trifluoromethyl)benzoic acid was formed and isolated by the synthetic procedure shown in *Scheme 3.3*. Base hydrolysis of the ethyl ester, **15**, using potassium hydroxide resulted in formation of the acid, **25**. This was stirred with NMM and TBTU in DMF, followed by purification with alumina gel

column chromatography to obtain the active ester, **26**. Twelve equivalents of this stable, isolated active ester were stirred with PAMAM generation 1.0 dendrimer in DMF, with NMM added as a base (*Scheme 3.4*). After removal of DMF, the resulting residue was washed with DCM followed by water. Methanol and its deuterated analogue were used as solvents in the analysis of the resulting product, **PAMAM-(F_8)**.

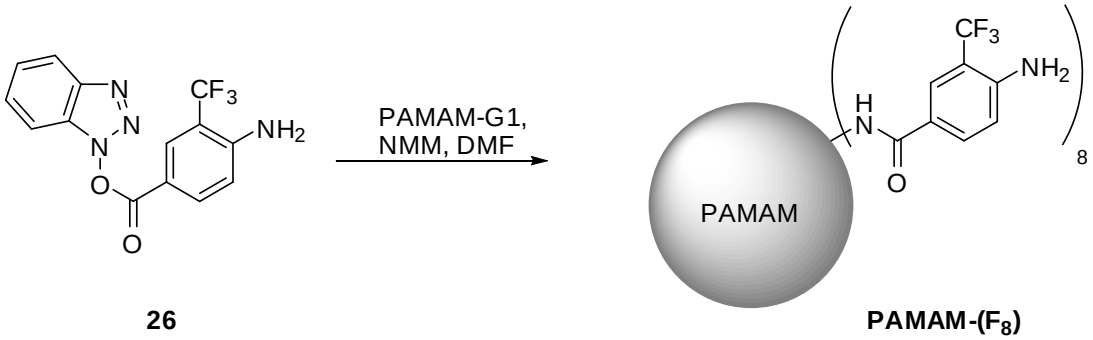

26 **PAMAM-(F_8)**

Scheme 3.4 *Reaction between the active ester compound and PAMAM generation 1.0, ethylenediamine core.*

Analysis of **PAMAM-(F_8)** by MALDI$^+$ indicated formation of the desired conjugate, with a signal corresponding to the functionalisation of each of the eight amine groups (*Figure 3.6*). This suggested complete reaction and indicated the potential of this system to behave in the required manner. The ^{19}F NMR spectrum of the product indicated one main species, shifted around 1 ppm away from the resonance associated with the fluorinated starting material (*Figure 3.6*). The ^{1}H NMR spectrum was more complex, but the relative integrals between the aromatic and alkyl regions were consistent with complete conversion to the desired compound.

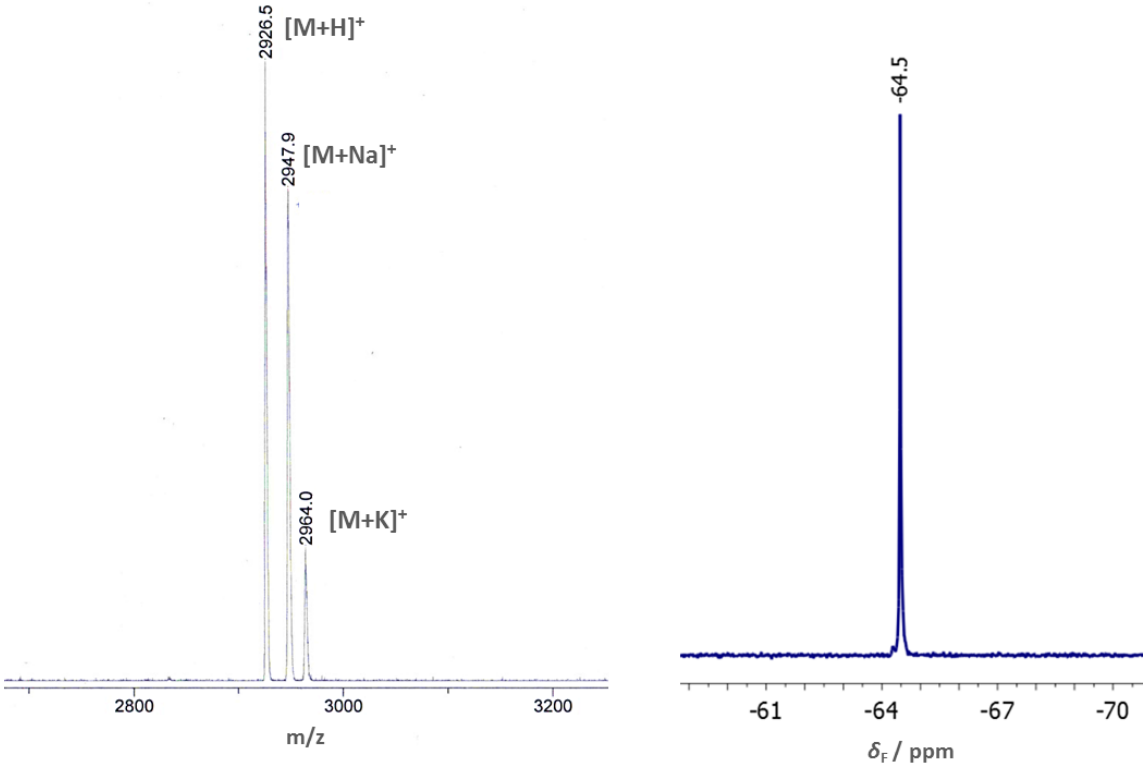

Figure 3.6 *MALDI^{+} (left) and ^{19}F NMR (right) spectra of* ***PAMAM-(F$_8$)*** *indicating complete conversion to desired octa-substituted product.*

3.3.3 Conjugate synthesis and characterisation

Due to success of the trial system, the analogous reaction with **[Dy.L^3]** was then attempted (*Scheme 3.5*). The reaction followed a similar sequence to that described for the chitosan conjugate above, with the complex first stirred in DMF with TBTU and NMM for 30 min to form the active ester, before a solution of PAMAM dissolved in DMF was added and stirred for a further 4 h. After removal of the solvent, the residue was dissolved in water and purified by extensive dialysis (MWCO = 5000 D).

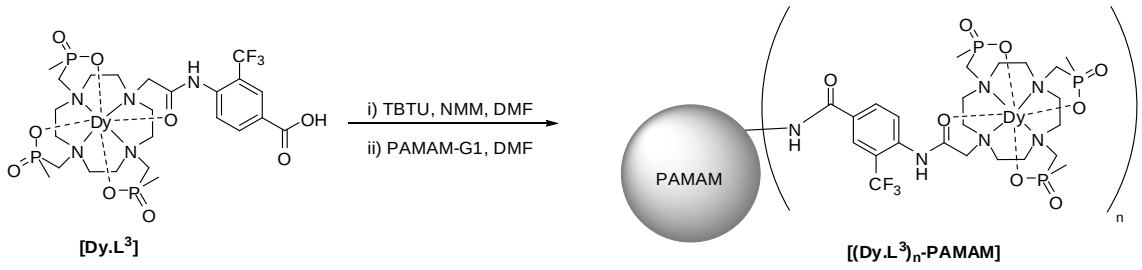

Scheme 3.5 *Synthesis of* ***[(Dy.L^3)$_n$-PAMAM]****.*

Unfortunately, unlike with the trial system this reaction did not proceed to completion, even with an excess of 20 equivalents of the complex. This behaviour was likely to be due to the introduction of the more sterically and electronically demanding lanthanide complexes in comparison to the smaller aromatic molecules used in the model system. A representative MALDI$^+$ spectrum is shown in *Figure 3.7*, which indicates the formation of a mixture of one to five molecules of **[Dy.L^3]** coupled to the dendrimer. Further complex was added to this mixture, but resulted in no further reaction being observed. Heating of the reaction was attempted, but appeared to cause degradation of the system and resulted in no high molecular weight species being observed. Seven was the highest number of conjugated complexes observed in any of the reactions, and by dialysing with a high MWCO (8000 D) the di- and tri-substituted PAMAM species could be removed, although this still left a mixture of higher order substituted compounds. It should be noted that, even for these mixtures, a single resonance was observed in the ^{19}F NMR spectrum, with similar characteristics to the signal observed in the previous chitosan complex (*Figure 3.7*). The products formed were also fully water soluble.

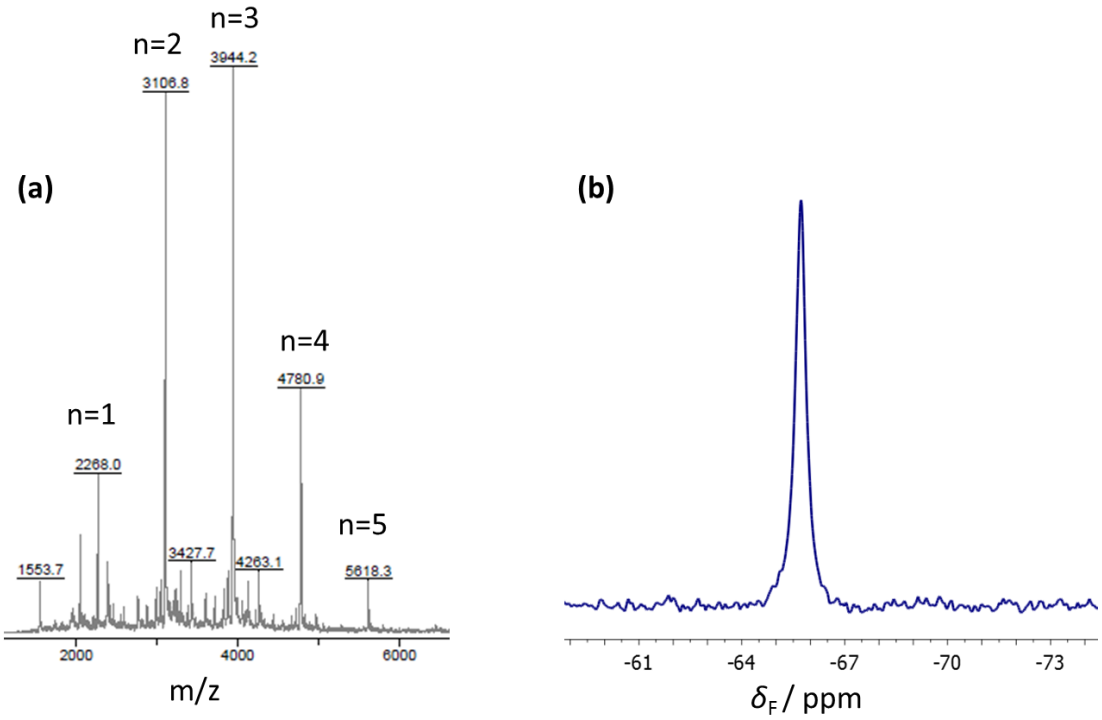

Figure 3.7 *(a) MALDI$^+$ and (b) ^{19}F NMR spectrum (D_2O, 9.4 T, 298 K; δ_F = -65.7 ppm, R_1 = 177 Hz, R_2 = 333 Hz) observed for* ***[(Dy.L^3)$_n$-PAMAM]****. Numbers above MALDI spectrum refer to peaks corresponding to molecular weights of PAMAM + (n x complex).*

3.3.4 Alternative approaches

Due to the difficulties apparent in functionalising all eight sites of the dendrimer with this complex, it was decided to investigate alternative compounds. The first idea was to insert a linker group between the complex and the dendrimer, in order to space the complexes from each other and the compact centre of the dendrimer. The linker chosen was β-alanine, which required a new synthetic pathway to form the complex (*Scheme 3.6*). The ethyl ester protected linker group was incorporated in the first step by stirring the acid, **25**, with 1-hydroxybenzotriazole (HOBt) hydrate and NMM in DMF, followed by addition of β-alanine ethyl ester hydrochloride to form the extended ethyl ester compound, **29**. The rest of the synthesis then followed the general scheme outlined for **[Dy.L^3]** (*Section 2.3.1*)**.** The resulting complex, **[Dy.L^3-βala]**, was reacted with PAMAM as described above, which again resulted in a mixture of species being formed. No evidence for complete conversion at all eight sites was found.

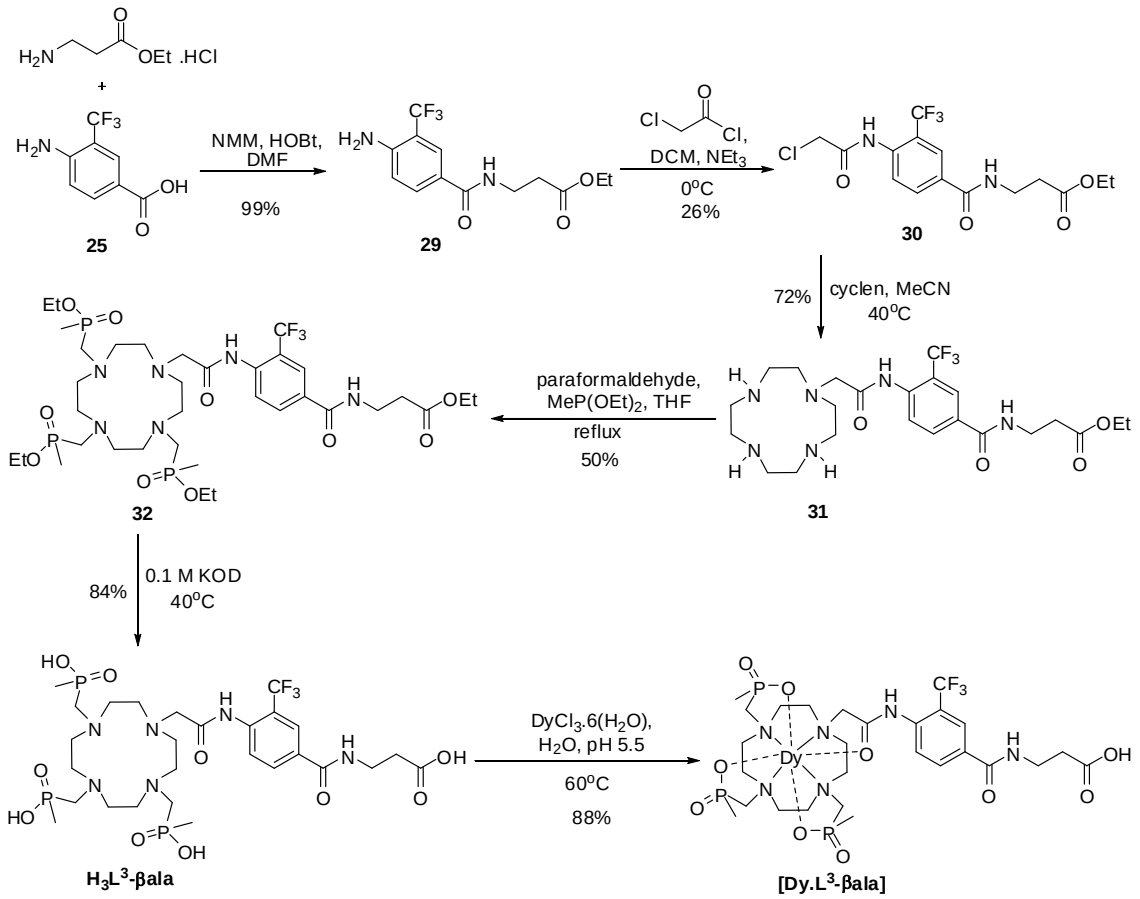

Scheme 3.6 *Synthetic route for the formation of* ***[Dy.L^3-βala]****.*

A second approach was investigated to attempt the conjugation at the ligand stage, rather than with the metal complexes, in an effort to overcome the problem of having a number of polar lanthanide ions in close proximity to each other whilst attempting the coupling reaction. This approach required a new synthetic route, in order to introduce a protecting group at the terminal carboxylate group that could be selectively cleaved (*Scheme 3.7*). The protecting group chosen was *tert*-butyl, as this can be cleaved under relatively mild conditions that will leave the phosphinate ethyl ester and the amide bond intact. The introduction of this group was achieved by stirring **25** in *tert*-butyl acetate with a few drops of perchloric acid, to form **35**, in a procedure adapted from Wright and co-workers.[14] The formation of the protected ligand then followed the usual pathway. The *tert*-butyl group was cleaved by stirring with trifluoroacetic acid in dichloromethane to give the acid, **39**.

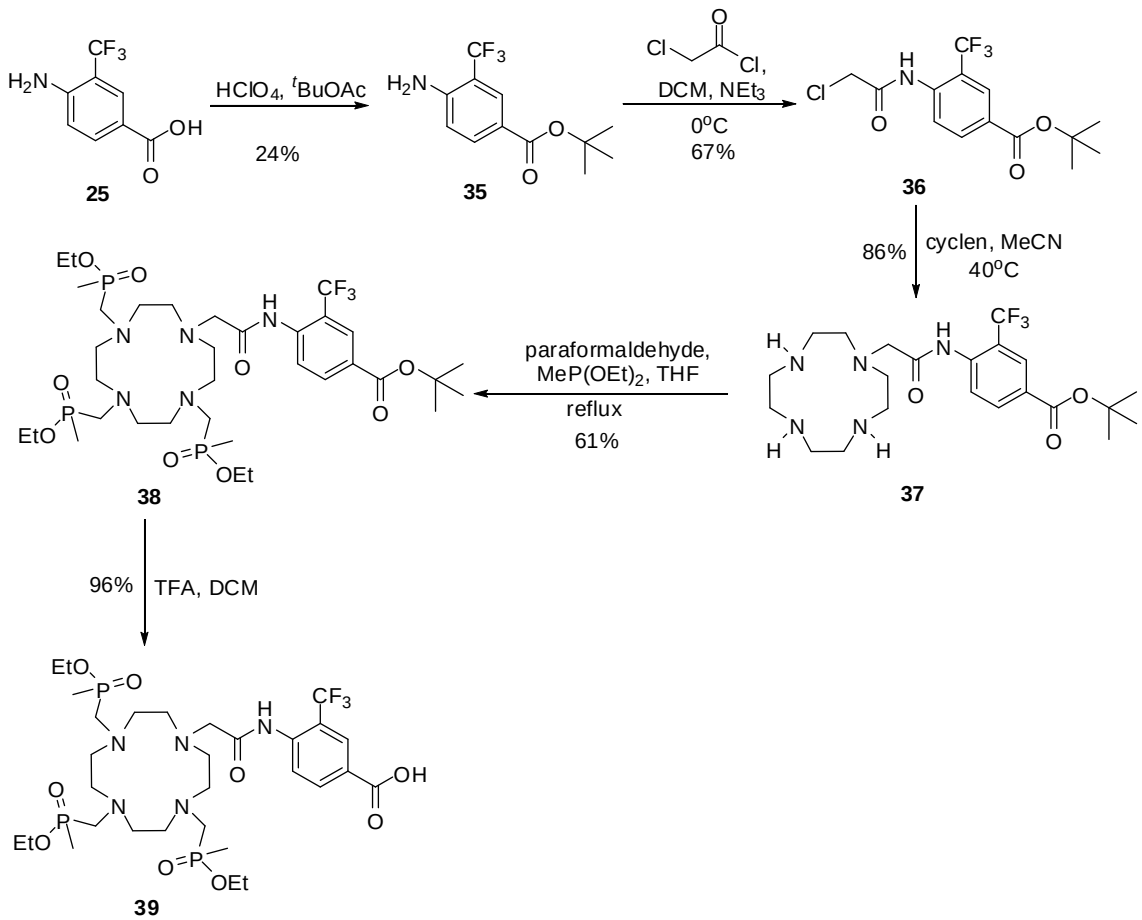

Scheme 3.7 *Synthetic route for the formation of tri-phosphinate ethyl ester protected* ***L³.***

The phosphinate ethyl ester protected analogue of **L^3** was then reacted with PAMAM in the usual manner. Again, no evidence was observed for the desired full completion of the reaction. Unfortunately, as the resulting polydisperse nature of these PAMAM conjugates investigated gave no benefit over the chitosan systems, they were not studied further.

3.4 Conclusions

In order to increase the fluorine density per unit concentration, while promoting one major signal in the ^{19}F NMR spectrum, high molecular weight adducts were investigated as potential platforms for the conjugation of multiple CF_3-containing lanthanide complexes. The first adduct investigated was glycol chitosan, a naturally derived polymer, in a modified form with a reduced molecular weight (6,500 D) and almost complete deacetylation. When a coupling reaction was performed with this chitosan compound and **[Dy.L^3]**, a conjugate between the two was successfully formed, with an average of 5 complexes per molecule of chitosan determined by aqueous GPC.

The ^{19}F NMR spectrum of this system displayed one major resonance (>90 %), with favourable relaxation properties. Phantom imaging experiments were then undertaken, which resulted in good quality, high resolution images being acquired. These systems gave rise to the highest comparative signal-to-noise ratio yet obtained for such fluorine-based probes within our group. These promising results led to the investigation of the conjugate *in vivo*. Unfortunately, the animal expired during the singular experiment that was performed, although the image obtained is still extremely promising as it is the first *in vivo* fluorine image to date from this work. Further studies need to be carried out on these conjugates, to determine whether they are tolerated by the animals and the biodistribution of the probes after administration. Studies are currently on-going to address these issues.

The other high molecular weight adduct that was investigated was a PAMAM conjugate, based on a dendrimer with eight primary amino surface groups. A trial reaction, with a small, fluorine-containing, organic compound successfully resulted in the functionalisation of all eight amine moieties and gave rise to signal in the ^{19}F NMR spectrum. However, when the reaction was repeated with fluorine-containing lanthanide complexes, complete reaction at each surface group could not be achieved. Instead, a mixture of products was obtained, with between one and seven complexes per molecule of PAMAM. Modifications of the complex structure were attempted, but gave no improvement and so this system was not investigated further. Nevertheless, if a system could be formed allowing full functionalisation of every primary amine group, this would have benefits over the chitosan system due to the defined nature of the probe. A possible solution could be to alter the nature of the active ester functional group, e.g. the acid group of the complex that forms an amide linker could be replaced with an arylisothiocyanate.

3.5 References

1. H. Kobayashi, S. Kawamoto, S.-K. Jo, H. L. Bryant, M. W. Brechbiel, and R. A. Star, *Bioconjugate Chem.*, 2003, **14**, 388–394.

2. G. H. Lee, Y. Chang, and T.-J. Kim, *Eur. J. Inorg. Chem.*, 2012, 1924–1933.

3. P. Harvey, I. Kuprov, and D. Parker, *Eur. J. Inorg. Chem.*, 2012, 2015–2022.

4. E. De-Luca, PhD Thesis, Durham University, 2010.

5. K. H. Chalmers, PhD Thesis, Durham University, 2011.

6. K. H. Chalmers, M. Botta, and D. Parker, *Dalton Trans.*, 2011, **40**, 904–913.

7. M. A. Mintzer and M. W. Grinstaff, *Chem. Soc. Rev.*, 2011, **40**, 173–190.

8. S. Langereis, A. Dirksen, T. M. Hackeng, M. H. P. van Genderen, and E. W. Meijer, *New J. Chem.*, 2007, **31**, 1152–1160.

9. R. Xu, Y. Wang, X. Wang, E.-K. Jeong, D. L. Parker, and Z.-R. Lu, *Exp. Biol. Med.*, 2007, **232**, 1081–1089.

10. W. C. Floyd, P. J. Klemm, D. E. Smiles, A. C. Kohlgruber, V. C. Pierre, J. L. Mynar, J. M. J. Fréchet, and K. N. Raymond, *J. Am. Chem. Soc.*, 2011, **133**, 2390–2393.

11. R. K. Tekade, P. V. Kumar, and N. K. Jain, *Chem. Rev.*, 2009, **109**, 49–87.

12. S. H. Medina and M. E. H. El-Sayed, *Chem. Rev.*, 2009, **109**, 3141–3157.

13. P. Govender, B. Therrien, and G. S. Smith, *Eur. J. Inorg. Chem.*, 2012, 2853–2862.

14. S. W. Wright, D. L. Hageman, A. S. Wright, and L. D. McClure, *Tetrahedron Lett.*, 1997, **38**, 7345–7348.

4. Strategies to Enhance Signal Intensity; Reducing Dynamic Motion

4.1 Introduction

It is well known that the ratio of R_2/R_1 is always greater than unity for systems in which paramagnetic relaxation is dominant, resulting in broadened lines and a reduction in signal strength. Chemical exchange processes can contribute further to increases in linewidth, accentuating this problem. Previous work has shown that linewidth broadening caused by dynamic motion effects could be reduced by increasing the overall rigidity of the complex being investigated. This was achieved by the introduction of phosphinate groups in place of the carboxylate pendant arms, resulting in significantly reduced linewidths. In addition, one major species in solution was observed (see *Section 1.6.3*).[1] However, the fluorine containing moieties in these compounds are connected to the macrocyclic ring *via* an amide bond, about which restricted rotation can occur in solution. This rotation is likely to lead to an increase in exchange broadening depending on temperature and local steric demand. Therefore, it was decided to investigate whether the incorporation of further rigidity into the system, in particular to the fluorine containing element, would result in an additional decrease in linewidth. Pyridyl nitrogens have previously been shown to be excellent donors for Ln(III) ions.[2] Therefore, if the CF_3 group is incorporated onto a coordinating pyridyl motif, as shown in *Scheme 4.1*, then this should lock the arm in place more effectively and prevent dynamic motion involving the fluorinated moiety.

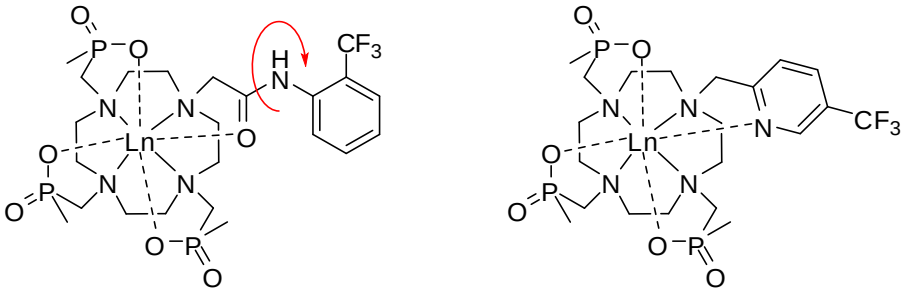

Scheme 4.1 *Comparison of mono-amide (left) and pyridine (right) analogues displaying rotation about amide bond and the locked coordinating pyridyl arm.*

Various systems were chosen to be investigated, as shown in *Scheme 4.2*. The first compounds consisted of the direct pyridyl equivalent of the monoamide phosphinate complex, **[Ln.L^5]**, and a chlorinated analogue, **[Ln.L^6]**. The corresponding carboxylate complex, **[Ln.L^7]** was also developed in order to investigate whether the influence of the pendant arms was comparable to the mono-amide system. A final complex was designed with the fluorine substituent at the *para*-position of the pyridine ring, **[Ln.L^8]$^-$**, varying the Ln to CF_3 distance, *r*. From previous knowledge (*Section 1.3.2.1*), it can be calculated that the ideal value for *r* is in the region of 5.5 to 6.5 Å in order to generate around a two-orders of magnitude increase in both longitudinal and transverse relaxation rates. For these complexes, it was predicted that *r* would lie in the region of 6-6.5 Å for the *meta*-substituted systems and 7-7.5 Å for the *para*-substituted system.

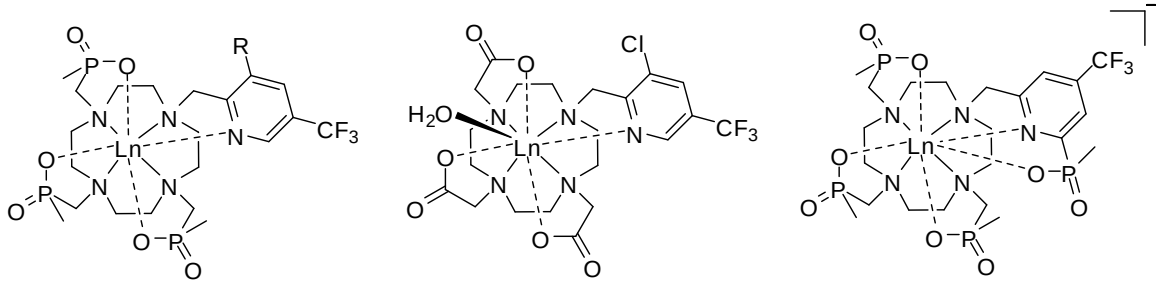

[Ln.L^5], R=H
[Ln.L^6], R=Cl

[Ln.L^7]

[Ln.L^8]$^-$

Scheme 4.2 *Complexes synthesised for the work described in this chapter.*

4.2 Synthetic Details

4.2.1 The *meta*-substituted pyridyl systems; [Ln.L^5], [Ln.L^6], and [Ln.L^7]

The synthesis of **L^5** began with the introduction of a carbon atom at the 2-position of the pyridine ring, utilising 2-bromo-5-trifluoromethyl pyridine as the starting material (*Scheme 4.3*). Numerous methods were attempted for this step, such as substitution of the bromo-group with a cyano moiety. However, the reaction that provided the highest yield involved lithiation using *n*-butyl lithium, followed by carboxylation with solid carbon dioxide, as developed by Schlosser and co-workers.[3] After work up, the desired acid product (**40**) was recrystallised from hexane. Esterification in methanol and sulphuric acid, followed by reduction with sodium borohydride, led to the desired

alcohol, **42**. Bromination of this alcohol was successfully achieved by stirring in phosphorus tribromide (to form **43**), although formation of the mesylate (**44**) by reaction with mesyl chloride was preferred due to the higher yield, faster reaction time, and ease of purity of the latter reaction, averting purification by column chromatography. The mesylate was reacted immediately after being formed to ensure degradation did not occur.

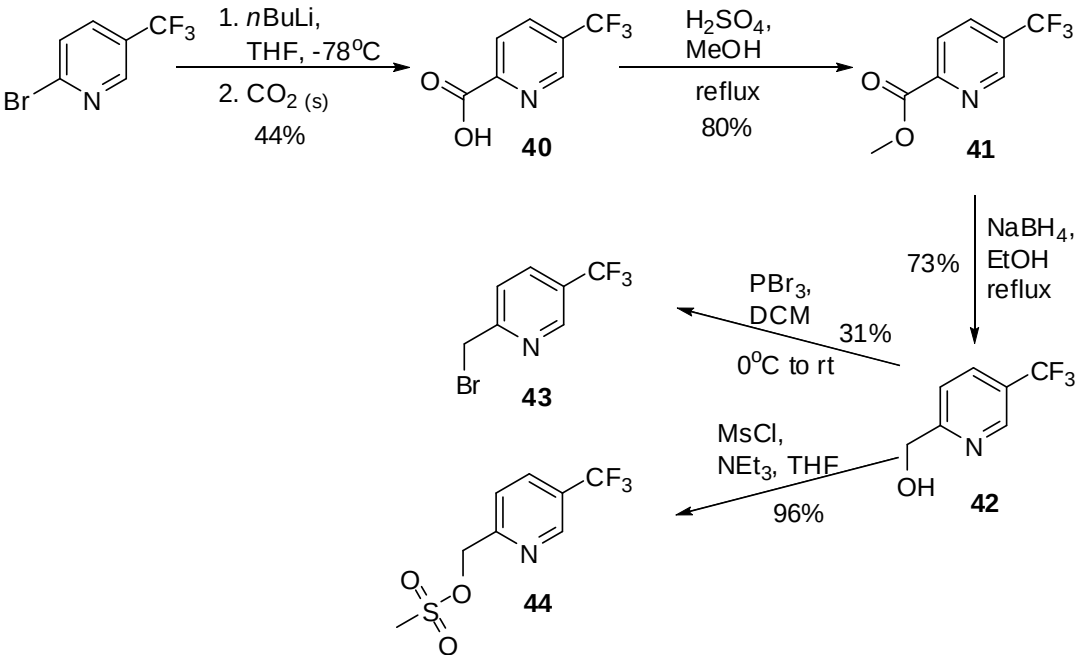

Scheme 4.3 *Synthetic procedure for the preparation of the pyridine arm precursors.*

While this pyridyl arm could be successfully synthesised in a moderate yield, a related commercially available precursor, 2-chloromethyl-3-chloro-5-trifluoromethyl pyridine, was obtained. This chloromethyl group can be directly reacted with the cyclen ring, reducing the number of synthetic steps required. The additional *meta*-chloro-substituent should not have any significant effect on the behaviour of the final complex, although both arms were used in tandem in order to confirm this. This substituent may also have an added advantage in that it could allow further functionalisation at a later stage.

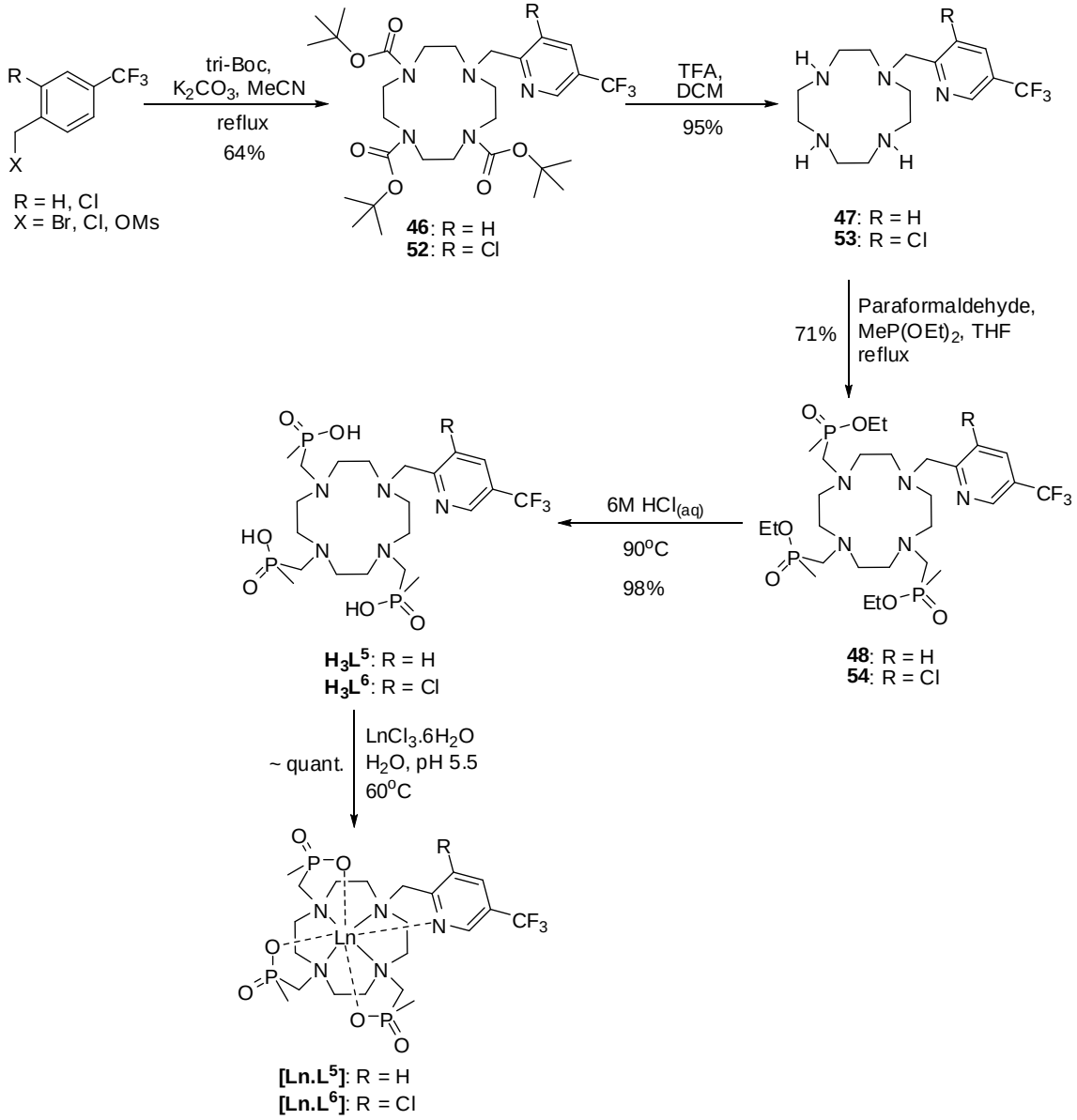

Scheme 4.4 *General procedure for the synthesis of* ***[Ln.L^5]*** *and* ***[Ln.L^6]*** *(yields stated for R=Cl, yields for R=H are comparable).*

The analogous complexes, **[Ln.L^5]** and **[Ln.L^6]**, were synthesised as shown in *Scheme 4.4*. The first step involved mono-addition of the relevant pyridine arm onto the cyclen ring. This was attempted by a direct addition with an excess of cyclen, as was successfully achieved in the synthesis detailed in an earlier chapter (*Section 2.3.1*). However, in this case the pyridine compounds were too reactive and could not be controlled, resulting in a mixture of mono-, di-, and tri-substituted products that were difficult to separate by column chromatography. Therefore, it was decided to use the

triprotected carbamate 1,4,7-tris-*tert*-butoxycarbonyl-1,4,7,10-tetraazacyclododecane (tri-Boc), which was synthesised according to published methods.[4,5] Mono-addition of the pyridine arm was achieved by refluxing in acetonitrile with an excess of base (potassium carbonate), followed by purification with silica gel column chromatography to generate the desired intermediates, **46** and **52**. The protecting groups were removed by stirring with trifluoroacetic acid in dichloromethane to form the mono-substituted cyclen derivatives, **47** and **53**.

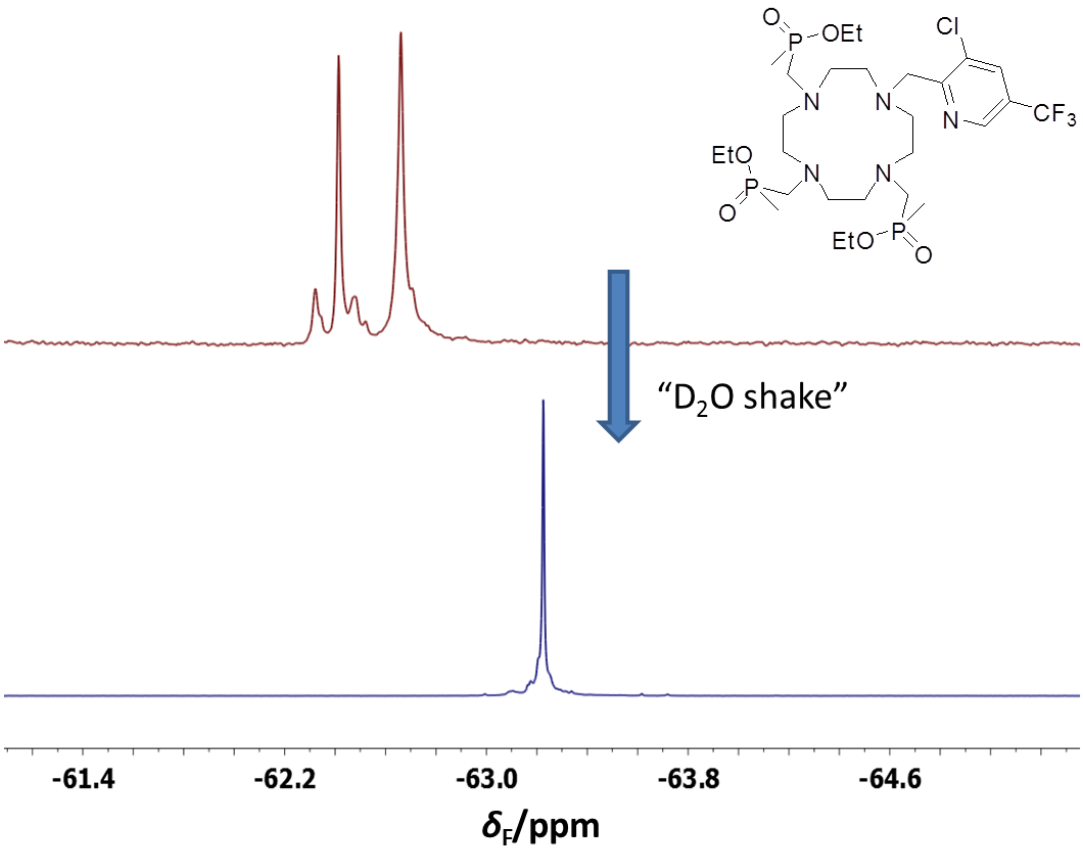

Figure 4.1 *^{19}F NMR spectra of **54**, highlighting the reduction of signals upon shaking the sample with a few drops of deuterium oxide (9.4 T, 295 K).*

Soxhlet equipment was then used to synthesise **48** and **54** in a one-pot synthesis *via* a co-condensation of the mono-alkylated macrocycle with paraformaldehyde and diethyl methylphosphonite. An Arbusov rearrangement yielded the desired triethylphosphinate esters, **48** and **54**, which were formed as a mixture of stereoisomers differing in configuration at each phosphorus centre. Separation was

achieved using a 3:1 mixture of alumina and silica. The resulting NMR spectra of these compounds in deuterated chloroform were complicated due to the formation of the $[H_2L]^{2+}$ complex and similar adducts, in well-defined conformations. The spectra were simplified significantly by agitating with a few drops of deuterium oxide (see *Figure 4.1*). Under these conditions, the ring is diprotonated and one major solution species was formed.

Base or acid hydrolysis of the ester groups is feasible, due to the stability of the pyridine moiety to both conditions. However, acid hydrolysis allowed a simpler work up (i.e. excess acid can be removed under reduced pressure) and generally required shorter reaction times. Therefore, the compounds were heated under reflux in 6 M hydrochloric acid to form the protonated phosphinic acid ligands. Metal complexation was achieved using an aqueous solution of the appropriate metal chloride at pH 5.5 and 60°C, before the pH was raised to 10 in order to precipitate any excess Ln(III) ions as the metal hydroxide. The free metal was removed by centrifugation before the pH was lowered to 5.5 once more and the complexes were purified by preparative scale HPLC.

An analogous carboxylate complex was also synthesised, **[Ln.L^7]** (*Scheme 4.5*). It was decided to only investigate the chloro-substituent in this case due to the availability of the starting material. The first step involved alkylation of 1,4,7-tris-(*tert*-butoxycarbonylmethyl)-1,4,7,10-tetraazacyclododecane (DO3A), which was synthesised according to literature methods,[6] with 2-chloromethyl-3-chloro-5-trifluoromethyl pyridine in a similar method to the reaction with the tricarbamate (tri-Boc). After purification by silica gel column chromatography the desired compound, **66**, was isolated. Deprotection of the *tert*-butyl ester groups was carried out using 6 M HCl to generate the tri-acid, followed by complexation with the lanthanide ion.

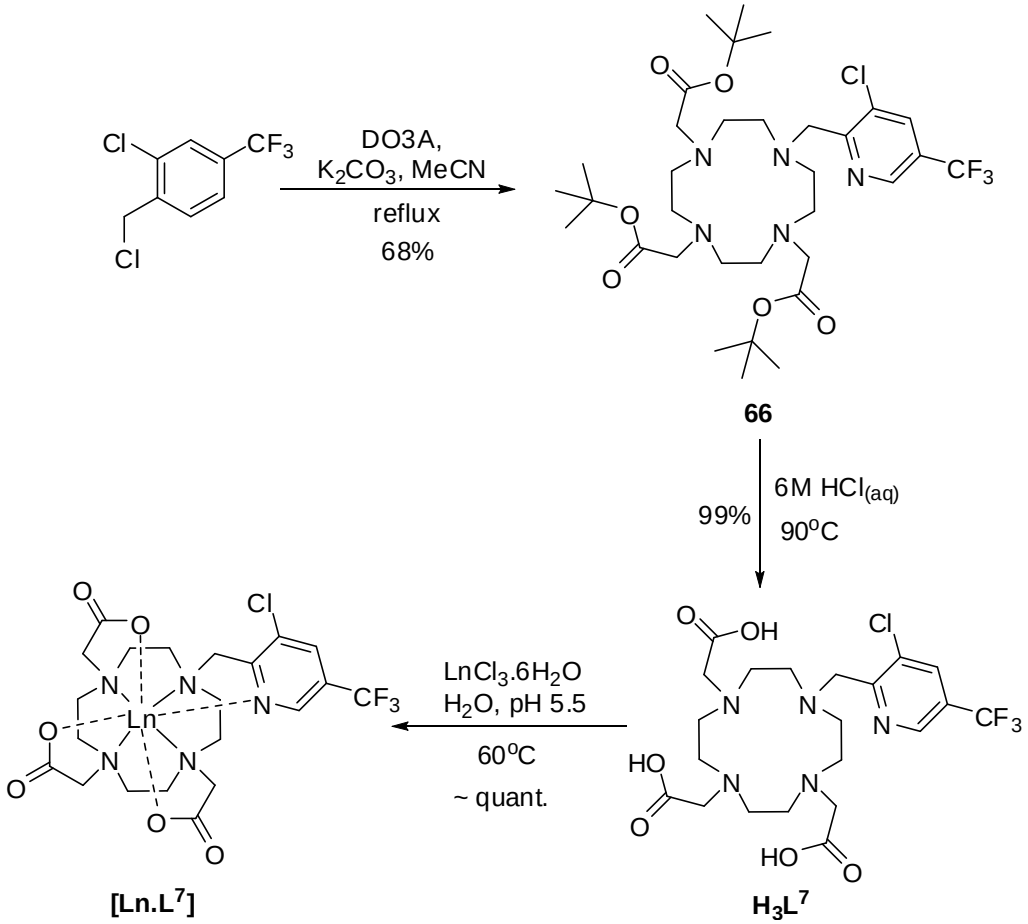

Scheme 4.5 *General procedure for the synthesis of* ***[Ln.L^7]****.*

4.2.2 The *para*-substituted pyridyl system; [Ln.L^8]$^-$

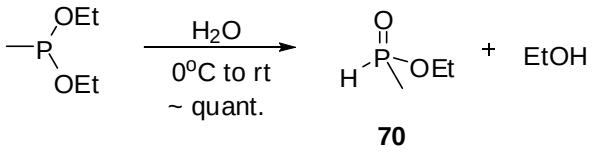

Scheme 4.6 *Synthesis of a 50/50 mixture of ethyl methylphosphinate and ethanol.*

The synthesis of **[Ln.L^8]$^-$** required the introduction of a new pyridine arm (*Scheme 4.7*). The first step consisted of halogenation of 6-methyl-4-trifluoromethyl-2(1H)-pyridone with a large excess of phosphorus oxychloride. Unreacted $POCl_3$ was carefully removed under reduced pressure, before work-up gave the desired chlorinated pyridine, **71**. Direct substitution of this chloro-group with diethyl methylphosphinite was attempted. However, no reaction was observed. Therefore, the phosphinite was

first stirred with one equivalent of deoxygenated water at room temperature to form a mixture of ethyl methylphosphinate (**70**) with one equivalent of ethanol (*Scheme 4.6*), which was confirmed by ^{1}H and ^{31}P NMR spectroscopy. This mixture was used directly in a palladium coupling reaction with **71**. Dry toluene was degassed three times *via* freeze-thaw cycles and was used to dissolve a mixture of the pyridine (**71**), the phosphinate, (**70**), and triethylamine. Tetrakis(triphenylphosphine)palladium(0) was added to the mixture and the solution degassed a further three times to ensure the removal of oxygen and prevent oxidation of the palladium catalyst. After being heated at 100°C overnight, the starting materials had been consumed and the pyridinyl phosphinate product (**72**) was obtained following silica gel column chromatography.

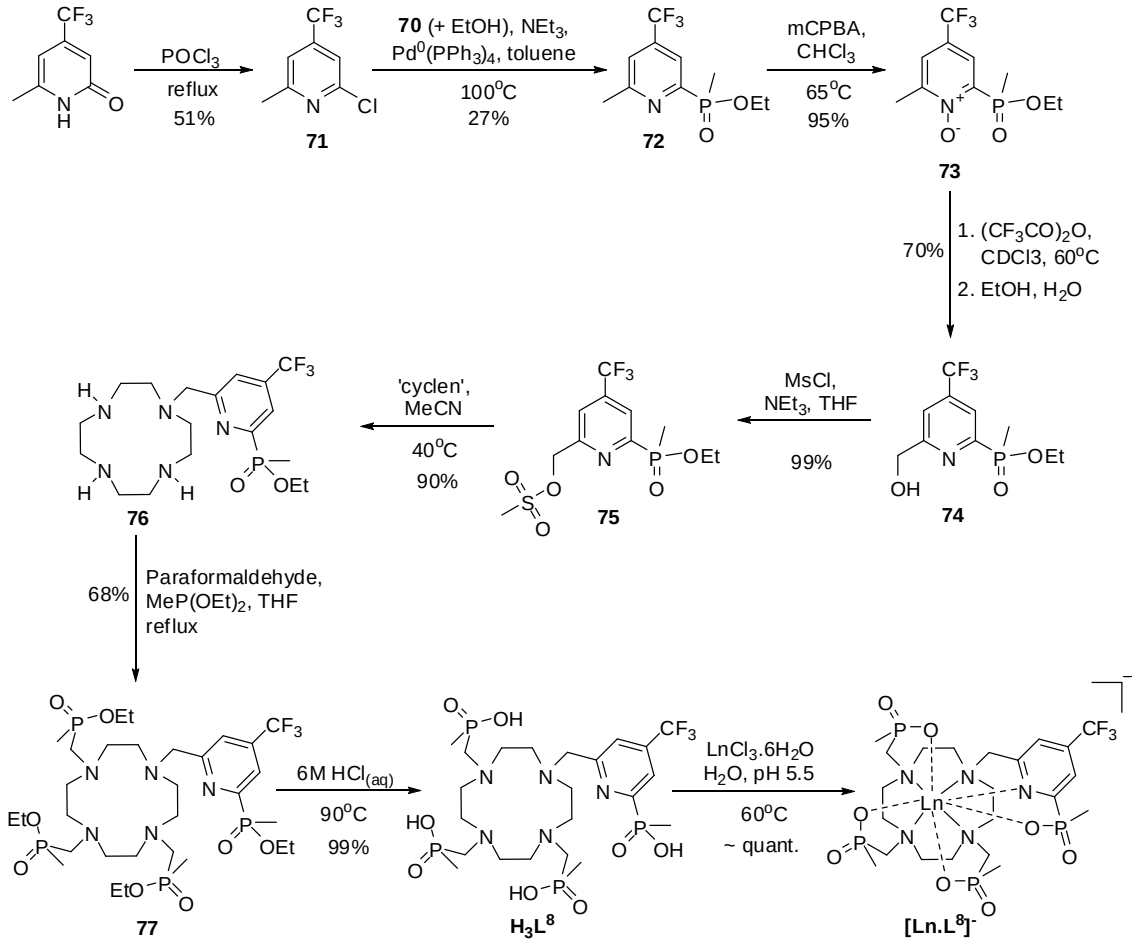

Scheme 4.7 *General procedure for the synthesis of* ***[Ln.L^{8}]$^{-}$***.

The 6-methyl group can be directly brominated, using *N*-bromosuccinimide as described elsewhere for related systems.[7] However, this is a rather capricious reaction

and so it was decided to proceed *via* the longer but cleaner pathway to form the mesylate. This sequence involved formation of the pyridyl N-oxide (**73**) using *meta*-chloroperoxybenzoic acid, followed by a thermal rearrangement to a trifluoroactetate ester intermediate, which can be hydrolysed *in situ* by a mixture of water and ethanol to generate the alcohol, **74**. The alcohol was purified by silica gel column chromatography before reaction with mesyl chloride and triethylamine gave the reactive mesylate compound (**75**). Again, this compound was used immediately after being formed. It is interesting to note that a "D_2O shake" experiment was also successful in significantly simplifying the ^{1}H and ^{19}F NMR spectra. This time it was evident for the alcohol compound, **74**, allowing the detailed multiplets to be observed. This is likely due to intermolecular associations *via* hydrogen bonding to form dimers or higher order aggregates. Shaking with a few drops of D_2O inhibits these processes, giving rise to the expected simple splitting pattern (*Figure 4.2*).

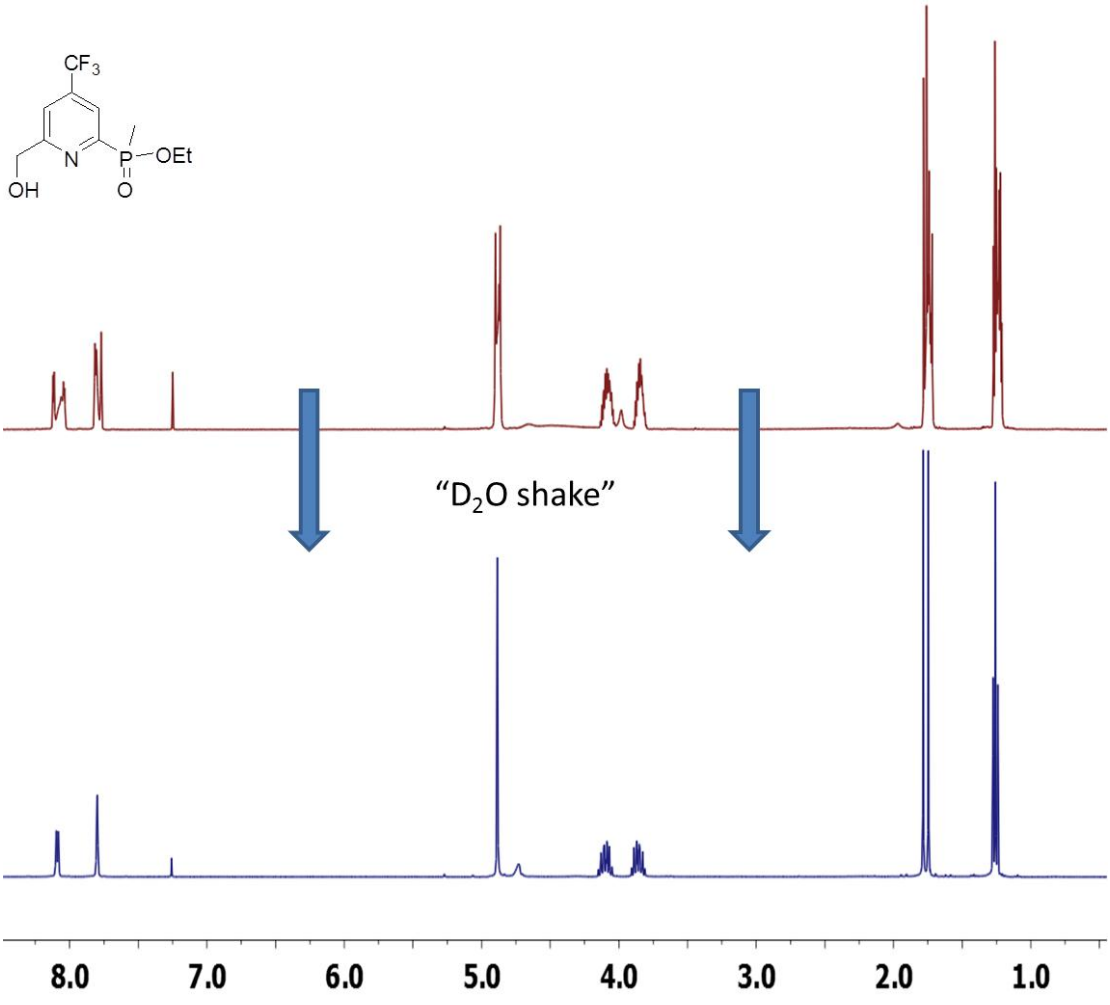

Figure 4.2 *^{1}H NMR spectra (400 MHz, 295 K, $CDCl_3$) of **74** indicating simplification of signals after a "D_2O shake".*

Unlike with the previous pyridyl compounds described, mono-addition using an excess of cyclen was successfully achieved in high yield under mild conditions. There was no evidence for the formation of unwanted over-alkylated side-products, possibly due to the slightly greater steric demand of this electrophile, associated with the phosphinate group. The rest of the synthesis followed the same pathway as described for **[Ln.L^5]** and **[Ln.L^6]**: formation of the tri-ethyl phosphinate ester (**77**), followed by deprotection to the tetra-acid species (**H$_3$L^8**) by heating in 6 M HCl, and finally formation of the desired complex, **[Ln.L^8]**$^-$.

4.3 Characterisation of Complexes

As detailed in *Chapter* 2, low resolution electrospray ionisation and high resolution accurate mass spectrometry measurements were carried out to confirm the presence of the complexes. Characteristic isotope patterns were observed for each complex, showing an excellent correlation with the calculated spectra. ^{19}F NMR spectroscopic data were collected for each complex, which was analysed and discussed in detail below. In most cases, there were two main observable signals in solution, even after purification by HLPC, indicating the formation of two major stereoisomers in solution.

The metal hydration state of the complex (*q* value) was assessed for the terbium complex of **L^6** by measuring the radiative lifetime of the lanthanide excited state, *k*, in H_2O and D_2O. The *q* value was calculated using *Equation 4.1*:[8]

$$q_{Tb} = 5(k_{H_2O} - k_{D_2O} - 0.06 - 0.01n) \qquad (4.1)$$

where k_{H_2O} and k_{D_2O} are the reciprocals of the luminescence lifetimes of the complex in each solvent, τ_{H_2O} and τ_{D_2O} respectively, and n is the number of carbonyl-bound amide NH oscillators. Values of 0.30 and 0.26 ms^{-1} were recorded experimentally for k_{H_2O} and k_{D_2O} respectively, resulting in a calculated q value of 0.1. This indicates that there are no bound water molecules on the Ln(III) ion for complexes of **L^6**, consistent with related phosphinate complexes.[1] It is highly likely that the other phosphinate

complexes, **[Ln.L^5]** and **[Ln.L^8]** will also possess a zero *q* value, while the less bulky carboxylate complex is expected to have one directly bound water molecule.

4.4 ^{19}F NMR Spectroscopic Studies

4.4.1 NMR Shift Behaviour

For each ligand, it was decided to investigate the ^{19}F NMR properties with two different lanthanide ions; one with a large positive Bleaney coefficient (C_J) and one with a large negative value. For **[Ln.L^5]**, **[Ln.L^6]**, and **[Ln.L^7]**, thulium (C_J = +53) and dysprosium (C_J = -100) were chosen, and for **[Ln.L^8]$^-$** erbium (C_J = +32) was used instead of thulium. The ^{19}F NMR spectroscopic data for these complexes are reported in *Table 4.1*, along with chemical shifts for the free ligands in each case, for comparison. In every case, no pH- or time-dependent variations were observed.

Table 4.1 *^{19}F NMR chemical shift data (ppm) for Ln(III) complexes (D_2O, 295 K).*

Complex	Ligand[(a)]	Dy	Tm	Er
[Ln.L^5][(b)]	-63.3	-154.7	10.7	---
		(-160.8)	(13.1)	---
[Ln.L^6][(b)]	-63.0	-162.4	17.1	---
		(-168.9)	(20.3)	---
[Ln.L^7][(b)]	-63.1	-115.1	-42.0	---
		(-42.0)	(-5.0)	---
[Ln.L^8]$^-$ [(c)]	-65.3	-67.0	---	-61.3
		---	---	---

(a) Chemical shift of the free ligands without the presence of Ln(III) ions. (b) Values in parenthesis refer to the minor isomer, with ratios of major to minor isomers around 4:1 for the three complexes. (c) Present as one major signal with a shoulder suggesting two isomers with shifts in close proximity.

The ^{19}F NMR spectra for complexes of the *meta*-substituted ligands (**L^5**, **L^6**, and **L^7**) displayed two signals, in a 4:1 ratio for each complex. With **[Dy.L^8]$^-$** and **[Er.L^8]$^-$**, however, the situation was less clear and they appeared to consist of one main species

in solution, although there is evidence of a shoulder to the main peak. It may well be the case that there are two isomers for the complexes of **L**[8] also, but due to the relatively small shift from the ligand signal, the two signals may overlap. Higher fields (up to 16.4 T) were utilised in an attempt to separate out the peaks. However, they could still not be resolved.

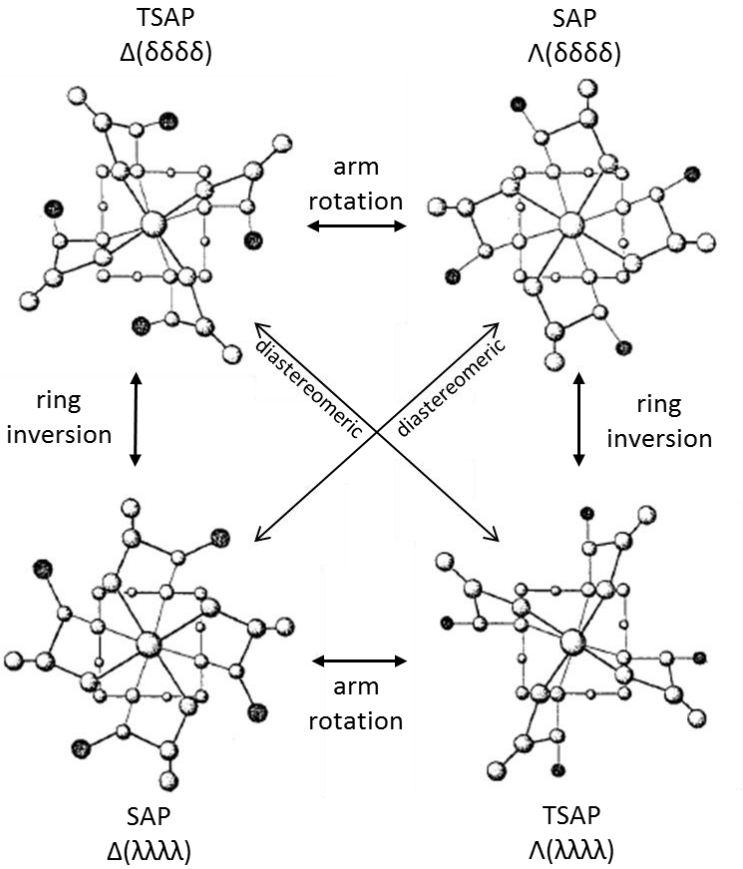

Figure 4.3 *Schematic representation of the common coordination geometries adopted by [LnDOTA]⁻ and related compounds.*[9]

Isomeric species with Ln(III) complexes of cyclen-based systems with carboxylate arms can be related to the presence of differing elements of chirality associated with the NCCN and NCCO metal-chelate rings. Each NCCN chelate ring is characterised by a torsion angle of +60° or -60°, assigned as a δ or λ configuration. Common configurations are favoured, i.e. δδδδ or λλλλ, with other possibilities being higher in energy and have often not been observed crystallographically. The behaviour of the NCCO chelate rings can be considered similarly, with a common torsion angle of +30°

or -30^{o} typically observed for each chelate, which gives rise to a common 'twist' of the four pendant arms.[9] This is illustrated in *Figure 4.3*.

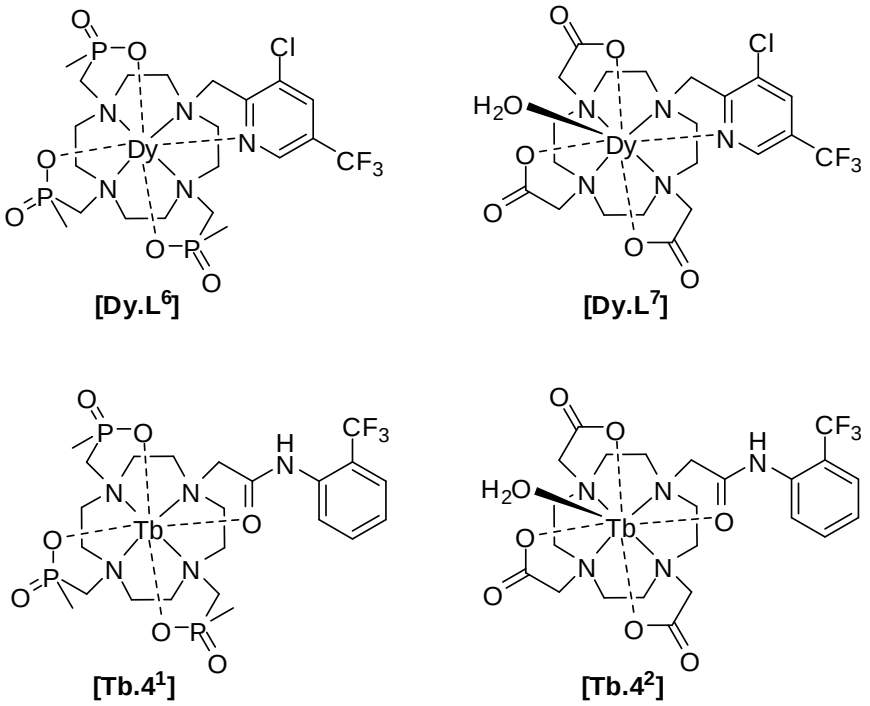

Table 4.2 *NMR data for* ***[Dy.L^6], [Dy.L^7], [Tb.4^1],*** *and* ***[Tb.4^2]*** *indicating the isomeric species observed by ^{19}F NMR spectroscopy (D_2O, 295 K).*

Complex	Major species (%)[(a)]	No. of species present in solution[(b)]
[Dy.L^6]	80	2
[Dy.L^7]	81	2
[Tb.4^1][(c)]	87	6
[Tb.4^2][(c)]	50	7

(a) Amount of major signal as percentage of total signal intensity. (b) Total number of observable species. (c) Taken from the literature.[1]

For phosphinate complexes, this is complicated further by the possibility of differing configurations at each phosphorus centre. However, it has been previously shown that Ln(III) complexes of cyclen with 3 phosphinate arms give rise to favourable low-energy systems in which the configuration is constant at each phosphorus chiral centre, i.e. *RRR* or *SSS* configurations.[10,11] For the previously investigated mono-amide

systems, **[Ln.4^1]** and **[Ln.4^2]**, further isomers had been observed.[1] These related to restricted rotation about the amide bond, which can be considered in terms of placing the CF_3 group '*cis*' or '*trans*' with respect to the coordinated amide oxygen. For the pyridyl systems reported here, these extra 'rotational isomers' are no longer possible due to the pyridine nitrogen binding to the Ln(III) ion, thereby 'locking' the CF_3 into one position, reducing the number of thermodynamically stable configurations available for the complex. This rigidification effect results in the simplified NMR spectra observed, with only two species being observed for both the phosphinate and carboxylate pyridine complexes (**[Ln.L^6]** and **[Ln.L^7]**) compared to 6 and 7 for the mono-amide analogues, **[Ln.4^1]** and **[Ln.4^2]** (*Table 4.2*).

Unfortunately, the major isomer constitutes around 80 % of the observed signal intensity for the pyridyl complexes, which is not quite as high as for **[Ln.4^1]** (87 %), albeit significantly better than for **[Ln.4^2]** (50 %). However, the ratio of isomers is considerably better than related unsubstituted pyridyl-containing cyclen complexes in which two diastereoisomeric species in ratio 2:1 were observed, corresponding to the regular square-antiprismatic (SAP) and twisted square-antiprismatic (TSAP) complexes for the major and minor isomers respectively.[2] It is likely that a similar situation occurs for the compounds reported here, i.e. a SAP coordination is adopted for the major species and a TSAP geometry for the minor species. It is interesting that the ^{19}F NMR spectrum of the carboxylate pyridyl complex, **[Ln.L^7]**, displays the same form as the analogous phosphinate complex (**[Ln.L^6]**), i.e. two species are observed in a 4:1 ratio. This indicates that the pyridyl moiety is effective at increasing the rigidity of the complex and can 'lock' the system into place with either the bulky phosphinate arms or the less sterically hindered carboxylate. In the carboxylate series of complexes, dynamic exchange processes between isomers with different configurations have been observed.

The ^{19}F NMR spectra for the dysprosium complexes of the discussed ligands are shown in *Figure 4.4*. As expected, the shifts for **[Ln.L^8]$^-$** were the smallest, with less than a 5 ppm difference between the complexes and the free ligand. This is due to the

reciprocal cubic dependence of the pseudocontact shift on the lanthanide-to-fluorine distance. In addition, a change in angle (Θ) is likely between the fluorine atoms and the principal axis of the complex (see *Section 1.3.1* for further details).[12,13] It is estimated that the CF_3 label is at least 0.5 Å further away from the Ln(III) centre in **[Ln.L^8]$^-$** than for the other complexes investigated, and so should experience a significantly smaller pseudocontact shift. Correlation of the shifts to the Ln-F distance are not directly quantifiable, however, as the substantial differences in the coordination spheres of these molecules will lead to deviations in the ligand field parameters and, as mentioned already, Θ is likely to be inconsistent between the two sets of compound. Further information, and determination of distances, can be gained from an analysis of the field dependence of relaxation (see *Section 4.4.2*).

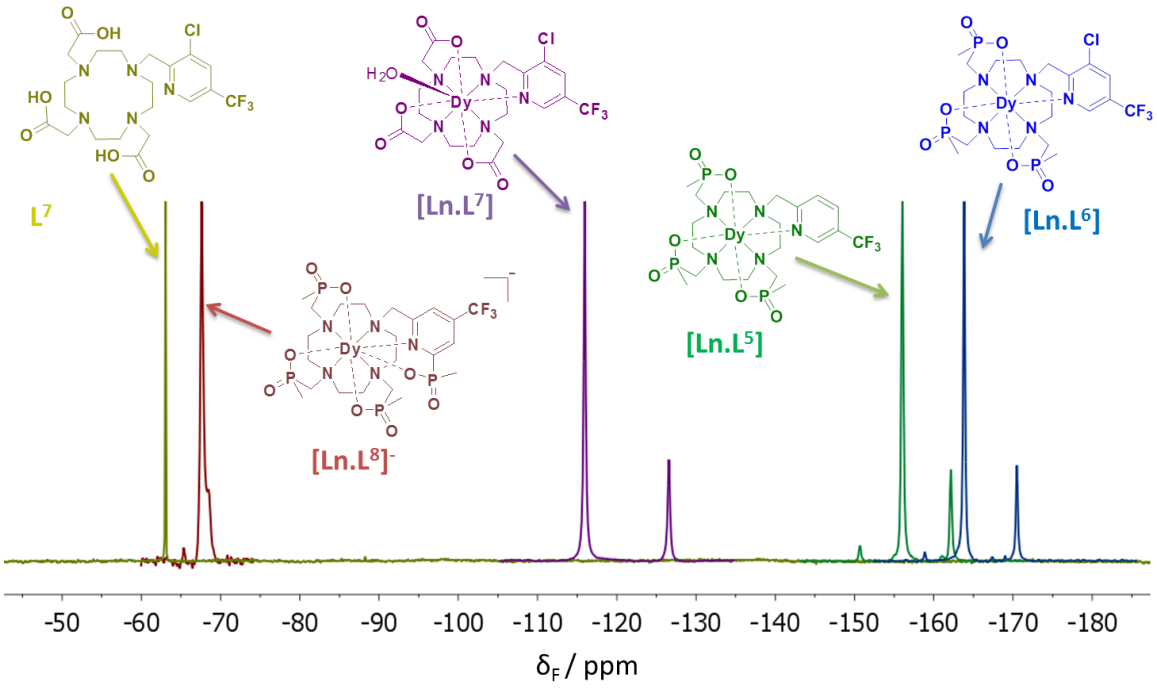

Figure 4.4 *^{19}F NMR spectra (376 MHz, D_2O, 295 K) of the Dy(III) complexes of L^5, L^6, L^7, and L^8 with the signal relating to the ligand L^7 for comparison.*

For the *meta*-substituted pyridyl systems, the dipolar shifts for the phosphinate complexes were considerably larger than for the analogous carboxylate compound. Comparisons with the related mono-amide compounds[1] suggest that the carboxylate complex possesses one bound water (q=1), while the phosphinate complexes possess

no bound water molecules (q=0). This change in hydration state results in significant variations in the coordination geometry about the Ln(III) ion, with the carboxylates being 9-coordinate overall, while the phosphinates adopt a more compact 8-coordinate geometry. This change will be associated with a variation in the ligand field coefficients, e.g. B_0^2 and B_2^2, giving a significant change in the observed shifts for the two sets of complex.

While the coordination mode about the lanthanide ion in **[Ln.L^5]** and **[Ln.L^6]** should be similar, the presence of the chloride substituent on the pyridyl ring of the latter complex may slightly alter the position the CF_3 group adopts, changing the angle between the fluorine atoms and the principal axis of the complex. This should have a marked effect on the pseudocontact shift of the system and may explain why, for example, **[Dy.L^6]** has around a 10 ppm larger shift than **[Dy.L^5]** with respect to the signal of the free ligands, which are nearly identical to each other.

The shift observed with **[Dy.L^6]** is almost 100 ppm to lower frequency of the ligand signal. To the best of our knowledge, this is the largest reported lanthanide induced fluorine shift for such compounds. This was an unexpected result, being much larger than the previous highest shift (<40 ppm) observed for related systems examined in Durham.[14] Therefore, it was decided to investigate the chemical shift and other NMR spectroscopic properties of this complex further, the results of which are discussed in *Section 4.5*.

4.4.2 ^{19}F NMR Relaxation Behaviour

The ^{19}F NMR relaxation data were obtained for each complex at 4.7, 9.4, 11.7, 14.1, and 16.5 T (188, 376, 470, 564, and 658 MHz respectively); data are summarised in *Table 4.3*.

Table 4.3 *^{19}F NMR longitudinal relaxation rate (R_1) data for **[Ln.L^5]**, **[Ln.L^6]**, **[Ln.L^7]**, and **[Ln.L^8]$^-$** at different field strengths (D_2O, 295 K). Values given in Hz.*

Complex	4.7 T	9.4 T	11.7 T	14.1 T	16.5 T
[Dy.L^5]$^{(a)}$	56 ±2.5	110 ±1.2	137 ±2.4	165 ±0.3	190 ±0.7
	(41 ±0.3)	(116 ±2.8)	(139 ±3.6)	(166 ±1.2)	(187 ±1.5)
[Tm.L^5]$^{(a)}$	54 ±2.2	99 ±3.6	128 ±0.4	147 ±0.5	165 ±0.6
	(64 ±1.6)	(107 ±3.3)	(132 ±1.2)	(166 ±1.2)	(187 ±1.5)
[Dy.L^6]$^{(a)}$	64 ±1.7	114 ±0.5	142 ±1.1	166 ±0.4	192 ±0.5
	(67 ±0.6)	(114 ±8.4)	(146 ±5.5)	(165 ±1.1)	(186 ±2.6)
[Tm.L^6]$^{(a)}$	59 ±0.5	107 ±0.4	132 ±1.6	152 ±0.6	173 ±1.2
	(67 ±0.6)	(111 ±4.4)	(140 ±0.3)	(153 ±2.7)	(168 ±6.5)
[Dy.L^7]$^{(a)}$	70 ±0.7	132 ±0.8	158 ±2.4	197 ±0.9	233 ±1.7
	(68 ±1.6)	(119 ±3.3)	(139 ±3.6)	(172 ±2.4)	(219 ±5.1)
[Tm.L^7]$^{(a)}$	27 ±0.4	54 ±2.2	71 ±1.2	90 ±2.1	113 ±3.1
	(32 ±2.5)	(80 ±8.3)	(117 ±11.8)	(210 ±17.3)	(316 ±14.6)
[Dy.L^8]$^{-}$ $^{(b)}$	34 ±0.2	66 ±0.7	87 ±1.8	100 ±0.9	112 ±2.2
[Er.L^8]$^{-}$ $^{(b)}$	20 ±0.6	49 ±0.3	58 ±1.0	69 ±0.6	78 ±0.5

(a) Values in parenthesis refer to minor isomer, with ratios of major to minor isomers around 4:1 for the three complexes. (b) Present as one major signal with shoulder suggesting two isomers with shifts in close proximity.

Comparison of the R_1 data between the complexes of the *meta*-substituted ligands (**L^5**, **L^6**, and **L^7**) and the *para*-substituted system (**L^8**) highlights the substantially slower longitudinal rates measured for the latter compound. This can be ascribed to a lengthening of the mean distance, *r*, between the Ln(III) ion and the CF_3 group. The relationship between the longitudinal relaxation rate and the separation, *r*, follows an

r^{-6} dependence, resulting in significant variation in R_1 with relatively small changes in distance. The separation (r), in addition to the rotational correlation time (τ_R) and the electronic relaxation time (T_{1e}) can be calculated, assuming values for paramagnetic susceptibility (μ_{eff}), by fitting sets of relaxation rate data at different magnetic field strengths to the classical equations describing relaxation, seeking a global minimum computationally (*Figure 4.5* and *Table 4.4*).[15]

$$R_1 = \frac{2}{15}\left(\frac{\mu_0}{4\pi}\right)^2 \frac{\gamma_F^2 \mu_{eff}^2}{r^6}\left(\frac{7\tau_{R+e}}{1+\omega_e^2\tau_{R+e}^2} + \frac{3\tau_{r+e}}{1+\omega_F^2\tau_{R+e}^2}\right) + \frac{2}{5}\left(\frac{\mu_0}{4\pi}\right)^2 \frac{\omega_F^2 \mu_{eff}^4}{(3kT)^2 r^6}\left(\frac{3\tau_R}{1+\omega_F^2\tau_R^2}\right)$$

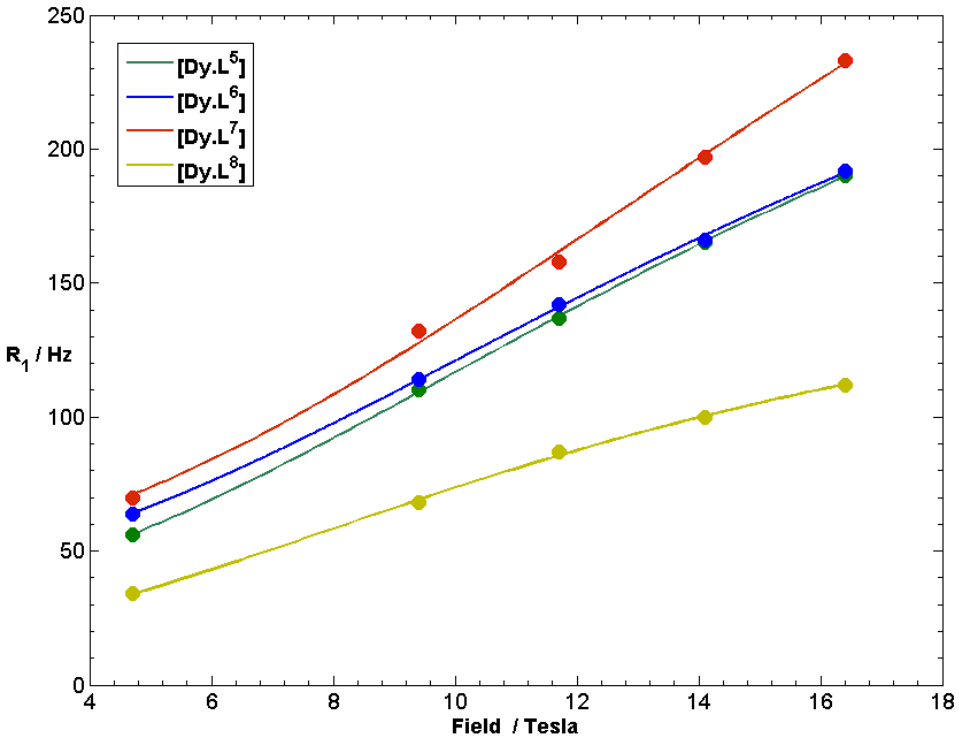

Figure 4.5 *Variation of ^{19}F NMR longitudinal relaxation rates with magnetic field for* ***[Dy.L^5]***, ***[Dy.L^6]***, ***[Dy.L^7]***, *and* ***[Dy.L^8]*** *(295 K, D_2O) showing the experimentally obtained values (circles) and fit (line) to the data, using global minimisation methods.*

From this, it can be seen that, for the dysprosium complexes, the Ln(III) to CF_3 distance for **[Dy.L^8]**$^-$ is over 0.5 Å larger than in the related *meta*-substituted pyridyl phosphinate complexes (**[Dy.L^5]** and **[Dy.L^6]**), as expected. This also fits well with the data gathered from analysis of the shift behaviour of these compounds, where the

lanthanide induced shift values (r^{-3} dependence) for the complexes of $\mathbf{L^8}$ were much smaller than for the other compounds.

Table 4.4 *Ln-CF_3 distance (r), rotational correlation time (τ_R), and electronic relaxation time (T_{1e}) for dysprosium complexes of L^5, L^6, L^7 and L^8.*

Complex	r / Å [(a)]	τ_R / ps [(a)]	T_{1e} / ps [(a)]
[Dy.L^5][(b)]	6.59	235	0.35
[Dy.L^6][(b)]	6.60	238	0.46
[Dy.L^7][(b)]	6.36	190	0.42
[Dy.L^8]$^-$	7.16	293	0.28

(a) Calculated by Levenberg-Marquadt minimisation of the non-linear squares error function of *Equation 1.7* (see *Section 1.3.2*). (b) Data given is for major isomer (minor isomer is comparable in each case).

It can also be observed that the R_1 value for the dysprosium carboxylate complex, **[Dy.L^7]**, is substantially larger than for the analogous phosphinate systems. At first glance, this appears to be due to the CF_3 group being positioned closer to the Ln(III) ion, which correlates with the r value calculated from the fitting calculations. However, this behaviour is reversed for the thulium(III) complexes (i.e. R_1 for **[Tm.L^7]** < **[Tm.L^5]**, **[Tm.L^6]**) suggesting that the system may be more complicated than this. There may be a structural change between the series of phosphinate and carboxylate complexes, which is backed up by the large differences in chemical shift between the two sets of compound. There may even be some form of structural change between the different complexes of $\mathbf{L^7}$, due to the smaller nature of the Tm(III) ion compared to Dy(III). This would explain the differences in relaxation behaviour observed here, as well as the relatively small shift displayed by **[Tm.L^7]** in comparison to the other systems. Global fitting for **[Ln.L^7]** with a series of Ln(III) ions would likely yield more accurate values of r than the singular value generated for the Dy(III) complex.

The values calculated for the rotational correlation time can be justified by comparing the increase in size from the carboxylate system to the phosphinate complex, which is roughly the equivalent of three extra methyl groups. At 298 K, τ_R scales as r^3, in a

simple Stokes-Einstein model, where *r* in this case is the radius of the 'sphere' occupied by the entire molecule. The molecular diameter of the phosphinate complexes is increased by the extra bulkiness of these arms, it is reasonable to expect an increase in τ_R of around 40-50 ps. This could also partially explain the increase in relaxation rates observed for **[Dy.L^7]** in comparison to the phosphinate complexes.

The electron relaxation time, T_{1e}, is related to the paramagnetic relaxation enhancement of the Ln(III) ion and is determined by the nature of the metal ion and by the local ligand field. The values calculated above are roughly of the same order, and are in good agreement with literature values.[16,17]

The transverse relaxation rates, R_2, can be estimated from the individual peak linewidths (at half-height), using a π x $\omega_{1/2}$ relationship in a Lorentzian fit (*Table 4.5*). For a given field, there is a reduction in R_2 for **[Dy.L^5]** and **[Dy.L^6]** in comparison with the mono-amide equivalents, **[Dy.4^1]** and **[Dy.4^2]**. However, this is offset by an accompanying decrease in longitudinal relaxation rates. Therefore, a more informative value is the R_1/R_2 ratio, bearing in mind that the R_2 will always be larger than R_1 and that for imaging purposes it is imperative to keep this ratio as close to one as possible. As chemical exchange processes also add to line broadening, it is important to keep these to a minimum also.

For the *meta*-substituted pyridine complexes, it can be seen that the phosphinate complexes, **[Dy.L^5]** and **[Dy.L^6]**, display a larger R_1/R_2 ratio, compared to the analogous carboxylate complex, **[Dy.L^7]**. This can be attributed to the enhanced rigidity created by the bulky phosphinate groups, reducing the intramolecular exchange processes between potential isomers, *via* arm rotation as discussed above. A surprising observation is the unexpectedly large transverse relaxation rate value for **[Dy.L^8]**. It had been anticipated that the R_2 value for this complex should be the lowest, due to the increase in the lanthanide to fluorine distance, *r*, in addition to the presence of an extra phosphinate moiety to further decrease dynamic motion of the system.

However, this value may be slightly misleading and is likely to be inflated due to the presence of a suspected overlapping isomer peak. This would explain the anomalous R_1/R_2 ratio observed for this compound.

Table 4.5 *Longitudinal (R_1) and transverse (R_2) relaxation rates and the ratio of the two for the Dy(III) complexes of* ***L[5]***, ***L[6]***, ***L[7]***, *and* ***L[8]***, *with comparisons to literature compounds (D_2O, 298 K, 4.7 T).*

Complex	R_1 / Hz	R_2 / Hz [(a)]	R_1/R_2
[Dy.LC[1]] [(b)]	75	116	0.65
[Dy.LP[1]] [(b)]	104	135	0.77
[Dy.L[5]] [(c)]	56	94	0.60
[Dy.L[6]] [(c)]	64	107	0.60
[Dy.L[7]] [(c)]	70	151	0.45
[Dy.L[8]]$^-$	34	141	0.24

(a) R_2 values were estimated as ($\pi\omega_{1/2}$) for a Lorentzian line fit. (b) Values taken from the literature.[1] (c) Data given is for major isomer (minor isomer is comparable in each case).

Unfortunately, when these pyridine complexes are compared to the analogous amide complexes, it can be seen that the R_1/R_2 ratio has not been improved by the incorporation of the CF_3 reporter group onto the pyridine moiety, as was envisioned in the design of the compounds. In fact, the values obtained are comparable with the carboxylate amide complex, **[Dy.4[2]]**, and are significantly lower than the phosphinate complex, **[Dy.4[1]]**. This, combined with the significant minor isomer observed with all of the pyridine complexes, suggests that these systems may show no improvement in imaging experiments compared to previous studies. However, a positive aspect to come out of these investigations is the unprecedented range of chemical shift values for the different Ln(III) complexes of the *meta*-substituted systems. In particular, **[Ln.L[6]]** shows up to a 100 ppm dipolar shift. An improved understanding of the physical basis of such large shifts would help in the design of future probes, particularly in the development of responsive systems that display large chemical shift non-equivalence between different forms. Therefore, a more in depth investigation of the ^{19}F NMR chemical shift behaviour of **[Ln.L[6]]** was undertaken.

4.5 Investigation into the Increased Chemical Shift Range of [Ln.L^6]

Due to the large variations in shift seen with the thulium and dysprosium complexes of **L^6** (around 180 ppm difference between the major isomers of each complex), it was decided to investigate the behaviour of this system further. This involved the synthesis of a series of lanthanide(III) complexes (from Eu(III) to Yb(III) plus Y(III) as a diamagnetic analogue), followed by full analysis of their ^{19}F NMR shift and relaxation properties (*Table 4.6*).

Table 4.6 *^{19}F NMR shift and longitudinal relaxation rate (R_1) data for **[Ln.L^6]** at different field strengths (D_2O, 295 K).*

Ln	Shift / ppm	R_1 / Hz [(b)]				
		4.7 T	9.4 T	11.7 T	14.1 T	16.5 T
Y[(a)]	-63.1	1.1 ±0.02	1.2 ±0.01	---	---	---
	(-63.1)	(1.1 ±0.02)	(1.2 ±0.02)	---	---	---
Eu[(a)]	-58.6	1.7 ±0.03	3.5 ±.0.01	4.3 ± 0.19	4.9 ± 0.03	5.7 ±0.03
	(-57.9)	(1.7 ±0.01)	(3.5 ±0.01)	(3.9 ±0.70)	(4.9 ±0.03)	(5.6 ±0.08)
Tb[(a)]	-158.4	56 ±1.4	89 ±0.3	117 ±3.2	133 ±1.0	150 ±3.8
	(-158.9)	(56 ±0.5)	(93 ±3.1)	(104 ±9.4)	(129 ±2.9)	(143 ±7.7)
Dy[(a)]	-162.4	64 ±1.7	114 ±0.5	142 ±1.1	166 ±0.4	192 ±0.5
	(-168.9)	(67 ±0.6)	(114 ±8.4)	(146 ±5.5)	(165 ±1.1)	(186 ±2.6)
Ho[(a)]	-107.8	67 ±0.8	129 ±0.6	154 ±1.9	189 ±0.7	218 ±0.2
	(-111.4)	(67 ±0.7)	(122 ±5.4)	(131 ±9.9)	(186 ±2.3)	(212 ±2.2)
Er[(a)]	-16.9	94 ±1.2	136 ±0.7	175 ±1.4	188 ±1.1	219 ±3.1
	(-13.6)	(104 ±5.5)	(142 ±7.2)	(176 ±13.1)	(192 ±3.9)	(236 ±8.1)
Tm[(a)]	17.1	59 ±0.5	107 ±0.4	132 ±1.6	152 ±0.6	173 ±1.2
	(20.3)	(67 ±0.6)	(111 ±4.4)	(140 ±0.3)	(153 ±2.7)	(168 ±6.5)
Yb[(a)]	-41.5	14 ±0.5	15 ±0.1	17 ±1.1	18 ±0.1	19 ±0.3
	(-38.9)	(11 ±0.02)	(16 ±0.21)	(17 ±0.8)	(17 ±0.6)	(20 ±0.6)

(a) Values in parenthesis refer to minor isomer, with ratios of major to minor isomers around 4:1 for each complexes.

Again, fitting of the longitudinal relaxation rates at five different magnetic field strengths was undertaken (*Figure 4.6*), in order to estimate the mean distance, *r*, between the lanthanide ion and the CF_3 group, and the rotational correlation time, τ_R. Global fitting of the combined data for all the Ln(III) complexes allows a more accurate estimation of these values. This was carried out using Levenburg-Marquadt minimisation of the non-linear squares error function of *Equation 1.7* (see *Section 1.3.2*). This resulted in values of 6.12 ±0.06 Å (*r*) and 238 ±12 ps (τ_R). These values fall in the expected range, but it is important to note that these are average values for all the complexes investigated and there will be around a 0.08 Å variation in *r* due to the "lanthanide contraction" from Dy to Yb.

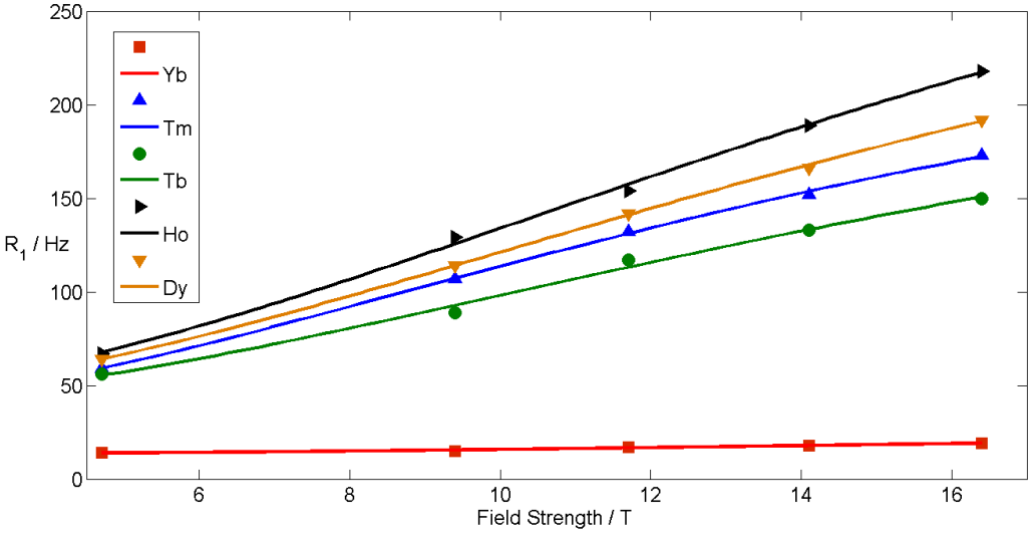

Figure 4.6 *Variation of ^{19}F NMR longitudinal relaxation rates with magnetic field for **[Ln.L^6]** (295 K, D_2O) showing the experimentally obtained values (symbols) and fit (line) to the data, using a global minimisation strategy.*

To understand the ^{19}F NMR chemical shift values observed, it is necessary to recall the origins of the pseudocontact shift (Δ_p) in paramagnetic lanthanide complexes, as discussed in *Section 1.3.1*. For an axially symmetric complex with spherical coordinates *r*, *Θ*, and ϕ with respect to the Ln(III) ion on the principal axis, the pseudocontact shift is given by:

$$\Delta_p = \frac{C_J \mu_B^2}{60(kT)^2}\left[\frac{(3\cos^2\theta - 1)}{r^3}B_0^2 + \frac{(sin^2\theta\,\cos 2\varphi)}{r^3}B_2^2\right]$$

where C_J is the Bleaney constant characteristic of the particular Ln(III) ion, μ_B is the Bohr magneton, Θ is the angle between the nucleus under consideration and the principal axis of the lanthanide ion, and B_0^2 and B_2^2 are second order crystal field terms determined by local symmetry and donor polarisability.[12,13]

It is generally assumed that for a given series of isostructural complexes, the ligand field coefficients are invariant amongst the lanthanides. Therefore, if the temperature is kept constant for all measurements, it is predicted that the comparative resonance for a given probe nucleus should be determined almost entirely by the Bleaney constants, as the spherical coordinates should remain relatively unaltered. Therefore, the ^{19}F NMR spectra for all of the Ln(III) complexes of **L^6** were superimposed, with the C_J values listed (*Figure 4.7*).

From this, it can be seen that the resonances are observed at chemical shifts that are in good overall agreement with the Bleaney constants and follow the predicted pattern; from high positive C_J values shifted to higher frequency (Tm, C_J = +53, δ_F = + 17.1 ppm), through to large negative C_J values shifted to lower frequency (Dy, C_J = -100, δ_F = - 162.4 ppm). Yttrium is the diamagnetic analogue, and has a Bleaney constant of zero. This can therefore be seen as the relative 'centre' for the shifts observed. While the shifts do proceed in the correct order as predicted by the C_J values, when plotted they do not fit precisely to a linear trend (*Figure 4.8*). It has been noted before that the Bleaney theory has limited applicability for quantitative studies.[18,19] Therefore, it was decided to investigate the parameters of the above equation in more detail.

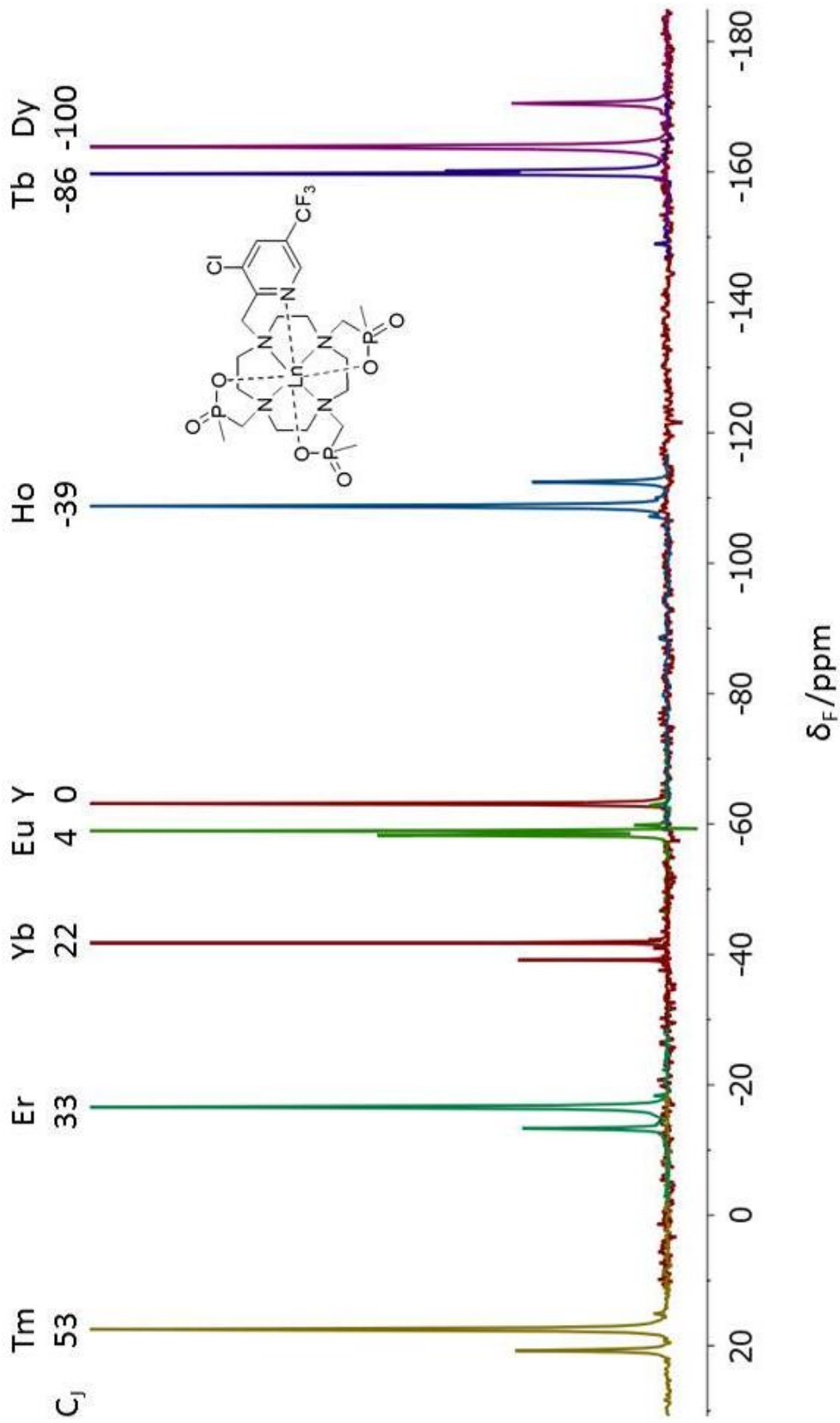

Figure 4.7 *^{19}F NMR shifts (376 MHz, 295 K, D_2O) for **[Ln.L^6]** with related Bleaney constants stated for each lanthanide ion (Y is the diamagnetic analogue).*

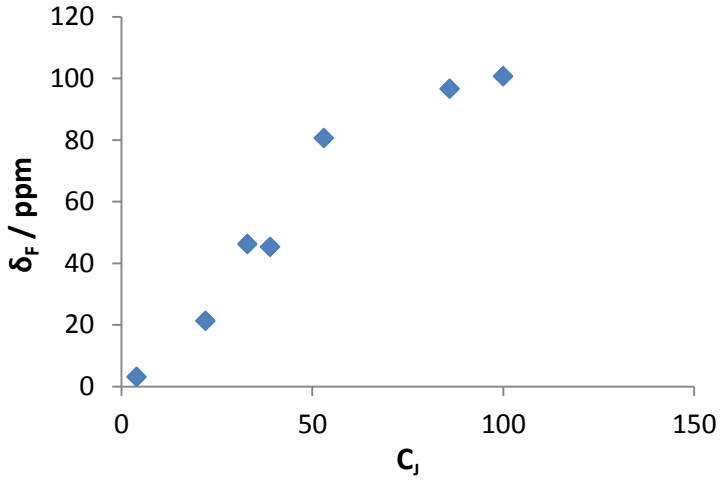

Figure 4.8 *Relationship between ^{19}F NMR chemical shift values obtained for* ***[Ln.L^6]*** *and the Bleaney constant for each lanthanide.*

The simplest parameter to confirm is the temperature, as this was verified separately using an ethylene glycol standard reference solution before each spectrum was measured. The distance, *r*, is likely to decrease across the series due to the "lanthanide contraction". However, this cannot contribute more than a 0.08 Å variation between the different lanthanide complexes. When this is incorporated into the shift values obtained with an inverse cubed dependence, there is little difference in the form of the plot from that shown in *Figure 4.8*. It is harder to assess the impact of changes to the other spherical polar coordinate parameters (Θ, φ) without crystal structure information.

This leaves the crystal field terms and their relative importance. They are generally assumed to be constant. However, it has been shown that there can be variations across the series by Gruber and co-workers. They found an increase in B_0^2 and an accompanying decrease in B_2^2 from Tb(III) to Yb(III) for lanthanide ions in the C_{3i} sites of Y_2O_3.[20] It is possible to estimate B_0^2 alone by measuring the splitting between the A and E energy levels present in the Eu $^5D_0 \leftarrow {}^7F_1$ transition (ΔJ = 1 band). Therefore, an emission spectrum was obtained for **[Eu.L^6]** (*Figure 4.9*).

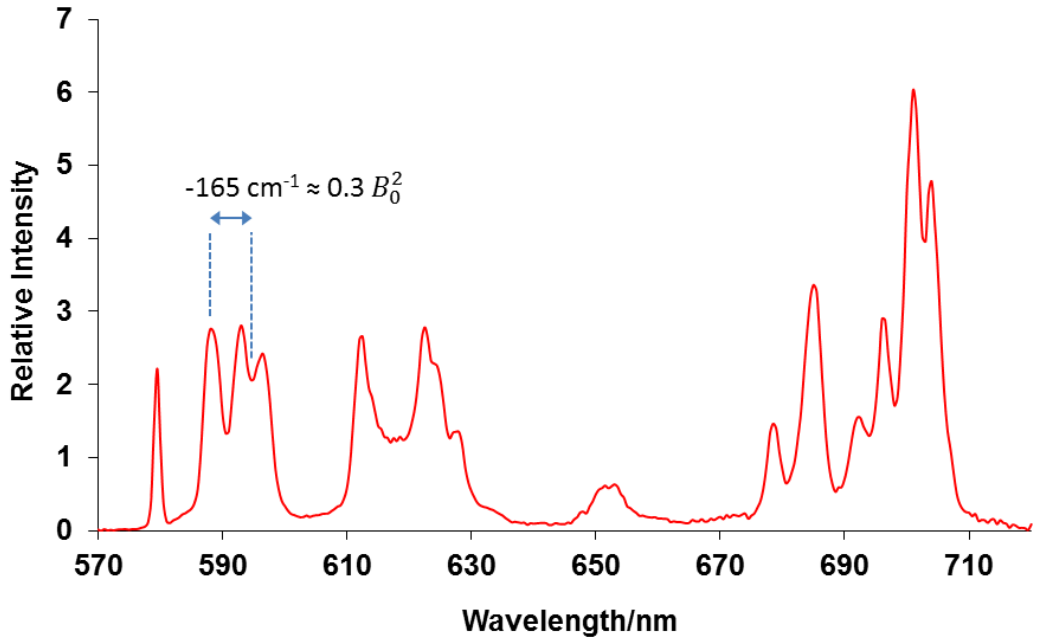

Figure 4.9 *Eu(III) emission spectrum for* ***[Eu.L^6]*** *(H_2O, 298 K, λ_{exc} = 276 nm).*

The splitting of the bands is roughly 0.3 B_0^2,[21] resulting in a value of -550 cm^{-1} for the second order ligand field splitting. This is large compared to other values obtained for related lanthanide complexes (typically of the order of around 200 cm^{-1}), which may explain the poor fitting of the data presented above. Bleaney had assumed that the crystal field splitting terms would be comparable to kT (≈ 205 cm^{-1} at 298 K) when making his predictions about chemical shift behaviour. However, with larger crystal field terms, such as the one observed in this case, this may not be accurate and further terms may need to be introduced in order to fully understand and predict chemical shift behaviour in lanthanide complexes. Previous studies have focussed on fairly dynamic systems, and it may be the case that the more rigid complexes discussed here are in fact improved 'models' to investigate in the future.

While the temperature was kept constant for the measurements carried out above, it was of interest to investigate the dependence of the observed chemical shifts on temperature, due to the inverse square relationship. Determination of temperature *in vivo* can provide information on physiological conditions of both healthy and diseased

tissue. For example, elevated temperatures have been observed in the imaging of cancerous tissue, which is linked to an increase in the rate of metabolism of glucose.[22,23] It is also critically important for monitoring thermal therapy techniques.[24] Currently, temperatures within a biological system can be monitored by the application of invasive external probes, which pose the risk of infection or acute damage, or by using non-invasive thermometry methods, such as T_1/T_2 relaxation measurements. However, these latter methods suffer from low accuracy readings. Thermal mapping of water is possible, but is associated with a very low sensitivity change of 0.01 ppm K^{-1}. This has led to the development of lanthanide based contrast agents as temperature probes as they can display increased chemical shift non-equivalence, leading to higher temperature sensitivity.[25–28] These have led to the development of probes that display sensitivity values up to 1.76 ppm K^{-1}.[29] Examples have also been published that allow simultaneous imaging of brain temperature and pH.[30,31] The majority of these examples utilise highly shifted ^{1}H resonances, but there has been an example that uses the temperature-dependent ^{19}F chemical shift of a CF_3 functionality.[32]

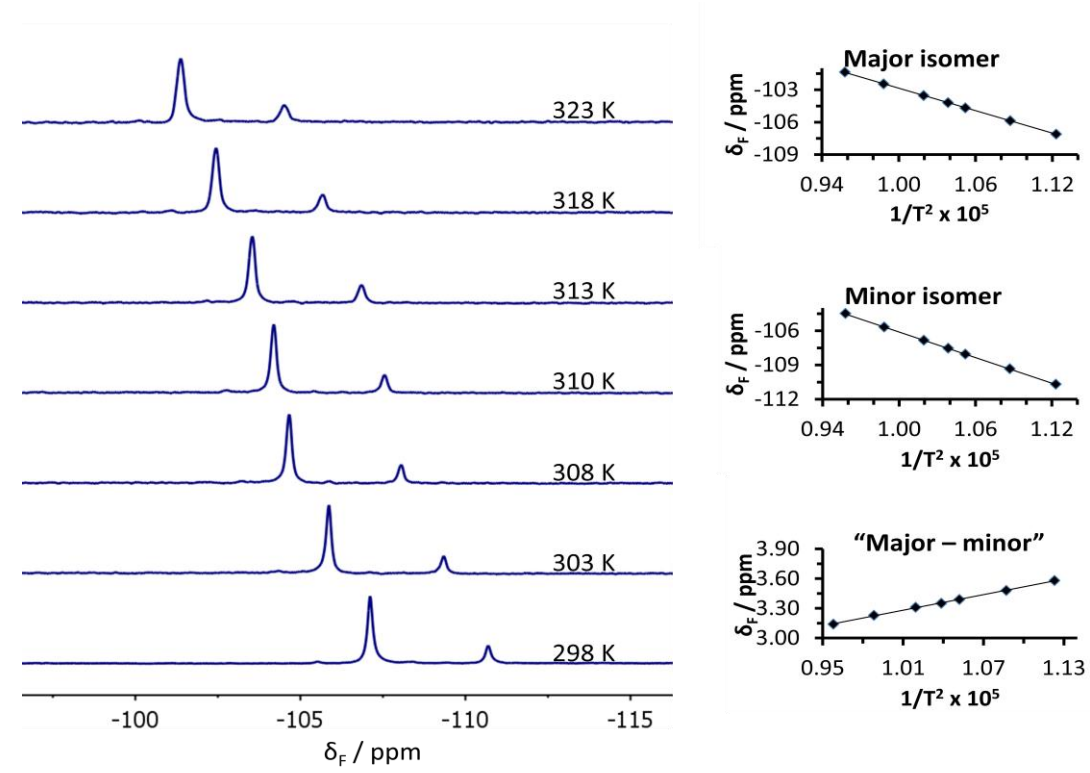

Figure 4.10 *^{19}F NMR spectra of **[Ho.L^6]** at a range of temperatures and accompanying plots of δ_F as a function of $1/T^2$.*

It is of interest to see how the systems reported here would compare to these previously reported temperature probes, and so for the Dy, Ho, and Tm complexes of **L^6**, the ^{19}F NMR spectrum was recorded at seven different temperatures over a range of 25 K (from 298 to 323 K). Examples of the spectra obtained for **[Ho.L^6]** are shown in *Figure 4.10*. An additional feature of these spectra that can be observed is the increase in linewidth with increasing temperature, due to an increase in chemical exchange processes at elevated temperatures. As can be seen, there is a considerable shift in both resonances over the temperature range tested, over 12 ppm in the case of the Dy(III) complex. By plotting δ_F as a function of $1/T^2$, a linear fit can be plotted (*Figure 4.10*). This allows a method of calculating the temperature from the ^{19}F NMR chemical shift. However, in order to do this it is necessary to calibrate the system when recording the NMR spectrum, which can be time consuming and difficult, especially with *in vivo* studies. The presence of two species in solution in this case is advantageous, as the second signal can be used as an internal reference. If the relative resonances are taken as a function of temperature, then it is possible to calculate the temperature from the difference between the two peaks, negating the need for calibration (*Table 4.7*).

Table 4.7 *Change in chemical shift per unit temperature for **[Ln.L^6]** (Ln = Dy, Ho, Tm) for major and minor isomers, with difference between the change in shifts also given.*

Complex	**$\Delta\delta_F$ / T (ppm K^{-1})**		
	Major isomer	*Minor isomer*	*Major - minor*
[Dy.L^6]	0.48	0.51	0.03
[Ho.L^6]	0.23	0.25	0.02
[Tm.L^6]	0.42	0.42	0.004

The values for the different lanthanide complexes above correlate well with the overall shifts of the compounds, i.e. the larger the shift of the complex the larger the change in the shift as a function of temperature (Dy > Tm > Ho), with an increase in temperature causing the resonances to become less shifted with respect to the

diamagnetic analogue. Unfortunately, whilst the internal calibration using both the major and minor isomer of a given complex does work in theory here, this method reduces the change in shift over a set temperature from up to 0.48 ppm K^{-1} down to 0.03 ppm K^{-1} (*Table 4.7*). In practice, this limits the application of such compounds and reduces the reliability of temperature values obtained. However, a suitable alternative would be to use two of the complexes in tandem. In particular, as the resonances for the Dy(III) and Tm(III) complexes are both highly shifted and move towards each other with an increase in temperature, using both together increases the change in shift to almost 1 ppm K^{-1} (*Figure 4.11*). This brings it up to the same magnitude as the currently employed compounds, although these suffer from increased complexity and low signal intensity,[30,31] or have much more severe line-broadening.[32] The simplicity and potential for fast acquisition of the complexes presented here are promising and warrant further investigation in the future, in particular into the applicability of these probes *in vivo*.

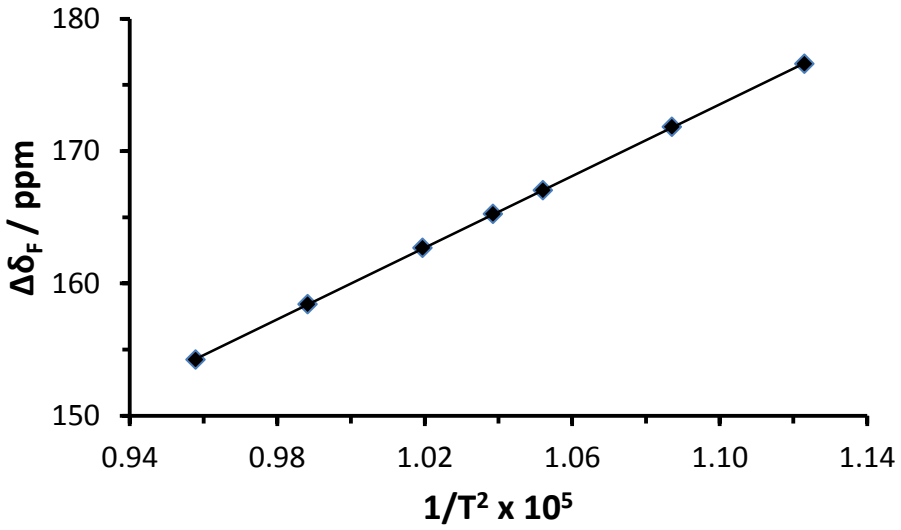

Figure 4.11 *Variation in the distance between the resonances for the major isomers of* ***[Tm.L^6]*** *and* ***[Dy.L^6]*** *as a function of $1/T^2$ (D_2O, 14.1 T, 0.93 ppm K^{-1}).*

4.6 Conclusions

When designing these fluorine-labelled lanthanide complexes, the initial aims were to improve the R_1/R_2 ratio by incorporating the CF_3 reporter group onto a pyridine moiety, in order to increase the conformational rigidity in comparison to previously studied mono-amide complexes. This should have reduced dynamic motion, thereby reducing exchange broadening. Unfortunately, there was no real improvement upon the R_1/R_2 ratio found with previous compounds and, while there was a decrease in the number of stable isomeric species, the pyridine based complexes exist as a two main species in solution, in around a 4:1 ratio. However, an unexpected result that arose from this study was the unprecedented range of chemical shifts observed, in particular for **[Ln.L^6]**. These were significantly larger than those previously observed for related compounds.

This led to a further investigation into the chemical shift behaviour of **[Ln.L^6]** to investigate the origin of these remarkable shifts and examine potential applications. It was found from the europium emission spectrum that the system possesses a relatively large second order crystal field splitting term that plays an important role in determining the magnitude of the pseudocontact shift experienced by the fluorine atoms, as a result of being close to the paramagnetic lanthanide ion. When plotted as a function of the Bleaney constant, the shifts do not correlate linearly as would be expected, although they do follow the correct general trend. It may be the case that for complexes with such large crystal field terms, the assumptions made by Bleaney in his calculations need to be rethought. Due to the large dipolar shift, it was suggested that these complexes may be able to act as NMR thermometers. Initial experiments were undertaken that demonstrate the feasibility of such an application, with almost a 1 ppm K^{-1} variation, using a combination of two different Ln(III) complexes.

The extent of the chemical shift range also opens another possible use for related systems. If the CF_3 group is replaced by a proton containing group, e.g. ^{t}Bu, it should be possible to generate high intensity shifted resonances in ^{1}H NMR spectroscopy. If relatively large shifts can be produced, then it may be possible to generate probes for

^{1}H MRS, with strong signals that are shifted well away from the water resonance and other background signals. In this way, it would incorporate the advantages of heteronuclei with those of imaging protons, i.e. no background signal combined with the high sensitivity and widespread use of ^{1}H magnetic resonance. This concept forms the basis of the work presented in the next chapter.

4.7 References

1. K. H. Chalmers, M. Botta, and D. Parker, *Dalton Trans.*, 2011, **40**, 904–913.

2. S. Aime, A. S. Batsanov, M. Botta, J. A. K. Howard, M. P. Lowe, and D. Parker, *New J. Chem.*, 1999, **23**, 669–670.

3. F. Cottet, M. Marull, O. Lefebvre, and M. Schlosser, *Eur. J. Org. Chem.*, 2003, 1559–1568.

4. S. Brandes, C. Gros, F. Denat, P. Pullumbi, and R. Guilard, *Bull. Soc. Chim. Fr.*, 1996, **133**, 65–73.

5. M. Woods, G. E. Kiefer, S. Bott, A. Castillo-Muzquiz, C. Eshelbrenner, L. Michaudet, K. McMillan, S. D. K. Mudigunda, D. Ogrin, G. Tircsó, S. Zhang, P. Zhao, and A. D. Sherry, *J. Am. Chem. Soc.*, 2004, **126**, 9248–9256.

6. O. Reany, T. Gunnlaugsson, and D. Parker, *J. Chem. Soc., Perkin Trans. 2*, 2000, 1819–1831.

7. P. Atkinson, K. S. Findlay, F. Kielar, R. Pal, D. Parker, R. A. Poole, H. Puschmann, S. L. Richardson, P. A. Stenson, A. L. Thompson, and J. Yu, *Org. Biomol. Chem.*, 2006, **4**, 1707–1722.

8. A. Beeby, I. M. Clarkson, R. S. Dickins, S. Faulkner, D. Parker, L. Royle, A. S. de Sousa, J. A. G. Williams, and M. Woods, *J. Chem. Soc., Perkin Trans. 2*, 1999, 493–504.

9. D. Parker, R. S. Dickins, H. Puschmann, C. Crossland, and J. A. K. Howard, *Chem. Rev.*, 2002, **102**, 1977–2010.

10. S. Aime, M. Botta, D. Parker, and J. A. G. Williams, *J. Chem. Soc., Dalton Trans.*, 1995, 2259–2266.

11. D. Parker and J. A. G. Williams, *J. Chem. Soc., Dalton Trans.*, 1996, 3613–3628.

12. B. Bleaney, *J. Magn. Reson.*, 1972, **8**, 91–100.

13. P. Harvey, I. Kuprov, and D. Parker, *Eur. J. Inorg. Chem.*, 2012, 2015–2022.

14. A. M. Kenwright, I. Kuprov, E. De Luca, D. Parker, S. U. Pandya, P. K. Senanayake, and D. G. Smith, *Chem. Commun.*, 2008, 2514–2516.

15. K. H. Chalmers, E. De Luca, N. H. M. Hogg, A. M. Kenwright, I. Kuprov, D. Parker, M. Botta, J. I. Wilson, and A. M. Blamire, *Chem. Eur. J.*, 2010, **16**, 134–148.

16. B. M. Alsaadi, F. J. C. Rossotti, and R. J. P. Williams, *J. Chem. Soc., Dalton Trans.*, 1980, 2147–2150.

17. S. Aime, L. Barbero, M. Botta, and G. Ermondi, *J. Chem. Soc., Dalton Trans.*, 1992, 225–228.

18. V. S. Mironov, Y. G. Galyametdinov, A. Ceulemans, C. Görller-Walrand, and K. Binnemans, *Chem. Phys. Lett.*, 2001, **345**, 132–140.

19. V. S. Mironov, Y. G. Galyametdinov, A. Ceulemans, C. Görller-Walrand, and K. Binnemans, *J. Chem. Phys.*, 2002, **116**, 4673–4685.

20. J. B. Gruber, R. P. Leavitt, C. A. Morrison, and N. C. Chang, *J. Chem. Phys.*, 1985, **82**, 5373–5378.

21. C. Gorller-Walrand, E. Huygen, K. Binnemans, and L. Fluyt, *J. Phys.: Condens. Matter*, 1994, **6**, 7797–7812.

22. H. Young, R. Baum, U. Cremerius, K. Herholz, O. Hoekstra, A. A. Lammertsma, J. Pruim, and P. Price, *Eur. J. Cancer*, 1999, **35**, 1773–1782.

23. R. A. Gatenby and R. J. Gillies, *Nat. Rev. Cancer*, 2004, **4**, 891–899.

24. V. Rieke and K. Butts Pauly, *J. Magn. Reson. Imaging*, 2008, **27**, 376–390.

25. S. Aime, M. Botta, M. Fasano, E. Terreno, P. Kinchesh, L. Calabi, and L. Paleari, *Magn. Reson. Imaging*, 1996, **35**, 648–651.

26. K. Roth, G. Bartholomae, H. Bauer, T. Frenzel, S. Kossler, J. Platzek, and H.-J. Weinmann, *Angew. Chem. Int. Ed.*, 1996, **35**, 655–657.

27. T. Frenzel, K. Roth, S. Koßler, B. Radüchel, H. Bauer, J. Platzek, and H.-J. Weinmann, *Magn. Reson. Med.*, 1996, **35**, 364–369.

28. S. K. Pakin, S. K. Hekmatyar, P. Hopewell, A. Babsky, and N. Bansal, *NMR Biomed.*, 2006, **19**, 116–124.

29. M. Milne and R. H. E. Hudson, *Chem. Commun.*, 2011, **47**, 9194–9196.

30. D. Coman, H. K. Trubel, R. E. Rycyna, and F. Hyder, *NMR Biomed.*, 2009, **22**, 229–239.

31. D. Coman, G. E. Kiefer, D. L. Rothman, A. D. Sherry, and F. Hyder, *NMR Biomed.*, 2011, **24**, 1216–1225.

32. *US Pat.*, US5690909, 1997.

5. Strategies to Enhance Signal Intensity; A New Approach

5.1 Introduction

The strong ^{1}H NMR background signal *in vivo* has significant limitations for magnetic resonance imaging and spectroscopy, particularly when attempting to distinguish between tissue types or developing responsive probes. This drawback has led to the development of heteronuclear imaging, with ^{19}F possessing the most promising attributes, due to its 100 % isotopic abundance and relatively high NMR sensitivity. The most important characteristic of fluorine, and the main reason it has been of interest, is the combination of these factors with the almost zero background signal *in vivo*. However, as has been shown here and in previous studies, fluorine imaging using conventional MR set-ups (with ^{19}F imaging coils) is far from trivial, leading to limited success in the work reported here.

The large, lanthanide induced chemical shifts observed for the fluorinated pyridine complexes of up to 100 ppm in the previous chapter has led to thoughts of developing an alternative method of circumventing the background signal, without the need for heteronuclear based probes and the added drawbacks involved. General ^{1}H NMR chemical shifts for compounds in biological systems fall within the 0-10 ppm range, with the majority of the signal arising from internal water and fat. If the corresponding ^{1}H NMR signal of a probe compound can be shifted away from these background signals, i.e. through the use of a paramagnetic lanthanide ion, then it should be possible to selectively image this resonance while excluding the endogenous signals. This selective imaging method would retain the advantages of using protons as the imaging nucleus. Namely, the current widespread use and understanding of ^{1}H MRI should allow far simpler analysis of such a probe, alleviating some of the difficulties witnessed through attempting to image fluorinated compounds. In addition, there are far more ^{1}H imaging coils available for use than the corresponding fluorine systems, increasing the range of experiments and applications that can be carried out.

In theory, any resonance greater than 10 ppm or lower than 0 ppm should be applicable to such studies, which is the range that individual proton frequencies are commonly shifted in paramagnetic lanthanide complexes, with chemical shift ranges up to -500 to +500 ppm often observed. However, the signal required must still possess compatible relaxation properties; i.e. increased longitudinal relaxation rates on the order of 100 Hz, without severe linewidths caused by greatly increased transverse relaxation rates and/or chemical exchange broadening. Ideally, a number of magnetically equivalent nuclei would contribute to the particular resonance, in order to maximise the signal intensity that could be obtained.

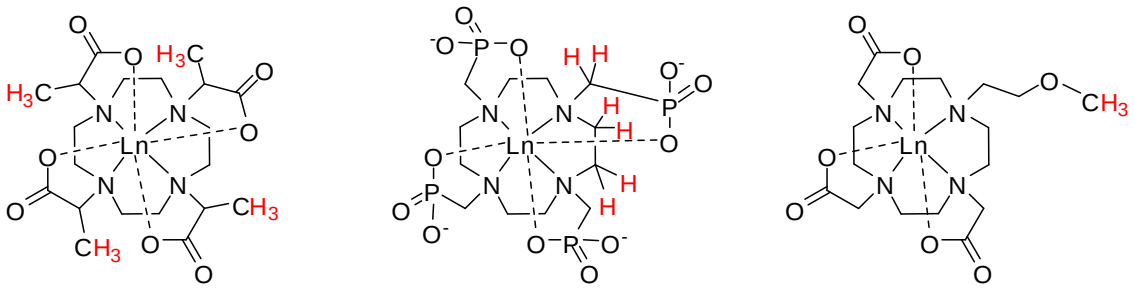

Scheme 5.1 *Previous examples of ^{1}H NMR shift probes, with proton nuclei of interest highlighted in red.*

There is some precedence in the literature for such shifted proton resonance probes as described above, with the first examples appearing 15 to 20 years ago. These examples were focussed primarily on the Yb(III), Tm(III), and Pr(III) complexes of **DOTMA**, **DOTP**, and **MOEDO3A** (*Scheme 5.1*). **[Yb-DOTMA]** possesses four equivalent methyl groups, giving rise to twelve magnetically equivalent proton nuclei, with a corresponding resonance located at -14.2 ppm. Aime and co-workers imaged this methyl signal selectively in a phantom imaging experiment in the presence of water, although to observe a 3 mM aqueous solution of the complex at 4.7 T and 300 K, with the parameters required, took 6 h and 23 min (R_1 = 15 Hz, R_2 ≈ 30 Hz under these conditions). Obviously the acquisition time required for this complex is far too long for clinical applications, but as a prototypical probe gave encouragement for further work, leading the researchers themselves to comment that the concept "may prove to be a valuable alternative in applications that currently require fluorine-containing probes."[1]

While the methyl signal of **[Yb-DOTMA]** does display a temperature dependent chemical shift (0.41 ppm K^{-1}), further responsive behaviour was sought, leading the same group to investigate the ^{1}H NMR resonances of **[Yb-DOTP]**.[2] The six proton resonances highlighted in *Scheme 5.1* (two equatorial ring-, two axial ring-, and two phosphonate arm-protons) are magnetically inequivalent, leading to six separate signals in the ^{1}H NMR spectrum that lie outside the standard diamagnetic range. Selecting a pair of these resonances and following the chemical separation between the two as a function of pH allowed linear dependences to be plotted over the pH range 5.0-7.5, with a change of 7 ppm per pH unit observed. By using pairs of resonances, the need for calibration is negated, and the large chemical shift range of the resonances should avoid interference with background signals.

Around the same time as these studies, Frenzel and co-workers developed a similar concept utilising the methoxy resonance of **[Pr-MOEDO3A]**, which resonates at -24.1 ppm at room temperature.[3,4] The work carried out mainly focussed on applications towards development of an NMR thermometer (0.13 ppm K^{-1}), and although the signal present was relatively broad, the complex was successfully used to monitor an *in vivo* temperature increase within the liver of a rat.

Despite these early successes, there followed a slight hiatus in the interest of these compounds, although further research has been published in this area in the last six or so years. Bansal and co-workers utilised the earlier promising results obtained with the **DOTMA** system, utilising Tm(III) in place of Yb(III).[5] The methyl shift of **[Tm-DOTMA]** resonates at -102 ppm, a large increase on the previously reported complexes. The magnitude of this shift allowed large improvements to be made in the imaging methods, resulting in strong phantom signals that could now be selectively acquired for 0.5 mM solutions in a matter of minutes, instead of hours (4 min 10 s acquisition time, 9.4 T, $R_2 \approx 250$ Hz). The complex was then applied to mapping temperature changes *in vivo*, with doses of 0.5-0.6 mmol kg^{-1}. While the results were promising, it would be difficult to incorporate further responsive behaviour (e.g. pH reporting) into the complex without interfering with the magnetic equivalence of the

methyl groups, thereby immediately reducing the signal intensity by a factor of 4. More recent work has involved encapsulation of a related Yb(III) complex inside liposomal nano-carriers, in order to increase the sensitivity and biocompatibility.[6]

Further work has also been undertaken with the thulium complex of **DOTP**. Using the same set of proton resonances, Hyder and co-workers have successfully generated temperature and pH distribution maps for rat brains *in vivo*, with a continuous infusion of the complex.[7] Although care was taken to ensure the rate of infusion of the compound was within the autoregulatory range of cerebral perfusion, the safe infusion doses quoted, of 1 mmol kg^{-1}, are ten times higher than the approved dose for related gadolinium contrast agents. The rats were also nephrectomised before the experiment, to prevent clearance of the complex *via* the kidneys, clearly limiting the feasibility of such studies. Another recent example describes the development of a new, but related complex that displays 2-3 times the level of temperature dependence compared with **[Tm-DOTMA]**, with values up to 1.76 ppm K^{-1} obtained.[8] However, the signals used for these measurements correspond to proton resonances that are significantly broadened, with R_1 and R_2 relaxation rates over 3,000 Hz (14.1 T, 308 K).

These examples demonstrate the potential for the development of a ^{1}H MR chemical shift reporter. Clearly, the main attributes required are a strong signal (ideally more than one equivalent proton) that is significantly shifted away from the standard diamagnetic range. Specific relaxation properties are also required, in order to achieve high signal intensity and be able to perform fast acquisition. The fluorinated pyridine complexes presented in the previous chapter seemingly meet these criteria; they display outstandingly large pseudocontact shifts, multiple equivalent nuclei that give rise to mainly one signal (≈ 80 %) in solution, and possess reasonable relaxation rates. Therefore, if the CF_3 group in the complex is replaced by a similar proton containing moiety, the resulting ^{1}H MR reporter should potentially retain these key properties.

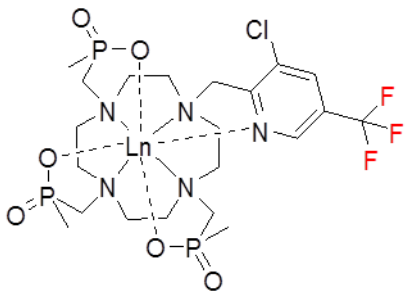

[Ln.L^6]

- 3 x imaging nuclei
- 83 % relative sensitivity
- Requires new coil development

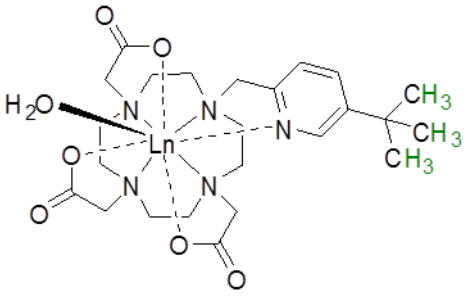

[Ln.L^9]

- 9 x imaging nuclei
- 100 % relative sensitivity
- Clinically used imaging nucleus

Scheme 5.2 *Comparison between the CF_3- and ^{t}Bu-based probes, highlighting the major advantages of the latter system (imaging nuclei indicated in red (^{19}F) and green (^{1}H)).*

This reasoning led to the design of the model complex, **[Ln.L^9]** (*Scheme 5.2*). The proton group chosen was a *tert*-butyl moiety, as it introduced the maximum possible number of equivalent proton nuclei, and should be relatively straightforward to synthesise. Providing that the properties of the complex were as expected, there are a number of advantages to using the ^{t}Bu moiety over the original CF_3 group. There are a higher number of imaging nuclei, ^{1}H NMR spectroscopy is intrinsically more sensitive than fluorine, and there is the added benefit of proton MRI being the clinically employed system. This latter point should increase the ease of imaging for the resulting complexes, alleviating some of the difficulties experienced with the previous fluorine experiments.

The carboxylate, rather than the phosphinate, structure was chosen for the model compound due to the ease of synthesis of the former. From the results of initial studies with **[Ln.L^9]**, improvements could easily be made to the structure, based on what has been learnt from the fluorine work. Similarly, providing the compound works as a proof-of-principle, efforts will be made to develop further complexes that display responsive behaviour. The Dy(III) and Tm(III) complexes will be examined, due to the

fact that these lanthanide ions should display the largest shifts, as predicted by Bleaney, and as observed in the previous chapter.

5.2 A Model System

5.2.1 Synthetic procedure

The *tert*-butyl moiety required for the imaging probe was introduced in the first step of the reaction by performing a Grignard reaction on 5-bromo-2-methylpyridine using *tert*-butyl magnesium chloride in anhydrous THF with copper(I) cyanide as a catalyst (*Scheme 5.3*), following a procedure adapted from Bell and co-workers.[9] However, applying large excesses of the catalyst, as suggested in the literature, gave rise to complicated work ups, with emulsions forming after quenching of the Grignard reagent with ammonium hydroxide and during subsequent aqueous washings. These mixtures were problematic to separate, resulting in poor yields and large amounts of cyanide waste being generated. In order to overcome these difficulties, a catalytic amount (≈ 10 mg) of CuCN was used, which yielded greatly improved yields and a more practicable purification procedure. Other simple Cu(I) salts were trialled with the reaction, but only the cyanide salt successfully resulted in formation of the desired product, **81**, which was isolated as a partially volatile liquid. In order to avoid potential loss of this volatile compound, extractions were performed with diethyl ether as the organic solvent, due to its relatively low boiling point, and further purification was not performed at this stage.

The remaining steps to synthesise the pyridine arm were similar to those described previously for **[Ln.L^8]$^-$** (*Section 4.2.2*). Firstly, *meta*-chloroperoxybenzoic acid was used to generate the pyridyl N-oxide, **82**, which was purified by silica gel column chromatography. A rearrangement followed, firstly to the trifluoroactetate ester intermediate, which was then hydrolysed *in situ* to form the alcohol, **83**. The alcohol was reacted with mesyl chloride, with triethylamine as a base, to give the reactive mesylate compound, **84**.

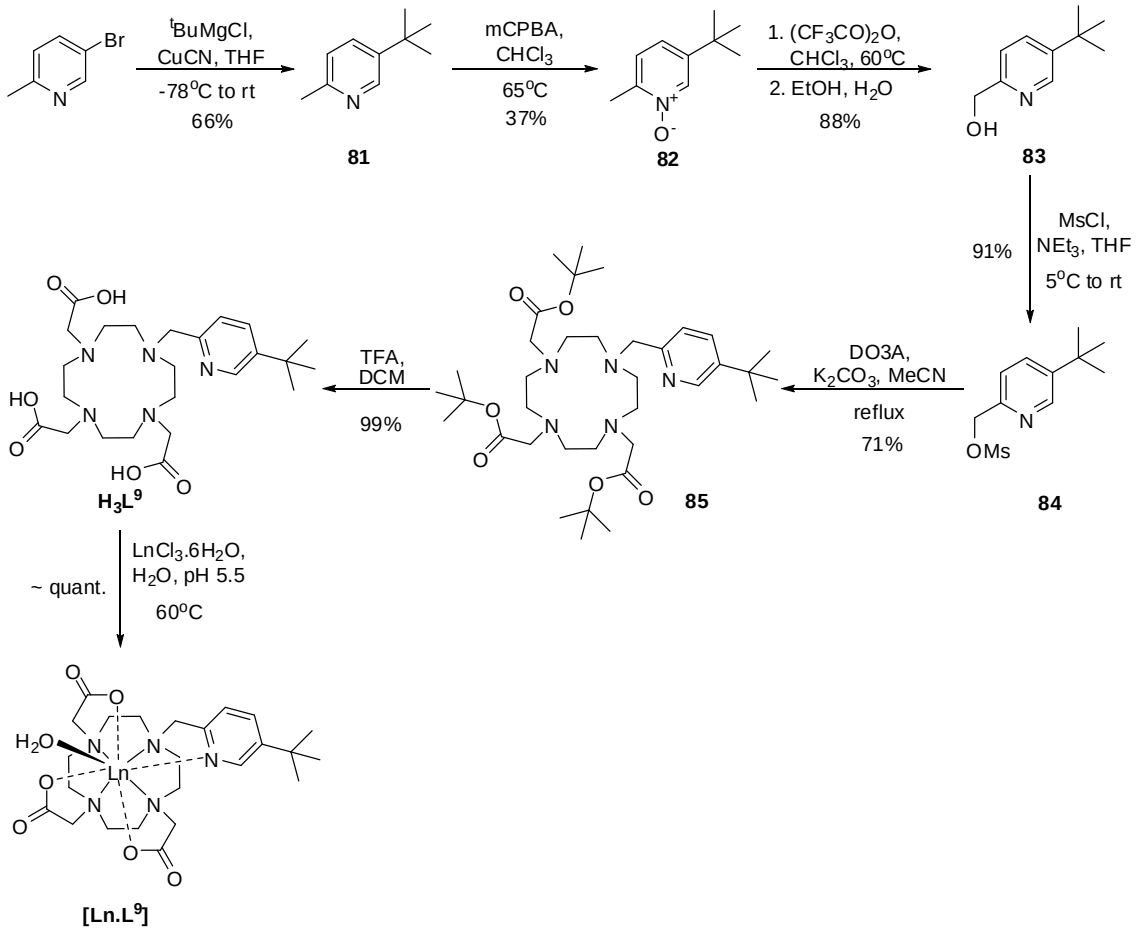

Scheme 5.3 *General procedure for the synthesis of* ***[Ln.L^9]****.*

The mesylate, **84**, was used immediately in an alkylation reaction with 1,4,7-tris-(*tert*-butoxycarbonylmethyl)-1,4,7,10-tetraazacyclododecane (DO3A), boiled under reflux in acetonitrile with potassium carbonate used as the base, to form the desired alkylated product, **85**, after purification with silica gel column chromatography. The *tert*-butyl ester groups were deprotected by stirring with trifluoroacetic acid in dichloromethane, to generate the acid compound. Metal complexation was achieved by stirring an aqueous mixture of the ligand, **L^9**, with the hydrated chloride salt of the chosen lanthanide ion at pH 5.5 and 60°C. Excess metal was removed by raising the pH to 10, causing Ln(III) hydroxide to precipitate out of solution. After removal of this precipitate, the pH was lowered back to 5.5 before the compound was lyophilised. The resulting solid was extracted with ethanol to eliminate further insoluble inorganic salts, before the solvent was removed to yield the desired complex, **[Ln.L^9]**.

5.2.2 Characterisation of the complexes

As detailed in *Chapter 2*, low resolution electrospray and high resolution accurate mass spectrometry were carried out to confirm the identity of each complex, with characteristic isotope patterns observed that correlated well with the calculated spectra. ^{1}H NMR spectroscopic data were collected for each complex and are discussed below.

5.2.3 ^{1}H NMR studies

5.2.3.1 Shift behaviour

After forming the complexes, an initial investigation was carried out into the chemical shift behaviour of the resonance associated with the *tert*-butyl group, which is easily identifiable due to the strong signal generated by the nine equivalent protons. The ^{1}H NMR spectra of the Tm(III) and Dy(III) complexes of **L^{9}** are shown in *Figure 5.1*. As can be seen, the *tert*-butyl groups give rise to strong, sharp resonances that are shifted well away from both the common resonance for a ^{t}Bu group ($\delta_H \approx 1$ ppm) and from the HOD signal present in the sample. As expected, the signals for the two complexes are shifted in opposite directions, with shifts of +10.8 and -20.5 ppm for the Tm(III) and Dy(III) complexes respectively. This is the sense predicted by the Bleaney constants,[10] and correlates well with the pattern observed for the fluorine analogues (*Section 4.5*)

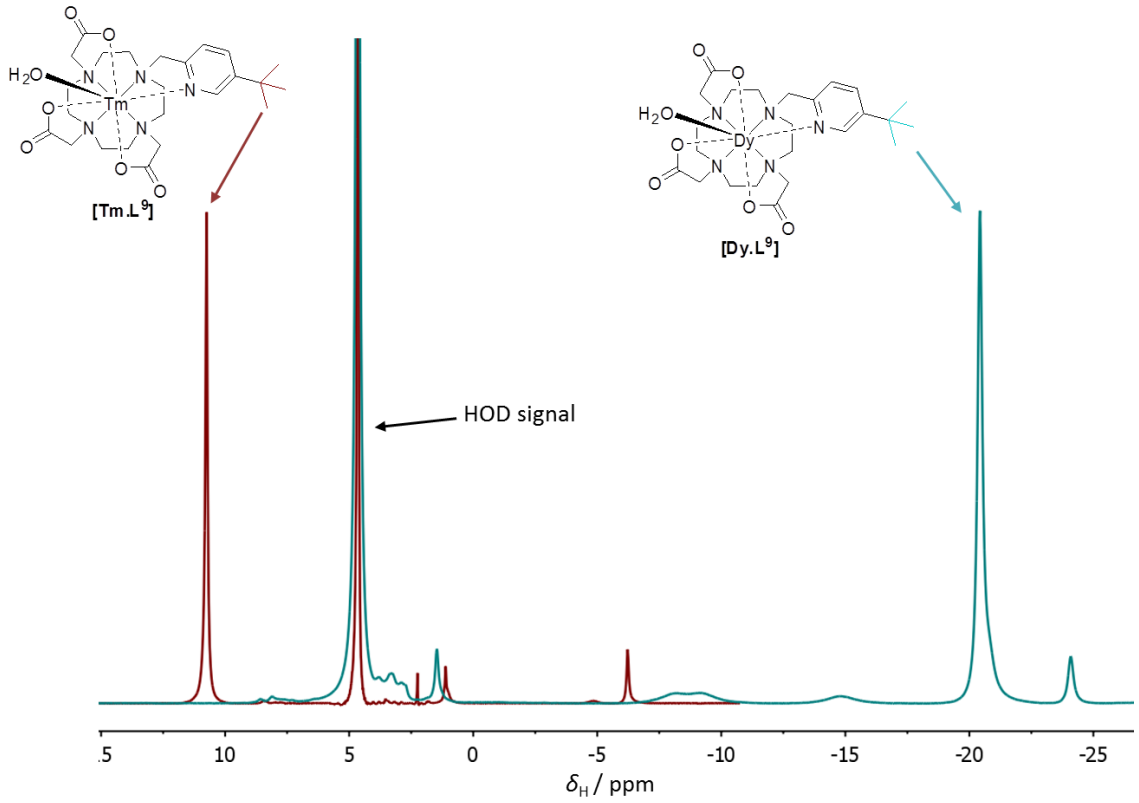

Figure 5.1 *Superimposed ^{1}H NMR spectra (D_2O, 9.4 T, 298 K) of* ***[Tm.L^{9}]*** *(red) and* ***[Dy.L^{9}]*** *(blue).*

The ^{1}H NMR spectra indicate that the compounds exist as a mixture of isomers in solution, as expected for pyridine based lanthanide complexes. These isomeric species are shown in more detail for the Tm(III) complex in *Figure 5.2*. The ratio of the isomers in **[Tm.L^{9}]** was roughly 5.5:1, with the signals for the major isomer being contained within those of the minor isomer; i.e. the shift range for the major isomer was -207.1 to +83.5 ppm, whereas the corresponding range for the minor isomer was -398.5 to +326.9 ppm. The ^{t}Bu signal for the minor isomer resonated at +52.0 ppm, which by integral analysis seemingly overlapped with a signal arising from the major isomer. The fact that the resonances associated with the major isomer were less shifted than the minor suggests that the preferred structure for the Tm(III) compound is q=0 twisted square anti-prismatic (TSAP), with the minor species adopting a square anti-prismatic (SAP) structure, with q=1.

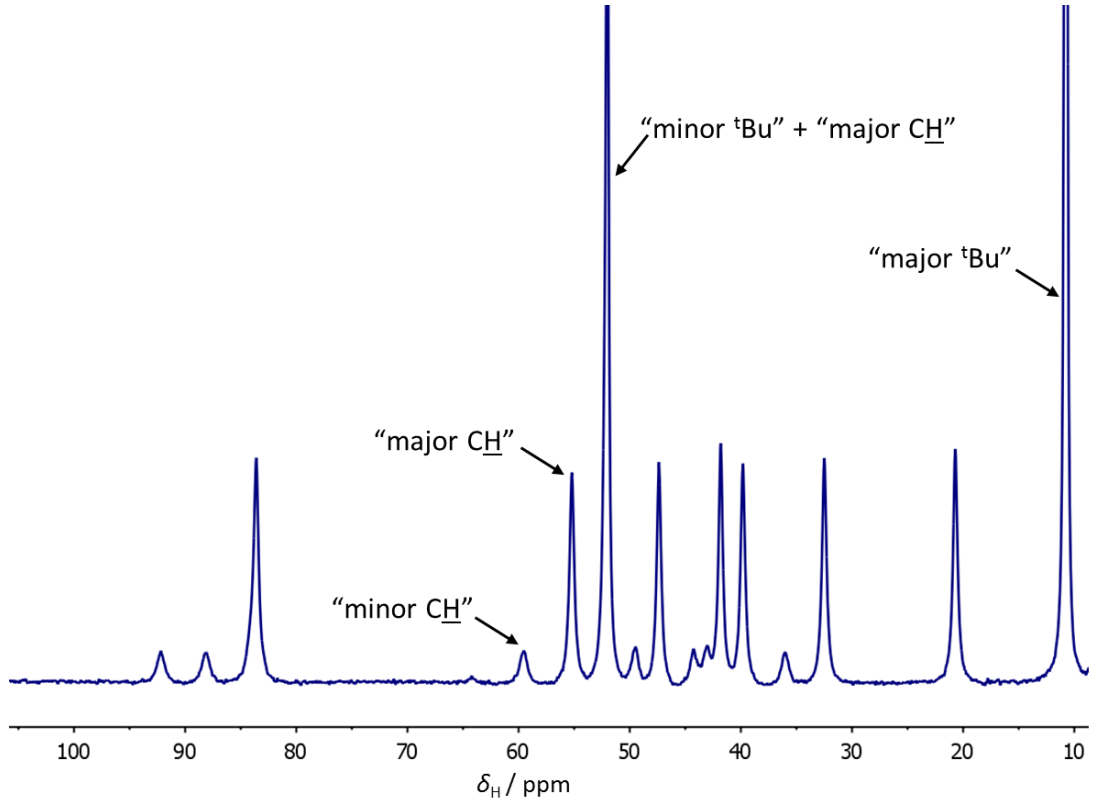

Figure 5.2 *^{1}H NMR spectrum of **[Tm.L^9]** indicating isomeric solution species (D_2O, 11.7 T, 298 K).*

For the Dy(III) compound, the NMR spectrum was more complicated to assign, due to the increase in line broadening associated with complexes of this lanthanide. However, there seemed to be a slight improvement in the ratio of the isomers (>6:1), with a possible switch in the nature of the major species, i.e. SAP for the major species and TSAP for the minor. Such a switching of the preferred conformer across the series of Ln(III) ions has been observed previously, and is usually associated with a change in hydration state. [11]

The *tert*-butyl resonances for the major species of each complex are shifted out of the 'biological window' of ^{1}H NMR spectroscopy, with the Dy(III) compound being of particular interest. As the shift observed occurs at a negative ppm value, it is over 20 ppm away from any other resonance that would be present *in vivo*, and should allow selective imaging of the signal. However, the R_1 and R_2 relaxation rates must first be considered to examine the suitability of such complexes as imaging probes.

5.3.2.2 Relaxation behaviour in solution

The longitudinal relaxation rates, R_1, for both the Tm(III) and Dy(III) complexes are shown in *Table 5.1*. As can be seen for Dy(III), the longitudinal relaxation rates were of the order required, i.e. around 100 Hz at 7 T and comparable to the relaxation rates obtained for the analogous CF_3-containing complexes presented in the previous chapter. As expected, R_1 values for the dysprosium complex were considerably higher than those for the thulium complex at a respective field, due to the increased effective magnetic moment, μ_{eff}, and electronic relaxation time, T_{1e}. In addition to the electronic relaxation times shown in *Table 5.1*, average values for the rotational correlation time (τ_R, 240 ±6 ps), and the Ln-^{t}Bu distance (r, 6.45 ±0.03 Å) could be estimated by global fitting of the relaxation rate data at variable magnetic fields, using the equation below (*Figure 5.3*). Again, these values were consistent with the values obtained for the related fluorinated compounds presented in the previous chapter.

Table 5.1 *^{1}H NMR longitudinal relaxation rate (R_1) data for the tert-butyl resonance of **[Ln.L^9]** at different field strengths (D_2O, 295 K). Values given in Hz.*

Complex	R_1 / Hz					μ_{eff} / μ_B [(a)]	T_{1e} / ps [(b)]
	4.7 T	9.4 T	11.7 T	14.1 T	16.5 T		
[Dy.L^9]	73 ±0.3	124 ±0.4	149 ±1.1	170 ±0.9	210 ±1.5	10.6	0.54 ±0.03
[Tm.L^9]	31 ±0.1	54 ±0.5	68 ±2.5	71 ±0.5	83 ±1.2	7.6	0.25 ±0.05

(a) Values taken from the literature.[12] (b) Calculated by fitting of the longitudinal relaxation rate data (see *Figure 5.3)*.

$$R_1 = \frac{2}{15}\left(\frac{\mu_0}{4\pi}\right)^2 \frac{\gamma_F^2 \mu_{eff}^2}{r^6}\left(\frac{7\tau_{R+e}}{1+\omega_e^2\tau_{R+e}^2} + \frac{3\tau_{r+e}}{1+\omega_F^2\tau_{R+e}^2}\right) + \frac{2}{5}\left(\frac{\mu_0}{4\pi}\right)^2 \frac{\omega_F^2 \mu_{eff}^4}{(3kT)^2 r^6}\left(\frac{3\tau_R}{1+\omega_F^2\tau_R^2}\right)$$

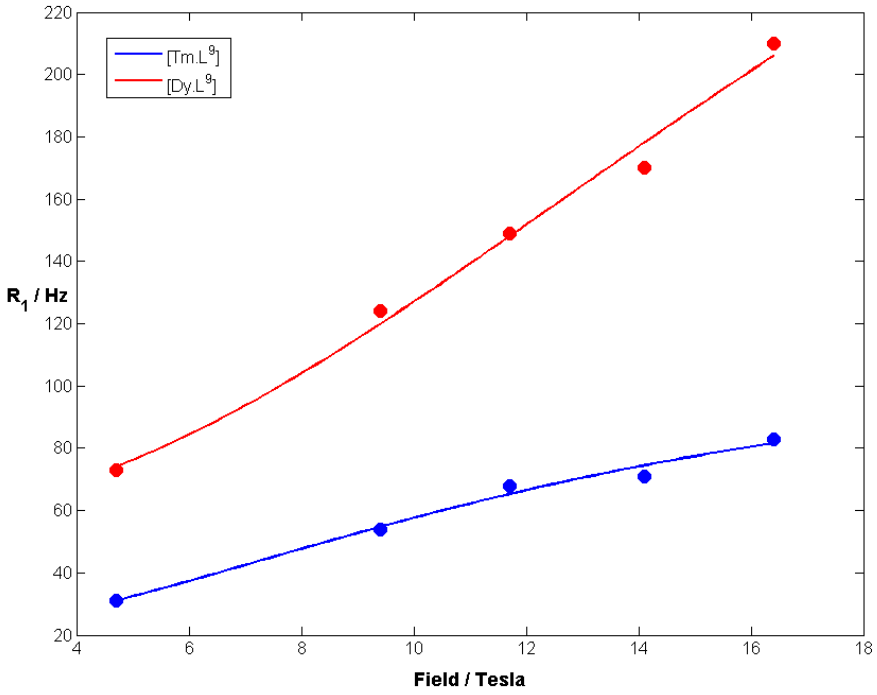

Figure 5.3 *Variation of ^{1}H NMR longitudinal relaxation rate with magnetic field for the tert-butyl resonance of **[Ln.L^9]** (295 K, D_2O) showing the experimentally obtained values (symbols) and fit (line) to the data, using a global minimisation method applied to the above equation.*

As before, another important consideration when considering probes for imaging purposes was the relationship between the longitudinal (R_1) and transverse (R_2) relaxation rates, as the latter is associated with line broadening. An increase in R_2 leads to an increase in linewidth, which will also be affected by chemical exchange processes. Therefore, in order to maximise signal intensity, it is imperative to maintain line broadening to a minimum and to make the R_1/R_2 ratio as close to one as possible. As can be seen in *Table 5.2*, at 9.4 T this ratio was almost 0.6, which is an improvement upon the carboxylated fluorine analogue, **[Ln.L^7]** (*Section 4.4.2*), though not as high as for some other related CF_3-containing complexes.[13] However, as a starting point for a model complex, this value was considered reasonable and sufficiently high to consider attempting imaging studies.

Table 5.2 *Longitudinal (R_1) and transverse (R_2) relaxation rates and the ratio of the two for the tert-butyl resonances of* ***[Dy.L^9]*** *and* ***[Tm.L^9]*** *(D_2O, 298 K).*

Complex	4.7 T			9.4 T		
	R_1 / Hz	R_2 / Hz [(a)]	R_1/R_2	R_1 / Hz	R_2 / Hz [(a)]	R_1/R_2
[Dy.L^9]	73	107	0.68	124	223	0.56
[Tm.L^9]	31	66	0.47	54	94	0.57

(a) R_2 values were estimated as ($\pi\omega_{1/2}$), for a Lorentzian line fit.

5.2.4 Removing the water signal

While the results obtained from the preliminary ^{1}H NMR studies were promising, before any imaging experiments could be attempted, it was necessary to determine whether the resonance of interest could be visualised selectively in the presence of a strong water signal, i.e. can the solvent signal be removed from the spectrum in order to observe only the resonance of the *tert*-butyl group of the complex? A potential solution involves saturation of the water signal, though this technique may affect other nearby signals, depending on the frequency separation between the solvent signal and the resonance of interest. A simple option would be to remove the data corresponding to the water peak from the FID trace selectively, after obtaining the spectrum. However, while this post-acquisition 'solvent suppression' technique is relatively straightforward in a standard NMR spectroscopy experiment and proved to be highly successful, it is difficult to apply to a more complicated *in vivo* MRI experiment. Therefore, an alternative pre-acquisition water suppression technique was applied (*Figure 5.4*).

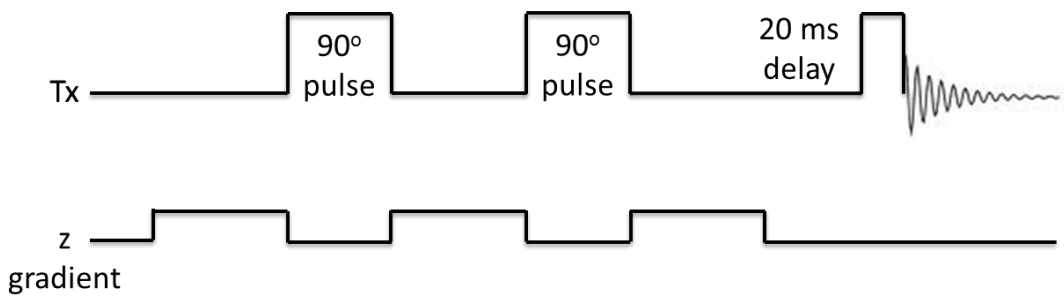

Figure 5.4 *Pulse sequence used for water suppression experiment.*

The pulse sequence used employed a pulse field gradient to remove all transverse magnetisation. A 90° pulse, followed by a second pulse field gradient removed magnetisation perpendicular to the first gradient. This process was repeated again to remove any final artefacts, essentially removing all magnetic polarisation from the system. A 20 ms delay was applied following these gradients, so that only resonances displaying fast relaxation rates could relax significantly, i.e. signals corresponding to the complex and not the solvent water signal. A 10-15° pulse then uniformly excited a wide spectral range. The following acquisition should then show signals corresponding predominantly to the complex and not the solvent. The results are shown in *Figure 5.5*.

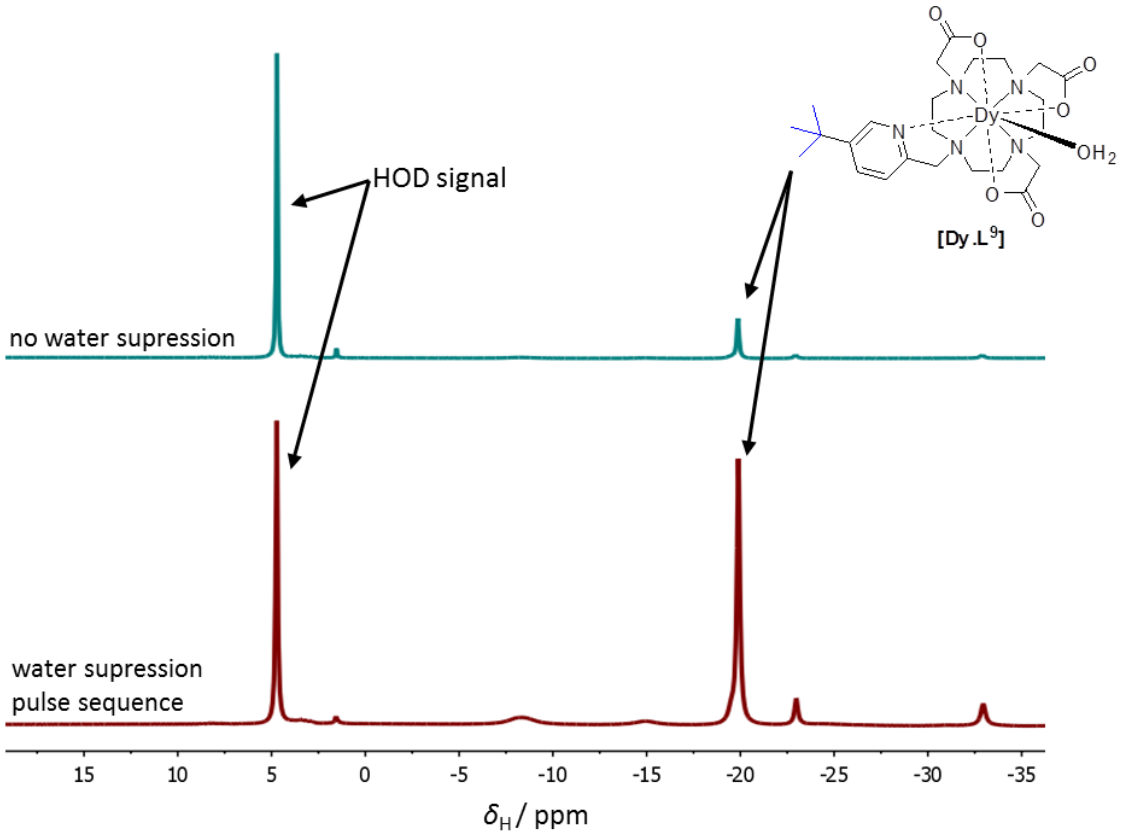

Figure 5.5 *^{1}H NMR spectra of **[Dy.L^9]** before (a) and after (b) application of the water suppression pulse sequence shown above.*

The above spectra showed that the water suppression method was partially successful. The water signal has been significantly attenuated after application of the pulse sequence. However, the solvent resonance has not been removed entirely, as a

proportion of the water resonance can still relax in the short delay time applied. It is also important to remember that, as the complex has a bound water molecule in exchange with the bulk solvent, there is additional relaxation of the water resonance by the paramagnetic Dy(III) ion, increasing the signal intensity. In pure water, the solvent signal would be even more pronounced, and so an alternative method was required.

As the signal of interest is shifted so far away from the water resonance, a seemingly simple solution to remove the solvent peak involves the use of digital filtering, i.e. set the spectral window around the peak of interest to 'cut off' unwanted signals. Advancements in modern NMR spectrometers have made this a feasible prospect, as previously, 'folding' of the water signal into the spectrum would have been observed. In order to test if this concept would work, **[Dy.L^{9}]** was dissolved in H_2O with a capillary insert containing deuterium oxide used to lock the NMR instrument and a standard ^{1}H NMR experiment was run with an increased sweepwidth (*Figure 5.6*).

The resulting spectrum (F*igure 5.6.a*) was dominated by the water signal, so much so that the *tert*-butyl resonance was only observed when the spectrum was blown up considerably. The spectral window was then moved, centred on the peak of interest, and reduced in size. Working at 14.1 T, sweepwidths of 9 kHz (15 ppm) and 2.4 kHz (4 ppm) were examined, and each resulted in successful filtering out of the solvent signal, so that the only resonances observed corresponded to signals arising from the complex (*Figure 5.6.b*). For the smaller sweepwidth, the acquisition time had to be increased slightly in order obtain sufficient data points for processing. However, due to the high intensity and fast relaxation exhibited by the ^{t}Bu signal, the total acquisition time for the resulting spectrum was still only 10 s, using a 2 mM sample at 298 K.

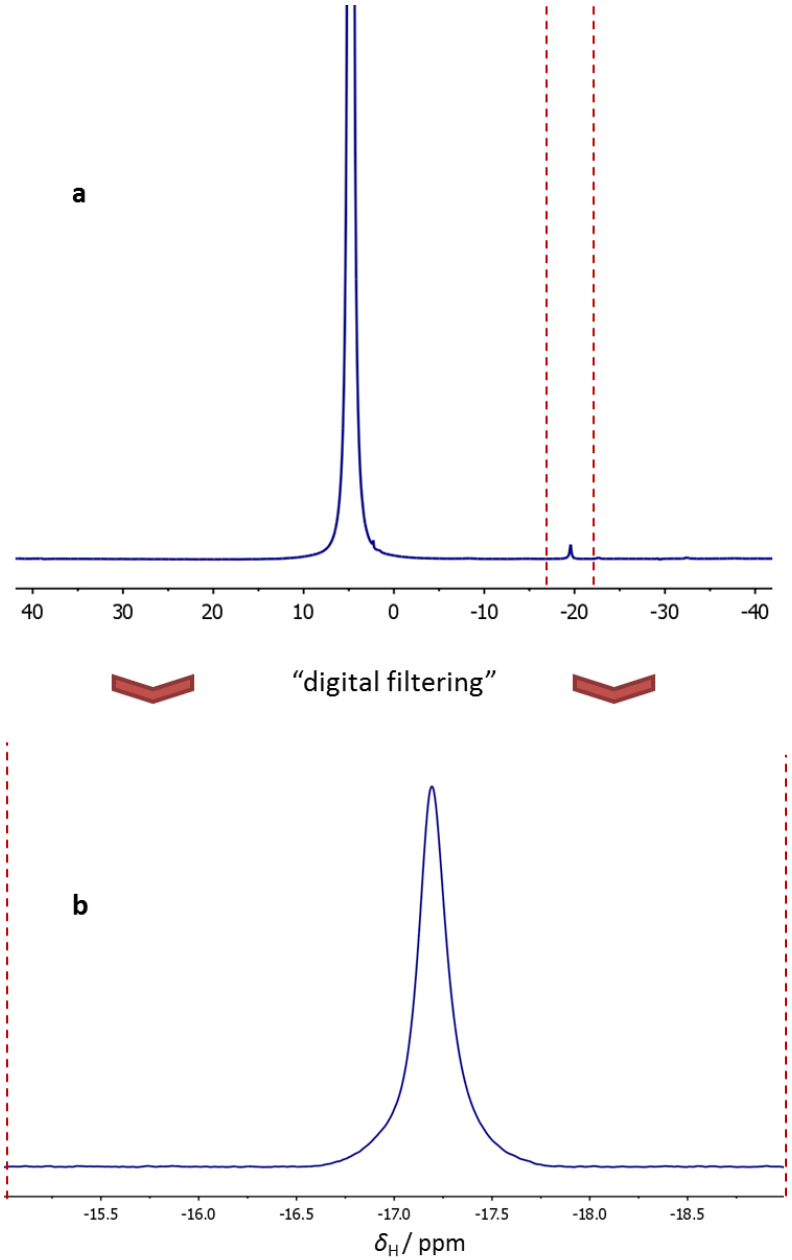

Figure 5.6 *^{1}H NMR spectra of **[DyL^9]** (2mM complex, H_2O, 298 K, 14.1 T). (a) Standard paramagnetic ^{1}H NMR experiment with large sweepwidth. (b) Resulting spectrum acquired after setting the spectral window around the peak of interest as indicated by the red lines in each spectrum (sweepwidth = 2.4 kHz, total acquisition time = 10 s).*

Digital filtering, therefore, seems to be a highly successful method of removing the solvent resonances, to allow selective observation of the signal of interest. It is a fast technique, fairly simple to implement, and should remove other 'background' ^{1}H NMR signals from the spectrum. However, it relies on the resonance of interest being

shifted far enough away from other signals to allow a reasonable sweepwidth to be used, and so would not be possible without the use of paramagnetic complexes, such as these introduced here. Digital filters on MRI instruments are very similar to those found on modern NMR spectrometers, and consequently this technique should be directly applicable in imaging experiments.

5.2.5 Imaging studies

Preliminary imaging studies were carried out at 7 T by Prof. Andrew Blamire at Newcastle Magnetic Resonance Centre. To begin with, the Dy(III) complex was examined, as the combination of higher relaxation rates and the largest shift from the water signal suggested it would have the best characteristics for potential imaging. However, current ^{1}H imaging coils were not designed for resonances outside of the standard ^{1}H NMR spectral shift range (ca. 0-10 ppm), resulting in broad background humps and water signal artefacts appearing outside of this range. This interference prevented any signal being observed for **[Dy.L^{9}]**.

Therefore, the Tm(III) complex was investigated instead. In order to overcome the background signal from the coil, a volume selection method was applied, which is a standard technique used for *in vivo* MRS for removing contamination of the signal from outside of the target region. The sequence used was a "STEAM" (stimulated echo acquisition mode) sequence, that consisted of a single 90^{o} water suppression pulse, followed by two further 90^{o} pulses before acquisitions, with pauses between the pulses related to TE/2 (half the echo time) and TM (the "mixing time"). The three 90^{o} pulses are selective on orthogonal spatial axes, and the result is a stimulated echo arising only from spins at the intersection of the three slices, i.e. a selected volume.

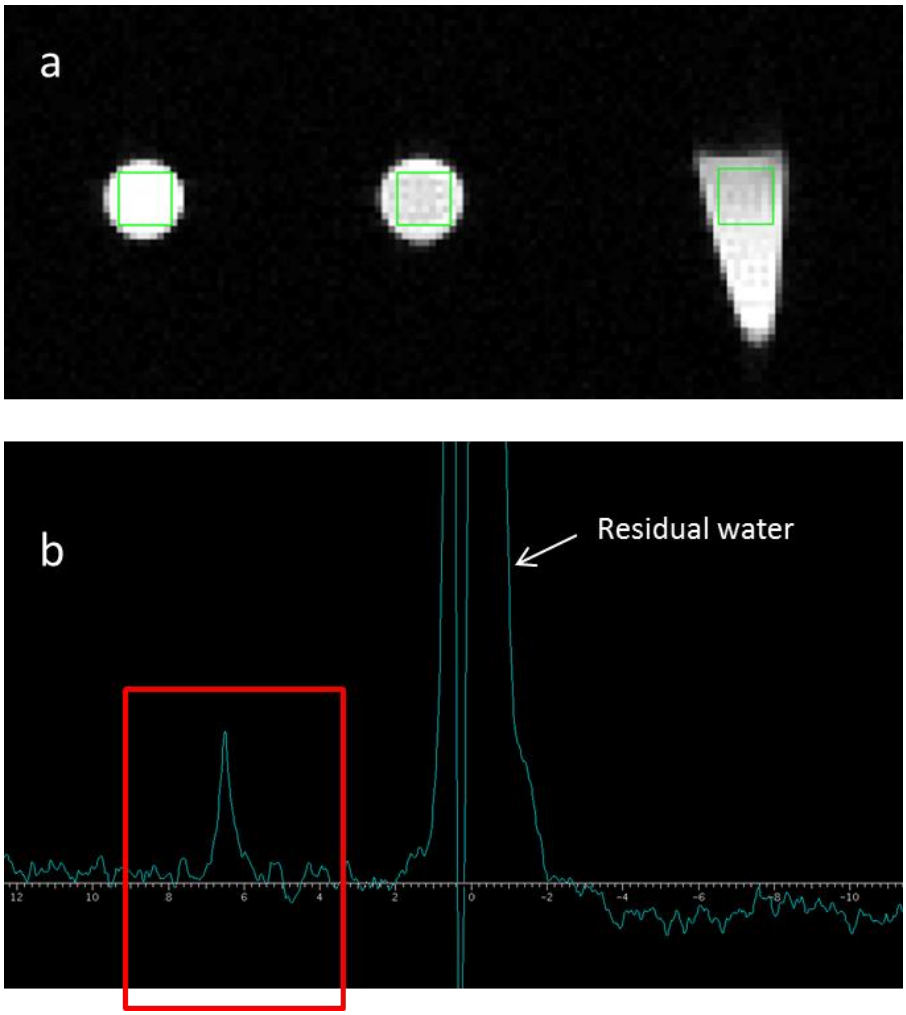

Figure 5.7 *(a) Sample (2 mM* ***[Tm.L^9]****, H_2O) contained in an Eppendorf tube displaying location of the 5x5x5 mm^3 selected volume (green box). (b) STEAM volume selected ^{1}H MRS with single pulse water suppression (7 T, 10 cm diameter volume imaging coil, TR = 82 ms, TE = 2.34 ms, TM = 4.52 ms, sweepwidth = 20.2 kHz, total acquisition time = 5 m 34 s). Resulting ^{t}Bu signal (red box) displays a linewidth of 30 Hz, with a calculated signal to noise ratio of around 10.*

Applying this "STEAM" method, a 5x5x5 mm cube was selected at the top of the sample tube (*Figure 5.7.a*). The section was shimmed, before various combinations of sweepwidth and sample points were trialled, with optimisation of the water suppression carried out each time, and resulted in a reasonable spectrum being obtained from a 5 ½ min acquisition time (*Figure 5.7.b*). The signal obtained was an encouraging start, but there were some limitations with the method used:

(i) The "STEAM" sequence removed the background noise from the coil and allowed a good local shim to be obtained, but the stimulated echo contains only half of the total signal available, i.e. half of the potential signal intensity is lost immediately.

(ii) "STEAM" has an echo time (TE) during which signal is lost by T_2 decay, in addition to signal being lost by T_1 processes during TM.

(iii) The linewidths and shift of this system require water suppression to be applied, rather than setting a small sweepwidth to filter out the water signal.

The results obtained left a lot of room for potential improvements to be made to the system. The data were also collected with a large volume imaging coil (10 cm diameter quadrature birdcage coil), in comparison to the 10 mm solenoid coil used for the previous fluorine imaging work (*Section 3.2.5*). The larger the coil, the lower the sensitivity, and so to acquire a reasonable spectrum from such a large coil was encouraging. Based on the data acquired, it was estimated that a 0.25 mM concentration of this compound could be observed in a 125 µL volume of tissue anywhere in a large animal in around 10 min of scanning, if the signal lost by the "STEAM" sequence (50 %) could be reclaimed.

While these results were promising, the unfamiliar imaging techniques required would be far easier to implement if a higher signal intensity could be generated from the complex. Despite the problems that arose when trying to observe the signal for the Dy(III) complex at -20.5 ppm, imaging of such a resonance should theoretically be possible and have pronounced improvements upon the signal observed thus far. A resonance so far away from the water signal should allow different imaging methods to be employed and larger sweepwidths to be used, as long as the signal can be observed over the background noise from the coil. Therefore, it was decided to redesign the probe in order to increase potential signal intensity, to improve the possibility of the resonance being observed and to allow imaging techniques and parameters to be refined.

5.3 Increasing the Sensitivity

5.3.1 Probe design

During phantom imaging experiments with the monopyridine-based complex, **[Ln.L^{9}]**, it became apparent that, in order to optimise conditions and methods used, an increase in signal intensity would be required. Any increase in signal intensity would obviously also be advantageous when applying the system to *in vivo* studies. Conjugating the complex onto a high molecular weight adduct was considered, in a similar manner to that described for the fluorine systems (*Chapter 3*). However, a more straightforward option was to add a second, equivalent *tert*-butyl group to the complex, hence doubling the signal that can be observed.

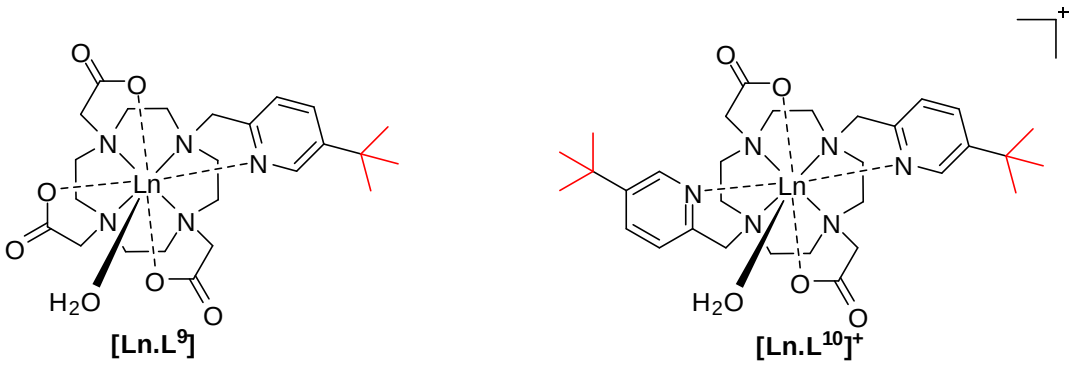

Scheme 5.4 *Comparison between the chemical structure of* ***[Ln.L^{9}]****, and* ***[Ln.L^{10}]$^{+}$****.*

This concept led to the development of the dipyridine-based complex, **[Ln.L^{10}]$^{+}$**. Providing the two *tert*-butyl groups are equivalent in the complex and that the relaxation and shift parameters remain reasonably similar to the previous complex, the resulting ^{1}H NMR signal should be twice as intense. The resulting complex is also monocationic, which may lead to unusual behaviour *in vivo*, compared with related lanthanide complexes previously investigated.

5.3.2 Synthesis and characterisation

The synthesis of **[Ln.L^{10}]$^{+}$** is shown in *Scheme 5.5*, with the mesylated pyridine compound, **84**, being prepared as detailed above. The mesylate was used to dialkylate the secondary amine sites of 1,7-bis(carboxymethyl)-1,4,7,10-tetraazacyclododecane

(DO2A), forming the fully alkylated intermediate, **89**. Fairly mild conditions were used in this alkylation step, as the mono-alkylated intermediate was also desired for later work (*Section 5.4*), resulting in a deceptively low apparent yield for the reaction. The two products were separated by silica gel column chromatography, before the *tert*-butyl ester groups of **89** were cleaved by heating in hydrochloric acid (6 M), to generate the deprotected ligand, $\mathbf{L^{10}}$. It should be noted that, in this case, it was decided to implement HCl for acid hydrolysis over trifluoroacetic acid, as it was hoped that the resulting complexes would be employed for *in vivo* experiments, and the resulting chloride salts should be much better tolerated than the comparable trifluoroacetate salts. The complexation reaction was carried out using an analogous procedure to that described for $\mathbf{[Ln.L^{9}]}$, to generate the desired series of monocationic complexes, $\mathbf{[Ln.L^{10}]^{+}}$.

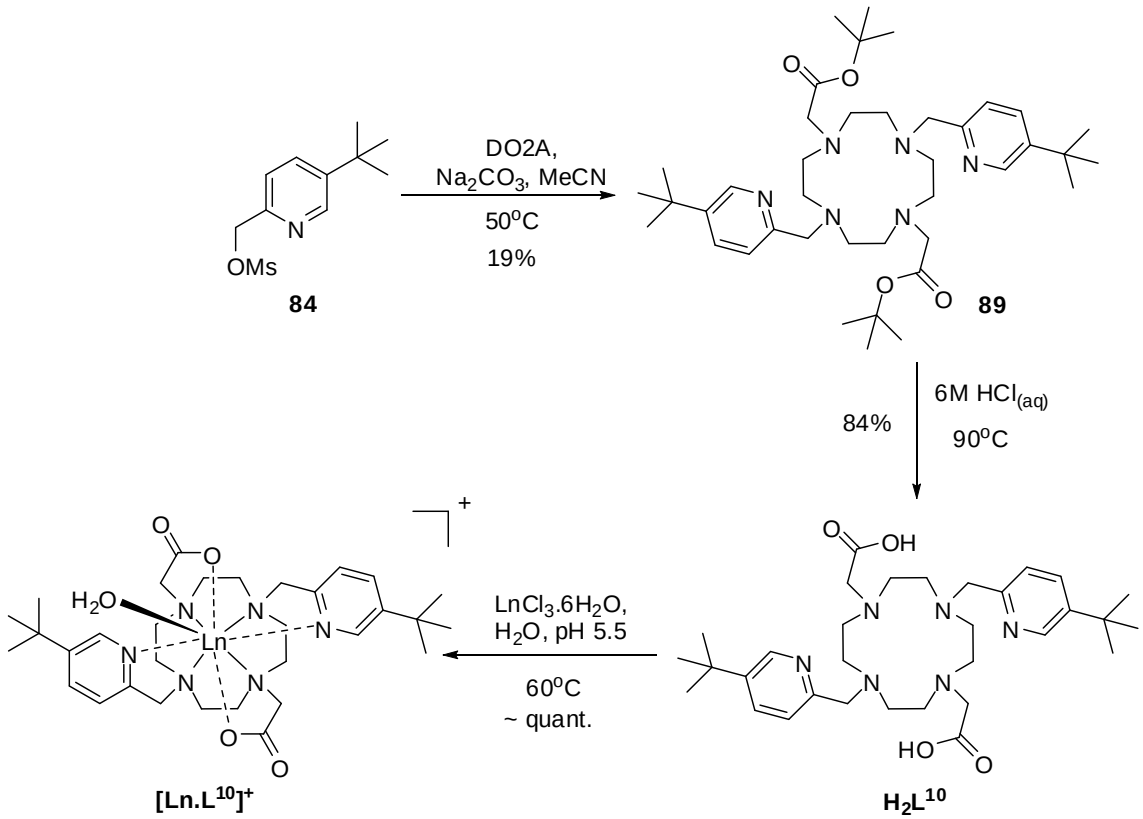

Scheme 5.5 *General procedure for the synthesis of* $\boldsymbol{[Ln.L^{10}]^{+}}$.

The Dy(III) and Tm(III) complexes were again examined, as they display the greatest shifts in each direction and allow direct comparison to the work presented for $\mathbf{[Ln.L^{9}]}$. The Tb(III) and Gd(III) analogues were also synthesised, as the former should display

similar properties in shift to Dy(III) and the latter is useful for MRI tumour uptake studies, using it as a conventional water proton contrast agent. The Tb(III) complex also allows the metal hydration state (q value) to be assessed by measuring the radiative lifetime of the lanthanide excited state, *k*, in both H_2O and D_2O, as described in *Section 4.3*. Values of 0.55 and 0.35 ms^{-1} were recorded experimentally for k_{H_2O} and k_{D_2O} respectively, resulting in a calculated q value of 0.7. This suggests that the complex possesses one bound water molecule, as to be expected with carboxylate based compounds. Again, complexes were characterised by low resolution electrospray and high resolution accurate mass spectrometry.

5.3.3 ^{1}H NMR studies

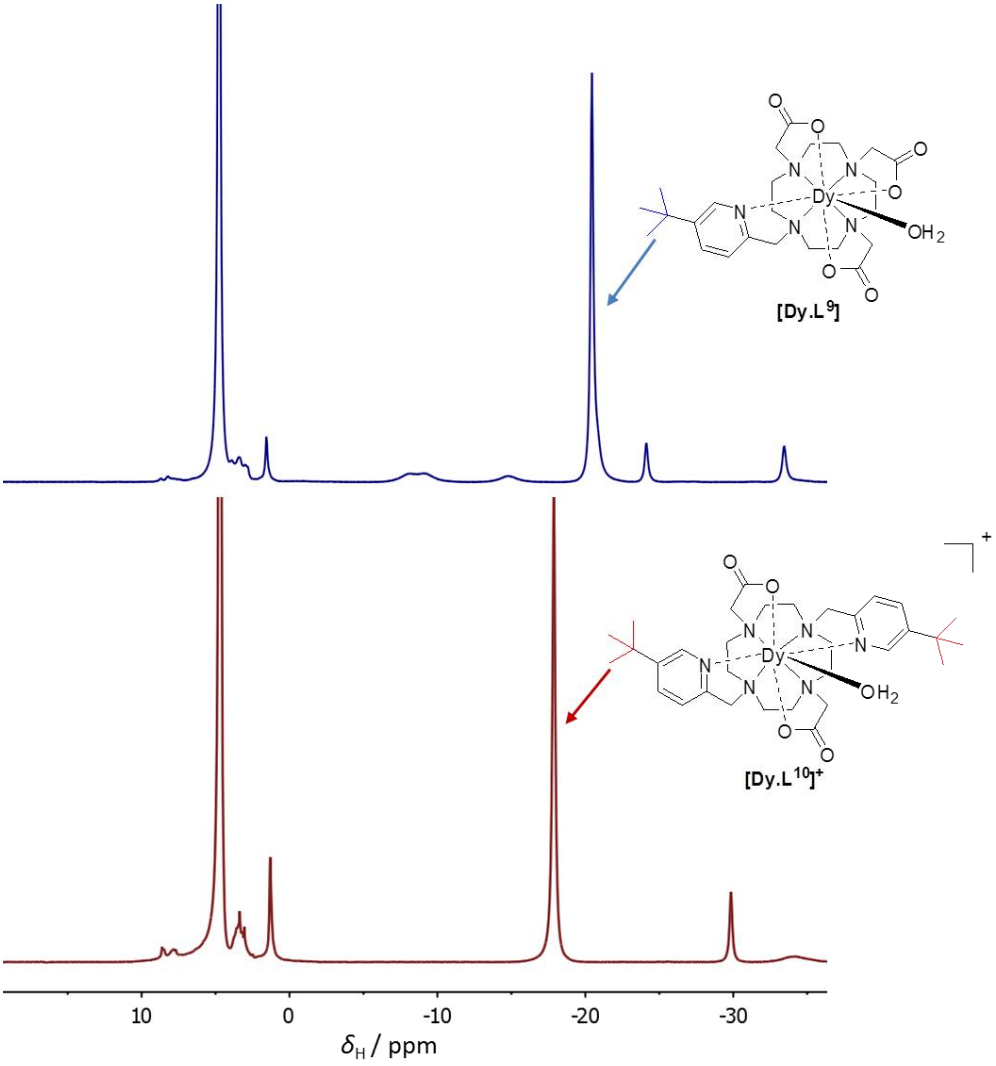

Figure 5.8 *^{1}H NMR spectra (D_2O, 9.4 T, 298 K) of **[Dy.L^9]** (top) and **[Dy.L^{10}]$^+$** (bottom).*

The ^{1}H NMR spectra obtained for **[Ln.L^{10}]$^{+}$** were comparable to those previously observed for **[Ln.L^{9}]**, as can be seen for the dysprosium complexes in *Figure 5.8*. For both the Dy(III) and Tm(III) complexes of **L^{10}**, the shifts were not quite as large as found for **L^{9}**. For **[Dy.L^{10}]$^{+}$**, this is less of an issue as the resonance observed for the *tert*-butyl group was -17.8 ppm, which should be far enough away from the water signal for imaging purposes. However, the shift for same group in **[Tm.L^{10}]$^{+}$** was +6.2 ppm, less than 2 ppm from the water resonance, and it is difficult to separate from signals arising from other biological background compounds. The shift for the Tb(III) complex was observed at -7.2 ppm, which may still be practical for imaging purposes, although at under half the shift of the Dy(III) complex it is unlikely to offer many benefits over the latter lanthanide. The spectrum for the Gd(III) complex was not analysed, due to the magnetic properties of gadolinium resulting in broad, unshifted resonances. No significant isomers were observed in the ^{1}H NMR spectra of the complexes, with one major species (>90%) formed in solution.

The longitudinal relaxation rates were then measured at five fields for the Dy(III), Tb(III), and Tm(III) complexes of **L^{10}** (*Table 5.3*). For **[Dy.L^{10}]$^{+}$**, R_1 was significantly faster than for the analogous mono-pyridine complex, with up to a 60 % increase depending on the magnetic field. For Tm(III), this behaviour was reversed, with a similar decrease in R_1 observed when comparing **[Tm.L^{9}]** to **[Tm.L^{10}]$^{+}$**. Combined with the low shift values obtained, these relatively slow relaxation rates made **[Tm.L^{10}]$^{+}$** unsuitable for imaging application, and so this complex was not investigated further. As for previous systems, global fitting of the longitudinal relaxation rate data to the equation shown in *Figure 5.3* allowed values for the Ln-^{t}Bu distance, *r*, and the rotational correlation time, τ_R, to be calculated as 6.43 ±0.04 Å and 277 ±6 ps respectively. Values for the electronic relaxation rates, T_{1e}, for the individual lanthanide could also be estimated from the fitted data, as shown in *Table 5.3*.

Table 5.3 *^{1}H NMR longitudinal relaxation rate (R_1) data for the tert-butyl resonance of **[Ln.L^{10}]$^+$** at different field strengths (D_2O, 295 K).*

Complex	δ_H / ppm	R_1 / Hz 4.7 T	9.4 T	11.7 T	14.1 T	16.5 T	T_{1e} / ps [(a)]
[Dy.L^{10}]$^+$	-17.8	119 ±0.4	178 ±0.7	203 ±0.6	230 ±0.8	256 ±0.5	0.76 ±0.03
[Tb.L^{10}]$^+$	-7.2	111 ±1.0	152 ±1.0	169 ±1.1	188 ±0.6	207 ±1.9	0.94 ±0.05
[Tm.L^{10}]$^+$	+6.2	21 ±0.3	40 ±0.3	51 ±0.4	59 ±0.3	68 ±0.6	0.20 ±0.06

(a) Calculated by fitting of the longitudinal relaxation rate data (see *Figure 5.X)*.

The longitudinal relaxation rates for the Dy(III) and Tb(III) complexes were similar, and so the relationship between the longitudinal and transverse relaxation rates was investigated (*Table 5.4*). The R_1/R_2 ratios obtained were a significant improvement upon the values calculated for the previous mono-pyridine (**L^9**) complexes (ca. 0.56 at 9.4 T) and were comparable with the values obtained with the best fluorine imaging probes investigated. These ratios were improved further still at lower fields, with values of 0.86 and 0.87 obtained at 4.7 T, for the Dy(III) and Tb(III) complexes respectively.

Table 5.4 *Longitudinal (R_1) and transverse (R_2) relaxation rates and the ratio of the two for the tert-butyl resonances of **[Dy.L^{10}]$^+$** and **[Tm.L^{10}]$^+$** (D_2O, 298 K).*

Complex	4.7 T			9.4 T		
	R_1 / Hz	R_2 / Hz [(a)]	R_1/R_2	R_1 / Hz	R_2 / Hz [(a)]	R_1/R_2
[Dy.L^{10}]$^+$	119	138	0.86	178	223	0.72
[Tb.L^{10}]$^+$	111	128	0.87	152	192	0.79

(a) R_2 values were estimated as ($\pi\omega_{1/2}$), for a Lorentzian line fit.

Such high values were very promising for applications in imaging, as high longitudinal relaxation rates coupled with relatively low transverse relaxation rates serve to increase potential signal intensity, vital for fast acquisition times. While the Tb(III) complex displayed reasonable shift and relaxation rate characteristics, when compared

to the Dy(III) complex there was no advantage in using the terbium system. Therefore, imaging studies focussed upon the use of **[Dy.L^{10}]$^{+}$** only.

5.3.4 Cell studies

Before undertaking imaging studies, it was decided to investigate whether the complex, **[Dy.L^{10}]$^{+}$**, could be utilised for cell labelling. A 100 µM solution of the complex was dissolved in the cell growth medium before being added to a sample of NIH 3T3 cells (4,000,000 cells per experiment, average cell volume 4000 µm^3). The cells were loaded with the complex for 4 h, before the cell growth medium was removed and the remaining cells were washed with pH 7.4 phosphate buffer saline solution (PBS) three times. After removal of this buffer solution, the cells were scraped off the well plate, diluted to a 1 mL final volume with PBS, and sonicated to break up the cell membrane. After sonification for 30 min, the sample was lyophilised, before being dissolved in the minimum volume of D_2O (200 µL) and the ^{1}H NMR acquired (*Figure 5.9*).

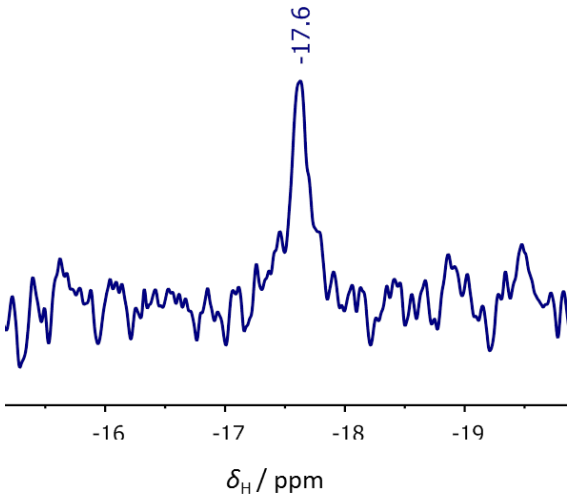

Figure 5.9 *^{1}H NMR spectrum of **[Dy.L^{10}]$^{+}$** loaded onto NIH 3T3 cells (D_2O, 14.1 T, 298 K, total acquisition time = 34 min, SNR = 2.5:1).*

A weak signal can be observed, with a total acquisition time of 34 min and signal-to-noise ratio (SNR) of 2.5:1. As a control, the ^{1}H NMR spectrum of the initially removed

PBS solution was acquired, which resulted in a strong, observable signal after a short acquisition time, with SNR = 22:1 after 26 s. The low intensity signal found for the cell loaded complex suggests that only a small proportion of the compound is permeabilised by the cell, with the rest remaining extracellular and being removed in the PBS washing step. However, for further studies the complex could be functionalised with a group known to efficiently permeabilise cell membranes. Alternatively, systems exist that have been shown to aid delivery of an agent into a cell. This lack of cell permeabilisation is not a limiting factor for further imaging studies, as the vast amount of contrast agents employed are extracellular probes, which are more likely to be cleared easily by the body.

5.3.5 Imaging studies

5.3.5.1 Phantom imaging

Preliminary imaging studies were carried out at 7 T by Prof. Andrew Blamire at the Newcastle Magnetic Resonance Centre using a 2 mM sample of **$[Dy.L^{10}]^{+}$,** contained within a cut-down 5mm NMR tube placed vertically (i.e. 90^{o} to B_0) in the bore of a 30 mm volume birdcage coil. This is the coil generally used for standard mouse MRI experiments. The increase in signal intensity, compared to the previous mono-pyridine complexes, allowed a resonance to be easily observed over the background noise, allowing images to be obtained and not just spectra as was the case in the previous experiment.

By applying a 2D thick slice imaging method, the water signal was observed separately from that of the compound resonance, which was shifted in the image due to the interaction between the imaging gradients and the chemical shift offset. Such splitting of images is commonly seen in clinical MRI as a water to fat shift, as spatial encoding assigns absolute frequency to a point in space. Frequency offset due to the gradient field adds to that ascribed to differences in chemical shift, causing an additional shift. Therefore, despite being in the same point in space, the two signals effectively split

into two separate images. This is useful when investigating techniques to eliminate the water signal, as relative signal intensities can be easily compared by eye.

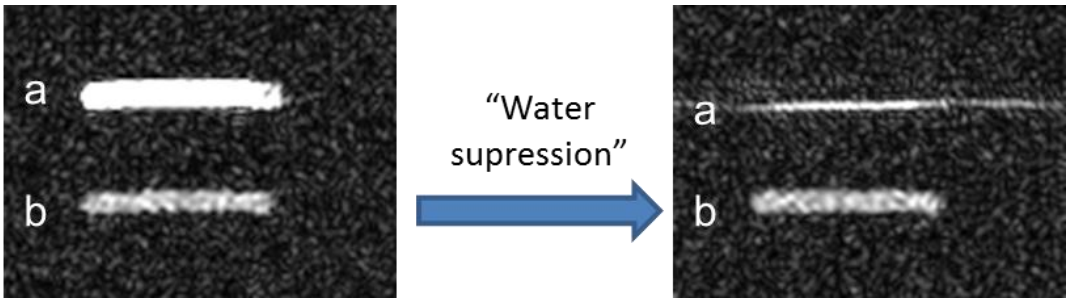

Figure 5.10 *Single slice gradient echo 2D scan (sagittal orientation, 2 mM complex, H_2O, SW = 25 kHz, TR = 30 ms, TE = 2.56 ms) displaying images for: (a) the water signal, (b) the tert-butyl resonance of* ***[Dy.L^{10}]$^+$****. Left-hand image acquired with no water suppression, right-hand image acquired with water suppression applied.*

As in the ^{1}H NMR studies, water suppression was attempted to remove the water signal, and was partially successful (*Figure 5.10*). However, there was an artefact clearly visible, attributed to coherences building from residual transverse magnetisation being acted upon by subsequent RF pulses in the imaging experiment. This process causes the signal to refocus and reappear, resulting in the appearance of the artefact signal. It may be possible to remove such 'left-over' resonances by refining the parameters, but it was decided instead to focus on investigating the effect that changing the sweepwidth (SW) had on the image, as shown in *Figure 5.11*.

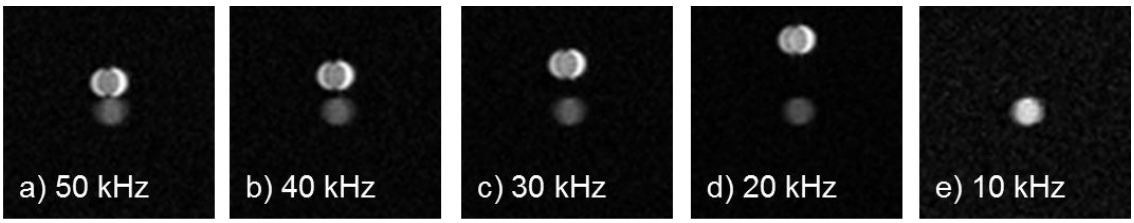

Figure 5.11 *Single slice gradient echo 2D scan (axial orientation, 2 mM complex, H_2O) displaying images for the water signal (top) and the tert-butyl resonance of* ***[Dy.L^{10}]$^+$*** *(bottom). (a-e) Sweepwidth is reduced from left to right as indicated by the SW values given for each scan.*

By centring the spectral window on the peak of interest, i.e. at -17.9 ppm, and reducing the sweepwidth, the water signal can be eliminated from the imaging field of view, although only when the SW was reduced to 10 kHz. This is to be expected, as at 7 T the two resonances are roughly 6.7 kHz apart. Therefore, to entirely eliminate the water signal, the scan must be centred at -17.9 ppm with a SW of less than double this separation. Lower SW values lead to longer acquisition times, and the results may be more complicated when transferred from a model system (small tube) to an extended object (animal). If a system could be developed that displayed an increased shift, this would allow a larger SW to be employed and potentially increase signal intensity. However, this method did allow good quality 3D images to be acquired with optimised parameters (*Figure 5.12*).

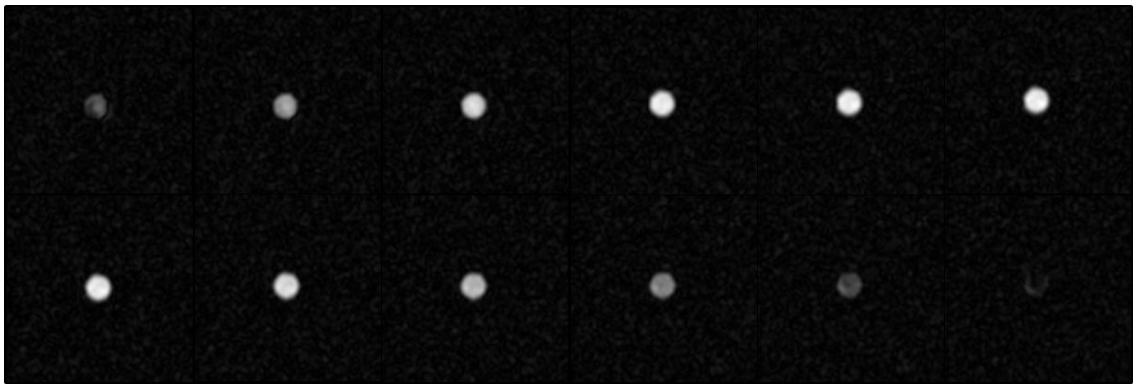

Figure 5.12 *Gradient echo 3D image of the tert-butyl resonance of* ***[Dy.L^{10}]$^{+}$*** *(2 mM complex, H_2O, TR = 10 ms, TE = 2.88 ms, SW = 20 kHz, total scan time = 6 min 19 s).*

From these images, the signal-to-noise ratio (SNR) could be calculated. For a 1x1x1 mm^3 volume, SNR was calculated to be 14, which compares favourably to the value of 9 achieved with the fluorinated glycol chitosan compound, **[Dy.L^3-chitosan]** (*Section 3.2.5*), and is almost 4 times larger than relative values obtained with similar fluorinated compounds that were previously tested.[14] The coil used in these proton imaging studies was also a standard mouse imaging coil, unlike the surface coil used for the fluorine work, which should make the methods refined above more amenable to *in vivo* studies.

5.3.5.2 *In vivo* imaging

Preliminary *in vivo* studies were carried out by Prof. Andrew Blamire and Dr. Ian Wilson, at the Newcastle Magnetic Resonance Centre, on SCID male mice (25 g) with HT29 tumours (human colorectal carcinoma). Measurements were taken 10-14 days after inoculation when tumours were around 10 mm in diameter, with the mouse anaesthetised with oxygen/1-2 % isofluorane. Solutions of **[Gd.L^{10}]$^{+}$** and **[Dy.L^{10}]$^{+}$** were administered to separate mice by intravenous injection in the tail, with each mouse receiving an overall dose of 0.06 mmol kg^{-1} of the respective complex per experiment.

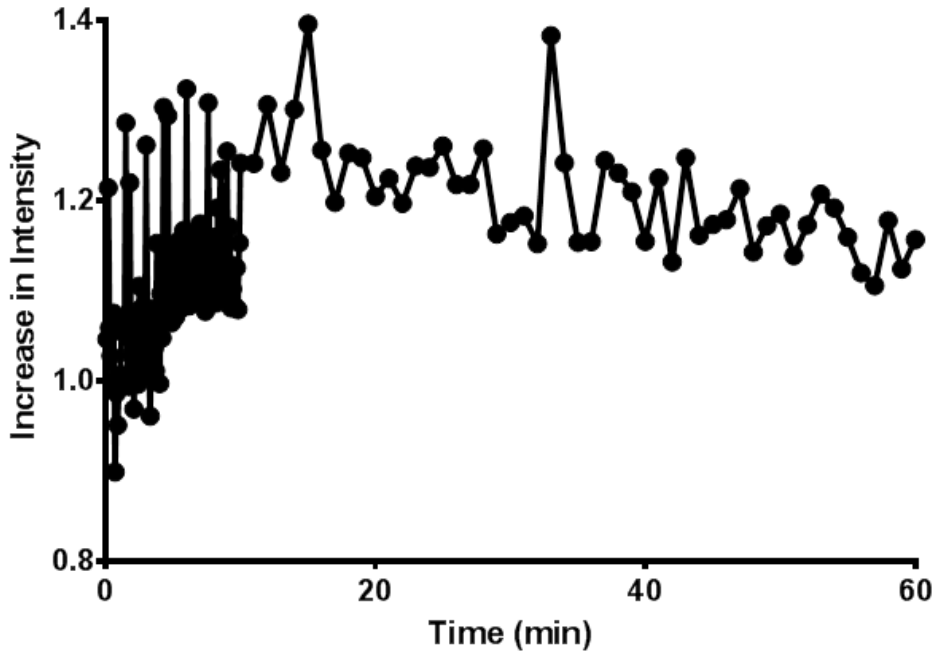

Figure 5.13 *Relative in vivo T_1-weighted ^{1}H MRI water signal intensity within an HT29 tumour on a SCID male mouse as a function of time after intravenous administration of* ***[Gd.L^{10}]$^{+}$****.*

Firstly, standard ^{1}H MRI experiments were run after administration of **[Gd.L^{10}]$^{+}$** using a 39mm birdcage volume coil. A dynamic scan experiment was run using a T_1-weighted sequence, focussing upon a slice containing the tumour. The signal intensity within the tumour was monitored as a function of time after administration of the complex (*Figure 5.13*). Within the first 10-15 min, around a 20 % increase in signal intensity was observed within the tumour, with little variation for the remainder of the experiment

(60 min in total). This level of increase was comparable with standard, commercial contrast agents, and the retention time observed was promising for further studies.

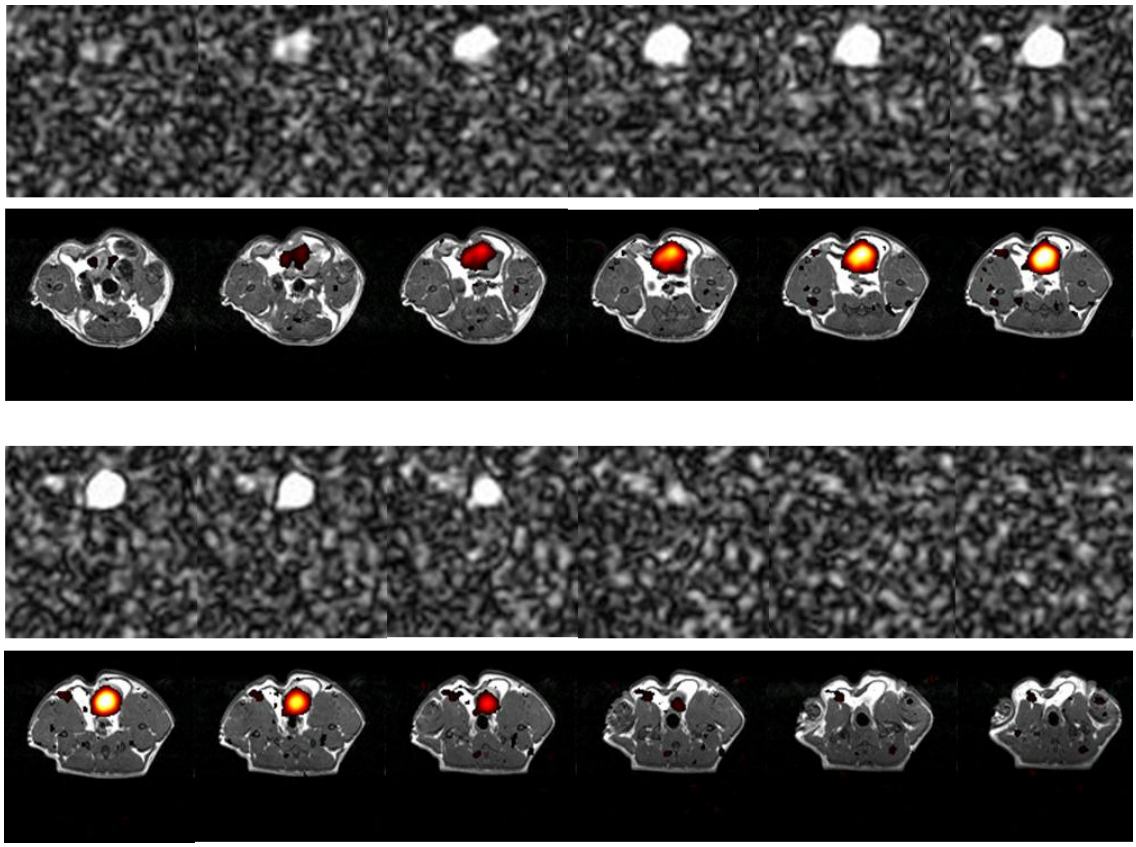

Figure 5.14 *Top rows; Gradient echo 3D sequence ^{1}H MR images obtained examining the ^{t}Bu resonance of* ***[Dy.L^{10}]$^{+}$*** *90 min after intravenous administration to a HT29 bearing SCID male mouse (0.06 mmol kg^{-1} complex, 7 T, TR = 10 ms, TE = 4.39 ms, SW = 5 kHz, total scan time = 5 min 28 s, maximum SNR = 20). Bottom rows; Overlay of above data onto the standard structural ^{1}H MR image.*

After obtaining promising results with the Gd(III) complex, the analogous experiment was run with **[Dy.L^{10}]$^{+}$**, using the same 39 mm birdcage volume coil. Due to the baseline roll generated by water and fat *in vivo*, a signal could not be observed to begin with. However, after refinement of the excitation pulse bandwidth, a strong signal could be observed. However, by the time the signal was observed, 90 min had passed since injection of the compound. Due to the length of time after administration of the complex, the signal could only be observed localised within the

bladder, confirmed by overlaying the sequence of images obtained for the *tert*-butyl resonance onto the standard structural scan (*Figure 5.14*). The excitation pulse was centred upon the resonance of interest (-17.9 ppm) with a 5 kHz sweepwidth, to avoid excitation of the water protons interfering with the image.

While it was unfortunate that the signal was only observed after 90 min, and hence only in the bladder, the acquisition of an image within a live animal was extremely encouraging. The signal was obtained within a relatively short amount of time (5 min 28 s) and the complex was well tolerated by the animal. Further studies are on-going to determine the biodistribution and clearance profile of the complex in the earlier stages of the experiment, before it reaches the bladder. If necessary, the concentration of the complex administered can be easily increased, as the approved dose for standard, related contrast agents is 0.1 to 0.2 mmol kg^{-1}.

5.4 A Responsive Proton CSI System

5.4.1 Probe design

As mentioned throughout this report, the development of responsive magnetic resonance probes is key for increasing the applicability of MRI for diagnosis, therapy, and drug design. Of particular significance are contrast agents that can report on local pH *in vivo*, as changes in pH are associated with various pathologies (e.g. stroke, infection, renal failure). Being able to monitor pH may be particularly important for the diagnosis of cancer, as cancerous tissue is often acidic due to poor perfusion, reduced bicarbonate levels, and increased lactic acid secretion.[15] Mapping of pH is also vital for developing therapies that are effective in regions of altered pH.[16]

The relevance of pH mapping *in vivo* has led to a variety of gadolinium-based contrast agents that respond to changes in pH, some of which are discussed in *Section 1.4.1*. However, for traditional Gd(III) probes, in order to calculate the pH it is necessary to determine the local concentration of the contrast agent, a very difficult task often

requiring the use of a secondary imaging method (e.g. PET, CT).[17] The use of heteronuclear MRI is far more relevant, as changes in pH can be signalled by a change in relative chemical shift, or a change in intensity between two resonances, both of which should be far easier to monitor in an imaging experiment.

These thoughts have led to the development of two forms of lanthanide-based probes within the group that report on variations in pH through changes in the ^{19}F NMR spectrum; one method utilises the protonation equilibrium of an amide bond to adjust the relative angle of the fluorine nuclei with respect to the principal axis of the lanthanide ion,[18,19] the other system is based on the 'on-off' ligation of a sulphonamide moiety.[19,20] This latter method should be possible to incorporate with the pyridine-based systems reported here, by placing a sulphonamide arm at the *trans* position to the pyridyl moiety, leading to the design of the potential pH-responsive chemical shift imaging (CSI) complex, **[Ln.L^{11}]**.

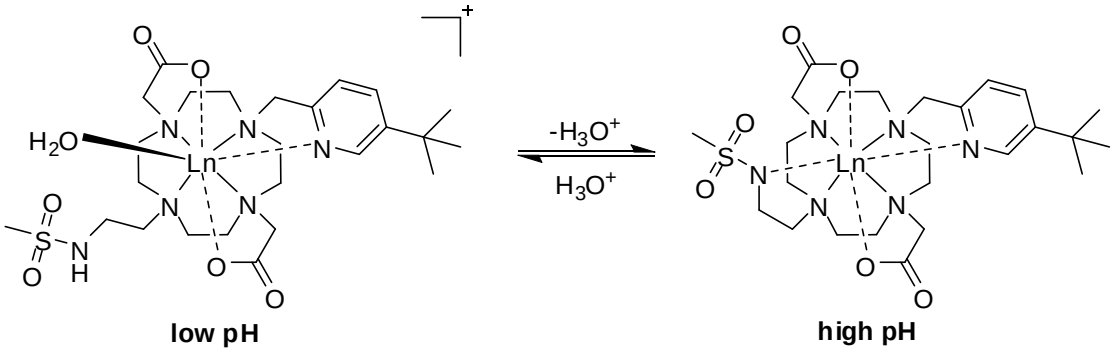

Scheme 5.7 *Design of the pH-responsive probe,* ***[Ln.L^{11}]****.*

As shown in *Scheme 5.7*, the concept of the probe works by variable coordination of the sulphonamide arm. At higher pH, the sulphonamide moiety is deprotonated and bound to the metal ion. As the pH lowers, protonation occurs and the coordination about the lanthanide changes, with the sulphonamide uncoordinated and the inclusion of a water molecule is to be expected to complete the coordination sphere. This change in coordination will affect the ligand field experienced by the Ln(III) ion, which in turn should affect the ^{1}H NMR shift of the *tert*-butyl resonance. By changing the

lanthanide ion complexed, other methods should also be available for monitoring pH, e.g. Gd(III) allows relaxivity measurements, Tb(III) for emission profiles.

5.4.2 Synthesis and characterisation

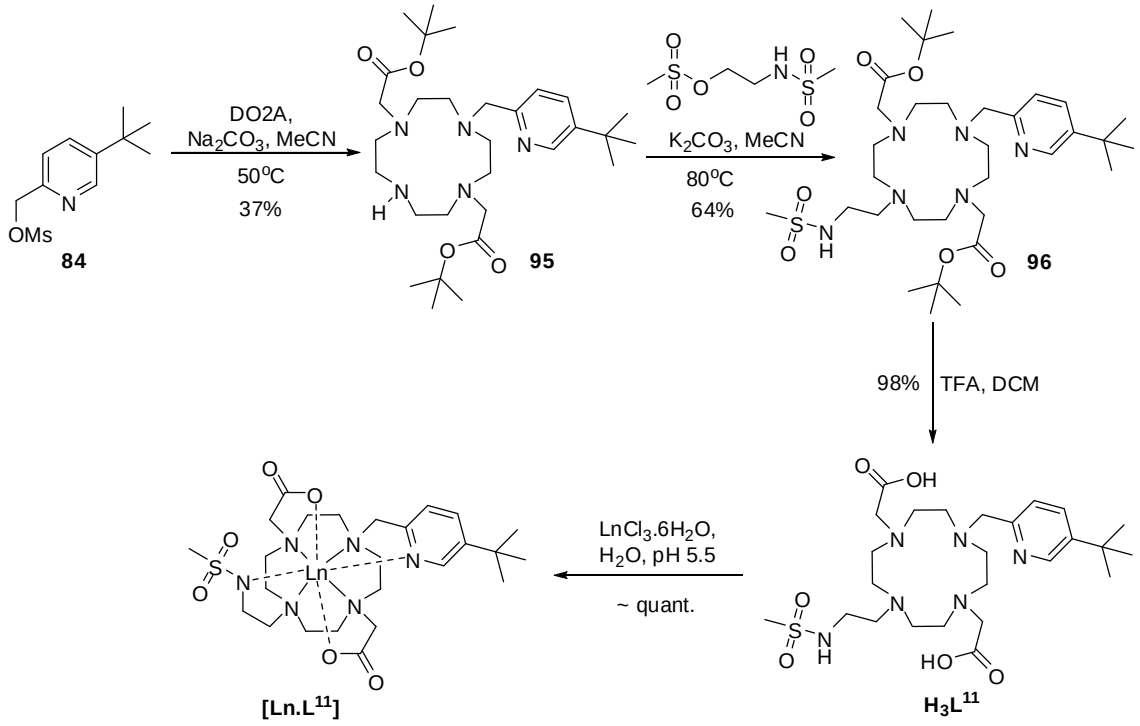

Scheme 5.8 *General procedure for the synthesis of* ***[Ln.L^{11}]****.*

The synthesis of **[Ln.L^{11}]** is shown in *Scheme 5.8*. The mono-pyridine compound, **95**, was formed in the same reaction as the di-pyridine compound, **89**, described for the synthesis of **[Ln.L^{10}]$^{+}$**. The desired compound was isolated by silica gel column chromatography, before alkylation with *N*-methanesulfonylaziridine (generated *in situ*) was performed by heating in acetonitrile with potassium carbonate added as a base. The fully substituted product, **96**, was purified by silica gel column chromatography. Deprotection of the *tert*-butyl ester groups was carried out using trifluoroacetic acid, to form the ligand, **L^{11}.** The lanthanide complexes were obtained in the usual manner, by reaction with $LnCl_3.6H_2O$ at pH 5.5.

Complexes were characterised by low resolution electrospray and high resolution accurate mass spectrometry. The metal hydration state (q value) was assessed at high and low pH by measuring the radiative lifetime of the lanthanide excited state, *k*, of the Tb(III) complex in both H_2O and D_2O, as described in *Section 4.3*. At pH 8, values of 0.47 and 0.42 ms^{-1} were recorded experimentally for k_{H_2O} and k_{D_2O} respectively, resulting in a calculated q value of 0.05. At pH 4, however, k_{H_2O} and k_{D_2O} were found to be 0.69 and 0.43 ms^{-1}, respectively, giving a q value of 1.0. This suggests that there are no waters bound to the Ln(III) ion at higher pH values, when the sulphonamide arm is deprotonated and coordinated to the metal. As the pH lowers, the sulphonamide nitrogen is protonated and is no longer coordinated. This leads to a space in the coordination sphere of the Ln(III) ion, allowing a water molecule to bind to the complex.

5.4.3 ^{1}H NMR studies

The chemical shifts attributed to the *tert*-butyl resonance of the complexes were far greater than anticipated, as shown in *Figure 5.15*. Significant increases were observed for each lanthanide, with around a 40 ppm gain in shift non-equivalence, when compared to the previous complexes investigated. The chemical shifts were observed at +44.3 ppm for the ^{t}Bu group in **[Tm.L^{11}]** and at -58.9 ppm in **[Dy.L^{11}]**. These unprecedentedly large shifts were promising for further studies, as an increased shift from the water signal allows a larger bandwidth to be used in imaging experiments, increasing the signal intensity that can be obtained per unit time. The major isomer for the Tm(III) complex seemed to account for around 80 % of the overall signal, with the *tert*-butyl signal for the minor species resonating at +28.1 ppm. The methyl substituent of the sulphonamide arm appeared to resonate as one major signal at +52.7 ppm, assigned by relative integral values. Previous studies have shown that such species arise from coordination isomers *via* each oxygen at the stereogenic S centre of the sulphonamide arm.[19]

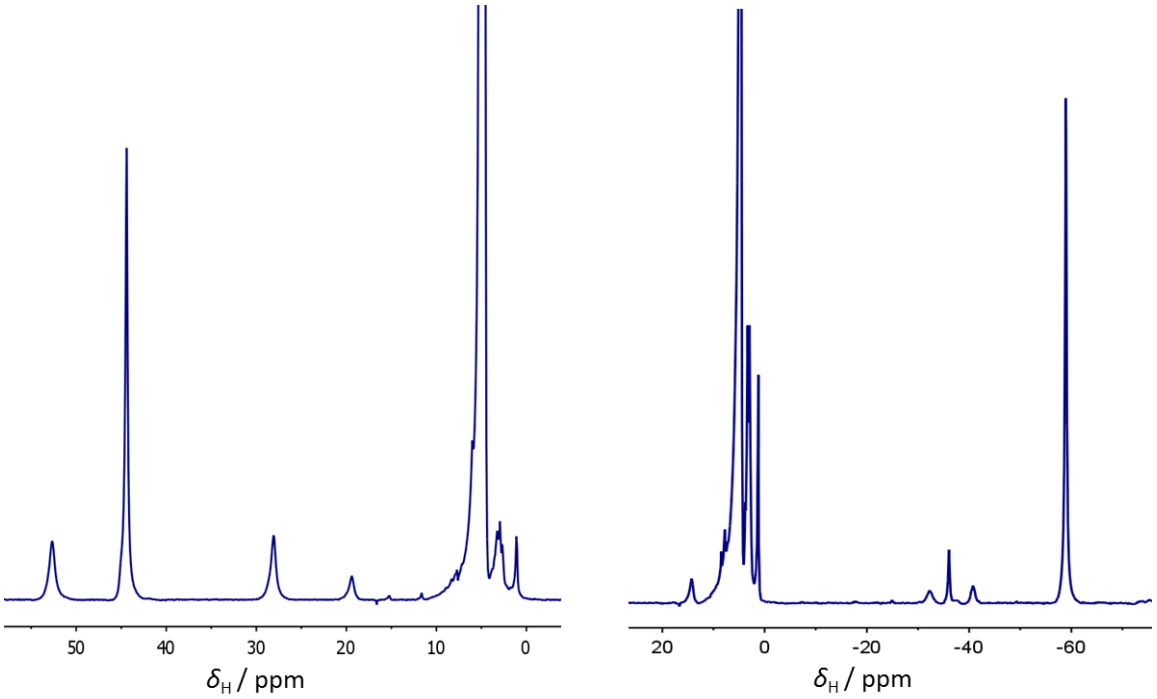

Figure 5.15 *^{1}H NMR spectra (D_2O, 9.4 T, 298 K, pD 8.5) for* ***[Tm.L^{11}]*** *(left) and* ***[Dy.L^{11}]*** *(right).*

Longitudinal relaxation rate, R_1, data were obtained for each complex at various magnetic field strengths (*Table 5.5*). The R_1 values calculated were more comparable with those obtained for **[Ln.L^{9}]** than for **[Ln.L^{10}]$^{+}$**, suggesting the two compounds may adopt a similar structure. The rates below for the dysprosium complex are significantly slower than for the relevant bis(pyridine) complex, which may result in a comparative loss of signal intensity in imaging experiments. Fitting of the longitudinal relaxation rate data was again undertaken, as described in *Section 5.2.3*, leading to the values of the electronic relaxation rate, T_{1e}, given in *Table 5.5*. Global fitting of all the data for the three complexes of **L^{11}** allowed average values of the rotational correlation time, τ_R, and the Ln(III)-^{t}Bu distance, r, to be estimated, as 214 ±8 ps and 6.57 ±0.04 Å respectively.

Table 5.5 *^{1}H NMR longitudinal relaxation rate (R_1) data for the tert-butyl resonance of **[Ln.L^{11}]** at different field strengths (D_2O, 295 K, pD 8.5).*

Complex	δ_H / ppm	R_1 / Hz					T_{1e} / ps [(a)]
		4.7 T	9.4 T	11.7 T	14.1 T	16.5 T	
[Dy.L^{11}]	-58.9	74 ±0.3	113 ±1.1	137 ±1.6	160 ±1.5	185 ±1.6	0.67 ±0.04
[Tb.L^{11}]	-55.8	63 ±0.7	89 ±1.1	108 ±0.7	123 ±1.2	139 ±1.0	0.74 ±0.04
[Tm.L^{11}]	+44.3	40 ±3.4	60 ±1.7	77 ±0.4	89 ±0.2	101 ±0.3	0.34 ±0.03

(a) Calculated by fitting of the longitudinal relaxation rate data (see *Figure 5.3)*.

The ratio of the longitudinal (R_1) and transverse (R_2) relaxation rates for the complexes of **L^{11}** were measured and compared (*Table 5.6*). For imaging purposes, a value as close to one as possible is ideal, as this allows fast acquisition whilst keeping line broadening to a minimum. However, for **[Ln.L^{11}]** the values obtained are low, especially in comparison to the values obtained for the complexes of **L^9** (≥ 0.56) and **L^{10}** (≥ 0.72). The smaller values of R_1/R_2 for this system may offset any potential signal gain arising from the increased shift of the sulphonamide complexes.

Table 5.6 *Longitudinal (R_1) and transverse (R_2) relaxation rates and the ratio of the two for the tert-butyl resonances of **[Dy.L^{11}]**, **[Tb.L^{11}]**, and **[Tm.L^{11}]** (D_2O, 298 K, 9.4 T).*

Complex	4.7 T			9.4 T		
	R_1 / Hz	R_2 / Hz [(a)]	R_1/R_2	R_1 / Hz	R_2 / Hz [(a)]	R_1/R_2
[Dy.L^{11}]	74	260	0.28	113	380	0.30
[Tb.L^{11}]	63	182	0.35	89	518	0.17
[Tm.L^{11}]	40	225	0.18	60	305	0.20

(a) R_2 values were estimated as ($\pi\omega_{1/2}$), for a Lorentzian line fit.

5.4.4 pH Dependent behaviour

The data for **[Ln.L^{11}]** presented above were collected above pH 8, as the ^{1}H NMR signal was strongest at these values. As the pH lowered, the resonance observed decreases in intensity until no signal can be observed around pH 4 (*Figure 5.16*). Over this pH range, there was no observable shift in the signal, nor was there an obvious appearance of a new, shifted resonance associated with the protonated form of the complex.

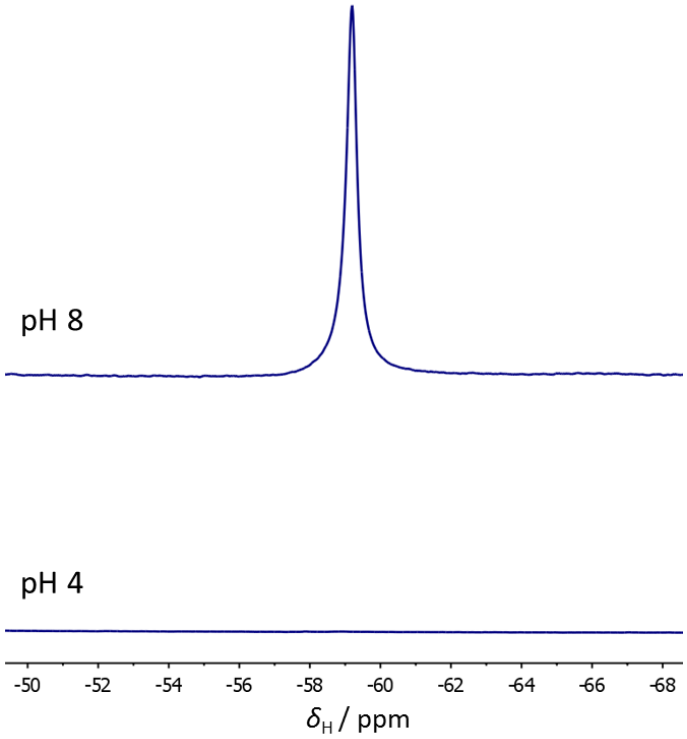

Figure 5.16 *^{1}H NMR spectra for **[Dy.L^{11}]** at high and low pH values indicating 'loss of signal' at low pH (2 mM complex, D_2O, 9.4 T, 298 K, total acquisition time = 2 min 13 sec).*

It is hypothesised that the major signal observed (e.g. -58.9 ppm for **[Dy.L^{11}]**) corresponds to the deprotonated form of the complex, which is fairly rigid in structure with little exchange occurring due to the fully coordinated nature of the complex. As the pH lowers, the sulphonamide arm becomes protonated and no longer coordinates to the lanthanide ion, resulting in a new signal associated with the ^{t}Bu group. However, as the protonated form of the sulphonamide is no longer bound to the metal, a significant increase in the rate of chemical exchange is experienced by the complex, both in terms of the "on-off" mechanism of the arm and with increased

interaction with solvent molecules. The increase in chemical exchange experienced leads to severe linewidth broadening, resulting in no signal being observed at low pH values. Such severe chemical exchange broadening is similar to the behaviour observed earlier with **[Tm.L^2]** (*Chapter 2*).[21]

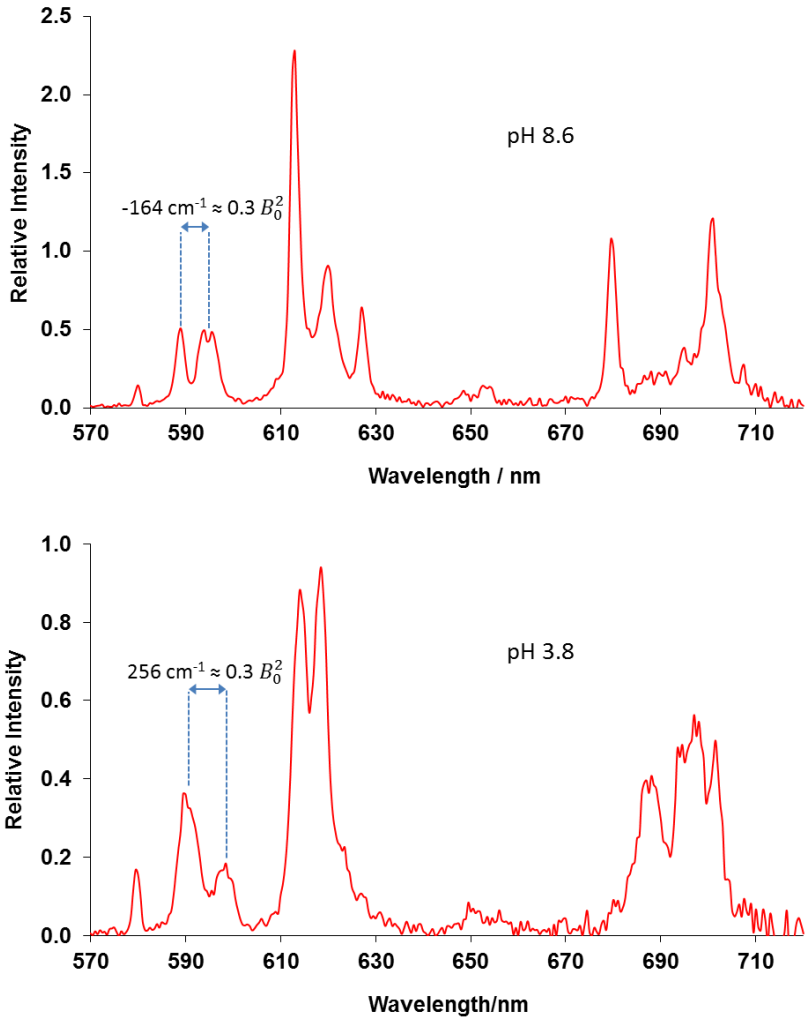

Figure 5.17 *Eu(III) emission spectra for* ***[Eu.L^6]*** *at pH 8.6 and 3.8 (H_2O, 298 K, λ_{exc} = 270 nm).*

In order to better understand the shift behaviour of **[Ln.L^{11}]**, the europium emission spectra were obtained at pH 4 and 8 (*Figure 5.17*). As introduced in the previous chapter, the splitting in the Δ*J* = 1 band is proportional to the second order ligand field term (Δ*J* = 1 splitting ≈ 0.3 B_0^2), which, in turn, is associated with the magnitude of the pseudocontact shift as described by Bleaney.[10] Therefore, the splitting of the Δ*J* = 1 band was measured at high and low pH, from which B_0^2 values were calculated to be -550 and +850 cm^{-1} respectively. The value obtained at pH 8.6 (-550 cm^{-1}) was

comparable to the value obtained for **[Eu.L^{6}]**, which also displayed a similarly large NMR chemical shift. The value obtained at pH 3.8 (+850 cm^{-1}) suggests that the broadened signal is even more shifted than for the high pH form, and may be shifted in the opposite direction, due to the change in sign. However, other ligand field terms, e.g. B_2^2, may also alter with pH, and the NMR spectra may not be directly proportional to the B_0^2 values calculated. The geometric terms associated with the pseudocontact shift, i.e. the angle and the distance, should remain relatively constant due to the pyridine moiety remaining unchanged upon protonation/deprotonation.

The 'loss of signal' observed as the pH was lowered made quantification of the pH response more challenging, as it was not possible to measure pH by monitoring a change in shift or as a function of the intensity of corresponding "acid-" and "base-form" resonances of the complex directly, as has been applied in previous examples.[18,19] In *Chapter 2*, an external reference (trifluoroethanol) was used to quantify a similar system, whereby the ^{19}F NMR signal for one of the forms of the complex, **[Tm.L^{2}]**, was exchange broadened and unobservable. The use of an external reference is also technically possible for use with the pH study of **[Ln.L^{11}]** by ^{1}H NMR spectroscopy. However, due to the nature of the shifted resonance being investigated, and the desire to carry out spectroscopic and imaging studies without interference from background signals, standard reference compounds are not suitable as they resonate too closely to solvent and other background peaks.

In order to circumvent this problem, it was recognised that the mono-pyridine DO3A complex, **[Ln.L^{9}]**, would make a useful external reference for this system, as it exists as predominantly one signal, with similar relaxation parameters to **[Ln.L^{11}]**, and by design is shifted out of the way of any background signals. It is also almost 40 ppm away from the signal of interest, and so will not interfere with analysis of the pH responsive behaviour. Most importantly, the resonance for **[Ln.L^{9}]** does not change with pH, allowing a fixed standard against which the intensity of the pH responsive resonance of **[Ln.L^{11}]** can be compared.

The dysprosium complexes were considered to be the most suitable for this investigation, due to the relatively large shifts present in each complex. Therefore, the relevant Dy(III) complexes of **L**[9] (1 mM) and **L**[11] (2 mM) were dissolved in the same NMR tube, and ^{1}H NMR spectra were obtained at a variety of pH values (*Figure 5.18*). Above pH 6.5, there was no change in the relative signal intensities observed. As the pH was lowered, the relative intensity of the **[Dy.L**[11]**]** resonance (-58.9 ppm) decreased in comparison to the intensity of the **[Dy.L**[9]**]** resonance (-20.5 ppm), which remained at a constant level throughout the experiment. Below pH 4, only the latter resonance could be observed. The ratio of intensities of the two signals was plotted as a function of pH, allowing a pK_a of 5.27 ±0.04 to be calculated. The behaviour observed was fully reversible.

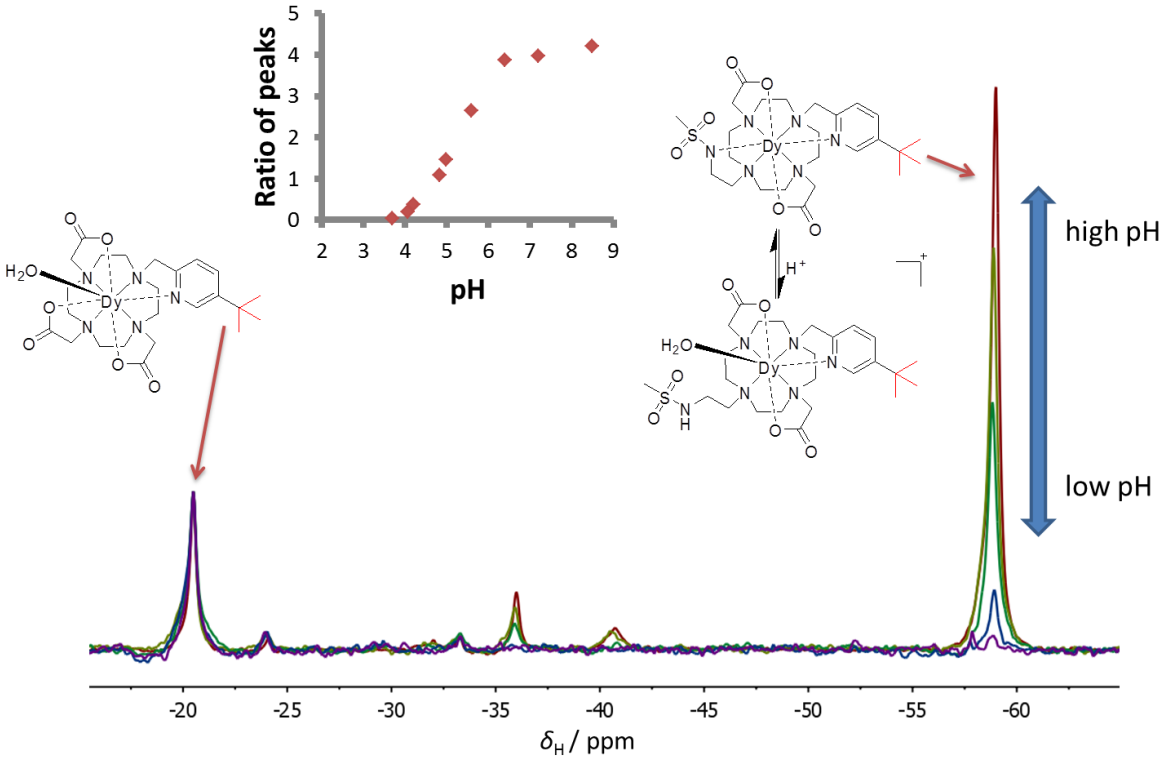

Figure 5.18 *^{1}H NMR spectra at a range of pH values (1 mM* ***[Dy.L**[9]**]**, *2 mM* ***[Dy.L**[11]**]**, *D_2O, 0.1 M NaCl, 9.4 T, 298 K). Inset shows plot of the ratio of signal intensities as a function of pH, with a calculated pK_a of* 5.27 ±0.04.

Further studies were required in order to verify the above observations. By substituting the lanthanide ion in the complex, other forms of analyses become

available with the same complex. Firstly, by using terbium, the intensity and form of the emission spectrum can be analysed as a function of pH (*Figure 5.19*). When the terbium emission spectrum of **[Tb.L^{11}]** was monitored with varying pH, a decrease in intensity was observed, accompanied by a slight change in spectral form. As the protonation equilibrium is associated with a change in hydration state (q), a significant decrease was expected with lowering of pH due to the increase in quenching processes that occurs with an increase in q. By plotting the intensity of the ΔJ = 1 band as a function of pH, a response curve could be generated with an associated pK_a value of 5.09 ±0.07, in good agreement with the data obtained from the ^{1}H NMR spectroscopic studies. Again, the observed behaviour was fully reversible.

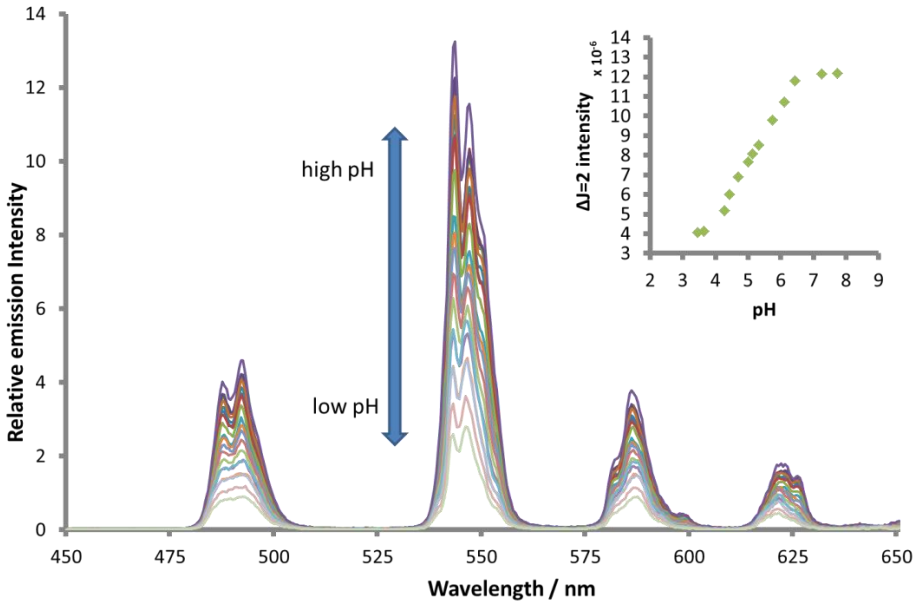

Figure 5.19 *Tb(III) emission spectra at varying pH and accompanying fit of the ΔJ = 1 band as a function of pH for* ***[Tb.L^{11}]****, with a calculated pK_a of* 5.09 ±0.07 *(H_2O, 0.1 M NaCl, 298 K, λ_{exc} = 270 nm).*

Similarly, by using gadolinium as the lanthanide ion in the same complex, the relaxivity of the system can be measured as a function of pH. As the hydration state changes from 0 to 1 as the pH is lowered, there was expected to be a corresponding increase in relaxivity due to a rise in the contribution of the inner sphere term. Such a change was observed when measuring the relaxivity of an aqueous solution of **[Gd.L^{11}]** over the relevant pH range (*Figure 5.20*). By plotting the relaxivity value as a function of pH, a

value of 4.86 ±0.12 could be calculated for the pK_a. This was again in fairly good agreement with the previous studies.

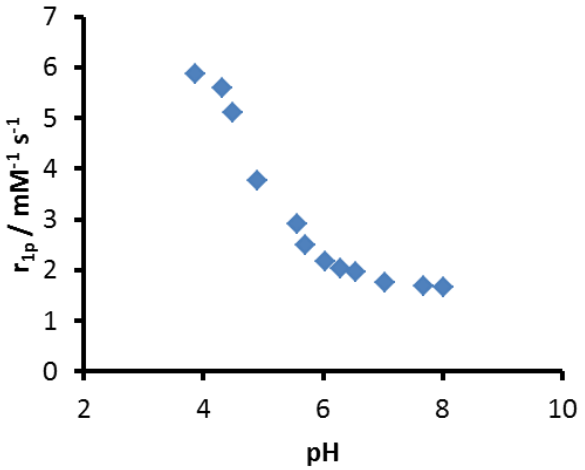

Figure 5.20 *Variation of water proton relaxivity with pH for an aqueous solution of* ***[Gd.L^{11}]****, with a calculated pK_a of 4.86* ±0.12 *(1mM complex, H_2O, 0.1 M NaCl, 1.4 T, 310 K).*

5.4.5 Temperature dependent behaviour

The majority of related ^{1}H NMR probes have focussed on applications as temperature sensors. Therefore, it was decided to investigate the temperature dependence of the *tert*-butyl resonance of **[Dy.L^{11}]**. The dysprosium complex was chosen as it displays the largest shift of the complexes investigated, and so should display the largest variation in chemical shift with increasing temperature for the complexes presented here. Therefore, the ^{1}H NMR chemical shift of the *tert*-butyl resonance was recorded at different temperature values over a range of 25 K.

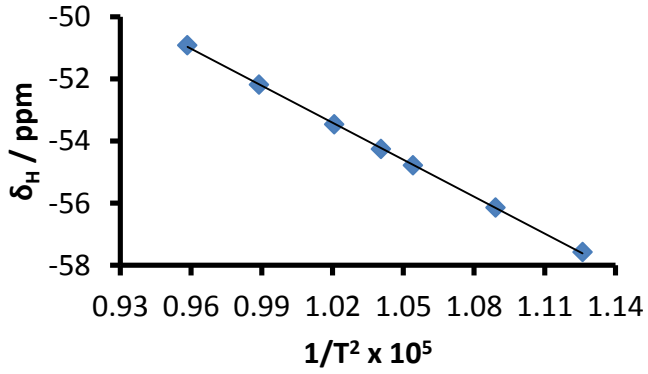

Figure 5.21 *Variation in the tert-butyl resonance of* ***[Dy.L^{11}]*** *as a function of $1/T^2$ (D_2O, 14.1 T, 0.27 ppm K^{-1}).*

Over the temperature range investigated, there was around a 7 ppm variation in the chemical shift observed. A linear fit can be generated by plotting δ_H as a function of the inverse square of the temperature (*Figure 5.21*), allowing the temperature to be calculated from the chemical shift value. The lack of an internal reference within the complex would make calibration difficult, particularly with regards to *in vivo* studies. The rate of change, 0.27 ppm K^{-1}, is also lower than the fluorinated probes presented in the previous chapter and other previously reported compounds,[8] although should still be significant enough for potential applications. The prospect of simultaneous temperature and pH reporting with one compound is particularly intriguing. This concept has been presented previously,[7] but no other pH responsive probe possesses such a high intensity ^{1}H NMR signal. Most examples examine the shifts of four equivalent proton nuclei, rather than nine protons as reported here. However, further studies would be required to overcome the issues of internal calibration, for both the pH and temperature responsive behaviour, before the system could be applied to *in vivo* experiments.

5.4.6 Imaging studies

Imaging studies were carried out with the dysprosium complex, **[Dy.L^{11}]**, due to the increased chemical shift and enhanced relaxation rates in comparison to the other Ln(III) ions. As discovered through the ^{1}H NMR analyses of the compounds, the shift for the *tert*-butyl resonance of **[Dy.L^{11}]** was considerably larger than the corresponding resonance of **[Dy.L^{10}]$^+$**, with values of -58.9 and -17.8 ppm respectively. This should allow a larger sweepwidth (SW) to be used in the imaging experiment, potentially increasing the signal intensity available. However, the longitudinal relaxation rate (R_1) of **[Dy.L^{10}]$^+$** is significantly faster than that for **[Dy.L^{11}]**, whereas the opposite is true for the transverse relaxation rate (R_2). This may serve to offset any gain attained by using a larger SW, as signal intensity increases with increasing R_1 and decreases with increasing R_2. Simulations suggest that the sensitivity ratio of the two complexes should be 1.42, in favour of **[Dy.L^{10}]$^+$**.

Therefore, a comparative imaging study was carried out at 7 T by Prof. Andrew Blamire at the Newcastle Magnetic Resonance Centre using separate 2 mM samples of **[Dy.L^{10}]$^{+}$** and **[Dy.L^{11}]** contained within cut-down 5mm NMR tubes placed vertically in the bore of a 30 mm volume birdcage coil. The compounds were initially run individually, to optimise the different parameters (TR, TE, flip angles, etc.), based on the relaxation rates of each complex, in addition to achieving efficient separation from the water signal. The two samples were then run at the same time, using alterations in these parameters and excitation frequencies to selectively image the resonances, in turn, for the water signal, **[Dy.L^{10}]$^{+}$**, and **[Dy.L^{11}]** (*Figure 5.22*).

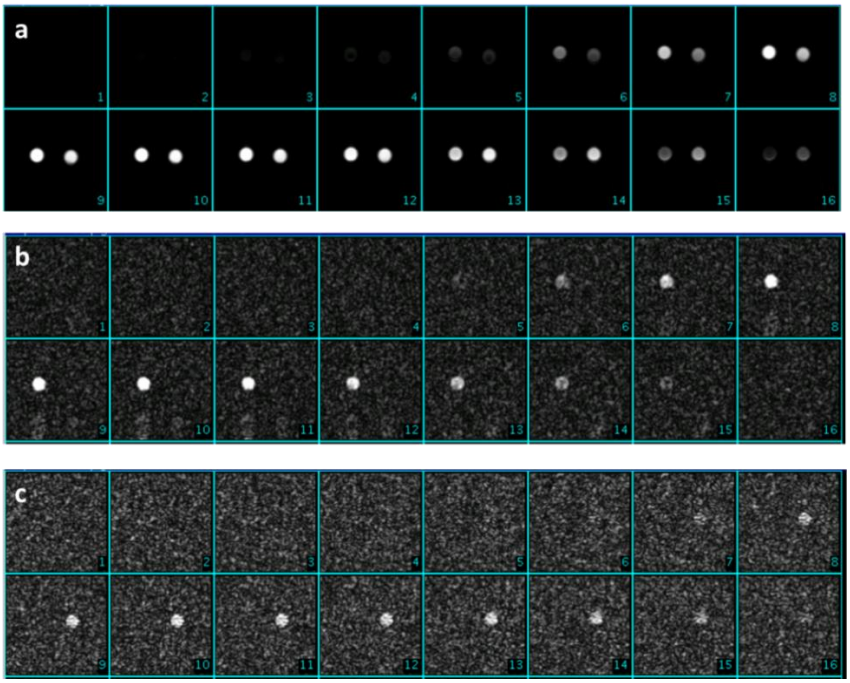

Figure 5.22 *Gradient echo 3D sequences (7 T, 298 K, H_2O, 2 mM **[Dy.L^{10}]$^{+}$**, left; 2 mM **[Dy.L^{11}]**, right) of two samples loaded into a 30 mm Birdcage imaging coil. (a) Water signal (tof = - 351 Hz, TR = 30 ms, TE = 2.21 ms, 8^{o} flip, 1 average), (b) **[Dy.L^{10}]$^{+}$** ^{t}Bu resonance at -17.8 ppm (tof = -7,077 Hz, TR = 8.62 ms, TE = 4.24 ms, 74^{o} flip, SW = 10 kHz, 10 averages, total acquisition time = 1 min 28 sec), (c) **[Dy.L^{11}]** ^{t}Bu resonance at -58.9 ppm (tof = -19,582 Hz, TR = 5.21 ms, TE = 2.24 ms, 52^{o} flip, SW = 17.8 kHz, 16 averages, total acquisition time = 1 min 25 sec).*

Using this frequency selective excitation pulse method allowed each resonance to be observed independently, by only exciting the peak of interest. For **[Dy.L^{10}]$^{+}$**, the calculated signal-to-noise ratio (SNR) was a factor of 1.20 higher than for **[Dy.L^{11}]**, comparable to the value predicted (1.42), due to the differences in the relaxation rates

between the two complexes. However, in order to completely remove the water signal, the imaging spectral bandwidth (i.e. the sweepwidth) must be smaller in magnitude than the shift difference between the solvent peak and the resonance of interest. Therefore, for **[Dy.L^{11}]**, the large shift separation allowed the use of a 20 kHz SW at 7 T.

However, the closer proximity of **[Dy.L^{10}]$^{+}$** to the water signal necessitated a much smaller excitation bandwidth to be employed, as the shift difference was only around 5.4 kHz. For the images above the SW for **[Dy.L^{10}]$^{+}$** was set at 10 kHz, which is clearly larger than this separation value. As the object is small, there were no major problems with this SW, although some residual water breakthrough was observed. When applied to an extended object (e.g. an animal), interference would have been far more significant, which is why a SW of 5 kHz was used for the *in vivo* experiment with **[Dy.L^{10}]$^{+}$** (*Section 5.3.5.2*). Such a low value for the SW was not ideal, due to the R_2 loss caused by the required longer RF pulse. An ideal probe would combine the properties of the two complexes; i.e. the highly shifted nature of **[Dy.L^{11}]** to facilitate removal of the water signal, with the more advantageous relaxation rates experienced by **[Dy.L^{10}]$^{+}$**.

For the imaging experiments carried out above, the **[Dy.L^{11}]** sample was maintained at pH 8, in order to maximise the signal obtained. However, it was also of interest to investigate the behaviour of this signal at variable pH values. Therefore, an experiment was designed that was similar to the ^{1}H NMR study carried out in *Section 5.4.4*, whereby a non-pH sensitive complex, **[Dy.L^{9}]**, would be used as an internal reference with which to compare the pH responsive signal of **[Dy.L^{11}]**. An equimolar mixture of **[Dy.L^{9}]** and **[Dy.L^{11}]** was dissolved in 0.1 M sodium chloride and the solution divided into four cut-down NMR tubes. The pH of these four solutions was adjusted to different values, covering the range over which the signal intensity was observed to change (pH 4-7). These four samples were then imaged, comparing the relative intensities of the *tert*-butyl resonances for each complex. The results of this study are shown in *Figure 5.23*.

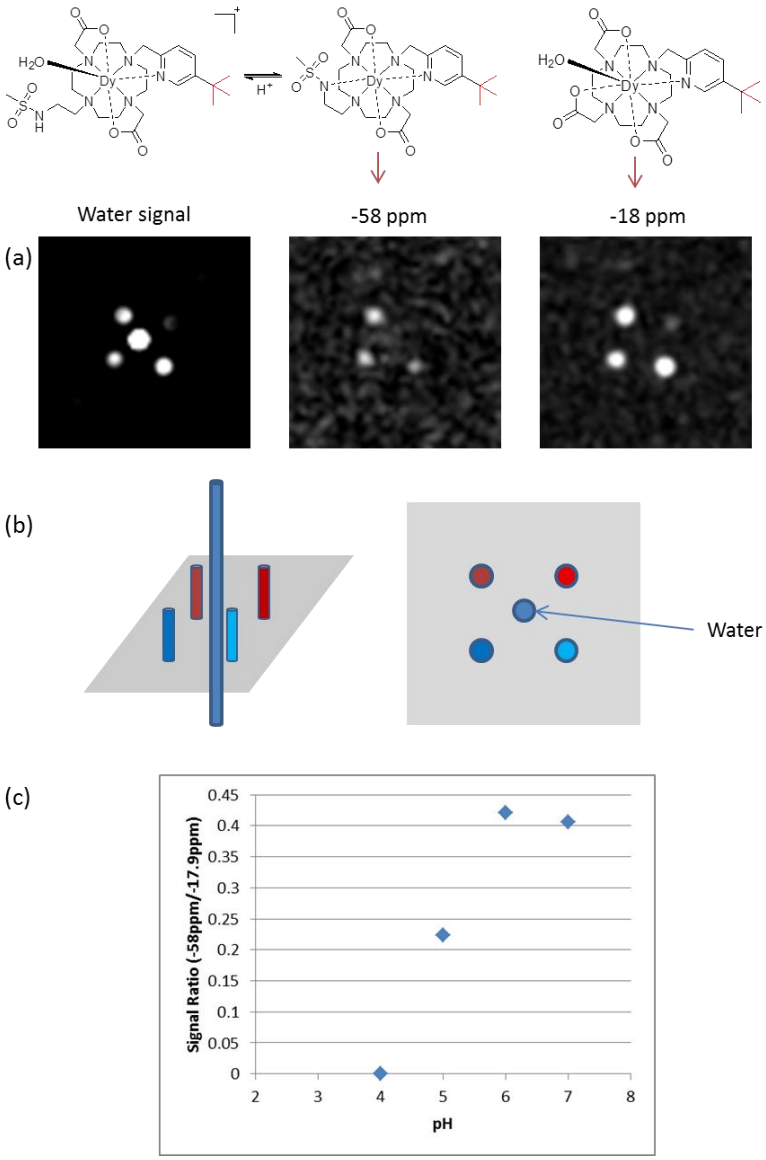

Figure 5.23 *(a) GE3D images acquired of the signals corresponding to (from left to right) water,* ***[Dy.L^{11}]****, and* ***[Dy.L^{9}]*** *(sweepwidth = 5 kHz, acquisition time = 4 min 6 s); (b) illustration of the experimental array used; (c) variation of the ratio of the* ***[Dy.L^{11}]:[Dy.L^{9}]*** *signal intensities as a function of pH (2 mM* ***[Dy.L^{9}]****, 2 mM* ***[Dy.L^{11}]****, 0.1 M NaCl, 7 T, 298 K, H_2O) .*

While there are too few data points for an accurate pK_a determination, the pH plot obtained from this imaging experiment closely resembles the curves generated from the previous NMR, luminescence, and relaxivity investigations. The experiment is a good proof-of-principle study, showing the correlation between ^{1}H NMR based work and imaging methods. It would be of interest to take this concept further, with enough data points for full analysis.

5.5 Conclusions and Future Work

The use of paramagnetic lanthanide ions to shift proton resonances outside of the standard diamagnetic ^{1}H NMR frequency range has been periodically of interest over the last twenty years, as shown by the examples highlighted at the beginning of this chapter. However, while some promising initial *in vivo* studies have been carried out, there have been some limitations with signal intensity, leading to long acquisitions or high dosages being required. These limiting factors have seemingly left this field of research lagging behind somewhat, in comparison to the more popular area of heteronuclear imaging, despite the many advantages of using a highly shifted proton resonance over, for example, a comparable fluorine signal.

The results presented here appear to go some way to bridging this gap, with encouraging preliminary imaging results. The complexes formed were, however, designed from the knowledge gained from the fluorine imaging work previously investigated. From the CF_3 containing systems, a great deal was learnt on the development of probes with the required characteristics. Initially, work focussed on the ideal positioning of the reporter group with respect to the lanthanide ion, both in terms of the separation distance and the relative angle formed that lead to relaxation rates of the desired magnitude and large ligand field splittings. This latter term was of particular importance for the proton work, as the largest ligand field splitting possible is required to shift the resonance of interest away from background signals, hence why the model proton probe was based on the fluorine systems that displayed the highest shifts, i.e. the pyridyl-based complexes. A great deal has also been learnt through previous studies and applied here on methods to minimise chemical exchange broadening effects, and hence increase signal intensity, which is a limiting feature of some of the previously reported systems.

The strong *in vivo* image collected upon the injection of **[Dy.L^{10}]$^{+}$** was particularly encouraging, despite being observed only in the bladder, as the signal was acquired within a clinically acceptable time and dose (5 min 28 s, 0.06 mmol kg^{-1}). By considering the fluorine results once more, a potential system becomes apparent for

future studies to improve further *in vivo* experiments. In the previous chapter, the phosphinate based complex, **[Ln.L^{6}]**, displayed ^{19}F NMR shifts that were almost double the magnitude compared to those observed for the comparative carboxylate complex, **[Ln.L^{7}]**, due to a change in the coordination sphere about the Ln(III) ion and the effect this has on the ligand field splitting parameters. The CF_3 and ^{t}Bu compounds have so far behaved in a relatively similar manner and, if the phosphinate analogues of both **[Ln.L^{9}]** and **[Ln.L^{10}]$^{+}$** (*Scheme 5.9*) follow this same trend, it may be possible to significantly increase the shift of the *tert*-butyl resonances observed, with around -35 to -40 ppm hypothesised for the Dy(III) complexes. If this was indeed the case, it would allow larger sweepwidths to be employed for imaging protocols, resulting in increased signal intensities to be observed, as the relaxation rates should remain relatively unchanged.

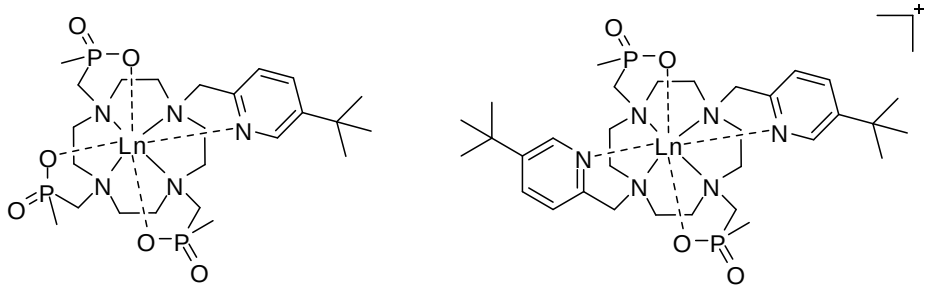

Scheme 5.9 *Potential phosphinate analogues of **[Ln.L^{9}]** and **[Ln.L^{10}]$^{+}$**.*

The pH-responsive behaviour of **[Ln.L^{11}]** shows good promise, but a few issues need to be addressed in order to make the system more applicable for *in vivo* studies. For the current system to be of use, it is necessary to have a method of calibrating the local signal intensity. For *in vitro* experiments, this is not an issue, as a second complex can be added at a known concentration and the relative signal intensities of the two complexes compared. However, for *in vivo* studies the measuring of the signal intensity is more problematic. If another complex was added to the animal system simultaneously, for it to work in the same way the two compounds would require identical biodistribution profiles, which clearly is unlikely with a significant change in structure. A potential solution could be to link the two complexes together, leading back to the work presented in *Chapter 3*. If both complexes were altered with a linking group attached to the pyridyl moiety, then it would be possible to covalently couple

them both to the same adduct, e.g. glycol chitosan. As long as the comparative proportions of each complex were known before injection, which can easily be verified by ^{1}H NMR spectroscopy, the signal intensities of the two complexes should allow mapping of pH, as the relative local concentrations will be known.

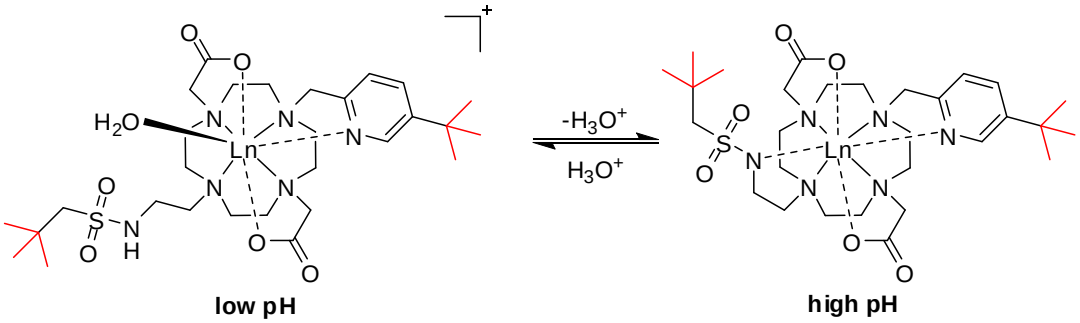

Scheme 5.10 *Alteration of sulphonamide arm to develop a system with two separate pH-dependent ^{t}Bu signals (highlighted in red).*

Another factor that needs to be addressed is the pK_a associated with the protonation equilibrium of the sulphonamide arm, which needs to be raised to around 7 to make the system more relevant to physiological pH values. It may be the case that this fortuitously occurs in biological media, as has been found with related compounds.[22] Therefore, pH studies need to be performed in a mixed background of various analytes and proteins, followed by serum to understand the potential behaviour of the system *in vivo*. Alternatively, the methyl subtituent of the sulphonamide could be altered to a different moiety, changing the associated pK_a value. A related compound has recently been developed within the group that incorporates a *tert*-butyl substituted sulphonamide arm, allowing pH to be monitored by the variation in chemical shift of this ^{t}Bu moiety. It would be of interest to combine the two systems, as shown in *Scheme 5.10*, as this would allow two separate signals of equal intensity to be used as markers for pH dependence. The signal for this sulphonamide ^{t}Bu complex has been observed at low pH, and so may also offer more information on the behaviour of the pyridine based system under acidic conditions.

5.6 References

1. S. Aime, M. Botta, M. Fasano, E. Terreno, P. Kinchesh, L. Calabi, and L. Paleari, *Magn. Reson. Imaging*, 1996, **35**, 648–651.

2. S. Aime, M. Botta, L. Milone, and E. Terreno, *Chem. Commun.*, 1996, 1265–1266.

3. T. Frenzel, K. Roth, S. Koßler, B. Radüchel, H. Bauer, J. Platzek, and H.-J. Weinmann, *Magn. Reson. Med.*, 1996, **35**, 364–369.

4. K. Roth, G. Bartholomae, H. Bauer, T. Frenzel, S. Kossler, J. Platzek, and H.-J. Weinmann, *Angew. Chem. Int. Ed.*, 1996, **35**, 655–657.

5. S. K. Pakin, S. K. Hekmatyar, P. Hopewell, A. Babsky, and N. Bansal, *NMR Biomed.*, 2006, **19**, 116–124.

6. Y. Yang, D. T. Schühle, G. Dai, J. K. Alford, and P. Caravan, *Contrast Media Mol. I.*, 2012, **7**, 276–279.

7. D. Coman, H. K. Trubel, R. E. Rycyna, and F. Hyder, *NMR Biomed.*, 2009, **22**, 229–239.

8. M. Milne and R. H. E. Hudson, *Chem. Commun.*, 2011, **47**, 9194–9196.

9. T. W. Bell, L. Y. Hu, and S. V. Patel, *J. Org. Chem.*, 1987, **52**, 3847–3850.

10. B. Bleaney, *J. Magn. Reson.*, 1972, **8**, 91–100.

11. S. Aime, M. Botta, M. Fasano, M. P. M. Marques, C. F. G. C. Geraldes, D. Pubanz, and A. E. Merbach, *Inorg. Chem.*, 1997, **36**, 2059–2068.

12. H. Gysling and M. Tsutsui, *Adv. Organomet. Chem.*, 1971, **9**, 361–395.

13. K. H. Chalmers, M. Botta, and D. Parker, *Dalton Trans.*, 2011, **40**, 904–913.

14. K. H. Chalmers, PhD Thesis, Durham University, 2011.

15. R. A. Gatenby and R. J. Gillies, *Nat. Rev. Cancer*, 2004, **4**, 891–899.

16. H. Adrogué and N. Madias, *N. Engl. J. Med.*, 1998, **338**, 26–34.

17. E. Que and C. Chang, *Chem. Soc. Rev.*, 2010, **39**, 51–60.

18. P. K. Senanayake, A. M. Kenwright, D. Parker, and S. K. Van Der Hoorn, *Chem. Commun.*, 2007, 2923–2925.

19. A. M. Kenwright, I. Kuprov, E. De Luca, D. Parker, S. U. Pandya, P. K. Senanayake, and D. G. Smith, *Chem. Commun.*, 2008, 2514–2516.

20. K. H. Chalmers, E. De Luca, N. H. M. Hogg, A. M. Kenwright, I. Kuprov, D. Parker, M. Botta, J. I. Wilson, and A. M. Blamire, *Chem. Eur. J.*, 2010, **16**, 134–148.

21. P. Harvey, K. H. Chalmers, E. De Luca, A. Mishra, and D. Parker, *Chem. Eur. J.*, 2012, **18**, 8748–8757.

22. R. Pal and D. Parker, *Chem. Commun.*, 2007, 474–476.

6. Experimental

6.1 Experimental Procedures

6.1.1 General Procedures

Commercially available reagents were used as received from suppliers. PAMAM dendrimer, ethylenediamine core, generation 1.0, was obtained as a 20 % solution in MeOH and the solvent was removed under reduced pressure immediately prior to use. 2-Methanesulphonate-*N*-methanesulphonylethylamine was prepared by Dr. Kanthi Senanayake following previously reported procedures.[1] Solvents were laboratory grade and dried using an appropriate drying agent when required. Water was purified by the 'Purite$_{STILL}$plus' system, with a conductivity of ≤ 0.04 μS cm^{-1}. Reactions requiring anhydrous conditions were carried out under an atmosphere of argon using Schlenk-line techniques. Where necessary, solvents were degassed using the freeze-thaw cycle method.

Thin-layer chromatography was carried out on silica plates (Merck Art 5554) or neutral alumina plates (Merck Art 5550) and visualised under UV irradiation (254 nm), or by staining with either iodine or Dragendorff's reagent (solution of bismuth nitrate and potassium iodide in AcOH and H_2O). Preparative column chromatography was carried out using silica (Merck Silica Gel 60, 230-400 mesh) or neutral alumina (Merck Aluminium Oxide 90, activity II-III, 70-230 mesh), with the latter pre-soaked in ethyl acetate overnight before use. Syringe filtration was carried out using Phenex™ PTFE membrane syringe filters (0.45 μm, 25 mm, Phenomenex®) and Millex® low protein binding hydrophilic LCR PTFE membrane syringe driven filter units (0.45 μm, 4 mm, Millipore®).

Anion exchange chromatography was performed using anion exchange resin DOWEX® 1x8 200-400 mesh Cl (Sigma Aldrich). Typically, the resin (1 g) was prepared by boiling in MeOH (50 mL) for 18 h, followed by washing with H_2O (500 mL). The resin was then stirred in $HCl_{(aq)}$ (1 M, 50 mL) for 2h then washed with H_2O until the resulting washing

were neutral pH. Suction dried resin was then added to solutions of the complex in H_2O for 2 h. Filtration and lyophilisation yielded the desired chloride salts of the complex.

Dialysis was performed with Dialysis Tubing Cellulose Membrane MWCO 550 D (Sigma Aldrich), Spectra/Por Dialysis Membrane MWCO 1,000 D (Spectrum Laboratories, Inc), or Float-A-Lyzer G2 filters MWCO 5,000 D (Spectrum Laboratories, Inc). All tubing was washed thoroughly with H_2O, as per manufacturer's advice. After addition of the complex to the tubing, the ends of the tubing were secured (clamps for the membranes, provided screw top for the filters) and the ensemble submerged in stirring H_2O (ca. 500 mL). The bulk H_2O was exchanged 4 times over a 72 h period, to ensure a positive dialysis gradient was maintained. Filtering of the tubing contents and lyophilisation yielded the desired product.

pH measurements were carried out at 295 K using a Jenway 3320 pH meter with a Sigma Aldrich micro-pH combination electrode. Calibration was performed using commercially available buffer solutions at pH 4.00 ±0.02, pH 7.00 ±0.02, and pH 10.00 ±0.02 (Merck). Diluted aqueous solutions of NaOH and HCl (or NaOD and DCl in D_2O) were used for pH adjustments. For measurements in D_2O, the pD was calculated as pD = pH + 0.41, where pH is the meter reading.

6.1.2 Characterisation: NMR Spectroscopy

^{1}H, ^{13}C, ^{19}F, and ^{31}P NMR spectra were recorded in commercially available deuterated solvents on a Varian Mecury-200 (^{1}H at 199.975 MHz, ^{13}C at 50.289 MHz, ^{19}F at 188.179 MHz, ^{31}P at 80.985 MHz), Varian Mercury-400 (^{1}H at 399.960 MHz, ^{13}C at 100.572 MHz, ^{19}F at 376.338 MHz, ^{31}P at 161.943 MHz), Bruker Avance-400 (^{1}H at 400.052 MHz, ^{13}C at 100.603 MHz, ^{19}F at 376.423 MHz, ^{31}P at 161.980 MHz), Varian Inova-500 (^{1}H at 499.722 MHz, ^{13}C at 125.671 MHz, ^{19}F at 470.253 MHz, ^{31}P at 202.375 MHz), Varian VNMRS-600 (^{1}H at 599.944 MHZ, ^{19}F at 564.511, ^{31}P at 242.862 MHz), or Varian VNMRS-700 (^{1}H at 699.731 MHz, ^{13}C at 175.948 MHz, ^{19}F at 658.405 MHz, ^{31}P at

283.256 MHz) spectrometer. All chemical shifts are given in ppm and coupling constants are in Hz. Longitudinal relaxation times (T_1) were measured in dilute D_2O solutions at 295 K using the inversion-recovery technique. For ^{19}F, the relaxation data were measured without proton decoupling and the chemical shifts are reported relative to fluorotrichloromethane.

The recorded free induction decays were processed using backward linear prediction, optimal exponential weighting, zero-filling, Fourier transform, phasing, and baseline correction (by polynomial fitting to signal-free spectrum areas). The signals were integrated by Lorentzian line fitting.

Relaxation data was fitted with the help of Alex Funk at Durham University, using a modified algorithm originally provided by Dr Ilya Kuprov at Oxford University. The algorithm uses the Solomon-Morgan-Bloembergen equations to fit the measured relaxation data using the Matlab internal Levenberg-Marquardt minimisation of the non-linear squares error function and the results were analysed iteratively. Some parameters were used globally in the series, and others used for each lanthanide individually. Magnetic moments for each Ln(III) were taken from the literature.[2] Each relaxation rate measurement was repeated three times to reduce experimental error. The number of transients used in the measurements was determined by the signal-to-noise ratio of the sample. The signal was fully recovered during the inversion-recovery sequence to minimise the experimental error. Fitting errors were determined by calculating the standard deviation of a set of relaxation times.

For non-deuterated solutions, a coaxial insert containing D_2O was used to lock the NMR instrument. Operating temperatures of the spectrometers were measured using an internal calibration solution of ethylene glycol, with the operating temperature measured before recording relaxation data.[3,4] Concentrations of the lanthanide complexes were calculated using the bulk magnetic susceptibility method, using 1 %

^{t}BuOH/H_2O solutions of the complexes, with a coaxial insert containing the same solution without the complex added.

Water proton T_1 measurements were recorded on a Bruker Minispec mq60 (60 MHz, 37°C), and are reported as the mean value of three measurements. The relaxivities, r_1, of the compounds were calculated as the slope of the function shown in *Equation 6.1*.

$$\frac{1}{T_{1,obs}} = \frac{1}{T_{1,d}} + r_1 x[Gd.L_n] \qquad (6.1)$$

where $T_{1,obs}$ is the measured T_1, $T_{1,d}$ is the diamagnetic contribution of the solvent (calculated to be 4000 ms), and [Gd.L_n] is the concentration in mM of the appropriate Gd(III) complex. The error for each relaxivity value was less than 0.6 mM^{-1} s^{-1}.

Variable temperature NMR spectroscopy was carried out using the Varian VNMRS-600 spectrometer with the assistance of Alex Funk at Durham University, using the ethylene glycol method described above to confirm the operating temperature of the spectrometer at each temperature measured.

6.1.3 Characterisation: Optical Techniques

All samples for optical analyses were contained in quartz cuvettes with a path length of 1 cm and a polished base. Measurements were recorded at 295 K.

UV/Vis absorbance spectra were measured on a Perkin Elmer Lambda 900 UV/Vis/NIR spectrometer, using FL Winlab software. Samples were measured relative to a reference of pure solvent contained in a matched cell.

Emission spectra were measured on a ISA Joblin-Yvon Spec Fluorolog-3 luminescence spectrometer, using DataMax v2.20 software. Excitation wavelengths were selected according the specific measurement. An integration time of 1.0 s, increment of 0.5 nm, and excitation and emission slit widths of 2.5 and 1.0 nm, respectively, were used throughout.

Lifetime measurements were carried out using a Perkin Elmer LS55B luminescence spectrometer. Lanthanide excited state lifetimes were measured by excitation of the sample by a short pulse of light, followed by monitoring the integrated intensity of light emitted during a fixed gate time, t_g, after a delay time of t_d. Excitation and emission wavelengths were selected based upon the Ln(III) complex. Measurements were made for at least 30 delay times over a period of three or more lifetimes. A gate time of 0.1 ms was used, with the excitation and emission slits set to 10 and 5 nm, respectively. The obtained decay curves were fitted to *Equation 6.2*, using Origin 6.0 software.

$$I = A_0 + A_1 e^{-kt} \qquad (6.2)$$

where I is the intensity at time t after the excitation pulse, A_0 is the intensity after decay is completed, A_1 is the pre-exponential factor, and k is the rate constant for decay of the excited state. The excited state lifetime, τ, is the inverse of the rate constant, k.

The inner sphere hydration number (q) of Eu(III) and Tb(III) complexes were obtained by measuring the excited state lifetime in H_2O and D_2O. The q value was calculated using *Equations 6.3* and *6.4*, which are derived elsewhere.[5]

$$q_{Eu} = 1.2(k_{H_2O} - k_{D_2O} - 0.25 - 0.075n) \qquad (6.3)$$

$$q_{Tb} = 5.0(k_{H_2O} - k_{D_2O} - 0.06 - 0.010n) \qquad (6.4)$$

where q_{Ln} is the inner sphere hydration number, k is the inverse of the excited state lifetime, τ, and n is the number of proximal amide NH oscillators, for coordinated amide carbonyl groups only.

6.1.4 Characterisation: Other Techniques

Both standard and high resolution electrospray mass spectrometry were recorded on a Thermo-Finnigan LTQ FT instrument, operating in positive or negative ion mode as stated, with MeOH as the carrier solvent. MALDI mass spectra were recorded on an Applied Biosystems Voyager-DE STR instrument with MeOH as the carrier solvent. LC-MS analyses were performed on a Waters system comprising a 3100 Mass Detector and a 2998 Photodiode array detector.

Gel permeation chromatography (GPC) was undertaken at Smithers Rapra UK, using a Viscotek Model 301 TDA instrument with associated pump, autosampler, and refractive index detector (with differential pressure and light scattering). Agilent PLaquagel-OH Guard plus 2 x PLaquagel-OH Mixed-M, 30 cm, 8 µm columns were used with an eluent composed of 0.5 M $NaNO_3$, 0.01 M NaH_2PO_4 at pH 2 at a flow rate of 1.0 mL/min at 30°C. The GPC system was calibrated using Pullulan polysaccharides and the data analysed using Malvern/Viscotek 'OmniSec' software.

Melting points were recorded using a Gallenkamp (Sanyo) apparatus and are uncorrected.

6.1.5 HPLC Analysis

Reverse phase Analytical HPLC traces were recorded at 298 K using Waters Mass Directed Auto Preparation (MDAP) system. XBridge C18 4.6 x 100 mm, i.d. 5 µm analytical column and XBridge C18 OBD 19 x 100 mm, i.d. 5 µm semi-preparative columns were used to analyse and purify the ligands and complexes. A gradient elution with a solvent system composed of H_2O + 0.1% HCOOH/MeOH was performed for a total run time of 16.5 min. The separation details are reported below (*Tables 6.1* and *6.2*).

Table 6.1 *Analytical procedure: flow rate = 1 ml/min; Solvent A = H_2O + 0.1 % HCOOH; Solvent B = MeOH + 0.1 % HCOOH.*

Time (min)	Solvent A (%)	Solvent B (%)	Curvature
0	90	10	0
10	5	95	6
13	5	95	6
13.5	90	10	6
16.5	90	10	1

Table 6.2 *Semi-preparative procedure: flow rate = 17 ml/min; Solvent A = H_2O + 0.1 % HCOOH; Solvent B = MeOH + 0.1 % HCOOH.*

Time (min)	Solvent A (%)	Solvent B (%)	Curvature
0	90	10	0
0.2	90	10	6
0.7	90	10	6
11	5	95	6
14	5	95	6
14.5	90	10	6
16.5	90	10	1

6.1.6 X-ray Studies

The single crystal X-ray data for **[Tm.L^2]** was collected at 120 K on a Gemini Ultra (Agilent Technologies) diffractometer (graphite monochromator, μ($Mo_{K\alpha}$), λ= 0.71073 Å) equipped with Cryostream (Oxford Cryosystems) open-flow nitrogen cryostat. Using Olex2[6] software, the structure was solved with the XS[7] structure solution program by Patterson methods and refined with the XL[7] refinement package with full-matrix least squares minimisation. All hydrogen atoms were placed in calculated positions and refined in riding mode, disordered atoms were refined isotropically with fixed SOF=0.5. CCDC 870354.

Crystal data for **[Tm.L^2]**: $C_{22}H_{37}F_3N_6O_{10}Tm$, M_r = 771.51, monoclinic, a = 7.55031(18), b = 32.7541(7), c = 11.8075(3) Å, β = 101.046(2)°, V = 2865.93(11) Å^3, space group $P2_1/c$, Z = 4, μ($Mo_{K\alpha}$) = 3.178, 20173 reflections measured, 7618 unique (R_{int} = 0.0659), which were used in all calculations. The final wR_2 was 0.1016 (all data) and R_1 was 0.0604 for 5270 reflections with $I>2\sigma(I)$, GOF = 1.085.

6.1.7 Enzyme Mediated Transformations

Enzyme activities were obtained at 25 or 37°C and 188 or 376 MHz using diluted PBS solutions of the complex (1 mM) in H_2O with a constant pH of 7.4. For each experiment, half of the sample without enzyme added was used as a negative control, while to the other half 5 mg of the enzyme was added as a lyophilised powder (15 units/mg, 1 unit hydrolyses 1.0 μmol of ethyl butyrate to butyric acid and ethanol per min at pH 8.0 at 25 °C). A coaxial D_2O insert was used to lock the NMR instrument.

6.1.8 Determination of Anion Binding Constants

Apparent binding constants were calculated from the emission/NMR spectroscopy data obtained following anion addition titrations using *Equation 6.5*. The equation was fitted to the data, using a non-linear least squares fitting algorithm in Microsoft Excel 2010, using the solver add-in. Highly concentrated anion solutions were added to minimise increase in sample volume. Eu(III) emission spectra were corrected for dilution effects.

$$[X] = \frac{{}^{f}/_{K} + f[Ln.L] - f^2[Ln.L]}{1-f} \qquad (6.5)$$

where [X] is the concentration of the anion in the solution, K is the binding constant, [Ln.L] is the total concentration of the complex in solution, and:

$$f = \frac{F - F_0}{F_1 - F_0}$$

where F is the ratio/intensity of the selected signals, F_0 is the initial ratio/intensity of the selected signals, F_1 is the final ratio/intensity of the selected signals.

6.1.9 Cell Studies

The NIH 3T3 (mouse skin fibroblast) cell line was selected for cellular studies, with the aid of Dr Robert Pal. Cells were maintained in exponential growth as monolayers in appropriate media, which were supplemented with 10 % foetal bovine serum (FBS) and 1 % penicillin and streptomycin. Cells were incubated at 37°C, 20 % average humidity and 5 % (v/v) CO_2.

6.1.10 Imaging Studies

Imaging studies were carried out by Prof. Andrew Blamire, Dr. Ross Maxwell, and Dr. Ian Wilson at Newcastle Magnetic Resonance Centre, using a 7 T Varian Unity Inova microimaging/Pre-clinical system equipped with broadband capability and actively shielded gradients. For the ^{19}F MRI studies, a purpose built four turn solenoid coil (20 mm diameter, 20 mm coil length) was used for *in vitro* experiments and a ^{19}F-tuned square surface coil (30 mm, m2m Imaging Corp.) was used for *in vivo* experiments. For the ^{1}H MRI studies, *in vitro* experiments were performed with a 30 mm i.d. birdcage volume coil (Rapid Biomedical) and *in vivo* experiments were performed with a 39 mm i.d. birdcage volume coil. All coils were used for both signal excitation and reception.

For phantom studies, dilute aqueous samples (2-5 mM) were placed in Eppendorf tubes or cut down (2-3 mm) NMR tubes and positioned on the axis of the coil. For *in vivo* studies, nude mice bearing a HT29 colorectal tumour xenograft were anaesthetised with oxygen/1-2 % isofluorane (for the ^{1}H MRI studies) or with a mixture of ketamine (0.75 mg/kg) and medetomidine (0.5-1.0 mg/kg) (for the ^{19}F MRI studies). Complexes were administered intravenously as saline solutions *via* the tail vein, with doses typically 0.06 mmol/kg.

6.2 Synthetic Procedures

1. 2-Chloro-*N*-(2-(trifluoromethyl)phenyl)acetamide[8]

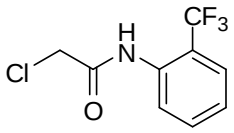

To a stirred solution of 2-aminobenzotrifluoride (1.00 g, 6.2 mmol) and NEt_3 (1.03 mL, 7.4 mmol) in anhydrous DCM (15 mL), chloroacetyl chloride (0.59 mL, 7.4 mmol) was added dropwise under argon at 0°C. After stirring for 2 h, the reaction mixture was allowed to warm to rt and stirred for a further 18 h. The resulting crude mixture was washed with $HCl_{(aq)}$ (pH 2-3, 2 x 20 mL), followed by H_2O (2 x 20 mL). The organic layer was dried over Na_2SO_4, filtered, and the solvent removed under reduced pressure, before the resulting crude oil was purified by silica gel column chromatography, eluting with a gradient starting from 100 % toluene to 20 % DCM/toluene, to yield a white solid (0.98 g, 67 %), m.p. 100-102°C. ^{1}H NMR (400 MHz, $CDCl_3$): δ = 8.77 (s, 1H, NH), 8.24 (d, *J* = 8 Hz, 1H, H^6), 7.67 (d, *J* = 8 Hz, 1H, H^3), 7.61 (t, *J* = 8 Hz, 1H, H^5), 7.31 (t, *J* = 8 Hz, 1H, H^4), 4.25 (s, 2H, $C\underline{H}_2Cl$); ^{19}F NMR (658 MHz, $CDCl_3$): δ = -60.7; ESI/$MS^{+/-}$ m/z 236.2 $[M-H]^-$.

2. 1,4,7,10-Tetraazacyclododecane-1,7-dicarboxylic acid dibenzyl ester[9]

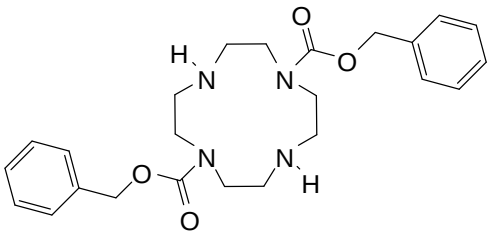

1,4,7,10-Tetraazacyclododecane (5.0 g, 29.0 mmol) was dissolved in a solution of aqueous dioxane (70 mL), followed by addition of disodium hydrogen phosphate (14.0 g, 98.6 mmol). The pH of the solution was adjusted to 2.7 by careful addition of conc. HCl. Benzyl chloroformate (11.9 mL, 70.0 mmol) in dioxane (20 mL) was added dropwise over a period of 2 h and the solution left to stir for a further 18 h at rt, yielding a colourless solution with a white precipitate. The solvent was evaporated

under reduced pressure and the residue dissolved in H_2O (100 mL), followed by adjustment of the pH to 7 by addition of conc. KOH (aq). The aqueous phase was extracted with Et_2O (2 x 100 mL), followed by DCM (2 x 100 mL). The organic phases were combined, dried over $MgSO_4$, filtered, and the solvent removed under reduced pressure to give a clear oil. This oil was repeatedly washed with Et_2O to yield a white solid (9.73 g, 76 %), m.p. 114-117°C. ^{1}H NMR (400 MHz, $CDCl_3$): δ = 7.45 – 7.30 (m, 10H, Ph), 5.18 (s, 4H, C$\underline{H}_2$Ph), 3.81 – 3.59 (m, 8H, cyclen-C$\underline{H}_2$), 3.15 – 2.79 (m, 8H, cyclen-C$\underline{H}_2$); ESI/MS$^+$ m/z 441.2 $[M+H]^+$, 463.3 $[M+Na]^+$.

3. 4,10-Bis-*tert*-butoxycarbonylmethyl-1,4,7,10-tetraazacyclododecane-1,7-dicarboxylic acid dibenzyl ester[10]

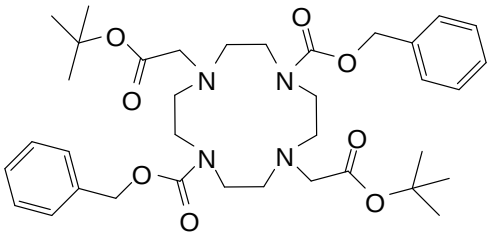

1,4,7,10-Tetraazacyclododecane-1,7-dicarboxylic acid dibenzyl ester (2.0 g, 4.54 mmol) and *tert*-butyl bromoacetate (1.83 g, 9.34 mmol) were dissolved in anhydrous MeCN (25 mL) followed by the addition of Cs_2CO_3 (4.0 g, 12.2 mmol). The mixture was left to heat under reflux for 18 h. The caesium salts were removed by filtration and the solvent removed under reduced pressure. The resulting dark yellow oil was purified by silica gel column chromatography, eluting with a gradient starting from 100 % DCM to 2 % MeOH/DCM to yield a light yellow oil (2.18 g, 72 %). ^{1}H NMR (400 MHz, $CDCl_3$): δ = 7.44 – 7.15 (m, 10H, Ph), 5.11 (s, 4H, C$\underline{H}_2$Ph), 3.56 – 3.10 (m, 12H, cyclen-C$\underline{H}_2$ and C$\underline{H}_2$CO$_2$^{t}Bu), 2.87 (br s, 8H, cyclen-C$\underline{H}_2$), 1.42 (s, 18H, ^{t}Bu); ESI/MS$^+$ m/z 699.4 $[M+H]^+$.

4. (7-*tert*-Butoxycarbonylmethyl-1,4,7,10-tetraazacyclododec-1-yl)-acetic acid *tert*-butyl ester[10]

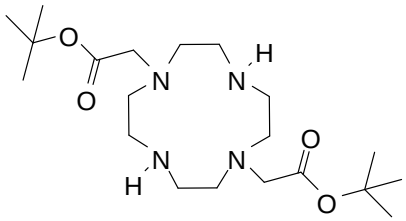

4,10-Bis-*tert*-butoxycarbonylmethyl-1,4,7,10-tetraazacyclododecane-1,7-dicarboxylic acid dibenzyl ester (2.10 g, 3.15 mmol) was dissolved in absolute EtOH (20 mL) to which $Pd(OH)_2/C$ (Pd content 10%, 30 mg) was added. The mixture was hydrogenated in a Parr hydrogenation apparatus (40 psi of H_2) for 3 days. The catalyst was filtered off using a syringe filter and/or celite before the solvent was removed under reduced pressure to yield a white solid (1.16 g, 55 %).

The following method was also successfully in achieving the desired compound, but in a lower yield; 4,10-Bis-*tert*-butoxycarbonylmethyl-1,4,7,10-tetraazacyclododecane-1,7-dicarboxylic acid dibenzyl ester (5.94 g, 8.89 mmol) was dissolved in absolute EtOH (50 mL) to which Pd/C (Pd content 20 %, 1.19 g) and ammonium formate (3.92 g, 62.2 mmol) were added. This reaction mixture was then boiled under reflux for 3 h, with careful supervision to ensure that the condenser did not become blocked. The solution was then filtered before the solvent was removed under reduced pressure to give a yellow-white solid. This crude solid was dissolved in DCM (50 mL) and extracted with $HCl_{(aq)}$ (1 M, 2 x 50 mL). The pH of the aqueous layer was adjusted to 10 with careful addition of conc. NaOH (aq) before being extracted with DCM (2 x 50 mL). The organic layers were combined and dried over $MgSO_4$, filtered, and the solvent removed under reduced pressure to give a white solid. To remove any formate present in the product, Amberlite® IRA-410 chloride form anion exchange resin was used, which was pre-treated using $NaOH_{(aq)}$. This yielded a white solid (2.15 g, 36 %).

Both methods resulted in identical products, which were characterised as follows; ^{1}H NMR (700 MHz, $CDCl_3$): δ = 3.28 (4 H, s, C<u>H</u>$_2$CO$_2$^{t}Bu), 2.77 (8 H, br s, cyclen-C<u>H</u>$_2$), 2.58 (8 H, br s, cyclen-C<u>H</u>$_2$), 1.43 (18 H, s, ^{t}Bu); ^{13}C NMR (176 MHz, $CDCl_3$): δ = 170.9 (CO_2), 80.9 (<u>C</u>(CH$_3$)$_3$), 57.2 (NH<u>C</u>H$_2$CO$_2$^{t}Bu), 52.0 (cyclen-<u>C</u>H$_2$), 45.7 (cyclen-<u>C</u>H$_2$), 28.2 (C(<u>C</u>H$_3$)$_3$); ESI/MS$^+$ m/z 401.4 $[M+H]^+$, 423.4 $[M+Na]^+$.

5. Di-*tert*-butyl 2,2'-(4-(2-oxo-2-(2-(trifluoromethyl)phenylamino)ethyl)-1,4,7,10-tetraazacyclododecane-1,7-diyl)diacetate

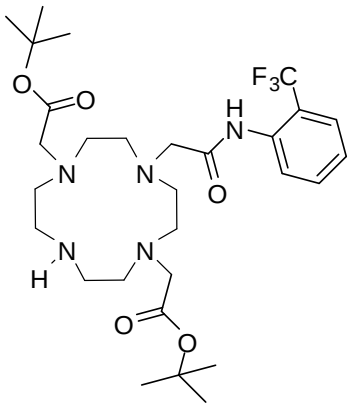

A solution of di-*tert*-butyl 2,2'-(1,4,7,10-tetraazacyclododecane-1,7-diyl)diacetate (DO2A) (1.1 g, 2.75 mmol) and Na_2CO_3 (0.29 g, 2.75 mmol) in anhydrous MeCN (50 mL) was stirred at rt under an inert atmosphere for 30 min. 2-Chloro-*N*-(2-(trifluoromethyl)phenyl)acetamide (0.58 g, 2.45 mmol) was added and the reaction mixture heated at 80°C overnight**.** The completion of reaction was verified by TLC, before the solution was filtered and the solvent removed under reduced pressure. The residue was purified by silica gel column chromatography, eluting with a gradient starting from 100 % DCM to 10 % MeOH/DCM, to yield a transparent sticky gum (0.83 g, 50 %). R_f (10 % MeOH/DCM) = 0.25. ^{1}H NMR (400 MHz, $CDCl_3$): δ = 10.19 (br s, 1 H, NH), 8.69 (br s, 1 H, NH), 7.87 (d, *J* = 8 Hz, 1H, $H^{3/6}$), 7.65 (d, *J* = 8 Hz, 1H, $H^{3/6}$), 7.59 (t, *J* = 8 Hz, 1H, $H^{4/5}$), 7.32 (t, *J* = 8 Hz, 1H, $H^{4/5}$), 3.66 (s, 2H, NC$\underline{H}_2$CONH), 3.36 (s, 4H, NC$\underline{H}_2$COO), 3.36 (s, 4H, NC$\underline{H}_2$COO), 3.05 – 3.11 (m, 4H, cyclen-C$\underline{H}_2$), 2.96 – 3.03 (m, 8H, cyclen-C$\underline{H}_2$), 2.89 - 2.95 (m, 4H, cyclen-C$\underline{H}_2$), 1.43 (s, 18H, ^{t}Bu); ^{13}C NMR (100 MHz, $CDCl_3$): *δ* = 170.3 (CO), 169.8 (CO), 134.5, 132.8, 128.2 (q, $^3J_{CF}$ = 5 Hz, C^3), 126.3, 125.7, 124.3 (q, $^1J_{CF}$ = 272 Hz, CF_3), 121.2 (q, $^2J_{CF}$ = 31 Hz, C^2), 81.8 (C($\underline{C}H_3)_3$), 58.2, 52.4, 52.0, 51.7, 49.6, 47.6, 28.1 (C($\underline{C}H_3)_3$) ; ^{19}F NMR (376 MHz, $CDCl_3$): *δ* = -61.2; HRMS Calcd for $C_{29}H_{46}F_3N_5O_5$ 602.3529. Found 602.3519**.**

6. 2,2'-(4-(2-(2-(Trifluoromethyl)phenylamino)-2-oxoethyl)-1,4,7,10-tetraazacyclododecane-1,7-diyl)diacetic acid (L^1)

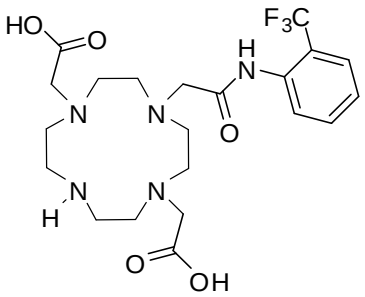

Di-*tert*-butyl 2,2'-(4-(2-oxo-2-(2-(trifluoromethyl)phenylamino)ethyl)-1,4,7,10-tetraaza-cyclododecane-1,7-diyl)diacetate (32 mg, 0.053 mmol) was dissolved in DCM (3 mL) with stirring. To this was added TFA (1 mL) and the mixture stirred at rt for 18 h. After this time, the solvent was removed under reduced pressure to give a yellow oil, which was repeatedly washed with DCM to yield the triflate salt as a pale yellow oil (24 mg, 92 %). ^{1}H NMR (200 MHz, D_2O): δ = 7.66 (d, J = 7 Hz, 1H, $H^{3/6}$) 7.54 (m, 1H, $H^{3/6}$), 7.40 (t, J = 7 Hz, 2H, $H^{4/5}$), 4.31 (s, 2H, C$\underline{H}_2$CONH), 3.40 (m, 6H, NC$\underline{H}_2$CO$_2$^{t}Bu, cyclen-C$\underline{H}_2$), 3.32 (s, 2H, cyclen-C$\underline{H}_2$), 3.19 (m, 4H, cyclen-C$\underline{H}_2$), 2.99 (m, 6H, NC$\underline{H}_2$CO$_2$^{t}Bu, cyclen-C$\underline{H}_2$), 2.79 (s, 2H, cyclen-C$\underline{H}_2$); ^{19}F NMR (188 MHz, D_2O): δ = - 61.7; ESI/MS$^+$ m/z 490.3 $[M+H]^+$.

7. [Ho.L^1]

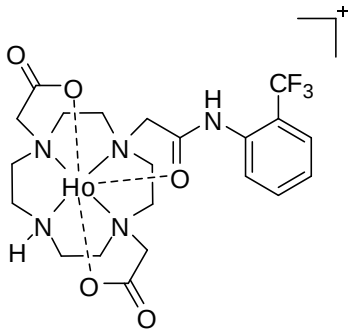

Ho(III)Cl_3.6H_2O (9.1 mg, 0.024 mmol) was added to a stirred solution of 2,2'-(4-(2-(2-(trifluoromethyl)phenylamino)-2-oxoethyl)-1,4,7,10-tetraazacyclododecane-1,7-diyl) diacetic acid (12 mg, 0.020 mmol) in water (3 mL) and the pH adjusted to 5.5 using $KOH_{(aq)}$. The reaction was left stirring overnight at 50°C. After cooling to rt, the pH was adjusted to 10 the precipitated metal hydroxide was removed by centrifugation. The

solution was adjusted back to pH 5.5 with $HCl_{(aq)}$ and lyophilised to give a pale yellow solid that was extracted into 20 % MeOH/DCM. This organic solution was again centrifuged to remove insoluble solid material before the solvent was removed under reduced pressure. The resulting white solid was dissolved in H_2O and stirred overnight with anion exchange resin (DOWEX 1x2 100-200 mesh Cl, pre-treated with 1M HCl) in Purite water to give the chloride salt. After filtration the water was lyophilised to yield a white solid (12 mg, 94 %). ^{19}F NMR (376 MHz, D_2O, pD 7.4): δ = -76.8; HRMS Calcd for $C_{21}H_{28}N_5O_5F_3{}^{165}Ho$ 652.1346. Found 652.1344.

8. [Tm.L^1]

An analogous procedure to that described for the synthesis of **[Ho.L^1]** was followed using 2,2'-(4-(2-(2-(trifluoromethyl)phenylamino)-2-oxoethyl)-1,4,7,10-tetraazacyclo-dodecane-1,7-diyl)diacetic acid (12 mg, 0.020 mmol) and $Tm(III)Cl_3.6H_2O$ (9.2 mg, 0.024 mmol) to give a white solid (12 mg, 95 %). ^{19}F NMR (376 MHz, D_2O, pD 7.4): δ = -67.6; HRMS Calcd for $C_{21}H_{28}N_5O_5F_3{}^{169}Tm$ 656.1385. Found 656.1395.

9. 2-Chloro-N-(2-(cyano)-6-trifluoromethylphenyl)-ethanamide[8]

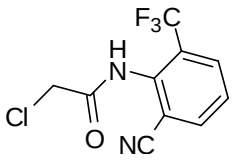

To a stirred solution of 2-amino-3-(trifluoromethyl)benzonitrile (1.00g, 5.37 mmol) in dry DMF (35 mL) was added sodium hydride in portions (60% dispersion in mineral oil, 0.54 g, 13.4 mmol) under argon at 0°C, which resulted in the development of H_2. Once no more H_2 was evolved, chloroacetyl chloride (1.71 mL, 21.5 mmol) was added dropwise. The reaction mixture was allowed to warm to room temperature and stirred for 48 h. The excess sodium hydride was quenched with H_2O (3 mL) and the solution concentrated under reduced pressure. To the crude mixture DCM was added and then washed successively with $HCl_{(aq)}$ (pH 2-3, 20 mL), $NaOH_{(aq)}$ (pH 8-9, 20 mL), and H_2O (20 mL). The organic layer was dried over K_2CO_3, filtered, and the solvent

removed under reduced pressure to give a black oil. This was purified over silica gel in DCM to yield a light yellow solid (0.91 g, 64 %), m.p. 116-117°C. ^{1}H NMR (700 MHz, $CDCl_3$): δ = 8.47 (s, 1H, NH), 7.94 (t, *J* = 8 Hz, 2H, H^3/H^5), 7.58 (t, *J* = 8 Hz, 1H, H^4), 4.31 (s, 2H $C\underline{H}_2Cl$); ^{13}C NMR (176 MHz, $CDCl_3$): δ = 165.0 (NH$\underline{C}$O), 136.8 (C^1), 136.4 (C^3), 130.7 (q, $^{3}J_{CF}$ = 5 Hz, C^5), 128.2 (C^4), 128.0 (q, $^{2}J_{CF}$ = 31 Hz, C^6), 122.4 (q, $^{1}J_{CF}$ = 274 Hz, CF_3), 115.2 (C^2), 115.0 (CN), 42.4 ($\underline{C}H_2Cl$); ^{19}F NMR (658 MHz, $CDCl_3$): δ = -61.8; ESI/MS$^{+/-}$ m/z 261.2 $[M-H]^-$, 285.2 $[M+Na]^+$; HRMS Calcd for $C_{10}H_6N_2OF_3ClNa$ 285.0018. Found 285.0026.

10. Di-tert-butyl 2,2'-(4-(2-(2-cyano-6-(trifluoromethyl)phenylamino)-2-oxoethyl)-1,4,7,10-tetraazacyclododecane-1,7-diyl)diacetate

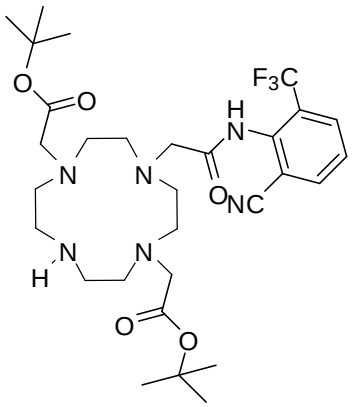

2-Chloro-N-(6-(cyano)-2-trifluoromethylphenyl)-ethanamide (0.157 g, 0.60 mmol) and (7-*tert*-Butoxycarbonylmethyl-1,4,7,10-tetraazacyclododec-1-yl)-acetic acid *tert*-butyl ester (0.30 g, 0.75 mmol) were dissolved in anhydrous MeCN (15 mL) under an atmosphere of argon. To this was added Na_2CO_3 (79.4 mg, 0.75 mmol) and the reaction mixture stirred at 50°C for 24 h. The reaction mixture was then filtered before the solvent was removed under reduced pressure to give an off-white solid, which was purified by silica gel column chromatography, eluting with a gradient starting from 100 % DCM to 5 % MeOH/DCM, to yield a white solid (0.143 g, 38 %). ^{1}H NMR (500 MHz, $CDCl_3$): δ = 10.21 (br s, 1H, NH), 9.62 (br s, 1H, NH), 7.97 – 7.85 (m, 2H, H^3/H^5), 7.53 (t, *J* = 8 Hz, 1H, H^4), 3.72 (s, 2H, NC$\underline{H}_2$CONH), 3.39 (s, 4H, NC$\underline{H}_2CO_2{}^t$Bu), 3.01 (m, 16H, cyclen-C$\underline{H}_2$), 1.37 (s, 18H, CH_3); ^{13}C NMR (126 MHz, $CDCl_3$): δ = 171.5 ($\underline{C}$ONH), 170.7 ($\underline{C}O_2{}^t$Bu), 138.8 (C^1), 136.7 (C^3), 131.1 (q, $^{3}J_{CF}$ = 5 Hz, C^5), 129.3 (q,

$^{2}J_{CF}$ = 31 Hz, C^{6}), 128.1 (C^{4}), 122.8 (q, $^{1}J_{CF}$ = 274 Hz, CF_3), 116.4 (C^{2}), 116.2 (CN), 82.0 ($\underline{C}(CH_3)_3$), 58.7 ($\underline{C}H_2CO_2{}^{t}Bu$), 53.6 (cyclen-$\underline{C}H_2$), 53.0 ($NCH_2CONH$), 52.4 (cyclen-$\underline{C}H_2$), 50.3 (cyclen-$\underline{C}H_2$), 47.8 (cyclen-$\underline{C}H_2$), 28.3 ($C(\underline{C}H_3)_3$); ^{19}F NMR (658 MHz, $CDCl_3$): δ = -61.1; ESI/MS^{+} m/z 627.5 $[M+H]^{+}$, 649.4 $[M+Na]^{+}$; HRMS Calcd for $C_{30}H_{46}N_6O_5F_3$ 627.3482. Found 627.3478.

11. 2,2'-(4-(2-(2-Cyano-6-(trifluoromethyl)phenylamino)-2-oxoethyl)-1,4,7,10-tetraazacyclododecane-1,7-diyl)diacetic acid (L^{2})

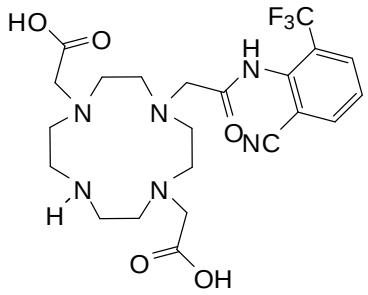

Di-*tert*-butyl 2,2'-(4-(2-(2-cyano-6-(trifluoromethyl)phenylamino)-2-oxoethyl)-1,4,7,10-tetraazacyclododecane-1,7-diyl)diacetate (64 mg, 0.10 mmol) was dissolved in DCM (3 mL). To this was added TFA (1 mL) and the mixture was stirred at rt for 3 h. After this time, the solvent was removed under reduced pressure to give a yellow oil, which was repeatedly washed with DCM to yield a pale yellow oil (48 mg, 91 %). ^{1}H NMR (200 MHz, D_2O): δ = 7.79 (d, *J* = 8 Hz, 2H, H^{3}/H^{5}), 7.42 (t, *J* = 8 Hz, 1H, H^{4}), 4.29 (s, 2H, $NC\underline{H}_2CONH$), 3.62 – 2.34 (m, 20H, $NC\underline{H}_2CO_2{}^{t}Bu$ and cyclen-$C\underline{H}_2$); ^{19}F NMR (188 MHz, D_2O): δ = -62.5; ESI/MS^{+} m/z 515.3 $[M+H]^{+}$, 533.3 $[M+Na]^{+}$.

12. [Ho.L^2]

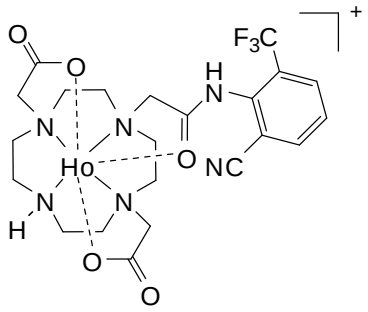

Ho(III)Cl_3.6H_2O (40.5 mg, 0.15 mmol) was added to a stirred solution of 2,2'-(4-(2-(2-cyano-6-(trifluoromethyl)phenylamino)-2-oxoethyl)-1,4,7,10-tetraazacyclododecane-1,7-diyl)diacetic acid (64 mg, 0.12 mmol) in water (3 mL) and the pH adjusted to 5.5 using $KOH_{(aq)}$. The reaction was left stirring overnight at 50°C. After cooling to rt, the pH was adjusted to 10 the precipitated metal hydroxide was removed by centrifugation. The solution was adjusted back to pH 5.5 with $HCl_{(aq)}$ and lyophilised to give a pale yellow solid that was extracted into 20 % MeOH/DCM. This organic solution was again centrifuged to remove insoluble solid material before the solvent was removed under reduced pressure. The resulting white solid was dissolved in H_2O and stirred overnight with anion exchange resin (DOWEX 1x2 100-200 mesh Cl, pre-treated with 1M HCl) in Purite water to give the chloride salt. After filtration the water was lyophilised to yield a white solid (81 mg, 97 %). ^{19}F NMR (376 MHz, D_2O, pD 7.4): δ = -63.6; ESI/MS$^+$ m/z 677.3 $[M]^+$; HRMS Calcd for $C_{22}H_{26}N_6O_5F_3{}^{165}$HoNa 699.1118. Found 699.1115.

13. [Tm.L^2]

An analogous procedure to that described for the synthesis of **[Ho.L^2]** was followed using 2,2'-(4-(2-(2-cyano-6-(trifluoromethyl)phenylamino)-2-oxoethyl) 1,4,7,10-tetra-azacyclododecane-1,7-diyl)diacetic acid (15 mg, 0.029 mmol) and Tm(III)Cl_3.6H_2O (13 mg, 0.035 mmol) to give a white solid (19 mg, 97 %). ^{19}F NMR (376 MHz, D_2O, pD 7.4): δ = -61.4; ESI/MS$^+$ m/z 681.4 $[M]^+$; HRMS Calcd for $C_{22}H_{27}N_6O_5F_3{}^{169}$Tm.$CH_3OH$ 713.1599. Found 713.1620.

14. [Eu.L^2]

An analogous procedure to that described for the synthesis of **[Ho.L^2]** was followed using 2,2'-(4-(2-(2-cyano-6-(trifluoromethyl)phenylamino)-2-oxoethyl)-1,4,7,10-tetra-azacyclododecane-1,7-diyl)diacetic acid (8 mg, 0.016 mmol) and Eu(III)$Cl_3.6H_2O$ (6.8 mg, 0.019 mmol) to give a white solid (10.4 mg, 98 %). ^{19}F NMR (376 MHz, D_2O, pD 7.3): δ = -62.5; ESI/MS$^+$ m/z 665.2 $[M]^+$; HRMS Calcd for $C_{22}H_{27}N_6O_5F_3{}^{151}Eu.CH_3OH$ 695.1456. Found 685.1438.

15. Ethyl 4-amino-3-(trifluoromethyl)benzoate[11]

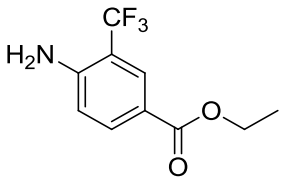

4-Amino-3-(trifluoromethyl)benzonitrile (5.00 g, 26.8 mmol) was added to a stirred solution of H_2SO_4 (5 mL), EtOH (25 mL), and H_2O (2 mL). The mixture was stirred at 95°C for 48 h with a $CaCl_2$ drying tube fitted to the top of the condenser. After this time, the reaction mixture was allowed to cool to rt before H_2O (50 mL) was added and the pH adjusted to 7 by careful addition of K_2CO_3. This was extracted into DCM (3 x 50 mL), dried over $MgSO_4$, filtered, and the solvent removed under reduced pressure. The resulting oil was purified by silica gel column chromatography, eluting with a gradient starting from 100 % toluene to 5 % DCM/toluene to yield a white solid (3.44 g, 55 %), m.p. 82-84°C. ^{1}H NMR (700 MHz, $CDCl_3$): δ = 8.12 (s, 1H, H^2), 7.92 (d, *J* = 9 Hz, 1H, H^6), 6.70 (d, *J* = 9 Hz, 1H, H^5), 4.68 (s, 2H, NH_2), 4.31 (q, *J* = 7 Hz, 2H, $C\underline{H}_2CH_3$), 1.34 (t, *J* = 7 Hz, 3H, $C\underline{H}_3$); ^{13}C NMR (176 MHz, $CDCl_3$): δ = 165.8 ($\underline{C}O_2$), 148.3 (C^4), 134.2 (C^6), 129.0 (q, $^3J_{CF}$ = 5 Hz, C^2), 124.5 (q, $^1J_{CF}$ = 272 Hz, CF_3), 119.2 (C^1), 116.2 (C^5), 112.6 (q, $^2J_{CF}$ = 31 Hz, C^3), 60.7 ($\underline{C}H_2CH_3$), 14.3 (CH_3); ^{19}F NMR (658 MHz, $CDCl_3$): δ = -63.1; ESI/MS$^+$ m/z 234.2 $[M+H]^+$; HRMS Calcd for $C_{10}H_{11}NO_2F_3$ 234.0742. Found 234.0749.

16. Ethyl 4-(2-chloroacetamido)-3-(trifluoromethyl)benzoate[11]

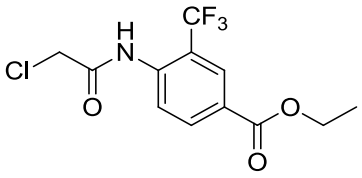

Chloroacetyl chloride (2.00 g, 17.7 mmol) was added dropwise to a stirred solution of ethyl 4-amino-3-(trifluoromethyl)benzoate (3.44 g, 14.8 mmol) and NEt_3 (1.79 g, 17.7 mmol) in anhydrous DCM (30 mL) at 0°C under argon. After 4 h, the crude mixture was washed with HCl (30 mL, 0.1 M), NaOH (30 mL, 0.1 M), and H_2O (30 mL). The combined organic extracts were dried over $MgSO_4$ and the solvent removed under reduced pressure. The resulting residue was purified by recrystallisation from hexane to yield white needles (2.82 g, 61 %), m.p. 98-101°C. ^{1}H NMR (500 MHz, $CDCl_3$): δ = 8.98 (s, 1H, NH), 8.50 (d, *J* = 9 Hz, 1H, H^5), 8.35 (d, *J* = 2 Hz, 1H, H^2), 8.26 (dd, *J* = 2, 9 Hz, 1H, H^6), 4.42 (q, *J* = 7 Hz, 2H, $C\underline{H}_2CH_3$), 4.27 (s, 2H, $C\underline{H}_2CO$), 1.43 (t, *J* = 7 Hz, 3H, CH_3); ^{13}C NMR (126 MHz, $CDCl_3$): δ = 165.0 (CO_2), 164.5 (CONH), 138.3 (C^4), 134.5 (C^6), 128.1 (q, $^3J_{CF}$ = 6 Hz, C^2), 127.2 (C^1), 123.7 (q, $^1J_{CF}$ = 274 Hz, CF_3), 122.7 (C^5), 119.8 (q, $^2J_{CF}$ = 31 Hz, C^3), 61.8 ($\underline{C}H_2CH_3$), 43.2 ($\underline{C}H_2CO$), 14.5 (CH_3); ^{19}F NMR (470 MHz, $CDCl_3$): δ = -61.3; ESI/MS^- m/z 308.2 $[M-H]^-$; HRMS Calcd for $C_{12}H_{10}NO_3F_3Cl$ 308.0301. Found 308.0288.

17. Ethyl-4-(2-(1,4,7,10-tetraazacyclododecan-1-yl)acetoamido)-3-(trifluoromethyl) benzoate[11]

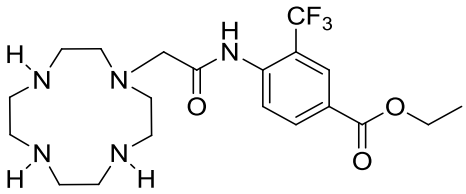

A solution of ethyl 4-(2-chloroacetamido)-3-(trifluoromethyl)benzoate (0.40 g, 1.29 mmol) in anhydrous MeCN (20 mL) was added dropwise to a stirred solution of 1,4,7,10-tetraazacyclododecane (2.22 g, 12.9 mmol) in anhydrous MeCN (30 mL) at 40°C under argon. After 5 h, the solvent was removed under reduced pressure and the residue dissolved in DCM (20 mL). The solution was washed repeatedly with H_2O

(4 x 20 mL), dried over $MgSO_4$, and the solvent removed under reduced pressure to yield a light yellow oil (0.43 g, 75 %). ^{1}H NMR (700 MHz, $CDCl_3$): δ = 8.30 (d, *J* = 9 Hz, 1H, H^5), 8.26 (s, 1H, H^2), 8.16 (d, *J* = 9 Hz, 1H, H^6), 4.36 (q, *J* = 7 Hz, 2H, $C\underline{H}_2CH_3$), 3.32 (s, 2H, $C\underline{H}_2CO$), 2.75 (m, 8H, cyclen-$C\underline{H}_2$), 2.67 (m, 4H, cyclen-$C\underline{H}_2$), 2.61 (m, 4H, cyclen-$C\underline{H}_2$), 1.38 (t, *J* = 7 Hz, 3H, CH_3); ^{13}C NMR (176 MHz, $CDCl_3$): δ = 170.1 ($\underline{C}O_2$), 164.9 ($\underline{C}$ONH), 139.1 (C^4), 133.9 (C^6), 127.7 (q, $^3J_{CF}$ = 5 Hz, C^2), 126.5 (C^1), 124.4 (C^5), 123.6 (q, $^1J_{CF}$ = 274 Hz, CF_3), 120.2 (q, $^2J_{CF}$ = 32 Hz, C^3), 61.4 ($\underline{C}H_2CH_3$), 61.1 ($\underline{C}H_2CO$), 53.1 (cyclen-$\underline{C}H_2$), 47.1 (cyclen-$\underline{C}H_2$), 46.0 (cyclen-$\underline{C}H_2$), 45.4 (cyclen-$\underline{C}H_2$), 14.2 ($CH_2\underline{C}H_3$); ^{19}F NMR (658 MHz, $CDCl_3$): δ = -60.4; ESI/MS^- m/z 444.4 $[M-H]^-$; HRMS Calcd for $C_{20}H_{29}N_5O_3F_3$ 444.2222. Found 444.2228.

18. Ethyl 3-(trifluoromethyl)-4-(2-(4,7,10-tris((ethoxy(methyl)phosphoryl)methyl) -1,4,7,10-tetraazacyclododecan-1-yl)acetamido)benzoate[11]

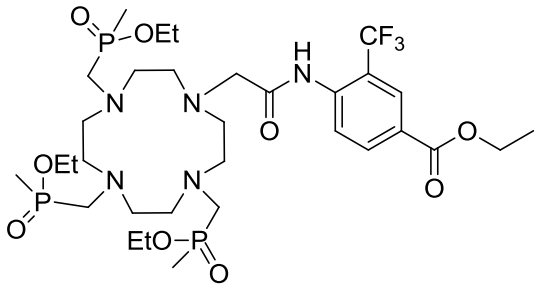

Ethyl-4-(2-(1,4,7,10-tetraazacyclododtetraazacyclododecan-1-yl)acetoamido)-3-(trifluoromethyl)] benzoate (0.40 g, 0.9 mmol) was heated to 80°C in anhydrous THF under argon. Paraformaldehyde (0.11 g, 3.6 mmol) followed by diethoxymethylphosphine (0.49 g, 3.6 mmol) were added before the solution was heated at reflux over molecular sieves for 15 h. After this time, the reaction mixture was cooled before excess paraformaldehyde was removed by filtration and the solvent removed under reduced pressure. The resulting orange oil was purified by mixed alumina/silica (4:1) gel column chromatography, eluting with a gradient starting from 100% DCM to 6 % MeOH/DCM to yield a pale yellow oil (0.40 g, 55 %). ^{1}H NMR (400 MHz, $CDCl_3$): δ = 9.97 (br s, 1 H, N$\underline{H}$), 8.46 (d, *J* = 9 Hz, 1H, H^5), 8.23 (s, 1H, H^2), 8.14 (d, *J* = 9 Hz, 1H, H^6), 4.33 (q, *J* =7 Hz, 2 H, $COOC\underline{H}_2CH_3$), 3.92 - 4.08 (m, 6H, $POC\underline{H}_2$), 3.23 (br s., 2H, $NC\underline{H}_2CO$), 2.57 – 3.12 (m, 22H, cyclen-$C\underline{H}_2$, $C\underline{H}_2P$), 1.51 (d, *J* = 16 Hz, 3H,

PC$\underline{H}_3$), 1.46 (d, *J* = 8 Hz, 3H, PC$\underline{H}_3$), 1.43 (d, *J* = 8 Hz, 3H, PC$\underline{H}_3$), 1.34 (t, *J* = 7 Hz, 3H, COOCH$_2$C$\underline{H}_3$), 1.26 (t, *J* = 8 Hz, 3H, POCH$_2$C$\underline{H}_3$), 1.23 (t, *J* = 8 Hz, 6H, POCH$_2$C$\underline{H}_3$); ^{13}C NMR (126 MHz, $CDCl_3$): δ = 173.8, 164.9, 139.1, 134.2, 127.6 (q, $^3J_{CF}$ = 5 Hz, C^2), 126.9, 125.8, 122.5 (q, $^1J_{CF}$ = 274 Hz, $\underline{C}F_3$), 122.6 (q, $^2J_{CF}$ = 34 Hz, C^3), 61.5, 60.4, 55.3, 54.5, 54.2, 53.4, 52.4, 21.0, 16.6, 14.2, 13.1; ^{19}F NMR (188 MHz, $CDCl_3$): δ = -60.7; ^{31}P NMR (81 MHz, $CDCl_3$): δ = 53.1, 52.1; ESI/MS$^+$ m/z 806.2 $[M+H]^+$; HRMS Calcd for $C_{32}H_{58}N_5O_9P_3F_3$ 806.3402. Found 806.3400.

19. 3-(Trifluoromethyl)-4-(2-(4,7,10-tris((hydroxy(methyl)phosphoryl)methyl)-1,4,7,10-tetraazacyclododecan-1-yl)acetamido)benzoic acid (L^3)[11]

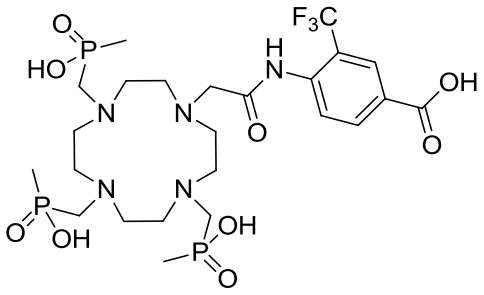

Freshly prepared aqueous KOD solution (5 mL, 0.1 M) was added to ethyl 3-(trifluoromethyl)-4-(2-(4,7,10-tris((ethoxy(methyl)phosphoryl)methyl)-1,4,7,10-tetraazacyclododecan-1-yl)acetamido)benzoate (0.30 g, 0.38 mmol). The solution was left to stir at 40°C and the reaction monitored by ^{1}H and ^{31}P NMR. After 72 h, the pH of the solution was lowered to ca. 6 by the addition of dilute $HCl_{(aq)}$. The solvent was removed under reduced pressure and the residue washed repeatedly with DCM (3 x 5 mL). The resulting oil was dissolved in EtOH. The white precipitate was removed by filtration and the solvent removed under reduced pressure to yield a pale yellow gum (0.20 g, 80%). ^{1}H NMR (400 MHz, D_2O): δ = 8.31 (s, 1H, H^2), 8.18 (d, *J* = 8 Hz, 1H, H^5), 7.60 (d, *J* = 8 Hz, 1H, H^6), 3.82 (s, 2 H, C$\underline{H}_2$CO), 3.51 (br s, 2H, cyclen-C$\underline{H}_2$), 3.32 (br s, 4H, cyclen-C$\underline{H}_2$), 3.17 (br s, 8H, cyclen-C$\underline{H}_2$), 2.96 (br s, 2H, cyclen-C$\underline{H}_2$), 1.29 (d, *J* = 14 Hz, 6 H, PC$\underline{H}_3$), 1.22 (d, *J* = 14 Hz, 3H, PC$\underline{H}_3$); ^{19}F NMR (376 MHz, D_2O): δ = -62.2; ^{31}P NMR (162 MHz, D_2O): δ = 36.2; ESI/MS$^+$ m/z 694.3 $[M+H]^+$.

20. [Dy.L^3]

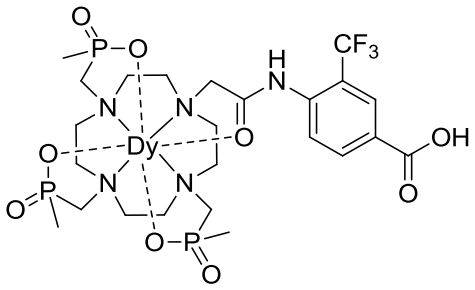

$Dy(III)Cl_3.6H_2O$ (13 mg, 0.035 mmol) was added to a stirred solution of 3-(trifluoromethyl)-4-(2-(4,7,10-tris((hydroxy(methyl)phosphoryl)methyl)-1,4,7,10-tetraazacyclododecan-1-yl)acetamido)benzoic acid (20 mg, 0.029 mmol) in water (3 mL) and the pH adjusted to 5.5 using $HCl_{(aq)}$. The reaction was left stirring overnight at 50°C. After cooling to rt, the pH was adjusted to 10 and precipitated metal hydroxide was removed by centrifugation. The solution was adjusted back to pH 5.5 with $HCl_{(aq)}$. The resulting solution was dialyzed (500 MW cut-off; Spectra/Pro® biotech cellulose ester dialysis membrane, Spectrum Laboratories), purified by semi-preparative RP-HPLC and lyophilized to obtain a white solid (12 mg, 50 %). ^{19}F NMR (376 MHz, D_2O, pH 6.5): δ = -64.5; HRMS Calcd for $C_{24}H_{38}{}^{160}DyF_3N_5O_9P_3$ 851.1165. Found 851.1195. HPLC, t_R = 4.77 min.

21. [Tm.L^3]

An analogous procedure to that described for **[Dy.L^3]** was followed, using $Tm(III)Cl_3.6H_2O$ (13 mg, 0.035 mmol) and 3-(trifluoromethyl)-4-(2-(4,7,10-tris((hydroxy(methyl)phosphoryl)methyl)-1,4,7,10-tetraazacyclododecan-1-yl) acetamido)benzoic acid (20 mg, 0.029 mmol) to obtain a white solid (18 mg, 72%). ^{19}F NMR (376 MHz, D_2O, pH 7.5): δ = -90.3; HRMS Calcd for $C_{24}H_{38}{}^{169}TmF_3N_5O_9P_3$ 858.1099. Found 858.1113. HPLC, t_R = 4.68 min.

22. [Dy.L^4]

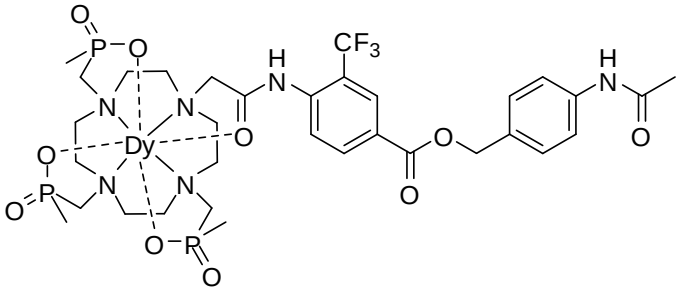

A solution of **[Dy.L^3]** (10 mg, 0.012 mmol), *N*-(4-(hydroxymethyl)phenyl)acetamide (10 mg, 0.058 mmol), DIPEA (3 mg, 0.023 mmol) and HATU (10 mg, 0.026 mmol) in anhydrous DMF (1 mL) was stirred at rt for 48 h, with the reaction monitored by LC-MS. After this time, the solvent was removed under reduced pressure. The residue was dissolved in water and dialysed (500 MW cut-off, Spectra/Pro® biotech cellulose ester dialysis membrane, Spectrum Laboratories), purified by semi-preparative RP-HPLC, and lyophilised to obtain an off white solid (4 mg, 35 %). ^{19}F NMR (376 MHz, H_2O, pH 6.5): δ = -69.4; HRMS Calcd for $C_{33}H_{48}{}^{160}DyF_3N_6O_{10}P_3$ 1022.1825. Found 1022.1786. HPLC, t_R = 7.56 min.

23. [Tm.L^4]

To a solution of **[Tm.L^3]** (10 mg, 0.012 mmol) in anhydrous DMSO (0.5 mL), was added K_2CO_3 (3 mg, 0.03 mmol) and the mixture stirred at rt for 30 min under argon. After this time, *N*-(4-(chloromethyl)phenyl)acetamide (4 mg, 0.023 mmol) was added and the reaction stirred for 18 h. The crude material was precipitated by dropping onto diethyl ether (15 mL) and isolated by centrifugation. The residue was dissolved in water and dialysed (500 MW cut-off, Spectra/Pro® biotech cellulose ester dialysis membrane, Spectrum Laboratories), purified by semi-preparative RP-HPLC, and lyophilised to obtain an off white solid (4 mg, 35 %). ^{19}F NMR (376 MHz, H_2O, pH 7.8): δ = -102.4; ESI/MS$^+$ m/z 1007.3 $[M+H]^+$. HPLC, t_R = 7.42 min.

24. [Dy.L^3-chitosan]

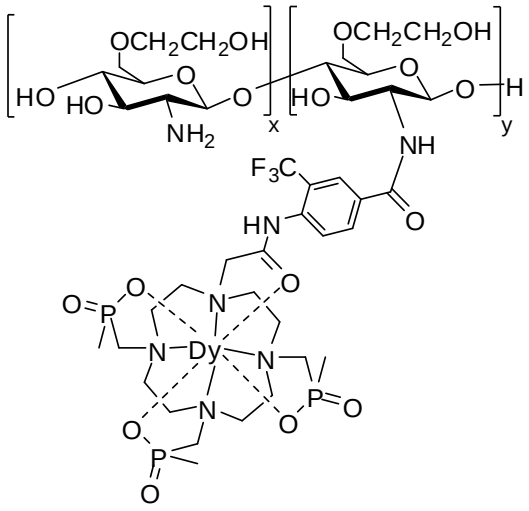

[Dy.L^3] (157 mg, 0.184 mmol) was dissolved in anhydrous DMF (2 mL) to which NMM (30 µL, 0.276 mmol) and TBTU (89 mg, 0.276 mmol) were added. The mixture was stirred at rt for 30 min under argon, before glycol chitosan (20 mg, MW ≈ 6500 D) dissolved in H_2O (0.2 mL) was added. The mixture was left stirring at 40°C for a further 18 h, before the solution was diluted with H_2O (10 mL) and dialysed against Purite water for 48 h (1000 MW cut-off), with the bulk solvent water refreshed periodically. The solvent was removed under reduced pressure, before the residue dissolved in H_2O and dialysed for a second time (5000 MW cut-off). The solution was lyophilised to yield a white solid (48 mg). ^{19}F NMR (376 MHz, D_2O, pD 6.5): δ = -65.7; Mean M_w = 10900 D by GPC analysis.

25. 4-Amino-3-(trifluoromethyl)benzoic acid[11]

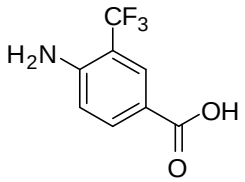

4-Amino-3-(trifluoromethyl)benzonitrile (1.00 g, 5.4 mmol) was dissolved in freshly prepared aqueous KOD solution (2.5 mL, 0.1 M) and the resulting solution left to stir at 40°C under argon, with the reaction monitored by ^{1}H and ^{19}F NMR spectroscopy. The

reaction had proceeded to completion over 72 h, after which the pH was lowered to 5.5 by the addition of HCl. The resulting white precipitate was filtered and the solvent removed under reduced pressure to yield a white solid (0.99 g, 90 %), m.p. 81-82°C. ^{1}H NMR (500 MHz, CD_3OD): δ = 8.05 (s, 1H, H^2), 7.89 (d, *J* = 8 Hz, 1H, H^6), 6.84 (d, *J* = 8 Hz, 1H, H^5), 4.90 (s, 2H, NH_2); ^{19}F NMR (376 MHz, CD_3OD): δ = -65.5; ESI/MS^- m/z 204.2 $[M-H]^-$.

26. 1H-1,2,3-Benzotriazol-1-yl 4-amino-3-(trifluoromethyl)benzoate[11]

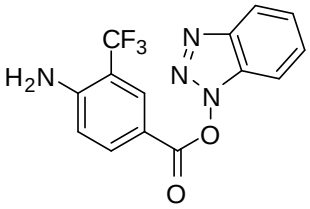

NMM (0.58 mL, 5.3 mmol) and TBTU (1.70 g, 5.3 mmol) were added to a solution of 4-amino-3-(trifluoromethyl)benzoic acid (0.90 g, 4.4 mmol) dissolved in anhydrous DMF (5 mL) and the resulting mixture stirred at rt for 30 min. After this time, the solvent was removed under reduced pressure, before the crude product was purified by alumina gel column chromatography, eluting with a gradient starting from 100 % DCM to 6 % MeOH/DCM, to yield a white solid (0.89 g, 63 %). ^{1}H NMR (400 MHz, $CDCl_3$): δ = 8.41 (s, 1H, H^2), 8.19 (d, *J* = 9 Hz, 1H, H^6), 8.12 (d, *J* = 9 Hz, 1H, Ar), 7.57 (m, 1H, Ar), 7.47 (m, 2H, Ar), 6.88 (d, *J* = 9 Hz, 1H, H^5), 4.94 (s, 2H, NH_2); ^{19}F NMR (376 MHz, $CDCl_3$): δ = -63.3; ESI/MS^+ m/z 323.2 $[M+H]^+$, 345.2 $[M+Na]^+$.

27. PAMAM-(F_8)

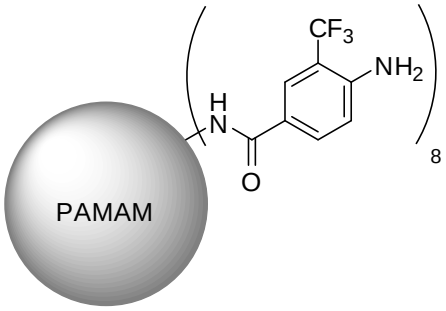

PAMAM dendrimer, ethylenediamine core, generation 1.0 (37 mg, 0.0258 mmol) was dissolved in DMF (1 mL). To this solution was added NMM (0.10 mL, 0.910 mmol) and 1H-1,2,3-benzotriazol-1-yl 4-amino-3-(trifluoromethyl)benzoate (100 mg, 0.310 mmol), before being stirred for 18 h at rt. After this time, the solvent was removed under reduced pressure. The residue was washed with DCM, followed by H_2O, to yield a yellow-brown gum (59 mg, 78 %). ^{19}F NMR (188 MHz, D_2O, pD 6.5): δ = -64.5; MALDI$^+$ 2926.5 $[M+H]^+$, 2947.9 $[M+Na]^+$, 2964.0 $[M+K]^+$.

28. [($Dy.L^3$)$_x$-PAMAM]

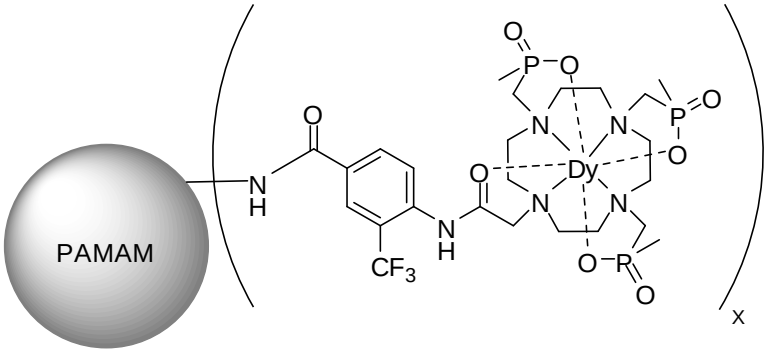

[$Dy.L^3$] (42 mg, 47.4 µmol), NMM (7.2 mg, 71.1 µmol) and TBTU (23 mg, 71.1 µmol) were dissolved in DMF (1 mL) and the solution stirred at rt for 30 min. After this time, a solution of PAMAM dendrimer, ethylenediamine core, generation 1.0 (6.8 mg, 4.74 µmol) in DMF (0.5 mL) was added and the resulting mixture stirred at rt for 3 h. The solvent was removed under reduced pressure. The residue was dissolved in H_2O (3 mL) and dialysed against Purite water for 48 h (1000 MW cut-off), with the bulk solvent water refreshed periodically. The solvent was removed under reduced pressure, before the residue dissolved in H_2O and dialysed for a second time

(5000 MW cut-off). The solution was lyophilised to yield a yellow gum (11 mg). ^{19}F NMR (376 MHz, D_2O, pD 6.5): δ = -65.7.

29. Ethyl 3-(4-amino-3-(trifluoromethyl)benzamido)propanoate

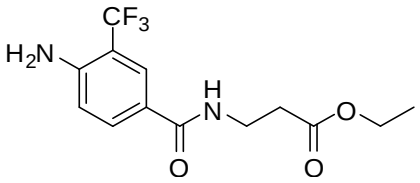

A solution of 4-amino-3-(trifluoromethyl)benzoic acid (2.00 g, 9.75 mmol), β-alanine ethyl ester hydrochloride (1.50 g, 9.75 mmol), EDC (2.06 g, 10.7 mmol), HOBt (1.60 g, 10.7 mmol), and NMM (2.14 mL, 19.5 mmol) in anhydrous DMF (10 mL) was stirred at rt for 18 h. After this time, the reaction mixture was concentrated under reduced pressure, then diluted with H_2O (20 mL). The resulting solution was extracted with ethyl acetate (2 x 20 mL). The organic layers were combined and washed with H_2O (20 mL) and brine (20 mL). The resulting organic layer was dried over $MgSO_4$, filtered, and the solvent removed under reduced pressure to give an off-white solid (2.93 g, 99 %). ^{1}H NMR (400 MHz, $CDCl_3$): δ = 7.87 (d, *J* = 2 Hz, 1H, H^2), 7.68 (dd, *J* = 9, 2 Hz, 1H, H^6), 6.79 (s, 1H, CONH), 6.72 (d, *J* = 9 Hz, 1H, H^5), 4.54 (s, 2H, NH_2), 4.15 (q, *J* = 7 Hz, 2H, $OC\underline{H}_2CH_3$), 3.68 (q, *J* = 6 Hz, 2H,$NC\underline{H}_2CH_2CO$), 2.62 (q, *J* = 6 Hz, 2H, $NCH_2C\underline{H}_2CO$), 1.25 (t, *J* = 7 Hz, 4H, $OCH_2C\underline{H}_3$); ^{19}F NMR (376 MHz, $CDCl_3$): δ = -63.4; ^{13}C NMR (101 MHz, $CDCl_3$): δ = 172.0 (CO_2), 165.0 (CONH), 146.2 (C^4), 130.6 (C^6), 125.2 (q, $^1J_{CF}$ = 5 Hz, C^2), 123.5 (q, $^1J_{CF}$ = 272 Hz, CF_3), 122.2 (C^1), 115.6 (C^5), 111.9 (q, $^1J_{CF}$ = 31 Hz, C^3), 59.8 ($O\underline{C}H_2CH_3$), 34.3 ($NCH_2\underline{C}H_2CO$), 33.0 ($N\underline{C}H_2CH_2CO$), 13.2 ($OCH_2\underline{C}H_3$); ESI/MS^+ m/z 305.2 $[M+H]^+$, 327.3 $[M+Na]^+$; HRMS Calcd for $C_{13}H_{15}N_2O_3F_3Na$ 327.0932. Found 327.0934.

30. Ethyl 3-(4-(2-chloroacetamido)-3-(trifluoromethyl)benzamido)propanoate

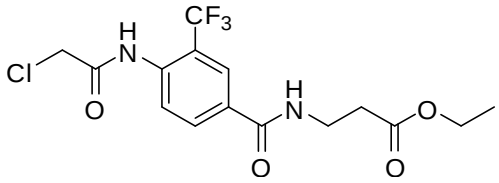

NEt_3 (1.48 mL, 10.6 mmol) was added to a solution of ethyl 3-(4-amino-3-(trifluoromethyl)benzamido)propanoate (2.93 g, 9.64 mmol) in anhydrous DCM (30 mL). The solution was cooled to 0°C, before chloroacetyl chloride (0.84 mL, 10.6 mmol) was added dropwise. The reaction mixture was allowed to warm to rt and stirred for 18 h. After this time, the solution was washed successively with $HCl_{(aq)}$ (0.1 M, 20 mL), $NaOH_{(aq)}$ (0.1 M, 20 mL), and H_2O (20 mL). The organic layer was dried over $MgSO_4$, filtered, and the solvent removed under reduced pressure to give a brown solid. This crude product was recrystallized from hexane to yield an off-white solid (0.94 g, 26 %). ^{1}H NMR (400 MHz, $CDCl_3$): δ = 8.91 (s, 1H, NH), 8.44 (d, *J* = 9 Hz, 1H, H^5), 8.13 (s, 1H, H^2), 7.92 (d, *J* = 9 Hz, 1H, H^6), 6.91 (s, 1H, NH), 4.25 (s, 2H, CH_2Cl), 4.18 (q, *J* = 7 Hz, 2H, $OC\underline{H}_2CH_3$), 3.73 (m, 2H, $NCH_2C\underline{H}_2CO$), 2.65 (m, 2H, $NC\underline{H}_2CH_2CO$), 1.28 (t, *J* = 7 Hz, 3H, $OCH_2C\underline{H}_3$); ^{19}F NMR (376 MHz, $CDCl_3$): δ = -61.3; ^{13}C NMR (101 MHz, $CDCl_3$): δ = 171.9 (CO_2), 164.1 (CONH), 163.3 (CONH), 136.0 (C^4), 130.1 (C^6), 129.8 (C^1), 124.8 (q, $^3J_{CF}$ = 5 Hz, C^2), 122.5 (q, $^1J_{CF}$ = 273 Hz, CF_3), 121.9 (C^5), 119.0 (q, $^2J_{CF}$ = 31 Hz, C^3), 60.0 ($O\underline{C}H_2CH_3$), 41.9 ($\underline{C}H_2Cl$), 34.5 ($NCH_2\underline{C}H_2CO$), 32.8 ($N\underline{C}H_2CH_2CO$), 13.2 ($OCH_2\underline{C}H_3$); ESI/MS^+ m/z 381.2 $[M+H]^+$, 403.2 $[M+Na]^+$; HRMS Calcd for $C_{15}H_{17}N_2O_4F_3Cl$ 381.0829. Found 381.0825.

31. Ethyl-3-(4-(2-(1,4,7,10-tetraazacyclododecan-1-yl)acetamido)-3-(trifluoromethyl)benzamido)propanoate

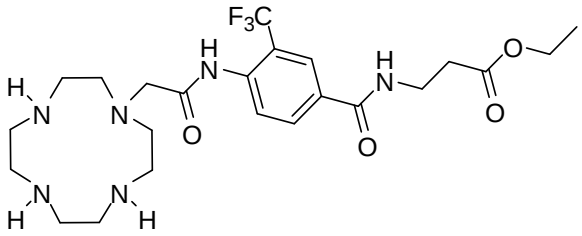

A solution of ethyl 3-(4-(2-chloroacetamido)-3-(trifluoromethyl)benzamido)propanoate (0.44 g, 1.14 mmol) in anhydrous MeCN (20 mL) was added dropwise to a stirred solution of 1,4,7,10-tetraazacyclododecane (1.97 g, 11.4 mmol) in anhydrous MeCN (30 mL) at 40°C under argon. After 5 h, the solvent was removed under reduced pressure and the residue dissolved in DCM (20 mL). The solution was washed repeatedly with H_2O (4 x 20 mL), dried over $MgSO_4$, and the solvent removed under reduced pressure to yield a light yellow oil (0.42 g, 72 %). ^{1}H NMR (400 MHz, $CDCl_3$): δ = 8.25 (d, *J* = 9 Hz, 1H, H^5), 8.09 (d, *J* = 2 Hz, 1H, H^2), 7.86 (dd, *J* = 9, 2 Hz, 1H, H^6), 6.90 (s, 1H, NH), 4.17 (q, *J* = 7 Hz, 2H, $OC\underline{H}_2CH_3$), 3.72 (m, 2H, $NCH_2C\underline{H}_2CO$), 3.34 (s, 2H, $NC\underline{H}_2CONH$), 2.78 (br m, 8H, cyclen-$C\underline{H}_2$), 2.70 (br m, 4H, cyclen-$C\underline{H}_2$), 2.63 (br m, 6H, $NC\underline{H}_2CH_2CO$/cyclen-$C\underline{H}_2$), 1.27 (t, *J* = 7 Hz, 3H, $OCH_2C\underline{H}_3$); ^{19}F NMR (376 MHz, $CDCl_3$): δ = -60.8; ^{13}C NMR (101 MHz, $CDCl_3$): δ = 171.8 (CO_2), 169.3 (CONH), 164.4 (CONH), 136.9 (C^4), 129.8 (C^6), 129.6 (C^1), 124.8 (q, $^3J_{CF}$ = 5 Hz, C^2), 124.1 (C^5), 122.6 (q, *J* = 274 Hz, CF_3), 120.0 (q, *J* = 30 Hz, C^3), 59.9 ($O\underline{C}H_2CH_3$), 59.9 ($N\underline{C}H_2CONH$), 52.1 (cyclen-$\underline{C}H_2$), 46.1 (cyclen-$\underline{C}H_2$), 45.1 (cyclen-$\underline{C}H_2$), 44.4 (cyclen-$\underline{C}H_2$), 34.5 ($NCH_2\underline{C}H_2CO$), 32.8 ($N\underline{C}H_2CH_2CO$), 13.2 ($OCH_2\underline{C}H_3$); ESI/MS^+ m/z 517.4 $[M+H]^+$; HRMS Calcd for $C_{23}H_{36}N_6O_4F_3$ 517.2750. Found 517.2767.

32. Ethyl-3-(3-(trifluoromethyl)-4-(2-(4,7,10-tris((ethoxy(methyl)phosphoryl) methyl)-1,4,7,10-tetraazacyclododecan-1-yl)acetamido)benzamido) propanoate

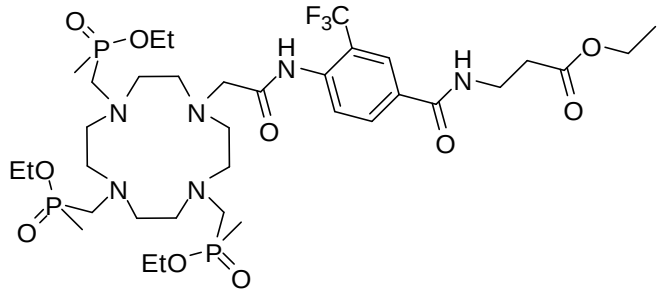

Ethyl-3-(4-(2-(1,4,7,10-tetraazacyclododecan-1-yl)acetamido)-3-(trifluoromethyl) benzamido)propanoate (0.16 g, 0.31 mmol) was heated to 80°C in anhydrous THF under argon. Paraformaldehyde (0.11 g, 3.68 mmol) followed by diethoxymethylphosphine (0.50 g, 3.68 mmol) were added before the solution was heated at reflux over molecular sieves for 15 h. After this time, the reaction mixture was cooled before excess paraformaldehyde was removed by filtration and the solvent removed under reduced pressure. The resulting orange oil was purified by mixed alumina/silica (4:1) gel column chromatography, eluting with a gradient starting from 100% DCM to 6 % MeOH/DCM to yield a pale yellow oil (0.14 g, 50 %). ^{1}H NMR (400 MHz, $CDCl_3$): δ = 10.31 (s, 1H, NH), 8.12 (s, 1H, H^2), 7.96 (d, *J* = 8 Hz, 1H, H^5), 7.69 (d, *J* = 8 Hz, 1H, H^6), 7.58 (s, 1H, NH), 4.39 (s, 2H, $NC\underline{H}_2CONH$), 4.15 (q, *J* = 7 Hz, 2H, $CO_2C\underline{H}_2CH_3$), 4.07 (m, 6H, $NC\underline{H}_2P$), 3.69 (m, 2H, $NCH_2C\underline{H}_2CO$), 3.44 (br s, 4H, cyclen-$C\underline{H}_2$), 3.19 (br m, 4H, cyclen-$C\underline{H}_2$), 3.09 (br s, 8H, cyclen-$C\underline{H}_2$), 2.65 (t, *J* = 6 Hz, 2H, $NC\underline{H}_2CH_2CO$), 1.54 (m, 9H, $PC\underline{H}_3$), 1.30 (m, 9H, $POCH_2C\underline{H}_3$), 1.25 (t, *J* = 7 Hz, 3H, $CO_2CH_2C\underline{H}_3$); ^{19}F NMR (376 MHz, $CDCl_3$): δ = -61.8; ^{31}P NMR (162 MHz, $CDCl_3$): δ = 50.7, 49.9; ESI/MS^+ m/z 877.6 $[M+H]^+$, 899.5 $[M+Na]^+$; HRMS Calcd for $C_{35}H_{62}N_6O_{10}F_3P_3Na$ 899.3590. Found 899.3610.

33. 3-(3-(trifluoromethyl)-4-(2-(4,7,10-tris((hydroxy(methyl)phosphoryl)methyl)-1,4,7,10-tetraazacyclododecan-1-yl)acetamido)benzamido)propanoic acid (L^3- βala)

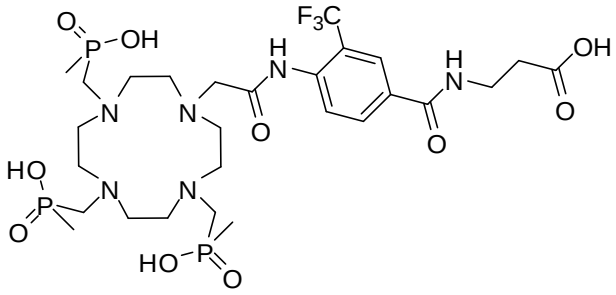

Freshly prepared aqueous KOD solution (5 mL, 0.1 M) was added to ethyl 3-(3-(trifluoromethyl)-4-(2-(4,7,10-tris((ethoxy(methyl)phosphoryl)methyl)-1,4,7,10-tetraazacyclododecan-1-yl)acetamido)benzamido)propanoate (0.10 g, 0.11 mmol). The solution was left to stir at 40°C and the reaction monitored by ^{1}H and ^{31}P NMR. After 72 h, the pH of the solution was lowered to ca. 6 by the addition of dilute $HCl_{(aq)}$. The solvent was removed under reduced pressure and the residue washed repeatedly with DCM (3 x 5 mL). The resulting oil was dissolved in EtOH. The white precipitate was removed by filtration and the solvent removed under reduced pressure to yield a pale yellow gum (73 mg, 84%). ^{1}H NMR (400 MHz, D_2O): δ = 7.91 (s, 1H, H^2), 7.74 (d, *J* = 8 Hz, 1H, H^5), 7.04 (d, *J* = 8 Hz, 1H, H^6), 3.51 (m, 10H, $NCH_2C\underline{H}_2CO/NC\underline{H}_2P/NC\underline{H}_2CONH$), 2.74 (br m, 10H, cyclen-$C\underline{H}_2$), 2.63 (br m, 6H, cyclen-$C\underline{H}_2$), 2.40 (t, *J* = 7 Hz, 3H, $NC\underline{H}_2CH_2CO$), 1.14 (d, $^{2}J_{HP}$ = 13 Hz, 9H, $PC\underline{H}_3$); ^{19}F NMR (376 MHz, D_2O): δ = -62.2; ^{31}P NMR (162 MHz, D_2O): δ = 38.9, 37.7; ESI/MS^- m/z 766.1 $[M-H]^-$.

34. [Dy.L^3-βala]

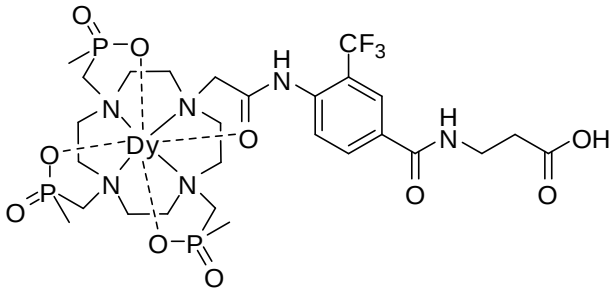

$Dy(III)Cl_3.6H_2O$ (24 mg, 0.063 mmol) was added to a stirred solution 3-(3-(trifluoromethyl)-4-(2-(4,7,10-tris((hydroxy(methyl)phosphoryl)methyl)-1,4,7,10-tetraazacyclododecan-1-yl)acetamido)benzamido)propanoic acid (40 mg, 0.052 mmol) in water (3 mL) and the pH adjusted to 5.5 using $HCl_{(aq)}$. The reaction was left stirring overnight at 50°C. After cooling to rt, the pH was adjusted to 10 and precipitated metal hydroxide was removed by centrifugation. The solution was adjusted back to pH 5.5 with $HCl_{(aq)}$. The resulting solution was dialysed (500 MW cut-off; Spectra/Pro® biotech cellulose ester dialysis membrane, Spectrum Laboratories), and lyophilised to obtain a white solid (42 mg, 88 %). ^{19}F NMR (188 MHz, D_2O, pH 6.5): δ = -65.6; ESI/MS$^-$ m/z 923.9 $[M-H]^-$.

35. *tert*-Butyl 4-amino-3-(trifluoromethyl)benzoate

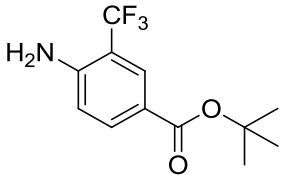

Perchloric acid (2-3 drops, 70 % in H_2O) was added to a stirred solution of 4-amino-3-(trifluoromethyl)benzoic acid (1.5 g, 7.32 mmol) in *tert*-butyl acetate (15 mL). The reaction mixture was stirred for 16 h at rt. After this time, H_2O (20 mL) was added and the organic layer extracted. This was then washed with H_2O (2 x 20 mL) and 5 % $Na_2CO_{3(aq)}$ (2 x 20 mL). The organic layer was dried over $MgSO_4$, filtered, and the solvent removed under reduced pressure. The resulting yellow solid was purified by silica gel column chromatography, eluting with a gradient starting from 100 % toluene to 10 % DCM/toluene to yield a white solid (0.450 g, 24 %). R_f (10 % DCM/toluene)

= 0.22, m.p. 122-125°C. ^{1}H NMR (400 MHz, $CDCl_3$): δ = 8.11 (d, *J* = 2 Hz, 1H, H^2), 7.92 (dd, *J* = 9, 2 Hz, 1H, H^6), 6.73 (d, *J* = 9 Hz, 1H, H^5), 1.60 (s, 9H, $C(C\underline{H}_3)_3$); ^{19}F NMR (376 MHz, $CDCl_3$); δ = -64.0; ^{13}C NMR (101 MHz, $CDCl_3$): δ = 163.88 ($\underline{C}OO^tBu$), 146.81 (C^4), 133.11 (C^6), 127.88 (q, $^3J_{CF}$ = 5 Hz, C^2), 123.54 (q, $^1J_{CF}$ = 272 Hz, $\underline{C}F_3$), 120.14 (C^1), 115.16 (C^5), 111.70 (q, $^2J_{CF}$ = 30.8 Hz, C^3), 79.84 ($\underline{C}(CH_3)_3$), 27.24 ($C(\underline{C}H_3)_3$); ESI/MS^- m/z 260.2 $[M-H]^-$; HRMS Calcd for $C_{12}H_{13}NO_2F_3$ 260.0898. Found 260.0901.

36. *tert*-Butyl 4-(2-chloroacetamido)-3-(trifluoromethyl)benzoate

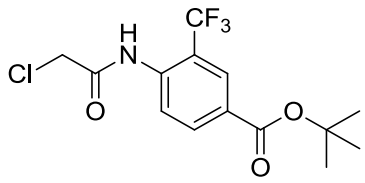

Chloroacetyl chloride (0.210 g, 1.86 mmol) was added dropwise to a stirred solution of *tert*-butyl 4-amino-3-(trifluoromethyl)benzoate (0.243 g, 0.93 mmol), NEt_3 (0.141 g, 1.40 mmol), and 4-dimethylaminopyridine (ca. 10 mg) in anhydrous THF (10 mL) at 0°C under argon for 2 h. After this time, the reaction was allowed to warm to rt and stirred for a further 18 h, before the crude mixture was concentrated under reduced pressure and diluted with DCM (15 mL). This organic mixture was washed with HCl (15 mL, 0.1 M), NaOH (15 mL, 0.1 M), and H_2O (15 mL). The combined organic extracts were dried over $MgSO_4$ and the solvent removed under reduced pressure. The resulting residue was purified over silica gel in toluene to yield a yellow solid (210 mg, 67 %). R_f (10 % DCM/toluene) = 0.32. ^{1}H NMR (400 MHz, $CDCl_3$): δ = 8.92 (s, 1H, NH), 8.43 (d, *J* = 9 Hz, 1H, H^5), 8.26 (d, *J* = 2 Hz, 1H, H^2), 8.17 (dd, *J* = 9, 2 Hz, 1H, H^6), 4.24 (s, 2H, $C\underline{H}_2CO$), 1.59 (s, 9H, ^{t}Bu); ^{13}C NMR (101 MHz, $CDCl_3$): δ = 164.2 (CO), 163.8 (CO), 137.7 (C^4), 134.1 (C^6), 128.5 (C^1), 127.7 (d, *J* = 6 Hz, C^2), 123.5 (q, $^1J_{CF}$ = 273 Hz, CF_3), 122.4 (s, 6C), 119.4 (q, $^2J_{CF}$ = 31 Hz, C^3), 82.0 ($\underline{C}(CH_3)_3$), 42.9 ($\underline{C}H_2CO$), 28.1 ($C(\underline{C}H_3)_3$); ^{19}F NMR (376 MHz, $CDCl_3$): δ = -61.3; ESI/MS^- m/z 336.2 $[M-H]^-$; HRMS Calcd for $C_{14}H_{14}NO_3F_3Cl$ 336.0614. Found 336.0612.

37. *tert*-Butyl-4-(2-(1,4,7,10-tetraazacyclododecan-1-yl)acetamido)-3-(trifluoromethyl)benzoate

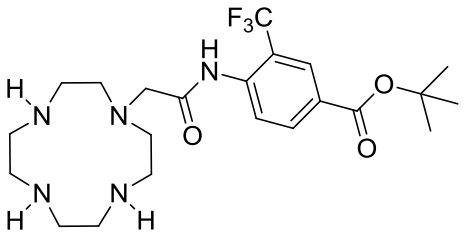

A solution of *tert*-butyl 4-(2-chloroacetamido)-3-(trifluoromethyl)benzoate (300 mg, 0.89 mmol) in anhydrous MeCN (10 mL) was added dropwise to a stirred solution of 1,4,7,10-tetraazacyclododecane (1.53 g, 8.90 mmol) in anhydrous MeCN (20 mL) at 40°C under argon. After 5 h, the solvent was removed under reduced pressure and the residue dissolved in DCM (20 mL). The solution was washed repeatedly with H_2O (4 x 20 mL), dried over $MgSO_4$, and the solvent removed under reduced pressure to yield a light yellow oil (360 mg, 86 %). ^{1}H NMR (400 MHz, $CDCl_3$): δ = 8.21 (d, *J* = 9 Hz, 1H, H^5), 8.16 (d, *J* = 2 Hz, 1H, H^2), 8.06 (dd, *J* = 9, 2 Hz, 1H, H^6), 3.27 (s, 2H, C$\underline{H}_2$CO), 2.71 (br m, 8H, cyclen-C$\underline{H}_2$), 2.63 (br m, 4H, cyclen-C$\underline{H}_2$), 2.56 (br m, 4H, cyclen-C$\underline{H}_2$), 1.52 (s, 9H, ^{t}Bu); ^{13}C NMR (176 MHz, $CDCl_3$): δ = 169.1 (CO), 163.1 (CO), 137.7 (C^4), 132.8 (C^6), 127.1 (C^1), 126.6 (q, *J* = 6 Hz, C^2), 123.4 (C^5), 122.7 (q, $^1J_{CF}$ = 274 Hz, CF_3), 119.2 (q, *J* = 30 Hz, C^3), 80.8 ($\underline{C}(CH_3)_3$), 60.1 (N$\underline{C}H_2$CO), 52.1 (cyclen-$\underline{C}H_2$), 46.1 (cyclen-$\underline{C}H_2$), 45.1 (cyclen-$\underline{C}H_2$), 44.4 (cyclen-$\underline{C}H_2$), 27.1 (C($\underline{C}H_3)_3$); ^{19}F NMR (658 MHz, $CDCl_3$): δ = -61.3; ESI/MS^+ m/z 474.8 $[M+H]^+$, ESI/MS^- m/z 472.7 $[M-H]^-$; HRMS Calcd for $C_{22}H_{35}N_5O_3F_3$ 474.2692. Found 474.2704.

38. *tert*-Butyl 3-(trifluoromethyl)-4-(2-(4,7,10-tris((ethoxy(methyl)phosphoryl) methyl)-1,4,7,10-tetraazacyclododecan-1-yl)acetamido)benzoate

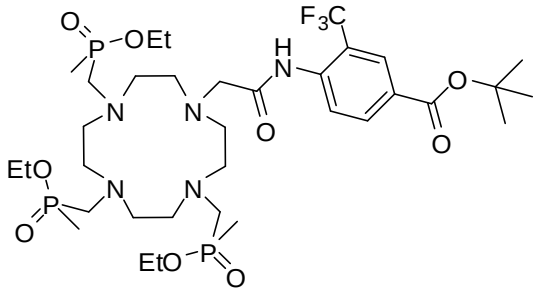

tert-Butyl-4-(2-(1,4,7,10-tetraazacyclododecan-1-yl)acetamido)-3-(trifluoromethyl) benzoate (0.31 g, 0.66 mmol) was heated to 80°C in anhydrous THF under argon. Paraformaldehyde (0.22 g, 7.35 mmol) followed by diethoxymethylphosphine (1.00 g, 7.35 mmol) were added before the solution was heated at reflux over molecular sieves for 15 h. After this time, the reaction mixture was cooled before excess paraformaldehyde was removed by filtration and the solvent removed under reduced pressure. The resulting orange oil was purified by mixed alumina/silica (3:1) gel column chromatography, eluting with a gradient starting from 100% DCM to 8 % MeOH/DCM to yield a pale yellow oil (0.34 g, 61 %). R_f (5 % MeOH/DCM, alumina plates) = 0.46. ^{1}H NMR (400 MHz, $CDCl_3$): δ = 8.47 (d, *J* = 9 Hz, 1H, H^5), 8.22 (s, 1H, H^2), 8.13 (d, *J* = 9 Hz, 1H, H^6), 4.08 (br m, 6H, POC$\underline{H}_2$CH$_3$), 3.84 (m, 2H, NC$\underline{H}_2$CONH), 3.29 (br s, 2H, cyclen-C$\underline{H}_2$), 3.15 (br s, 2H, cyclen-C$\underline{H}_2$), 2.88 (br m, 18H, cyclen-C$\underline{H}_2$/NC$\underline{H}_2$P), 1.58 (s, 9H, $CO_2{}^t$Bu), 1.50 (m, 9H, PC$\underline{H}_3$), 1.31 (m, 9H, POCH$_2$C$\underline{H}_3$); ^{19}F NMR (376 MHz, $CDCl_3$): δ = -61.6; ^{31}P NMR (162 MHz, $CDCl_3$): δ = 51.9, 51.1; ESI/MS$^+$ m/z 835.1 $[M+H]^+$; HRMS Calcd for $C_{34}H_{62}N_5O_9F_3P_3$ 834.3713. Found 834.3690.

39. 3-(Trifluoromethyl)-4-(2-(4,7,10-tris((ethoxy(methyl)phosphoryl)methyl)-1,4,7,10-tetraazacyclododecan-1-yl)acetamido)benzoic acid

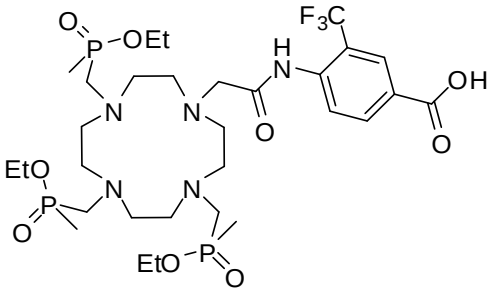

tert-Butyl-3-(trifluoromethyl)-4-(2-(4,7,10-tris((ethoxy(methyl)phosphoryl)methyl)-1,4,7,10-tetraazacyclododecan-1-yl)acetamido)benzoate (250 mg, 0.30 mmol) was dissolved in DCM (5 mL). To this was added TFA (2 mL) and the mixture was stirred at rt for 3 h. After this time, the solvent was removed under reduced pressure to give a crude yellow oil, which was repeatedly washed with DCM to yield a pale yellow oil (224 mg, 96 %). ^{1}H NMR (400 MHz, CD_3OD): δ = 8.33 (s, 1H, H^2), 8.27 (d, *J* = 8 Hz, 1H, H^6), 7.88 (d, *J* = 8 Hz, 1H, H^5), 4.14 (m, 8H, POC$\underline{H}_2$CH$_3$/C$\underline{H}_2$CONH), 3.84 (m, 6H, NC$\underline{H}_2$P), 3.37 (br m, 12H, cyclen-C$\underline{H}_2$), 3.22 (br m, 2H, cyclen-C$\underline{H}_2$), 3.08 (br m, 2H, cyclen-C$\underline{H}_2$), 1.52 (d, *J* = 14 Hz, 9H, PC$\underline{H}_3$), 1.31 (t, *J* = 7 Hz, 9H); ^{19}F NMR (376 MHz, CD_3OD): δ = -62.6; ^{31}P NMR (81 MHz, CD_3OD): δ = 54.9, 54.0; ESI/MS$^+$ m/z 779.0 $[M+H]^+$, 800.9 $[M+Na]^+$; HRMS Calcd for $C_{30}H_{54}N_5O_9F_3P_3$ 778.3087. Found 778.3102.

40. 5-(Trifluoromethyl)pyridine-2-carboxylic acid[12]

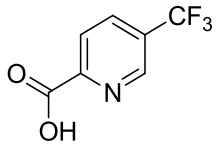

Butyllithium (2.5 M in hexanes, 22.1 mmol) was added dropwise to 2-bromo-5-(trifluoromethyl)pyridine (5.00 g, 22.1 mmol) in anhydrous THF (20 mL) at -78°C. After stirring for 2 h, the mixture was poured onto an excess of freshly crushed $CO_{2(s)}$. The solvent was removed under reduced pressure and the residue dissolved in $NaOH_{(aq)}$ (2M, 50 mL). This was washed with diethyl ether (2 x 50 mL) and acidified to pH 2 before being extracted by diethyl ether (2 x 50 mL) and dried with $MgSO_4$. The solvent was removed under reduced pressure and the residue recyrstallised from hexane to

yield colourless needles (1.86 g, 44 %). ^{1}H NMR (400 MHz, $CDCl_3$): δ = 8.96 (s, 1H, H^6), 8.41 (d, *J* = 8 Hz, 1H, H^3), 8.25 (d, *J* = 8 Hz, 1H, H^4); ^{19}F NMR (376 MHz, $CDCl_3$): δ = -62.6; ESI/MS^+ m/z 192.1 $[M+H]^+$; HRMS Calcd for $C_7H_3NO_2F_3$ 190.0110. Found 190.0116.

41. Methyl 5-(trifluoromethyl)pyridine-2-carboxylate

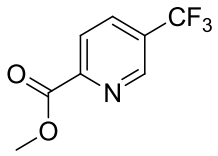

Concentrated H_2SO_4 (2 mL) was added to a stirred solution of 5-(trifluoromethyl)pyridine-2-carboxylic acid (1.50 g, 7.85 mmol) in methanol (25 mL). The reaction mixture was then boiled under reflux for 24 h before being cooled and concentrated under vacuum. The residue was diluted in water (25 mL), neutralised with $K_2CO_{3\ (aq)}$, and extracted with DCM (3 x 25 mL). The organic layers were combined, washed with brine (2 x 25 mL) and dried over Na_2SO_4. The solvent was removed under reduced pressure to yield a white solid (1.28 g, 80 %). R_f (50% EtOAc/hexane) = 0.49. ^{1}H NMR (400 MHz, $CDCl_3$): δ = 9.02 (s, 1H, H^6), 8.29 (d, *J* = 8 Hz, 1H, H^3), 8.13 (d, *J* = 8 Hz, 1H, H^4), 4.07 (s, 3H, CH_3); ^{19}F NMR (376 MHz, $CDCl_3$): δ = -62.6; ESI/MS^+ m/z 206.1 $[M+H]^+$, 228.2 $[M+Na]^+$; HRMS Calcd for $C_8H_7F_3NO_2$ 206.0412. Found 206.0429.

42. (5-(Trifluoromethyl)pyridin-2-yl)methanol

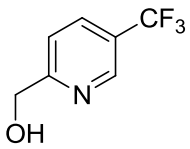

$NaBH_4$ (0.369 g, 9.75 mmol) was added to methyl 5-(trifluoromethyl)pyridine-2-carboxylate (1.00 g, 5.00 mmol) in EtOH (40 mL) and the resulting suspension boiled under reflux for 18 h. After this time, the mixture was allowed to cool to rt then quenched with saturated NH_4Cl solution. The solvent was removed under reduced pressure and the residue dissolved in H_2O (20 mL), which was then extracted with

EtOAc (2 x 20 mL). The organic layers were combined, washed with H_2O (30 mL) and brine (30 mL), and dried over Na_2SO_4. The solvent was removed under reduced pressure to yield a colourless oil (0.643 g, 73 %). R_f (50 % EtOAc/hexane) = 0.37. ^{1}H NMR (400 MHz, $CDCl_3$): δ = 8.79 (s, 1H, H^6), 7.92 (d, J = 7 Hz, 1H, H^4), 7.46 (d, J = 7 Hz, 1H, H^3), 4.83 (s, 2H, CH_2), 4.29 (s, 1H, OH); ^{13}C NMR (101 MHz, $CDCl_3$): δ = 163.4 (C^2), 145.6 (q, $^3J_{CF}$ = 4 Hz, C^6), 133.9 (q, $^3J_{CF}$ = 3 Hz, C^4), 128.5 (C^3), 125.5 (q, $^2J_{CF}$ = 33 Hz, C^5), 123.4 (q, $^1J_{CF}$ = 272 Hz, CF_3), 64.2 ($\underline{C}H_2OH$); ^{19}F NMR (376 MHz, $CDCl_3$): δ = -62.8; ESI/MS$^+$ m/z 178.1 $[M+H]^+$; HRMS Calcd for $C_7H_7F_3NO$ 178.0468. Found 178.0480.

43. 2-(Bromomethyl)-5-(trifluoromethyl)pyridine

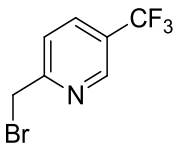

Phosphorus tribromide (0.40 mL, 4.23 mmol) was added dropwise to a solution of (5-(trifluoromethyl)pyridin-2-yl)methanol (500 mg, 2.82 mmol) in anhydrous DCM (15 mL) at 0°C under argon. The reaction mixture was allowed to warm to rt and stirred for 2 h. After this time, the reaction was quenched with $NaHCO_{3(aq)}$ (15 mL), extracted with DCM (2 x 20 mL), and dried over $MgSO_4$ before the solvent was removed under reduced pressure. The crude material was purified by silica gel column chromatography, eluting with a gradient starting from 100 % hexane to 20 % ethyl acetate/hexane to yield a pale yellow oil (210 mg, 31 %). R_f (20 % ethyl acetate/hexane) = 0.49. ^{1}H NMR (400 MHz, $CDCl_3$): δ = 8.81 (s, 1H, H^6), 7.92 (d, J = 8 Hz, 1H, H^4), 7.57 (d, J = 8 Hz, 1H, H^3), 4.57 (s, 2H, CH_2); ^{13}C NMR (101 MHz, $CDCl_3$): δ = 160.6 (q, $^4J_{CF}$ = 1 Hz, C^3), 146.5 (q, $^3J_{CF}$ = 4 Hz, C^6), 134.3 (q, $^3J_{CF}$ = 4 Hz, C^4), 125.9 (q, $^2J_{CF}$ = 33 Hz, C^5), 123.3 (q, $^1J_{CF}$ = 272 Hz, CF_3), 123.2 (C^2), 32.5 ($\underline{C}H_2Br$); ^{19}F NMR (376 MHz, $CDCl_3$): δ = -62.9; ESI/MS$^+$ m/z 240.1 $[M+H]^+$; HRMS Calcd for $C_7H_6BrF_3N$ 239.9655. Found 239.9636.

44. (5-(Trifluoromethyl)pyridin-2-yl)methyl methanesulphonate

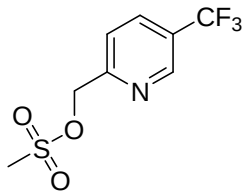

(5-(Trifluoromethyl)pyridin-2-yl)methanol (0.64 g, 3.63 mmol) was dissolved in THF (5mL) and cooled to 5°C. Triethylamine (1 mL, 7.26 mmol) and mesyl chloride (0.42 mL, 5.45 mmol) were added dropwise to this solution, upon which a white solid precipitated from solution. Once addition was complete, the reaction mixture was allowed to warm to rt and stirred for 15 min before the solvent was removed under reduced pressure. The residue was dissolved in brine (50 mL) and extracted with DCM (2 x 50 mL). The organic layers were combined, dried over $MgSO_4$, and the solvent removed under reduced pressure to yield a yellow oil (0.89 g, 96 %). R_f (10 % MeOH/DCM) = 0.81. ^{1}H NMR (400 MHz, $CDCl_3$): δ = 8.87 (s, 1H, H^6), 8.01 (d, *J* = 8 Hz, 1H, H^4), 7.64 (d, *J* = 8 Hz, 1H, H^3), 5.40 (s, 2H, CH_2), 3.15 (s, 3H, $SO_2C\underline{H}_3$); ^{13}C NMR (101 MHz, $CDCl_3$): δ = 157.7 (q, $^4J_{CF}$ = 1 Hz, C^3), 146.5 (q, $^3J_{CF}$ = 4 Hz, C^6), 134.4 (q, $^3J_{CF}$ = 4 Hz, C^4), 126.5 (q, $^2J_{CF}$ = 33 Hz, C^5), 123.2 (q, $^1J_{CF}$ = 273 Hz, CF_3), 121.6 (C^2), 70.3 ($SO_2\underline{C}H_3$), 38.0 ($\underline{C}H_2OMS$); ^{19}F NMR (376 MHz, $CDCl_3$): δ = -62.5; ESI/MS$^+$ m/z 256.2 $[M+H]^+$, 278.2 $[M+Na]^+$; HRMS Calcd for $C_8H_9F_3NO_3S$ 256.0255. Found 256.0253.

45. 1,4,7-Tris-*tert*-butoxycarbonyl-1,4,7,10-tetraazacyclododecane[13,14]

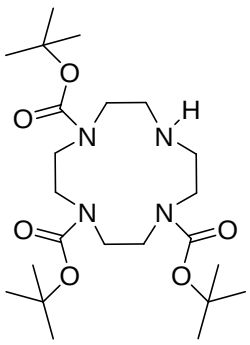

A solution of di-*tert*-butyl dicarbonate (10.1 g, 46.7 mmol) in chloroform (65 mL) was added dropwise over 2 h, at 0°C, to a stirred solution of cyclen (2.86 g, 15.6 mmol) and

triethylamine (6.5 mL, 46.7 mmol) in chloroform (85 mL) under argon. The reaction mixture was then stirred at rt for 18 h before being washed with H_2O (2 x 100 mL). The organic phase was dried over Na_2SO_4, filtered, and the solvent removed under reduced pressure. The resulting white solid was purified by silica gel column chromatography, eluting with diethyl ether to yield a white solid (4.47 g, 61 %). R_f (Et_2O) = 0.21. ^{1}H NMR (400 MHz, $CDCl_3$): δ = 3.61 (br s, 4H, cyclen-C$\underline{H}_2$), 3.33 (br s, 8H, cyclen-C$\underline{H}_2$), 2.83 (br s, 4H, cyclen-C$\underline{H}_2$), 1.46 (s, 9H, ^{t}Bu), 1.44 (s, 18H, ^{t}Bu); ^{13}C NMR (101 MHz, $CDCl_3$): δ = 155.6 ($\underline{C}O_2{}^t$Bu), 155.4 ($\underline{C}O_2{}^t$Bu), 79.3 ($\underline{C}(CH_3)_3$), 79.2 ($\underline{C}(CH_3)_3$), 51.0 (cyclen-$\underline{C}H_2$), 49.5 (cyclen-$\underline{C}H_2$), 46.0 (cyclen-$\underline{C}H_2$), 45.0 (cyclen-$\underline{C}H_2$), 28.7 (C($\underline{C}H_3)_3$), 28.5 (C($\underline{C}H_3)_3$); ESI/MS$^+$ m/z 473.5 $[M+H]^+$; HRMS Calcd for $C_{23}H_{45}N_4O_6$ 473.3323. Found 473.3339.

46. Tri-*tert*-butyl-10-((5-(trifluoromethyl)pyridin-2-yl)methyl)-1,4,7,10-tetraazacyclododecane-1,4,7-tricarboxylate

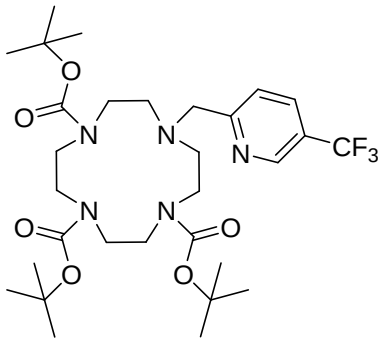

Both 2-(bromomethyl)-5-(trifluoromethyl)pyridine and (5-(trifluoromethyl)pyridin-2-yl) methyl methanesulphonate were used as starting materials to form the *title compound* following identical procedures. For example, a stirred mixture of 1,4,7-tris-*tert*-butoxycarbonyl-1,4,7,10-tetraazacyclododecane (1.60 g, 3.39 mmol), (5-(trifluoromethyl)pyridin-2-yl)methyl methanesulphonate (0.787 g, 3.08 mmol), and K_2CO_3 (0.639 g, 4.62 mmol) in anhydrous MeCN (25 mL) was boiled under reflux for 18 h under argon. After this, the reaction mixture was cooled and filtered before the solvent was removed under reduced pressure. The resulting yellow oil was purified by silica gel column chromatography, eluting with a gradient starting from 100 % DCM to 2 % MeOH/DCM to yield a yellow sticky solid (0.99 g, 51 %). ^{1}H NMR (400 MHz, $CDCl_3$): δ = 8.82 (s, 1H, H^6), 7.85 (d, *J* = 7 Hz, 1H, H^3), 7.48 (d, *J* = 7 Hz, 1H, H^4), 3.92 (s, 2H, NC$\underline{H}_2$py), 3.48 (br m, 12H, cyclen-C$\underline{H}_2$), 2.74 (br m, 4H, cyclen-C$\underline{H}_2$), 1.49 (s, 18H, ^{t}Bu),

1.42 (s, 9H, ^{t}Bu); ^{13}C NMR (101 MHz, $CDCl_3$): δ = 155.2 ($\underline{C}O_2{}^{t}Bu$), 154.5 (C^2), 145.0 (q, $^3J_{CF}$ = 6 Hz, C^6), 132.2 (q, $^3J_{CF}$ = 6 Hz, C^4), 124.1 (q, $^2J_{CF}$ = 33 Hz, C^5), 123.6 (C^3), 122.6 (q, $^1J_{CF}$ = 270 Hz, CF_3), 78.6 ($\underline{C}(CH_3)_3$), 57.1 ($N\underline{C}H_2py$), 54.0 (cyclen-$\underline{C}H_2$), 53.2 (cyclen-$\underline{C}H_2$), 52.4 (cyclen-$\underline{C}H_2$), 49.0 (cyclen-$\underline{C}H_2$), 46.9 (cyclen-$\underline{C}H_2$), 27.7 ($C(\underline{C}H_3)_3$), 27.4 ($C(\underline{C}H_3)_3$); ^{19}F NMR (376 MHz, $CDCl_3$) δ = -63.3; ESI/MS$^+$ m/z 632.5 $[M+H]^+$, 654.5 $[M+Na]^+$; HRMS Calcd for $C_{30}H_{49}N_5O_6F_3$ 632.3635. Found 632.3621.

47. 1-((5-(Trifluoromethyl)pyridin-2-yl)methyl)-1,4,7,10-tetraazacyclododecane

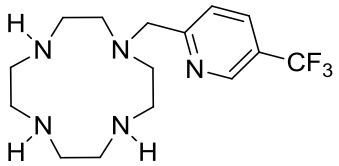

Tri-*tert*-butyl-10-((5-(trifluoromethyl)pyridin-2-yl)methyl)-1,4,7,10-tetraazacyclo dodecane-1,4,7-tricarboxylate (685 mg, 1.08 mmol) was dissolved in DCM (5 mL) with stirring. To this was added TFA (3 mL) and the mixture was stirred at rt for 18 h. After this time, the solvent was removed under reduced pressure before being repeatedly washed with DCM. The resulting oil was dissolved in $KOH_{(aq)}$ (1 M, 20 mL) and extracted with DCM (3 x 10 mL). The solvent was removed under reduced pressure to yield an orange oil (320 mg, 89 %). ^{1}H NMR (200 MHz, $CDCl_3$): δ = 8.69 (d, *J* = 2 Hz, 1H, H^6), 7.84 (dd, *J* = 8, 2 Hz, 1H, H^4), 7.55 (d, *J* = 8 Hz, 1H, H^3), 3.78 (s, 2H, $NC\underline{H}_2py$), 2.76 (m, 4H, cyclen-$C\underline{H}_2$), 2.65 (m, 8H, cyclen-$C\underline{H}_2$), 2.54 (m, 4H, cyclen-$C\underline{H}_2$); ^{13}C NMR (101 MHz, $CDCl_3$): δ = 162.8 (C^2), 144.8 (q, $^3J_{CF}$ = 4 Hz, C^6), 132.8 (q, $^3J_{CF}$ = 3 Hz, C^4), 124.0 (q, $^2J_{CF}$ = 33 Hz, C^5), 122.6 (q, $^1J_{CF}$ = 272 Hz, CF_3), 121.5 (C^3), 59.8 ($N\underline{C}H_2py$), 50.7 (cyclen-$\underline{C}H_2$), 46.1 (cyclen-$\underline{C}H_2$), 45.2 (cyclen-$\underline{C}H_2$), 44.1 (cyclen-$\underline{C}H_2$); ^{19}F NMR (188 MHz, $CDCl_3$) δ = -62.8; ESI/MS$^+$ m/z 332.3 $[M+H]^+$; HRMS Calcd for $C_{15}H_{25}N_5F_3$ 332.2062. Found 332.2061.

48. Triethyl-(10-((5-(trifluoromethyl)pyridin-2-yl)methyl)-1,4,7,10-tetraazacyclododecane-1,4,7-triyl)tris(methylene)tris(methylphosphinate)

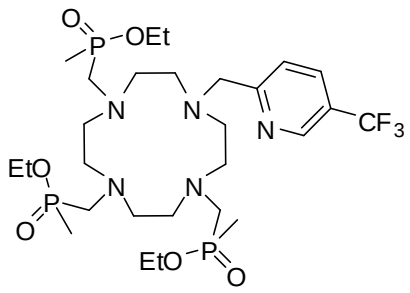

1-((5-(Trifluoromethyl)pyridin-2-yl)methyl)-1,4,7,10-tetraazacyclododecane (300 mg, 0.91 mmol) was heated to 80°C in anhydrous THF under argon. Paraformaldehyde (220 mg, 7.36 mmol) followed by diethoxymethylphosphine (1.00 g, 7.36 mmol) were added before the solution was heated at reflux over molecular sieves for 15 h. After this time, the excess paraformaldehyde was removed by filtration and the solvent removed under reduced pressure. The resulting orange oil was purified by mixed alumina/silica (4:1) gel column chromatography, eluting with a gradient starting from 100 % DCM to 8 % MeOH/DCM, to yield a yellow oil (180 mg, 29 %), which consisted of a mixture of diastereoisomers. ^{1}H NMR (400 MHz, $CDCl_3$): δ = 8.84 (s, 1H, H^6), 7.98 (d, *J* = 8 Hz, 1H, H^4), 7.78 (d, *J* = 8 Hz, 1H, H^3), 4.70 (s, 2H, $NC\underline{H}_2py$), 4.07 (m, 6H, $POC\underline{H}_2CH_3$), 3.84 (s, 2H, $NC\underline{H}_2P$), 3.42 (br s, 4H, $NC\underline{H}_2P$), 3.05 (br m, 16H, cyclen-$C\underline{H}_2$), 1.53 (br m, 9H, $P\underline{C}H_3$), 1.31 (br m, 9H, $POCH_2\underline{C}H_3$); ^{19}F NMR (376 MHz, $CDCl_3$): δ = -62.9; ^{31}P NMR (162 MHz, $CDCl_3$) δ = 52.2, 52.0; ESI/MS^+ m/z 692.2 $[M+H]^+$; HRMS Calcd for $C_{27}H_{52}N_5O_6F_3P_3$ 692.3077. Found 692.3064.

49. (10-((5-(Trifluoromethyl)pyridin-2-yl)methyl)-1,4,7,10-tetraazacyclododecane-1,4,7-triyl)tris(methylene)tris(methylphosphinic acid) (L^5)

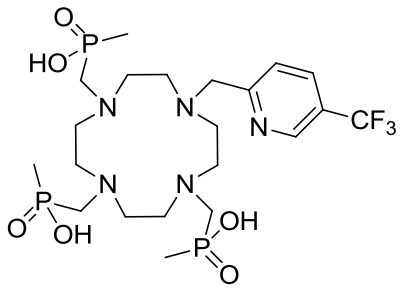

Triethyl (10-((5-(trifluoromethyl)pyridin-2-yl)methyl)-1,4,7,10-tetraazacyclododecane-1,4,7-triyl)tris(methylene)tris(methylphosphinate) (60 mg, 0.087 mmol) was dissolved in HCl (6 M, 5 mL) and stirred for 18 h at 90°C. The solvent was removed under reduced pressure and the residue washed repeatedly with DCM (3 x 5 mL) and the resulting oil was dissolved in EtOH. The white precipitate was removed by filtration and the solvent removed under reduced pressure to yield the hydrochloride salt as a viscous yellow oil (48 mg, 91 %). ^{1}H NMR (400 MHz, D_2O): δ = 9.04 (s, 1H, H^6), 8.49 (s, 1H, H^4), 7.93 (s, 1H, H^3), 4.30 (s, 2H, NC$\underline{H}_2$py), 3.33 (br s, 6H, NC$\underline{H}_2$P), 3.17 (br m, 16H, cyclen-C$\underline{H}_2$), 1.33 (m, 9H, P$\underline{C}H_3$); ^{19}F NMR (376 MHz, $CDCl_3$): δ = -63.3; ^{31}P NMR (162 MHz, $CDCl_3$) δ = 53.2; ESI/MS^+ m/z 608.3 $[M+H]^+$, ESI/MS^- m/z 606.3 $[M-H]^-$.

50. [Dy.L^5]

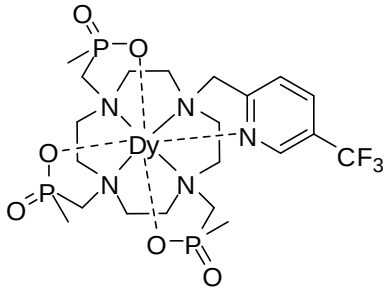

$Dy(III)Cl_3.6H_2O$ (22 mg, 0.059 mmol) was added to a solution of (10-((5-(trifluoromethyl)pyridin-2-yl)methyl)-1,4,7,10-tetraazacyclododecane-1,4,7-triyl) tris (methylene)tris(methylphosphinic acid) (30 mg, 0.049 mmol) dissolved in H_2O (3 mL). The pH was adjusted to 5.5 before stirring the solution for 18 h at 40°C. After this time, the solution was allowed to cool to rt before the pH was raised to 10, causing

a white solid to precipitate out of solution. This precipitate was removed by centrifugation and the pH of the resulting solution neutralised. The solvent was removed under reduced pressure to yield a yellow solid, which was purified by preparative HPLC to yield a yellow solid (37 mg, 98 %). ^{19}F NMR (376 MHz, D_2O, pD 6.9): δ =-155.0 (major), -162.1 (minor); ESI/MS$^+$ m/z 806.2 $[M+K]^+$; HRMS Calcd for $C_{21}H_{36}{}^{161}DyF_3N_5O_6P_3{}^{35}Cl$ 800.0789. Found 800.0809.

51. [Tm.L^5]

An analogous procedure to that described for **[Dy.L^5]** was followed using (10-((5-(trifluoromethyl)pyridin-2-yl)methyl)-1,4,7,10-tetraazacyclododecane-1,4,7-triyl) tris(methylene)tris(methylphosphinic acid) (30 mg, 0.049 mmol) and Tm(III)Cl_3 (23 mg, 0.059 mmol) to yield a yellow solid (37 mg, 97 %). ^{19}F NMR (376 MHz, D_2O, pD 6.9): δ = 10.9 (major), 13.5 (minor); ESI/MS$^+$ m/z 774.3 $[M+H]^+$, 812.2 $[M+K]^+$; HRMS Calcd for $C_{21}H_{36}{}^{169}TmF_3N_5O_6P_3{}^{35}Cl$ 808.0861. Found 808.0838.

52. Tri-*tert*-butyl 10-((3-chloro-5-(trifluoromethyl)pyridin-2-yl)methyl)-1,4,7,10-tetraazacyclododecane-1,4,7-tricarboxylate

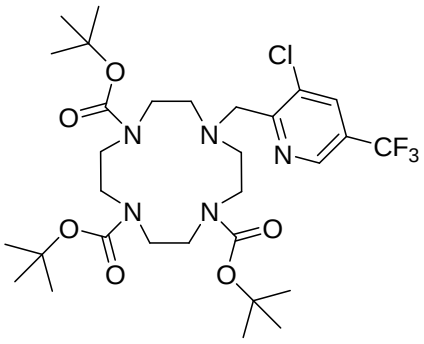

A stirred mixture of 1,4,7-tris-*tert*-butoxycarbonyl-1,4,7,10-tetraazacyclododecane (2.26 g, 4.79 mmol), 3-chloro-2-(chloromethyl)-5-(trifluoromethyl)pyridine (1.00 g, 4.35 mmol), and K_2CO_3 (0.90 g, 6.53 mmol) in anhydrous MeCN (25 mL) was boiled under reflux for 18 h under argon. The reaction mixture was cooled and filtered before the solvent was removed under reduced pressure. The resulting yellow oil was purified by silica gel column chromatography, eluting with a gradient starting from

100 % DCM to 5 % MeOH/DCM to yield a pale yellow oil (1.84 g, 64 %). R_f (5 % MeOH/DCM) = 0.61. ^{1}H NMR (400 MHz, $CDCl_3$): δ = 8.75 (d, *J* = 1 Hz, 1H, H^6), 7.90 (d, *J* = 1 Hz, 1H, H^4), 4.13 (s, 2H, NC$\underline{H}_2$py), 3.59 (br s, 4H, cyclen-C$\underline{H}_2$), 3.40 (br s, 8H, cyclen-C$\underline{H}_2$), 2.84 (br s, 4H, cyclen-C$\underline{H}_2$), 1.47 (s, 9H, C(C$\underline{H}_3$)$_3$), 1.43 (s, 18H, C(C$\underline{H}_3$)$_3$); ^{13}C NMR (101 MHz, $CDCl_3$): δ = 159.1 (C^2), 155.7 ($\underline{C}O_2{}^tBu$), 155.4 ($\underline{C}O_2{}^tBu$), 143.6 (q, $^3J_{CF}$ = 4 Hz, C^6), 134.1 (q, $^3J_{CF}$ = 4 Hz, C^4), 132.0 (C^3), 126.2 (q, $^2J_{CF}$ = 34 Hz, C^5), 122.6 (q, $^1J_{CF}$ = 273 Hz, CF_3), 79.5 ($\underline{C}(CH_3)_3$), 79.2 ($\underline{C}(CH_3)_3$), 54.8 (N$\underline{C}H_2$py), 53.7 (cyclen-$\underline{C}H_2$), 50.1 (cyclen-$\underline{C}H_2$), 48.0 (cyclen-$\underline{C}H_2$), 47.7 (cyclen-$\underline{C}H_2$), 28.7 (C($\underline{C}H_3$)$_3$), 28.5 (C($\underline{C}H_3$)$_3$); ^{19}F NMR (376 MHz, $CDCl_3$): δ = -62.3; ESI/MS$^+$ m/z 666.5 $[M+H]^+$; HRMS Calcd for $C_{30}H_{48}ClF_3N_5O_6$ 666.3238. Found 666.3240.

53. 1-((3-Chloro-5-(trifluoromethyl)pyridin-2-yl)methyl)-1,4,7,10-tetraazacyclododecane

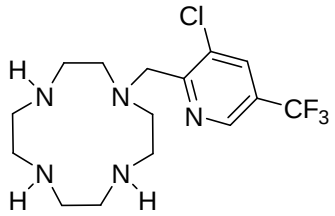

Tri-*tert*-butyl-10-((3-chloro-5-(trifluoromethyl)pyridin-2-yl)methyl)-1,4,7,10-tetraaza-cyclododecane-1,4,7-tricarboxylate (150 mg, 0.225 mmol) was dissolved in DCM (2 mL) with stirring. To this was added TFA (1 mL) and the mixture was stirred at rt for 18 h. After this time, the solvent was removed under reduced pressure before being repeatedly washed with DCM. The resulting oil was dissolved in $KOH_{(aq)}$ (1 M, 10 mL) and extracted with DCM (3 x 5 mL). The solvent was removed under reduced pressure to yield an orange oil (78 mg, 95 %). ^{1}H NMR (400 MHz, $CDCl_3$): δ = 8.68 (s, 1H, H^6), 7.87 (s, 1H, H^4), 3.92 (s, 2H, NC$\underline{H}_2$py), 2.76 (br m, 4H, cyclen-C$\underline{H}_2$), 2.67 (br s, 8H, cyclen-C$\underline{H}_2$), 2.53 (br s, 4H, cyclen-C$\underline{H}_2$); ^{13}C NMR (101 MHz, $CDCl_3$): δ = 159.9 (C^2), 143.6 (q, $^3J_{CF}$ = 4 Hz, C^6), 134.5 (q, $^3J_{CF}$ = 4 Hz, C^4), 132.2 (C^3), 126.6 (q, $^2J_{CF}$ = 34 Hz, C^5), 122.7 (q, $^1J_{CF}$ = 273 Hz, CF_3), 58.2 (N$\underline{C}H_2$py), 51.7 (cyclen-$\underline{C}H_2$), 46.9 (cyclen-$\underline{C}H_2$), 46.0 (cyclen-$\underline{C}H_2$), 44.8 (cyclen-$\underline{C}H_2$); ^{19}F NMR (376 MHz, $CDCl_3$): δ = -62.7; ESI/MS$^+$ m/z 366.3 $[M+H]^+$; HRMS Calcd for $C_{15}H_{24}ClF_3N_5$ 366.1684. Found 366.1672.

54. Triethyl-(10-((3-chloro-5-(trifluoromethyl)pyridin-2-yl)methyl)-1,4,7,10-tetraazacyclododecane-1,4,7-triyl)tris(methylene)tris(methylphosphinate)

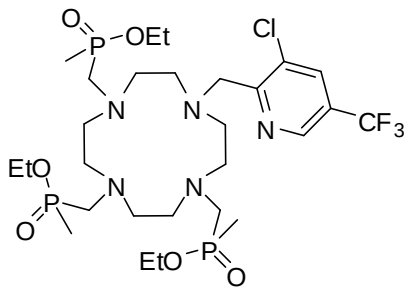

1-((3-Chloro-5-(trifluoromethyl)pyridin-2-yl)methyl)-1,4,7,10-tetraazacyclododecane (100 mg, 0.273 mmol) was heated to 80°C in anhydrous THF under argon. Paraformaldehyde (110 mg, 3.68 mmol) followed by diethoxymethylphosphine (500 mg, 3.68 mmol) were added. The solution was heated at reflux over molecular sieves for 15 h. After this time, the excess paraformaldehyde was removed by filtration and the solvent removed under reduced pressure. The resulting orange oil was purified by mixed alumina/silica (4:1) gel column chromatography, eluting with a gradient starting from 100 % DCM to 8 % MeOH/DCM, to yield a yellow oil (130 mg, 71 %), which was present as a mixture of diastereoisomers. ^{1}H NMR (400 MHz, $CDCl_3$): δ = 8.73 (s, 1H, H^6), 7.90 (s, 1H, H^4), 4.74 (s, 2H, NC$\underline{H}_2$py), 4.06 (m, 9H, POC$\underline{H}_2$CH$_3$), 3.03 (br m, 8H, NC$\underline{H}_2$P/cyclen-C$\underline{H}_2$), 2.79 (br m, 14H, NC$\underline{H}_2$P/cyclen-C$\underline{H}_2$), 1.53 (m, 9H, PC$\underline{H}_3$), 1.31 (m, 9H, POCH$_2$C$\underline{H}_3$); ^{13}C NMR (101 MHz, $CDCl_3$): δ = 158.8 (C^3), 142.5 (q, *J* = 4 Hz, C^6), 133.2 (q, $^{3}J_{CF}$ = 4 Hz, C^4), 131.0 (C^3), 129.8 (q, $^{2}J_{CF}$ = 34 Hz, C^5), 121.6 (q, $^{1}J_{CF}$ = 273 Hz, CF_3), 59.3 (d, $^{2}J_{CP}$ = 7 Hz, POC$\underline{H}_2$CH$_3$), 56.2 (NC$\underline{H}_2$py), 53.9 (m, NC$\underline{H}_2$P/cyclen-C$\underline{H}_2$), 53.2 (m, NC$\underline{H}_2$P/cyclen-C$\underline{H}_2$), 52.8 (m, NC$\underline{H}_2$P/cyclen-C$\underline{H}_2$), 51.5 (m, NC$\underline{H}_2$P/cyclen-C$\underline{H}_2$), 15.7 (d, $^{3}J_{CP}$ = 6 Hz, PCH$_2$C$\underline{H}_3$), 12.7 (d, $^{1}J_{CP}$ = 89 Hz, PC$\underline{H}_3$), 12.5 (d, *J* = 92 Hz, PC$\underline{H}_3$); ^{19}F NMR (376 MHz, $CDCl_3$): δ = -63.2; ^{31}P NMR (162 MHz, $CDCl_3$): δ = 54.3, 53.4; ESI/MS$^+$ m/z 726.4 $[M+H]^+$, 748.4 $[M+Na]^+$; HRMS Calcd for $C_{27}H_{51}N_5O_6F_3ClP_3$ 726.2693. Found 726.2698.

55. (10-((3-Chloro-5-(trifluoromethyl)pyridin-2-yl)methyl)-1,4,7,10-tetraazacyclododecane-1,4,7-triyl)tris(methylene)tris(methylphosphinic acid) (L^6)

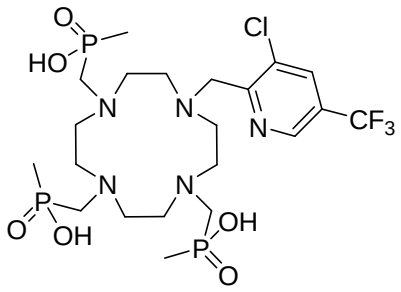

Triethyl-(10-((3-chloro-5-(trifluoromethyl)pyridin-2-yl)methyl)-1,4,7,10-tetraazacyclo-dodecane-1,4,7-triyl)tris(methylene)tris(methylphosphinate) (125 mg, 0.17 mmol) was dissolved in HCl (6 M, 10 mL) and stirred for 18 h at 90°C. The solvent was removed under reduced pressure and the residue washed repeatedly with DCM (3 x 5 mL) before the resulting oil was dissolved in EtOH. The white precipitate was removed by filtration and the solvent removed under reduced pressure to yield the hydrochloride salt as a yellow oil (107 mg, 98 %). ^{1}H NMR (400 MHz, D_2O) δ = 8.72 (s, 1H, H^6), 8.11 (s, 1H, H^4), 3.59 (m, 2H, NC$\underline{H}_2$py), 3.43 (br s, 8H, NC$\underline{H}_2$P/cyclen-C$\underline{H}_2$), 3.07 (br m, 14H, cyclen-C$\underline{H}_2$), 1.26 (br m, 9H, PC$\underline{H}_3$); ^{19}F NMR (376 MHz, $CDCl_3$) δ = -63.0; ^{31}P NMR (162 MHz, $CDCl_3$) δ = 53.4; ESI/MS^- m/z 640.3 $[M-H]^-$.

56. [Dy.L^6]

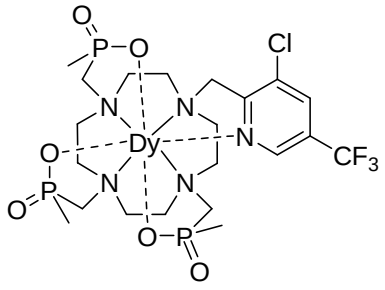

$Dy(III)Cl_3.6H_2O$ (8.8 mg, 0.0234 mmol) was added to a solution of (10-((3-chloro-5-(trifluoromethyl)pyridin-2-yl)methyl)-1,4,7,10-tetraazacyclododecane-1,4,7-triyl)tris (methylene)tris(methylphosphinic acid) (10.7 mg, 0.0167 mmol) dissolved in H_2O (5 mL). The pH was adjusted to 5.5 before stirring the solution for 18 h at 40°C. After

this time, the solution was allowed to cool to rt before the pH was raised to 10, causing a white solid to precipitate out of solution. This precipitate was removed by centrifugation and the pH of the resulting solution neutralised. The solvent was removed under reduced pressure to yield a yellow solid, which was purified by preparative HPLC to yield an off-white solid (13 mg, 97 %). ^{19}F NMR (376 MHz, D_2O, pH 6.5): δ = -163.5 (major), -170.2 (minor); ESI/MS$^-$ m/z 837.4 $[M+Cl]^-$; HRMS Calcd for $C_{21}H_{35}{}^{35}Cl_2{}^{160}DyF_3N_5O_6P_3$ 833.0381. Found 833.0401.

57. [Er.L^6]

An analogous procedure to that described for **[Dy.L^6]** was followed using (10-((3-chloro-5-(trifluoromethyl)pyridin-2-yl)methyl)-1,4,7,10-tetraazacyclododecane-1,4,7-triyl)tris(methylene)tris(methylphosphinic acid) (5 mg, 0.00831 mmol) and Er(III)Cl_3 (4.7 mg, 0.0124 mmol) to yield an off-white solid (6.4 mg, 95 %). ^{19}F NMR (376 MHz, D_2O, pH 6.5): δ = -16.8 (major), -13.5 (minor); ESI/MS$^+$ m/z 805.0 $[M+H]^+$; HRMS Calcd for $C_{21}H_{35}{}^{35}Cl^{166}ErF_3N_5O_6P_3Na$ 827.0642. Found 827.0616.

58. [Tb.L^6]

An analogous procedure to that described for **[Dy.L^6]** was followed using (10-((3-chloro-5-(trifluoromethyl)pyridin-2-yl)methyl)-1,4,7,10-tetraazacyclododecane-1,4,7-triyl)tris(methylene)tris(methylphosphinic acid) (10 mg, 0.0156 mmol) and Tb(III)Cl_3 (6.9 mg, 0.0187 mmol) to yield an off-white solid (12 mg, 98 %). ^{19}F NMR (376 MHz, D_2O, pH 6.5): δ = -160.1 (major), -160.8 (minor); ESI/MS$^+$ m/z 820.3 $[M+Na]^+$; HRMS Calcd for $C_{21}H_{35}{}^{35}Cl^{159}TbF_3N_5O_6P_3Na$ 820.0592. Found 820.0617.

59. [Tm.L^6]

An analogous procedure to that described for **[Dy.L^6]** was followed using (10-((3-chloro-5-(trifluoromethyl)pyridin-2-yl)methyl)-1,4,7,10-tetraazacyclododecane-1,4,7-triyl)tris(methylene)tris(methylphosphinic acid) (10 mg, 0.0156 mmol) and Tm(III)Cl_3

(7.2 mg, 0.0187 mmol) to yield an off-white solid (12 mg, 98 %). ^{19}F NMR (376 MHz, D_2O, pH 6.5): δ = 17.1 (major), 20.3 (minor); ESI/MS$^+$ m/z 830.2 $[M+Na]^+$; HRMS Calcd for $C_{21}H_{35}{}^{35}Cl^{169}TmF_3N_5O_6P_3Na$ 830.0681. Found 830.0701.

60. [Ho.L^6]

An analogous procedure to that described for **[Dy.L^6]** was followed using (10-((3-chloro-5-(trifluoromethyl)pyridin-2-yl)methyl)-1,4,7,10-tetraazacyclododecane-1,4,7-triyl)tris(methylene)tris(methylphosphinic acid) (10 mg, 0.0156 mmol) and Ho(III)Cl_3 (7.1 mg, 0.0187 mmol) to yield an off-white solid (12 mg, 97 %). ^{19}F NMR (376 MHz, D_2O, pH 6.5): δ = -108.7 (major), -112.4 (minor); ESI/MS$^+$ m/z 826.2 $[M+Na]^+$; HRMS Calcd for $C_{21}H_{35}{}^{35}Cl^{165}HoF_3N_5O_6P_3Na$ 826.0642. Found 826.0659.

61. [Gd.L^6]

An analogous procedure to that described for **[Dy.L^6]** was followed using (10-((3-chloro-5-(trifluoromethyl)pyridin-2-yl)methyl)-1,4,7,10-tetraazacyclododecane-1,4,7-triyl)tris(methylene)tris(methylphosphinic acid) (5 mg, 0.0078 mmol) and Gd(III)Cl_3 (3.5 mg, 0.0094 mmol) to yield an off-white solid (5.8 mg, 94 %). ^{19}F NMR (376 MHz, D_2O, pH 6.5): δ = -63.8 (broad); ESI/MS$^+$ m/z 819.2 $[M+Na]^+$; HRMS Calcd for $C_{21}H_{35}{}^{35}Cl^{154}GdF_3N_5O_6P_3Na$ 815.0547. Found 815.0559.

62. [Eu.L^6]

An analogous procedure to that described for **[Dy.L^6]** was followed using (10-((3-chloro-5-(trifluoromethyl)pyridin-2-yl)methyl)-1,4,7,10-tetraazacyclododecane-1,4,7-triyl)tris(methylene)tris(methylphosphinic acid) (10 mg, 0.0156 mmol) and Eu(III)Cl_3 (6.9 mg, 0.0187 mmol) to yield an off-white solid (12 mg, 98 %). ^{19}F NMR (376 MHz, D_2O, pH 6.5): δ = -58.9 (major), -58.2 (minor); ESI/MS$^+$ m/z 814.2 $[M+Na]^+$; HRMS Calcd for $C_{21}H_{35}{}^{35}Cl^{151}EuF_3N_5O_6P_3Na$ 812.0537. Found 812.0553.

63. [Y.L^6]

An analogous procedure to that described for **[Dy.L^6]** was followed using (10-((3-chloro-5-(trifluoromethyl)pyridin-2-yl)methyl)-1,4,7,10-tetraazacyclododecane-1,4,7-triyl)tris(methylene)tris(methylphosphinic acid) (5 mg, 0.00831 mmol) and Y(III)Cl_3 (3.8 mg, 0.0124 mmol) to yield an off-white solid (5.7 mg, 95 %). ^{19}F NMR (376 MHz, D_2O, pH 6.5): δ = -63.1 (major), -63.0 (minor); ESI/MS$^+$ m/z 750.2 $[M+Na]^+$; HRMS Calcd for $C_{21}H_{35}{}^{35}ClYF_3N_5O_6P_3Na$ 750.0397. Found 750.0415.

64. [Yb.L^6]

An analogous procedure to that described for **[Dy.L^6]** was followed using (10-((3-chloro-5-(trifluoromethyl)pyridin-2-yl)methyl)-1,4,7,10-tetraazacyclododecane-1,4,7-triyl)tris(methylene)tris(methylphosphinic acid) (10 mg, 0.0156 mmol) and Er(III)Cl_3 (7.2 mg, 0.0187 mmol) to yield an off-white solid (12 mg, 97 %). ^{19}F NMR (376 MHz, D_2O, pH 6.5): δ = -41.8 (major), -39.1 (minor); ESI/MS$^-$ m/z 845.1 $[M+Cl]^-$; HRMS Calcd for $C_{21}H_{35}{}^{35}Cl_2{}^{170}YbF_3N_5O_6P_3$ 843.0482. Found 843.0463.

65. 1,4,7-Tris(*tert*-butoxycarbonylmethyl)-1,4,7,10-tetraazacyclododecane [15]

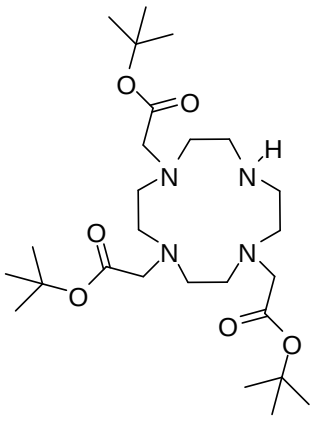

To a solution of 1,4,7,10-tetraazacyclododecane (2.54 g, 14.7 mmol) and $NaHCO_3$ (3.72 g, 44.3 mmol) in anhydrous MeCN (50 mL) was added *tert*-butylbromoacetate (6.56 mL, 44.5 mmol) under an atmosphere of argon. The reaction mixture was stirred for 18 h at rt, before being filtered. The solvent was removed under reduced pressure

to give a yellow oil, which was purified by recrystallization from toluene to yield a white solid (2.72 g, 36 %), m.p. 178-180°C. ^{1}H NMR (400 MHz, $CDCl_3$): δ = 10.06 (s, 1H, NH), 3.37 (s, 4H, CH_2CO), 3.28 (s, 2H, CH_2CO), 3.09 (br s, 4H, cyclen-C$\underline{H}_2$), 2.89 (br m, 12H, cyclen-C$\underline{H}_2$), 1.45 (s, 27H, ^{t}Bu); ESI/MS^{+} m/z 515.3 $[M+H]^{+}$.

66. *tert*-Butyl-2,2',2''-(10-((3-chloro-5-(trifluoromethyl)pyridin-2-yl)methyl)-1,4,7,10-tetraazacyclododecane-1,4,7-triyl)triacetate

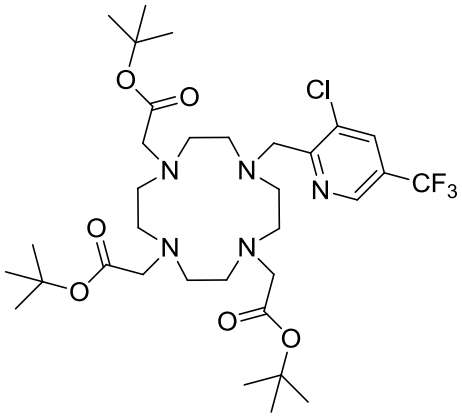

A stirred mixture of *tert*-butyl 2,2',2''-(1,4,7,10-tetraazacyclododecane-1,4,7-triyl)triacetate (0.90 g, 1.74 mmol), 3-chloro-2-(chloromethyl)-5-(trifluoromethyl) pyridine (0.48 mg, 2.09 mmol), K_2CO_3 (0.34 g, 2.44 mmol), and KI (ca. 5 mg) in anhydrous MeCN (25 mL) was boiled under reflux for 18 h under argon. The reaction mixture was cooled and filtered before the solvent was removed under reduced pressure. The resulting yellow oil was purified by silica gel column chromatography, eluting with a gradient starting from 100 % DCM to 6 % MeOH/DCM to yield a yellow oil (0.84 g, 68 %). R_f (10 % MeOH/DCM) = 0.40. ^{1}H NMR (400 MHz, $CDCl_3$): δ = 8.38 (d, J = 2 Hz, 1H, H^{6}), 7.87 (d, J = 2 Hz, 1H, H^{4}), 3.81 (s, 2H, NC$\underline{H}_2$py), 3.60 – 2.64 (br m, 12H, NC$\underline{H}_2CO_2{}^{t}$Bu/cyclen-C$\underline{H}_2$), 2.13 (br m, 10H, cyclen-C$\underline{H}_2$), 1.39 (s, 18H, ^{t}Bu), 1.18 (s, 9H, ^{t}Bu); ^{13}C NMR (101 MHz, $CDCl_3$): δ = 171.8 ($\underline{C}O_2{}^{t}$Bu), 159.6 (C^{2}), 141.9 (q, $^{3}J_{CF}$ = 4 Hz, C^{6}), 132.9 (q, $^{3}J_{CF}$ = 7 Hz, C^{4}), 130.2 (C^{3}), 125.0 (q, $^{2}J_{CF}$ = 34 Hz, C^{5}), 121.5 (q, $^{1}J_{CF}$ = 273 Hz, CF_3), 81.1 ($\underline{C}(CH_3)_3$), 55.8 (N$\underline{C}H_2CO_2{}^{t}$Bu), 54.2 (cyclen-$\underline{C}H_2$), 52.5 (cyclen-$\underline{C}H_2$), 26.8 (C($\underline{C}H_3)_3$), 26.7 (C($\underline{C}H_3)_3$); ^{19}F NMR (376 MHz, $CDCl_3$): δ = -63.4; ESI/MS^{+} m/z 730.5 $[M+Na]^{+}$; HRMS Calcd for $C_{33}H_{53}ClF_3N_5NaO_6$ 730.3534. Found 730.3530.

67. 2,2',2''-(10-((3-Chloro-5-(trifluoromethyl)pyridin-2-yl)methyl)-1,4,7,10-tetraazacyclododecane-1,4,7-triyl)triacetic acid (L^7)

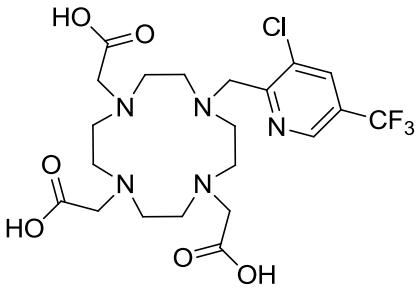

tert-Butyl-2,2',2''-(10-((3-chloro-5-(trifluoromethyl)pyridin-2-yl)methyl)-1,4,7,10-tetraazacyclododecane-1,4,7-triyl)triacetate (100 mg, 0.141 mmol) was dissolved in HCl (6 M, 10 mL) and stirred for 18 h at 90°C. The solvent was removed under reduced pressure and the residue washed repeatedly with DCM (3 x 5 mL) and the resulting oil was dissolved in EtOH. The white precipitate was removed by filtration and the solvent removed under reduced pressure to yield the hydrochloride salt as a yellow oil (75.5 mg, 99 %). ^{1}H NMR (400 MHz, D_2O): δ = 8.53 (s, 1H, H^6), 8.19 (s, 1H, H^4), 4.07 (br s, 2H, NC$\underline{H}_2$py), 3.75 – 3.25 (br m, 12H, NC$\underline{H}_2$CO$_2$H/cyclen-C$\underline{H}_2$), 3.10 (br m, 10H, cyclen-C$\underline{H}_2$); ^{19}F NMR (376 MHz, D_2O): δ = -63.1; ESI/MS$^+$ m/z 540.3 $[M+H]^+$, ESI/MS$^-$ m/z 538.3 $[M-H]^-$.

68. [Dy.L^7]

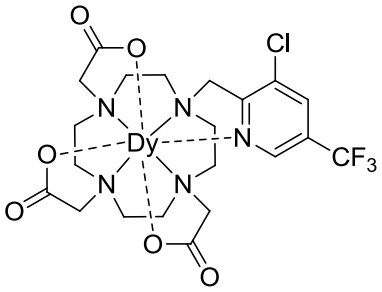

$Dy(III)Cl_3.6H_2O$ (33.5 mg, 8.9 mmol) was added to a solution of 2,2',2''-(10-((3-chloro-5-(trifluoromethyl)pyridin-2-yl)methyl)-1,4,7,10-tetraazacyclododecane-1,4,7-triyl)triacetic acid (40 mg, 0.074 mmol) dissolved in H_2O (5 mL). The pH was adjusted to 5.5 before stirring the solution for 18 h at 40°C. After this time, the solution was allowed to cool to rt before the pH was raised to 10, causing a white solid to

precipitate out of solution. This precipitate was removed by centrifugation and the pH of the resulting solution neutralised. The solvent was removed under reduced pressure to give a yellow solid, which was purified by preparative HPLC to yield an off-white solid (49 mg, 95 %). ^{19}F NMR (376 MHz, D_2O, pH 6.5): δ = -115.9 (major), -126.5 (minor); ESI/MS$^+$ m/z 722.8 $[M+Na]^+$; HRMS Calcd for $C_{21}H_{26}{}^{35}Cl^{160}DyF_3N_5O_6Na$ 719.0668. Found 719.0652.

69. [Tm.L^7]

An analogous procedure to that described for **[Dy.L^7]** was followed using 2,2',2''-(10-((3-chloro-5-(trifluoromethyl)pyridin-2-yl)methyl)-1,4,7,10-tetraazacyclododecane-1,4,7-triyl)triacetic acid (30 mg, 0.00556 mmol) and Tm(III)Cl_3 (25.6 mg, 0.0667 mmol) to yield an off-white solid (38 mg, 97 %). ^{19}F NMR (376 MHz, D_2O, pH 6.5): δ = -40.9 (major), -5.6 (minor); ESI/MS$^+$ m/z 728.7 $[M+Na]^+$; HRMS Calcd for $C_{21}H_{26}{}^{35}Cl^{169}TmF_3N_5O_6Na$ 706.0939. Found 706.0915.

70. Ethyl methylphosphinate

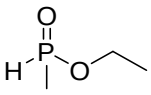

Argon was bubbled through H_2O (0.066 mL, 3.67 mmol) for 30 min to deoxygenate it and was added dropwise to diethyl methylphosphonite (0.50 g, 3.67 mmol), cooled to 0°C, before being stirred at rt for 18 h. The resulting clear, equimolar solution of the *title compound* and ethanol was used without further purification (100 % conversion by ^{1}H NMR spectroscopy). ^{1}H NMR (400 MHz, $CDCl_3$): δ = 7.22 (dq, $^1J_{H-P}$ = 536, $^2J_{H-H}$ = 2 Hz, 1H, P<u>H</u>), 4.11 (dqd, $^2J_{H-H}$ = 24, $^3J_{H-H}$ = 7, $^3J_{H-P}$ = 4 Hz, 2H, OC<u>H</u>$_2$CH$_3$), 1.54 (dd, $^2J_{H-P}$ = 15, $^3J_{H-H}$ = 2 Hz, 3H, PC<u>H</u>$_3$), 1.23 (t, $^3J_{H-H}$ = 7 Hz, 3H, OCH$_2$C<u>H</u>$_3$); ^{13}C NMR (101 MHz, $CDCl_3$): δ = 62.3 (d, $^2J_{C-P}$ = 7 Hz, O<u>C</u>H$_2$CH$_3$), 16.1 (OCH$_2$<u>C</u>H$_3$), 14.9 (d, $^1J_{C-P}$ = 95 Hz, P<u>C</u>H$_3$); ^{31}P NMR (162 MHz, $CDCl_3$): δ = 34.9; ESI/MS$^+$ m/z 109.1 $[M+H]^+$, 131.1 $[M+Na]^+$; HRMS Calcd for $C_3H_{10}O_2P$ 109.0414. Found 109.0418.

71. 2-Chloro-4-(trifluoromethyl)-6-methylpyridine

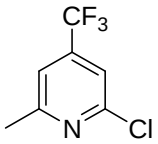

6-Methyl-4-trifluoromethyl-2(1H)-pyridone (0.5 g, 2.82 mmol) was dissolved in phosphorus oxychloride (15 mL) and the resulting mixture boiled under reflux for 3 h. After this time, the excess $POCl_3$ was removed under reduced pressure. The residue was poured onto ice and extracted with DCM (3 x 20 mL). The organic phases were combined and washed with $NaHCO_{3(aq)}$ (0.1 M, 20 mL) and brine (20 mL), before being dried over Na_2SO_4. The solvent was removed under reduced pressure to yield a colourless oil (0.28 g, 51 %). R_f (2% MeOH/DCM) = 0.86. ^{1}H NMR (400 MHz, $CDCl_3$): δ = 7.30 (s, 1H, H^3), 7.23 (s, 1H, H^5), 2.55 (s, 3H, CH_3); ^{13}C NMR (101 MHz, $CDCl_3$): δ = 161.1 (C^6), 151.4 (C^2), 141.4 (q, $^2J_{CF}$ = 34 Hz, C^4), 122.0 (q, $^1J_{CF}$ = 274 Hz, CF_3), 117.8 (q, $^3J_{CF}$ = 3 Hz, C^3), 117.6 (q, $^3J_{CF}$ = 4 Hz, C^5), 24.13 (CH_3); ^{19}F NMR (376 MHz, $CDCl_3$): δ = -64.8; ESI/MS^+ m/z 195.1 $[M+H]^+$; HRMS Calcd for $C_7H_6ClF_3N$ 196.0136. Found 196.0141.

72. Ethyl methyl(4-(trifluoromethyl)-6-methylpyridin-2-yl)-2-phosphinate

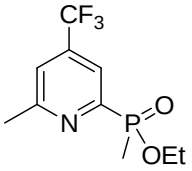

2-Chloro-4-(trifluoromethyl)-6-methylpyridine (2.05 g, 10.5 mmol), ethyl methylphosphinate (1.59 g, 14.7 mmol, 1:1 EtOH solution), and triethylamine (3 mL) were added to dry, degassed toluene (10 mL). Tetrakis(triphenylphosphine) palladium(0) (100 mg, 0.087 mmol) was added and the reaction mixture was degassed a further three times before being stirred at 100°C for 18 h under argon. After this time, the solution was diluted with DCM (100 mL) and washed with HCl (1 M, 2 x 50 mL) and H_2O (3 x 50 mL). The organic phase was dried over K_2CO_3 and filtered before the solvent was removed under reduced pressure. The resulting yellow oil was purified by silica gel column chromatography, eluting with a gradient starting from

100 % DCM to 2 % MeOH/DCM. The resulting yellow oil was dissolved in hexane and the insoluble white solid filtered to remove excess triphenylphosphine that elutes with the product. The solvent was removed under reduced pressure to yield a clear oil that crystallises upon standing (740 mg, 27 %). R_f (2 % MeOH/DCM) = 0.36. ^{1}H NMR (400 MHz, $CDCl_3$): δ = 8.03 (d, $^4J_{H\text{-}H}$ = 7 Hz, 1H, H^5), 7.46 (dd, $^4J_{H\text{-}H}$ = 7, $^3J_{H\text{-}P}$ = 2 Hz, 1H, H^3), 4.06 (ddq, $^1J_{H\text{-}H}$ = 10, $^3J_{H\text{-}P}$ = 8, $^3J_{H\text{-}H}$ = 7 Hz, 1H, $OC\underline{H}_2^{(A)}CH_3$), 3.81 (ddq, $^3J_{H\text{-}P}$ = 14, $^1J_{H\text{-}H}$ = 10, $^3J_{H\text{-}H}$ = 7 Hz, 1H, $OC\underline{H}_2^{(B)}CH_3$), 2.64 (s, 3H, py-$C\underline{H}_3$), 1.73 (d, $^2J_{H\text{-}P}$ = 15 Hz, 3H, $PC\underline{H}_3$), 1.22 (t, $^3J_{H\text{-}H}$ = 7 Hz, 3H, $OCH_2C\underline{H}_3$); ^{13}C NMR (101 MHz, $CDCl_3$): δ 161.1 (d, $^3J_{C\text{-}P}$ = 20 Hz, C^6), 156.0 (d, $^1J_{C\text{-}P}$ = 158 Hz, C^2), 138.7 (qd, $^2J_{C\text{-}F}$ = 34, $^3J_{C\text{-}P}$ = 11 Hz, C^4), 122.6 (qd, $^1J_{CF}$ = 274, $^4J_{C\text{-}P}$ = 3 Hz, $\underline{C}F_3$), 121.1 (dq, $^4J_{C\text{-}P}$ = 7, $^3J_{CF}$ = 4 Hz, C^5), 120.3 (dq, $^2J_{C\text{-}P}$ = 23, $^3J_{CF}$ = 4 Hz, C^3), 61.2 (d, $^2J_{C\text{-}P}$ = 7 Hz, $O\underline{C}H_2CH_3$), 24.7 (py-$\underline{C}H_3$), 16.4 (d, $^3J_{C\text{-}P}$ = 6 Hz, $OCH_2\underline{C}H_3$), 13.3 (d, $^1J_{C\text{-}P}$ = 105 Hz, $P\underline{C}H_3$); ^{19}F NMR (376 MHz, $CDCl_3$): δ = -64.8; ^{31}P NMR (162 MHz, $CDCl_3$): δ = 38.9; ESI/MS^+ m/z 290.2 $[M+Na]^+$; HRMS Calcd for $C_{10}H_{13}F_3NaNO_2P$ 290.0537. Found 290.0534.

73. 2-(Ethoxy(methyl)phosphoryl)-6-methyl-4-(trifluoromethyl)pyridine 1-oxide

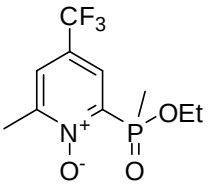

m-CPBA (0.81 g, 4.69 mmol) was added to a stirred solution of ethyl methyl(4-(trifluoromethyl)-6-methylpyridin-2-yl)-2-phosphinate (0.627 g, 2.35 mmol) in chloroform (20 mL). The resulting solution was stirred at 65°C for 18 h under argon before being washed with $NaHCO_{3(aq)}$ (0.5 M, 50 mL). The aqueous layer was extracted with DCM (3 x 25 mL). The organic layers were combined, dried over $MgSO_4$, and the solvent removed under reduced pressure to yield a yellow oil (0.63 g, 95 %). ^{1}H NMR (400 MHz, $CDCl_3$): δ = 8.07 (dd, $^3J_{H\text{-}P}$ = 8, $^4J_{H\text{-}H}$ = 2 Hz, 1H, H^3), 7.61 (d, $^4J_{H\text{-}H}$ = 2 Hz, 1H, H^5), 4.12 (dq, $^1J_{H\text{-}H}$ = 10, $^3J_{H\text{-}P}$ = 7 Hz, 1H, $OC\underline{H}_2^{(A)}CH_3$), 3.89 (dq, $^1J_{H\text{-}H}$ = 10, $^3J_{H\text{-}P}$ = 7 Hz, 1H, $OC\underline{H}_2^{(B)}CH_3$), 2.48 (s, 3H, py-$C\underline{H}_3$), 1.90 (d, $^2J_{H\text{-}P}$ = 17 Hz, 3H, $PC\underline{H}_3$), 1.24 (t, $^3J_{H\text{-}H}$ = 7 Hz, 3H, $OCH_2C\underline{H}_3$); ^{13}C NMR (101 MHz, $CDCl_3$): δ = 150.8 (d, $^3J_{C\text{-}P}$ = 3 Hz, C^6), 143.5 (d, $^1J_{C\text{-}P}$ = 138 Hz, C^2), 127.1 (dq, $^4J_{C\text{-}P}$ = 7, $^3J_{C\text{-}F}$ = 4 Hz, C^5), 127.0 (dq, $^2J_{C\text{-}P}$ = 7,

$^{3}J_{C\text{-}F}$ = 4 Hz, C^{3}), 125.5 (qd, $^{2}J_{C\text{-}F}$ = 36, $^{3}J_{C\text{-}P}$ = 10 Hz, C^{4}), 122.3 (q, $^{1}J_{C\text{-}F}$ = 272 Hz, $\underline{C}F_3$), 62.1 (d, $^{2}J_{C\text{-}P}$ = 7 Hz, $O\underline{C}H_2CH_3$), 17.5 (py-$\underline{C}H_3$), 16.3 (d, $^{3}J_{C\text{-}P}$ = 6 Hz, $OCH_2\underline{C}H_3$), 14.0 (d, $^{1}J_{C\text{-}P}$ = 112 Hz, $P\underline{C}H_3$); ^{19}F NMR (376 MHz, $CDCl_3$): δ = -63.8; ^{31}P NMR (162 MHz, $CDCl_3$): δ = 34.1; ESI/MS^{+} m/z 306.2 $[M+Na]^{+}$; HRMS Calcd for $C_{10}H_{13}F_3NaNO_3P$ 306.0462. Found 306.0483.

74. Ethyl-methyl(4-(trifluoromethyl)-6-(hydroxymethyl)pyridin-2-yl)-2-phosphinate

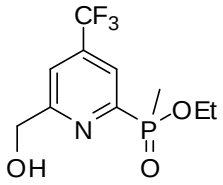

Trifluoroacetic anhydride (2 mL) was added to a solution of 2-(ethoxy(methyl) phosphoryl)-6-methyl-4-(trifluoromethyl)pyridine 1-oxide (80 mg, 0.282 mmol) in $CHCl_3$ (3 mL). The resulting mixture was heated at 60°C for 3 h under an inert atmosphere and the reaction was monitored by ^{31}P NMR spectroscopy and TLC. Upon completion (mixture of alcohol and trifluoroacetate), the mixture was cooled to rt and the solvent removed under reduced pressure. The resulting bright yellow oil was stirred in EtOH (5 mL) and H_2O (5mL) for 1 h. After this time the solution was concentrated (ca. 2 mL) and extracted with DCM (3 x 10 mL). The organic layers were combined, dried over $MgSO_4$, and the solvent removed *in vacuo* to give a yellow oil. This crude oil was purified by silica gel column chromatography, eluting with a gradient starting from 100 % DCM to 5 % MeOH/DCM to yield a yellow oil (56 mg, 70 %). R_f (10 % MeOH/DCM) = 0.50. ^{1}H NMR (400 MHz, $CDCl_3$): δ = 8.09 (d, $^{3}J_{H\text{-}P}$ = 6 Hz, 1H, H^{3}), 7.80 (s, 1H, H^{5}), 4.89 (s, 2H, py-$C\underline{H}_2OH$), 4.73 (br s, 1H, py-$CH_2O\underline{H}$), 4.10 (ddq, $^{3}J_{H\text{-}P}$ = 14, $^{1}J_{H\text{-}H}$ = 10, $^{3}J_{H\text{-}H}$ = 7 Hz, 1H, $OC\underline{H}_2{}^{(A)}CH_3$), 3.86 (ddq, $^{3}J_{H\text{-}P}$ = 14, $^{1}J_{H\text{-}H}$ = 10, $^{3}J_{H\text{-}H}$ = 7 Hz, 1H, $OC\underline{H}_2{}^{(B)}CH_3$), 1.77 (d, $^{2}J_{H\text{-}P}$ = 15 Hz, 3H, $PC\underline{H}_3$), 1.26 (t, $^{3}J_{H\text{-}H}$ = 7 Hz, 3H, $OCH_2C\underline{H}_3$); ^{13}C NMR (176 MHz, $CDCl_3$): δ = 163.9 (d, $^{3}J_{C\text{-}P}$ = 18 Hz, C^{6}), 155.1 (d, $^{1}J_{C\text{-}P}$ = 157 Hz, C^{2}), 139.2 (qd, $^{2}J_{C\text{-}F}$ = 34, $^{3}J_{C\text{-}P}$ = 11 Hz, C^{4}), 122.4 (q, $^{1}J_{CF}$ = 263 Hz, $\underline{C}F_3$), 121.3 (d, $^{2}J_{C\text{-}P}$ = 23 Hz, C^{3}), 118.6 (C^{5}), 64.5 (py-$\underline{C}H_2OH$), 61.5 (d, $^{2}J_{C\text{-}P}$ = 6 Hz, $O\underline{C}H_2CH_3$), 16.3 (d, $^{3}J_{C\text{-}P}$ = 6 Hz, $OCH_2\underline{C}H_3$), 13.3 (d, $^{1}J_{C\text{-}P}$ = 105 Hz, $P\underline{C}H_3$); ^{19}F NMR (658 MHz, $CDCl_3$):

δ = -64.9; ^{31}P NMR (293 MHz, $CDCl_3$): δ = 38.9; ESI/MS$^+$ m/z 306.3 $[M+Na]^+$; HRMS Calcd for $C_{10}H_{14}F_3NO_3P$ 284.0653. Found 284.0663.

75. (4-(Trifluoromethyl)-6-phosphono)pyridin-2-yl)methyl methanesulfonate

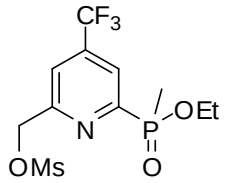

Triethylamine (55 µL, 0.40 mmol) and mesyl chloride (23 µL, 0.30 mmol) were added to a solution of ethyl methyl(4-(trifluoromethyl)-6-(hydroxymethyl)pyridin-2-yl)-2-phosphinate (56 mg, 0.20 mmol) in anhydrous THF (2 mL) cooled to 5°C. After addition, the solution was allowed to reach rt and monitored by TLC. After stirring for 15 min, the reaction was complete and the solvent was removed under reduced pressure. The residue was dissolved in brine (10 mL) and extracted with DCM (2 x 10 mL). The organic phases were combined, dried over $MgSO_4$, and the solvent removed under reduced pressure to yield a yellow oil (72 mg, 99 %). ^{1}H NMR (400 MHz, $CDCl_3$): δ = 8.26 (d, $^3J_{H\text{-}P}$ = 5 Hz, 1H, H^5), 7.81 (s, 1H, H^3), 5.45 (s, 2H, py-C$\underline{H}_2$OMs), 4.14 (dqd, $^1J_{H\text{-}H}$ = 14, $^3J_{H\text{-}H}$ = 7 Hz, $^3J_{H\text{-}P}$ = 3 Hz, 1H, OC$\underline{H}_2^{(A)}$CH$_3$), 3.89 (dq, $^1J_{H\text{-}H}$ = 14, $^3J_{H\text{-}H}$ = 7, 1H, OC$\underline{H}_2^{(B)}$CH$_3$), 3.17 (s, 3H, SC$\underline{H}_3$), 1.81 (d, $^2J_{H\text{-}P}$ = 15 Hz, 3H, PC$\underline{H}_3$), 1.29 (t, $^3J_{H\text{-}H}$ = 7 Hz, 3H, OCH$_2$C$\underline{H}_3$); ^{19}F NMR (376 MHz, $CDCl_3$): δ = -65.1; ^{31}P NMR (162 MHz, $CDCl_3$): δ = 39.3; ESI/MS$^+$ m/z 362.2 $[M+H]^+$, 385.2 $[M+Na]^+$; HRMS Calcd for $C_{11}H_{15}F_3NaNO_3PS$ 384.0261. Found 384.0258.

76. Ethyl-6-((1,4,7,10-tetraazacyclododecan-1-yl)methyl)-4-(trifluoromethyl) pyridin-2-yl(methyl)phosphinate

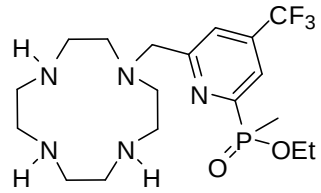

(4-(Trifluoromethyl)-6-phosphono)pyridin-2-yl)methyl methanesulfonate (72 mg, 0.20 mmol) was added dropwise to a stirred solution of 1,4,7,10-tetraazacyclododecane (340 mg, 1.98 mmol) in anhydrous MeCN (5 mL) at 40°C under argon. After 12 h, the solvent was removed under reduced pressure and the residue dissolved in DCM (10 mL). The solution was washed repeatedly with H_2O (4 x 10 mL), dried over $MgSO_4$, and the solvent removed under reduced pressure to yield a light yellow oil (79 mg, 90 %). ^{1}H NMR (400 MHz, $CDCl_3$): δ = 8.14 (d, $^{3}J_{H\text{-}P}$ = 6 Hz, 1H, H^3), 7.86 (s, 1H, H^5), 4.12 (m, 1H, $OC\underline{H}_2{}^{(A)}CH_3$), 3.92 (s, 2H, py-$C\underline{H}_2$), 3.86 (m, 1H, $OC\underline{H}_2{}^{(B)}CH_3$), 2.81 (br m, 4H, cyclen-$C\underline{H}_2$), 2.68 (br s, 8H, cyclen-$C\underline{H}_2$), 2.57 (br m, 4H, cyclen-$C\underline{H}_2$), 1.79 (d, $^{2}J_{H\text{-}P}$ = 15 Hz, 3H, $PC\underline{H}_3$), 1.27 (t, $^{3}J_{H\text{-}H}$ = 7 Hz, 3H, $OCH_2C\underline{H}_3$); ^{13}C NMR (101 MHz, $CDCl_3$): δ = 162.9 (d, $^{3}J_{C\text{-}P}$ = 19 Hz, C^6), 156.0 (d, $^{1}J_{C\text{-}P}$ = 157 Hz, C^2), 139.2 (qd, $^{2}J_{C\text{-}F}$ = 34, $^{3}J_{C\text{-}P}$ = 11 Hz, C^4), 122.8 (q, $^{1}J_{C\text{-}F}$ = 274 Hz, $\underline{C}F_3$), 121.8 (m, C^3), 121.1 (m, C^5), 61.5 (d, $^{2}J_{C\text{-}P}$ = 7 Hz, $O\underline{C}H_2CH_3$), 60.7 (py-$\underline{C}H_2$), 52.10 (cyclen-$\underline{C}H_2$), 47.43 (cyclen-$\underline{C}H_2$), 46.49 (cyclen-$\underline{C}H_2$), 45.57 (cyclen-$\underline{C}H_2$), 16.6 (d, $^{3}J_{C\text{-}P}$ = 6 Hz, $OCH_2\underline{C}H_3$), 13.6 (d, $^{1}J_{C\text{-}P}$ = 105 Hz, $P\underline{C}H_3$); ^{19}F NMR (376 MHz, $CDCl_3$): δ = -64.7; ^{31}P NMR (162 MHz, $CDCl_3$): δ = 39.0; ESI/MS^+ m/z 438.2 $[M+H]^+$; HRMS Calcd for $C_{18}H_{32}F_3N_5O_2P$ 438.2238. Found 438.2240.

77. Triethyl (10-((6-(ethoxy(methyl)phosphoryl)-4-(trifluoromethyl)pyridin-2-yl)-1,4,7,10-tetraazacyclododecane-1,4,7-triyl)tris(methylene)tris (methylphosphinate)

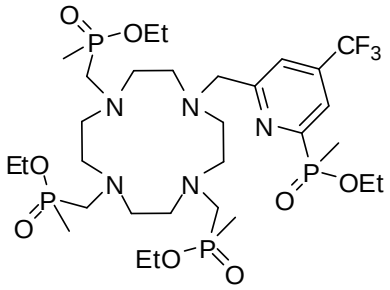

Ethyl 6-((1,4,7,10-tetraazacyclododecan-1-yl)methyl)-4-(trifluoromethyl)pyridin-2-yl(methyl)phosphinate (114 mg, 0.261 mmol) was heated to 80°C in anhydrous THF under argon. Paraformaldehyde (110 mg, 3.67 mmol) followed by diethoxymethylphosphine (500 mg, 0.367 mmol) were added. The solution was boiled under reflux over molecular sieves for 15 h. After this time, excess paraformaldehyde was removed by filtration and the solvent removed under reduced pressure. The resulting orange oil was purified by mixed alumina/silica (4:1) gel column chromatography, eluting with a gradient starting from 100 % DCM to 8 % MeOH/DCM, to yield a yellow oil (141 mg, 68 %) as a mixture of diastereoisomers; ^{1}H NMR (400 MHz, $CDCl_3$): δ = 8.11 (d, $^{3}J_{HP}$ = 6 Hz, 1H, H^5), 8.03 (s, 1H, H^3), 4.74 (s, 2H, NC$\underline{H}_2$py), 4.07 (br m, 8H, POC$\underline{H}_2$CH$_3$/NC$\underline{H}_2$P), 3.81 (m, 6H, POC$\underline{H}_2$CH$_3$/NC$\underline{H}_2$P), 3.42 (br s, 2H, cyclen-C$\underline{H}_2$), 3.05 (br m, 6H, cyclen-C$\underline{H}_2$), 2.76 (br s, 8H, cyclen-C$\underline{H}_2$), 1.78 (d, $^{2}J_{H\text{-}P}$ = 15 Hz, 3H, pyPC$\underline{H}_3$), 1.68 – 1.40 (br m, 12H, POCH$_2$C$\underline{H}_3$), 1.39 – 1.15 (br m, 12H, POCH$_2$C$\underline{H}_3$); ^{19}F NMR (376 MHz, $CDCl_3$): δ = -64.8; ^{31}P NMR (162 MHz, $CDCl_3$): δ = 59.0, 53.1; ESI/MS$^+$ m/z 798.6 $[M+H]^+$; HRMS Calcd for $C_{30}H_{59}F_3N_5O_8P_4$ 798.3266. Found 798.3248.

78. (10-((6-(Methyl) phosphinic acid-4-(trifluoromethyl)pyridin-2-yl)methyl)-1,4,7,10-tetraazacyclododecane-1,4,7-triyl)tris(methylene)tris (methylphosphinic acid) (L^8)

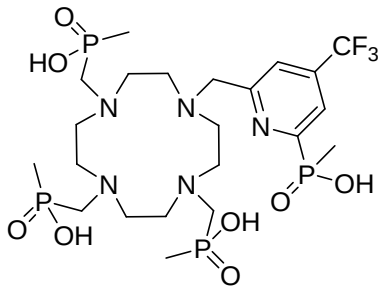

Triethyl (10-((6-(ethoxy(methyl)phosphoryl)-4-(trifluoromethyl)pyridin-2-yl)-1,4,7,10-tetraazacyclododecane-1,4,7-triyl)tris(methylene)tris(methylphosphinate) (54 mg, 0.068 mmol) was dissolved in HCl (6 M, 5 mL) and stirred for 18 h at 90°C. The solvent was removed under reduced pressure and the residue washed repeatedly with DCM (3 x 5 mL) before the resulting oil was dissolved in EtOH. The white precipitate was removed by filtration and the solvent removed under reduced pressure to yield the trihydrochloride salt of **L^8** as a yellow oil (46 mg, 99 %). ^{1}H NMR (400 MHz, D_2O): δ = 8.02 (d, $^3J_{HP}$ = 5 Hz, 1H, H^5), 7.89 (s, 1H, H^3), 3.64 (s, 2H, NC$\underline{H}_2$py), 3.45 (br m, 10H, NC$\underline{H}_2$P/cyclen-C$\underline{H}_2$), 3.10 (br m, 12H, cyclen-C$\underline{H}_2$), 1.51 (d, $^2J_{HP}$ = 15 Hz, 3H, PC$\underline{H}_3$), 1.34 (d, $^2J_{HP}$ = 14 Hz, 9H, PC$\underline{H}_3$); ^{19}F NMR (376 MHz, D_2O): δ = -65.3; ^{31}P NMR (162 MHz, $CDCl_3$): δ = 53.1; ESI/MS^+ m/z 686.3 $[M+H]^+$, ESI/MS^- m/z 684.4 $[M-H]^-$.

79. $[Dy.L^8]^-$

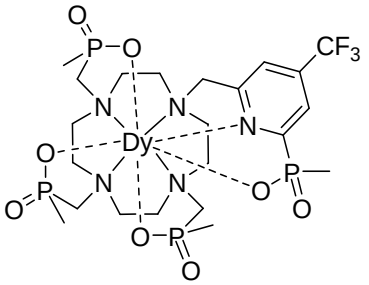

$Dy(III)Cl_3.6H_2O$ (38 mg, 0.101 mmol) was added to a solution of (10-((6-(methyl)phosphinic acid-4-(trifluoromethyl)pyridin-2-yl)methyl)-1,4,7,10-tetraazacyclo-

dodecane-1,4,7-triyl)tris(methylene)tris(methylphosphinic acid) (46 mg, 0.067 mmol) dissolved in H_2O (3 mL). The pH was adjusted to 5.5 before stirring the solution for 18 h at 40°C. After this time, the solution was allowed to cool to rt before the pH was raised to 10, causing a white solid to precipitate out of solution. This precipitate was removed by centrifugation and the pH of the resulting solution neutralised. The solvent was removed under reduced pressure to give a yellow solid, which was purified by preparative scale RP-HPLC to yield an off-white solid (51 mg, 90 %); ^{19}F NMR (376 MHz, D_2O, pH 6.5): δ = -67.0; ESI/MS$^-$ m/z 844.2 $[M]^-$; HRMS Calcd for $C_{22}H_{38}{}^{160}DyF_3N_5O_8P_4$ 841.0869. Found 841.0892.

80. [Er.L^8]

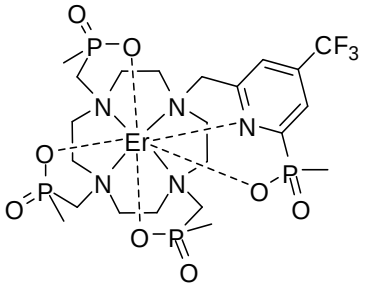

An analogous procedure to that described for **[Dy.L^8]** was followed using (10-((6-(methyl)phosphinic acid-4-(trifluoromethyl)pyridin-2-yl)methyl)-1,4,7,10-tetraazacyclo-dodecane-1,4,7-triyl)tris(methylene)tris(methylphosphinic acid) (69 mg, 0.110 mmol) and Er(III)Cl_3 (63 mg, 0.164 mmol) to yield an off-white solid (82 mg, 88 %); ^{19}F NMR (376 MHz, D_2O, pH 6.5): δ = -61.3; ESI/MS$^-$ m/z 847.2 $[M]^-$; HRMS Calcd for $C_{22}H_{38}{}^{164}ErF_3N_5O_8P_4$ 845.0909. Found 845.0932.

81. 5-*tert*-Butyl-2-methylpyridine

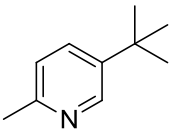

Copper(I) cyanide (10 mg) was added to anhydrous THF (50 mL) and the resulting suspension cooled to -78°C. To this was added *tert*-butylmagnesium chloride (14.5 mL,

2.0 M solution in diethyl ether, 29.1 mmol) and the mixture was maintained at -78°C and stirred for 20 min under an atmosphere of argon. After this time, 5-bromo-2-methylpyridine (2.5 g, 14.5 mmol) was added. The reaction was stirred for 3 h at -78°C before being allowed to warm to rt and stirred for a further 18 h. Upon completion of the reaction (followed by TLC), sat. $NH_4OH_{(aq)}$ was added dropwise to quench any excess Grignard reagent remaining in solution. This immediately caused the formation of a white precipitate in a brown solution, transforming into a clear solution containing a dark brown precipitate upon further addition. This mixture was then extracted with diethyl ether (3 x 50 mL) to obtain a colourless organic layer, separated from the deep blue aqueous layer. The organic layers were combined, dried over $MgSO_4$, and the solvent removed under reduced pressure to yield a partially volatile yellow liquid that was used without any further purification (1.42 g, 66 %). R_f (50 % ethyl acetate/hexane) = 0.35. ^{1}H NMR (400 MHz, $CDCl_3$): δ = 8.31 (d, *J* = 2 Hz, 1H, H^6), 7.63 (dd, *J* = 8, 2 Hz, 1H, H^4), 7.10 (d, *J* = 8 Hz, 1H, H^3), 2.39 (s, 3H, Me), 1.24 (s, 9H, ^{t}Bu); ^{13}C NMR (101 MHz, $CDCl_3$): δ = 157.6 (C^2), 148.0 (C^6), 146.5 (C^5), 137.4 (C^4), 126.1 (C^3), 36.2 ($\underline{C}(CH_3)_3$), 33.2 ($C(\underline{C}H_3)$), 23.6 ($\underline{C}H_3$); ESI/MS$^+$ m/z 150.2 $[M+H]^+$; HRMS Calcd for $C_{10}H_{16}N$ 150.1283. Found 150.1279.

82. 5-*tert*-Butyl-2-methylpyridine 1-oxide

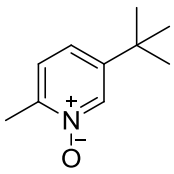

m-CPBA (2.17 g, 12.6 mmol) was added to a stirred solution of 5-*tert*-butyl-2-methylpyridine (1.25 g, 8.39 mmol) in chloroform (30 mL). The resulting solution was stirred at rt for 18 h under argon before being quenched with sat. $Na_2SO_{4(aq)}$ (10 mL) and stirred for 10 min. The organic layer was extracted and washed with sat. $NaHCO_{3(aq)}$ (30 mL). The aqueous layer was extracted with ethyl acetate (3 x 25 mL). All organic layers were combined, dried over Na_2SO_4, and the solvent removed under reduced pressure. The resulting yellow liquid was purified by silica gel column chromatography, eluting with a gradient starting from 100 % DCM to 5 % MeOH/DCM

to yield a yellow liquid (0.51 g, 37 %). R_f (10 % MeOH/DCM) = 0.39. ^{1}H NMR (400 MHz, $CDCl_3$): δ = 8.32 (d, *J* = 2 Hz, 1H, H^6), 7.21 (dd, *J* = 8, 2 Hz, 1H, H^4), 7.18 (d, *J* = 8 Hz, 1H, H^3), 2.50 (s, 3H, Me), 1.31 (s, 9H, ^{t}Bu); ^{13}C NMR (101 MHz, $CDCl_3$): δ = 147.4 (C^2), 145.7 (C^6), 137.4 (C^5), 125.7 (C^3), 123.7 (C^4), 33.6 ($\underline{C}(CH)_3$), 30.6 ($C(\underline{C}H)_3$), 17.3 ($\underline{C}H_3$); ESI/MS$^+$ m/z 166.2 $[M+H]^+$; HRMS Calcd for $C_{10}H_{16}NO$ 166.1232. Found 166.1268.

83. (5-*tert*-Butylpyridin-2-yl)methanol

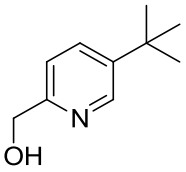

Trifluoroacetic anhydride (10 mL) was added to a solution of 5-*tert*-butyl-2-methylpyridine 1-oxide (450 mg, 2.73 mmol) in $CHCl_3$ (15 mL). The resulting mixture was heated at 60°C for 36 h under an inert atmosphere. After this time, the solvent was removed under reduced pressure and completion of reaction to the trifluoroacetate intermediate was confirmed by ^{1}H NMR analysis. The resulting bright yellow oil was stirred in a mixture of EtOH (5 mL) and H_2O (5mL) for 1 h to convert the trifluoroacetate intermediate into the desired alcohol. The solution was concentrated (ca. 2 mL) and extracted with ethyl acetate (3 x 10 mL). The organic layers were combined, dried over $MgSO_4$, and the solvent removed under reduced pressure to yield a dark yellow oil (396 mg, 88 %). R_f (10 % MeOH/DCM) = 0.42. ^{1}H NMR (400 MHz, $CDCl_3$): δ = 8.57 (s, 1H, H^6), 7.71 (d, *J* = 8 Hz, 1H, H^4), 7.18 (d, *J* = 8 Hz, 1H, H^3), 4.77 (s, 2H, $C\underline{H}_2OH$), 1.34 (s, 9H, ^{t}Bu); ^{13}C NMR (101 MHz, $CDCl_3$): δ = 153.4 (C^2), 148.5 (C^6), 141.6 (C^5), 137.8 (C^3), 123.7 (C^4), 59.5 ($\underline{C}H_2OH$), 33.4 ($\underline{C}(CH)_3$), 29.5 ($C(\underline{C}H)_3$); ESI/MS$^+$ m/z 166.2 $[M+H]^+$; HRMS Calcd for $C_{10}H_{16}NO$ 166.1232. Found 166.1248.

84. (5-*tert*-Butylpyridin-2-yl)methyl methanesulfonate

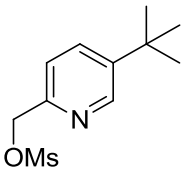

(5-*tert*-Butylpyridin-2-yl)methanol (396 mg, 2.40 mmol) was dissolved in THF (10 mL) and cooled to 5°C. Triethylamine (0.67 mL, 4.79 mmol) and mesyl chloride (0.28 mL, 3.60 mmol) were added dropwise to this solution, upon which a white solid precipitated out of solution. Once addition was complete, the reaction mixture was allowed to warm to rt and stirred for 2 h, before the solvent was removed under reduced pressure. During this time, the reaction was monitored by TLC to ensure that complete conversion to the mesylate had occurred. The residue was treated with brine (10 mL) and extracted with DCM (2 x 10 mL). The organic layers were combined, dried over $MgSO_4$, and the solvent removed under reduced pressure to yield an orange oil, which was used immediately (530 mg, 91 %). R_f (10 % MeOH/DCM) = 0.76. ^{1}H NMR (400 MHz, $CDCl_3$): δ = 8.68 (d, *J* = 2 Hz, 1H, H^6), 7.89 (dd, *J* = 8, 2 Hz, 1H, H^4), 7.52 (d, *J* = 8 Hz, 1H, H^3), 5.39 (s, 2H, $C\underline{H}_2OMs$), 3.12 (s, 3H, $SO_2C\underline{H}_3$), 1.37 (s, 9H, ^{t}Bu); ESI/MS$^+$ m/z 244.2 $[M+H]^+$.

85. *tert*-Butyl-2,2',2''-(10-((5-*tert*-butylpyridin-2-yl)methyl)-1,4,7,10-tetraazacyclododecane-1,4,7-triyl)triacetate

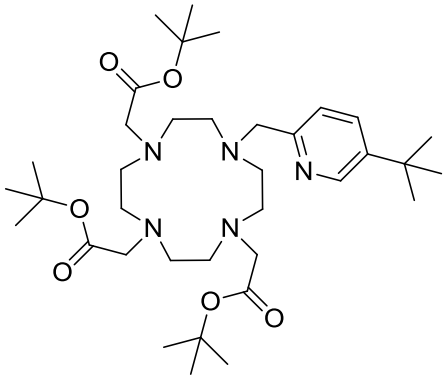

A stirred mixture of *tert*-butyl 2,2',2''-(1,4,7,10-tetraazacyclododecane-1,4,7-triyl)triacetate (DO3A) (19 mg, 0.038 mmol), (5-*tert*-butylpyridin-2-yl)methyl methanesulfonate (11 mg, 0.045 mmol), and K_2CO_3 (9 mg, 0.065 mmol) in anhydrous

MeCN (5 mL) was heated at 60°C for 18 h under argon. After this time, the reaction mixture was cooled and filtered before the solvent was removed under reduced pressure. The resulting yellow oil was purified by silica gel column chromatography, eluting with a gradient starting from 100 % DCM to 3 % MeOH/DCM to yield a pale yellow oil (18 mg, 71 %). R_f (10 % MeOH/DCM) = 0.40. ^{1}H NMR (400 MHz, $CDCl_3$): δ = 8.28 (d, *J* = 3 Hz, 1H, H^6), 7.65 (dd, *J* = 8, 3 Hz, 1H, H^4), 7.09 (d, *J* = 8 Hz, 1H, H^3), 3.07 (br m, 12H, NC$\underline{H}_2$COO^{t}Bu/cyclen-C$\underline{H}_2$/NC$\underline{H}_2$py), 2.31 (br m, 12H, NC$\underline{H}_2$COO^{t}Bu/cyclen-C$\underline{H}_2$/NC$\underline{H}_2$py), 1.49 (s, 9H, py-C(C$\underline{H}_3$)$_3$), 1.39 (br s, 18H, COOC(C$\underline{H}_3$)$_3$), 1.29 (s, 9H, COOC(C$\underline{H}_3$)$_3$); ^{13}C NMR (101 MHz, $CDCl_3$): δ = 172.7 (C$\underline{O}$O^{t}Bu), 155.8 (C^2), 145.8 (C^6), 144.2 (C^5), 133.7 (C^3), 122.0 (C^4), 81.8 (COO$\underline{C}$(CH$_3$)$_3$), 58.3 ($\underline{C}$H$_2$), 55.4 ($\underline{C}$H$_2$), 33.3 (py$\underline{C}$(CH$_3$)$_3$), 31.0 (pyC(C$\underline{H}_3$)$_3$), 27.9 (COOC(C$\underline{H}_3$)$_3$); ESI/MS$^+$ m/z 662.6 [M+H]$^+$, 684.6 [M+Na]$^+$; HRMS Calcd for $C_{36}H_{64}N_5O_6$ 662.4857. Found 662.4852.

86. 2,2',2''-(10-((5-*tert*-Butylpyridin-2-yl)methyl)-1,4,7,10-tetraazacyclododecane-1,4,7-triyl)triacetic acid (L^9)

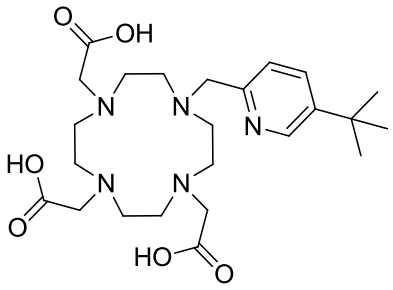

tert-Butyl-2,2',2''-(10-((5-*tert*-butylpyridin-2-yl)methyl)-1,4,7,10-tetraazacyclo-dodecane-1,4,7-triyl)triacetate (15 mg, 0.02 mmol) was dissolved in DCM (1 mL) with stirring. To this was added TFA (1 mL) and the mixture stirred at rt for 18 h. After this time, the solvent was removed under reduced pressure to give a yellow oil. This yellow oil was repeatedly washed with DCM to yield the triflate salt of **L^9** as a pale yellow oil (11 mg, 99 %). ^{1}H NMR (400 MHz, D_2O): δ = 8.57 (d, *J* = 2 Hz, 1H, H^6), 8.40 (dd, *J* = 8, 2 Hz, 1H, H^4), 7.85 (d, *J* = 8 Hz, 1H, H^3), 3.97 (br s, 2H, NC$\underline{H}_2$COO^{t}Bu/cyclen-C$\underline{H}_2$/NC$\underline{H}_2$py), 3.72 (br m, 2H, NC$\underline{H}_2$COO^{t}Bu/cyclen-C$\underline{H}_2$/NC$\underline{H}_2$py), 3.50 (br m, 4H, NC$\underline{H}_2$-COO^{t}Bu/cyclen-C$\underline{H}_2$/NC$\underline{H}_2$py), 3.32 (br m, 6H, NC$\underline{H}_2$COO^{t}Bu/cyclen-C$\underline{H}_2$/NC$\underline{H}_2$py), 3.21 (br m, 2H, NC$\underline{H}_2$COO^{t}Bu/cyclen-C$\underline{H}_2$/NC$\underline{H}_2$py), 2.94 (br m, 4H, NC$\underline{H}_2$COO^{t}Bu/cyclen-

C<u>H</u>$_2$/NC<u>H</u>$_2$py), 2.78 (br m, 4H, NC<u>H</u>$_2$COO^{t}Bu/cyclen-C<u>H</u>$_2$/NC<u>H</u>$_2$py), 1.22 (s, 9H, C(C<u>H</u>$_3$)$_3$); ESI/MS$^+$ m/z 494.4 $[M+H]^+$, 517.4 $[M+Na]^+$; HRMS Calcd for $C_{24}H_{40}N_5O_6$ 494.2979. Found 494.2970.

87. [Dy.L^9]

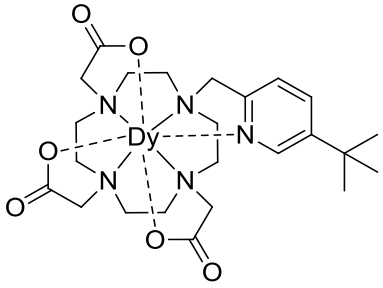

Dy(III)Cl$_3$.6H$_2$O (4.6 mg, 0.012 mmol) was added to a stirred solution of 2,2',2''-(10-((5-*tert*-butylpyridin-2-yl)methyl)-1,4,7,10-tetraazacyclododecane-1,4,7-triyl)triacetic acid (5.0 mg, 0.010 mmol) in water (2 mL) and the pH adjusted to 5.5 using NaOH$_{(aq)}$. The reaction was left stirring at 50°C overnight. After cooling to rt, the pH was increased to 10 and precipitated metal hydroxide removed by centrifugation. The pH was lowered back to 5.5, before the solvent was removed under reduced pressure and the residue taken up into ethanol. Any remaining metal hydroxide precipitate and other insoluble material was again removed by centrifugation. The solvent was removed under reduced pressure to yield a white solid (6.3 mg, 97 %). ^{1}H NMR (400 MHz, D$_2$O, pD 6.5): δ = -20.5 (^{t}Bu); ESI/MS$^+$ m/z 654.3 $[M+H]^+$; HRMS Calcd for $C_{24}H_{36}{}^{160}DyN_5NaO_6$ 673.1815. Found 673.1824.

88. [Tm.L^9]

An analogous procedure to that described for the synthesis of **[Dy.L^9]** was followed using 2,2',2''-(10-((5-*tert*-butylpyridin-2-yl)methyl)-1,4,7,10-tetraazacyclododecane-1,4,7-triyl)triacetic acid (4.0 mg, 0.0081 mmol) and Tm(III)Cl$_3$.6H$_2$O (3.7 mg, 0.0097 mmol) to give a white solid (5.2 mg, 98 %). ^{1}H NMR (400 MHz, D$_2$O, pD 6.5): δ = + 10.8 (^{t}Bu); ESI/MS$^+$ m/z 682.3 $[M+Na]^+$; HRMS Calcd for $C_{24}H_{36}TmN_5NaO_6$ 682.1906. Found 682.1880.

89. *tert*-Butyl 2,2'-(4,10-bis((5-*tert*-butylpyridin-2-yl)methyl)-1,4,7,10-tetraazacyclododecane-1,7-diyl)diacetate

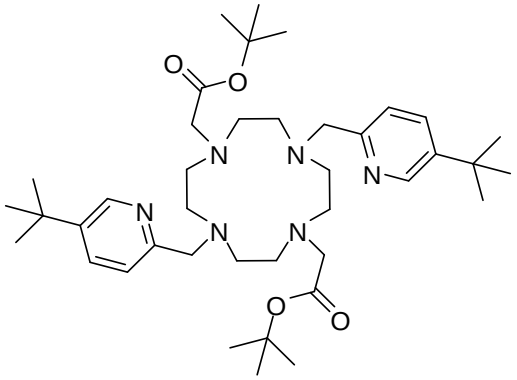

(5-*tert*-Butylpyridin-2-yl)methyl methanesulfonate (530 mg, 2.18 mmol) and (7-*tert*-butoxycarbonylmethyl-1,4,7,10-tetraazacyclododec-1-yl)-acetic acid *tert*-butyl ester (DO2A) (874 mg, 2.18 mmol) were dissolved in anhydrous MeCN (15 mL) under an atmosphere of argon. To this was added Na_2CO_3 (231 mg, 2.18 mmol) and the reaction mixture stirred at 50°C for 48 h. During this time, the reaction was monitored by TLC to ensure complete consumption of the mesylate starting material had occured. Upon completion, the reaction mixture was filtered before the solvent was removed under reduced pressure. The resulting orange oil was purified by silica gel column chromatography, eluting with a gradient starting from 100 % DCM to 10 % MeOH/DCM to yield a yellow-orange sticky solid (284 mg, 19 %). R_f (15 % MeOH/DCM) = 0.68. ^{1}H NMR (600 MHz, $CDCl_3$): δ = 8.36 (d, *J* = 2 Hz, 2H, H^6), 7.63 (dd, *J* = 8, 2 Hz, 2H, H^4), 7.07 (d, *J* = 8 Hz, 2H, H^3), 3.68 (br s, 4H, $NC\underline{H}_2py$), 2.76 (br m, 10H, $NC\underline{H}_2CO_2{}^tBu$/cyclen-$C\underline{H}_2$), 2.37 (br m, 8H, cyclen-$C\underline{H}_2$), 2.14 (br s, 2H, cyclen-$C\underline{H}_2$), 1.27 (s, 18H, ^{t}Bu), 1.23 (s, 18H, ^{t}Bu); ^{13}C NMR (151 MHz, $CDCl_3$): δ = 172.0 ($\underline{C}OO^tBu$), 155.1 (C^2), 146.0 (C^6), 144.5 (C^5), 133.7 (C^4), 122.1 (C^3), 81.7 ($CO_2\underline{C}(CH_3)_3$), 58.1 ($N\underline{C}H_2py$), 57.2 ($N\underline{C}H_2CO_2{}^tBu$), 53.4 (cyclen-$\underline{C}H_2$), 50.3 (cyclen-$\underline{C}H_2$), 33.3 ($py\underline{C}(CH_3)_3$), 31.0 ($pyC(\underline{C}H_3)_3$), 27.9 ($CO_2C(\underline{C}H_3)_3$); ESI/MS$^+$ m/z 696.1 $[M+H]^+$; HRMS Calcd for $C_{40}H_{67}N_6O_4$ 695.5224. Found 695.5197.

90. 2,2'-(4,10-Bis((5-*tert*-butylpyridin-2-yl)methyl)-1,4,7,10-tetraazacyclododecane-1,7-diyl)diacetic acid (L^{10})

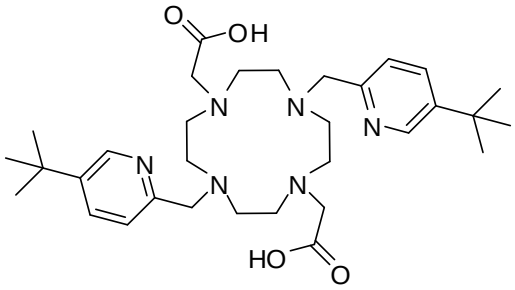

tert-Butyl-2,2'-(4,10-bis((5-*tert*-butylpyridin-2-yl)methyl)-1,4,7,10-tetraazacyclo-dodecane-1,7-diyl)diacetate (18.3 mg, 0.026 mmol) was dissolved in HCl (6 M, 3 mL) and stirred for 18 h at 90°C. The solvent was removed under reduced pressure and the residue washed repeatedly with DCM (3 x 5 mL), before being dissolved in EtOH. The resulting white precipitate was removed by filtration and the solvent removed under reduced pressure to yield the hydrochloride salt as a pale yellow gum (12.7 mg, 84 %). ^{1}H NMR (400 MHz, D_2O): δ = 8.73 (d, *J* = 2 Hz, 2H, H^6), 8.51 (dd, *J* = 8, 2 Hz, 2H, H^4), 7.89 (d, *J* = 8 Hz, 2H, H^3), 3.81 (br s, 4H, NC$\underline{H}_2$py), 3.46 (br s, 4H, NC$\underline{H}_2CO_2{}^t$Bu), 3.35 (br s, 4H, cyclen-C$\underline{H}_2$), 3.17 (br s, 4H, cyclen-C$\underline{H}_2$), 2.99 (br s, 4H, cyclen-C$\underline{H}_2$), 2.74 (br m, 4H, cyclen-C$\underline{H}_2$), 1.27 (s, 18H, ^{t}Bu); ESI/MS$^+$ m/z 583.9 $[M+H]^+$.

91. $[Dy.L^{10}]^+$

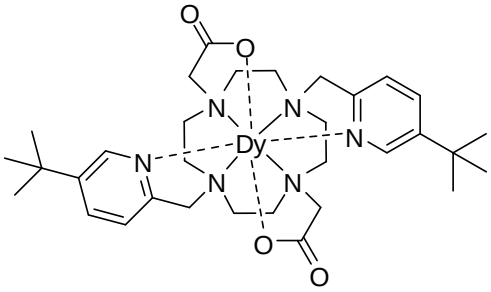

$Dy(III)Cl_3.6H_2O$ (19 mg, 0.052 mmol) was added to a stirred solution of 2,2'-(4,10-bis((5-*tert*-butylpyridin-2-yl)methyl)-1,4,7,10-tetraazacyclododecane-1,7-diyl)diacetic acid (25 mg, 0.043 mmol) in water (2 mL) and the pH adjusted to 5.5 using $NaOH_{(aq)}$. The reaction was left stirring at 50°C overnight. After cooling to rt, the pH was increased to

10 and precipitated metal hydroxide removed by centrifugation. The pH was lowered back to 5.5, before the solvent was removed under reduced pressure and the residue taken up into ethanol. Any remaining metal hydroxide precipitate and other insoluble material was again removed by centrifugation. The solvent was removed under reduced pressure to yield a white solid (30.5 mg, 96 %). ^{1}H NMR (400 MHz, D_2O, pD 6.5): δ = - 17.8 (^{t}Bu); ESI/MS^{+} m/z 744.9 $[M]^{+}$; HRMS Calcd for $C_{32}H_{48}{}^{160}DyN_6O_4$ 740.2989. Found 740.2997.

92. $[Tm.L^{10}]^{+}$

An analogous procedure to that described for the synthesis of **$[Dy.L^{10}]^{+}$** was followed using 2,2'-(4,10-bis((5-*tert*-butylpyridin-2-yl)methyl)-1,4,7,10-tetraazacyclododecane-1,7-diyl)diacetic acid (10.5 mg, 0.019 mmol) and Tm(III)$Cl_3.6H_2O$ (8.7 mg, 0.023 mmol) to give a white solid (13.5 mg, 95 %). ^{1}H NMR (400 MHz, D_2O, pD 6.5): δ = + 6.2 (^{t}Bu); ESI/MS^{+} m/z 750.0 $[M]^{+}$; HRMS Calcd for $C_{32}H_{48}TmN_6O_4$ 749.3079. Found 749.3100.

93. $[Tb.L^{10}]^{+}$

An analogous procedure to that described for the synthesis of **$[Dy.L^{10}]^{+}$** was followed using 2,2'-(4,10-bis((5-*tert*-butylpyridin-2-yl)methyl)-1,4,7,10-tetraazacyclododecane-1,7-diyl)diacetic acid (20 mg, 0.034 mmol) and Tb(III)$Cl_3.6H_2O$ (15 mg, 0.041 mmol) to give a white solid (24 mg, 97 %). ^{1}H NMR (400 MHz, D_2O, pD 6.5): δ = - 7.2 (^{t}Bu); ESI/MS^{+} m/z 739.9 $[M]^{+}$; HRMS Calcd for $C_{32}H_{48}TbN_6O_4$ 739.2991. Found 739.2985.

94. $[Gd.L^{10}]^{+}$

An analogous procedure to that described for the synthesis of **$[Dy.L^{10}]^{+}$** was followed using 2,2'-(4,10-bis((5-*tert*-butylpyridin-2-yl)methyl)-1,4,7,10-tetraazacyclododecane-1,7-diyl)diacetic acid (12.7 mg, 0.022 mmol) and Gd(III)$Cl_3.6H_2O$ (9.7 mg, 0.026 mmol) to give a white solid (16 mg, 98 %). ESI/MS^{+} m/z 738.9 $[M]^{+}$; HRMS Calcd for

$C_{32}H_{48}{}^{154}GdN_6O_4$ 734.2946. Found 734.2935. r_{1p} = 5.21 $mM^{-1}s^{-1}$ (H_2O, 0.1 M NaCl, 60 MHz, 310 K).

95. tert-Butyl-2,2'-(4-((5-tert-butylpyridin-2-yl)methyl)-1,4,7,10-tetraazacyclododecane-1,7-diyl)diacetate

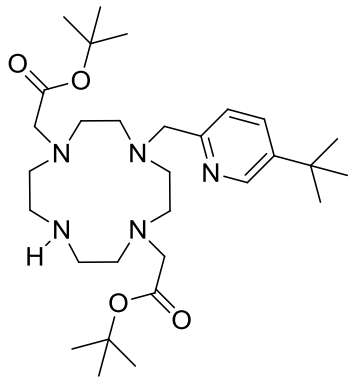

(5-*tert*-Butylpyridin-2-yl)methyl methanesulfonate (530 mg, 2.18 mmol) and (7-*tert*-butoxycarbonylmethyl-1,4,7,10-tetraazacyclododec-1-yl)-acetic acid *tert*-butyl ester (DO2A) (874 mg, 2.18 mmol) were dissolved in anhydrous MeCN (15 mL) under an atmosphere of argon. To this was added Na_2CO_3 (231 mg, 2.18 mmol) and the reaction mixture stirred at 50°C for 48 h. During this time, the reaction was monitored by TLC to ensure complete consumption of the mesylate starting material had occured. Upon completion, the reaction mixture was then filtered before the solvent was removed under reduced pressure. The resulting orange oil was purified by silica gel column chromatography, eluting with a gradient starting from 100 % DCM to 10 % MeOH/DCM to yield a yellow sticky solid (470 mg, 37 %). R_f (15 % MeOH/DCM) = 0.56. ^{1}H NMR (600 MHz, $CDCl_3$): δ = 8.82 (d, *J* = 2 Hz, 1H, H^6), 7.60 (dd, *J* = 8, 2 Hz, 1H, H^4), 7.14 (d, *J* = 8 Hz, 1H, H^3), 3.65 (s, 2H, $NC\underline{H}_2py$), 3.07 (s, 12H, $NC\underline{H}_2COO$/cyclen-$C\underline{H}_2$), 2.78 (br m, 4H, cyclen-$C\underline{H}_2$), 2.57 (br s, 4H, cyclen-$C\underline{H}_2$), 1.38 (s, 18H, $COOC(C\underline{H}_3)_3$), 1.32 (s, 9H, $pyC(C\underline{H}_3)_3$); ^{13}C NMR (151 MHz, $CDCl_3$): δ = 170.5 ($\underline{C}OO^tBu$), 154.2 (C^2), 147.8 (C^6), 145.0 (C^5), 133.3 (C^4), 123.2 (C^3), 81.3 ($COO\underline{C}(CH_3)_3$), 56.6 ($N\underline{C}H_2py$), 54.0 ($N\underline{C}H_2COO$), 53.4 (cyclen-$\underline{C}H_2$), 50.6 (cyclen-$\underline{C}H_2$), 50.3 (cyclen-$\underline{C}H_2$), 46.6 (cyclen-$\underline{C}H_2$), 33.5 ($py\underline{C}(CH_3)_3$), 31.0 ($pyC(\underline{C}H_3)_3$), 28.1 ($COOC(\underline{C}H_3)_3$); ESI/MS^+ m/z 549.0 $[M+H]^+$, 576.9 $[M+Na]^+$; HRMS Calcd for $C_{30}H_{54}N_5O_4$ 548.4176. Found 548.4176.

96. *tert*-Butyl 2,2'-(4-((5-*tert*-butylpyridin-2-yl)methyl)-10-(2-(methylsulfonamido) ethyl)-1,4,7,10-tetraazacyclododecane-1,7-diyl)diacetate

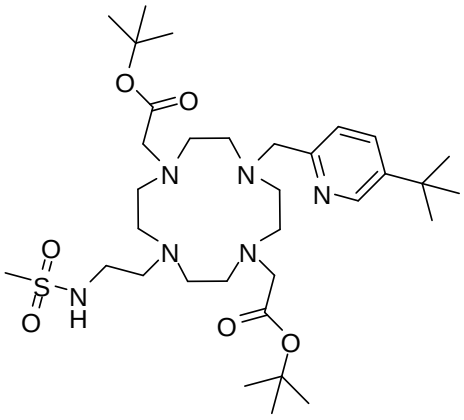

A solution of tert-butyl-2,2'-(4-((5-tert-butylpyridin-2-yl)methyl)-1,4,7,10-tetraaza-cyclododecane-1,7-diyl)diacetate (110 mg, 0.201 mmol), 2-methanesulphonate-*N*-methanesulphonylethylamine (44 mg, 0.201 mmol), and K_2CO_3 (56 mg, 0.402 mmol) in anhydrous MeCN (10 mL) were heated at 80°C for 18 h, before the solution was cooled to rt and filtered. The solvent was removed under reduced pressure to produce a yellow-brown oil that was purified by silica gel column chromatography, eluting with a gradient starting from 100 % DCM to 7 % MeOH/DCM to yield a yellow sticky solid (86 mg, 64 %). ^{1}H NMR (600 MHz, $CDCl_3$): δ = 8.66 (d, *J* = 2 Hz, 1H, H^6), 7.60 (dd, *J* = 8, 2 Hz, 1H, H^4), 7.02 (d, *J* = 8 Hz, 1H, H^3), 3.62 (s, 2H, $NC\underline{H}_2py$), 3.32 (m, 2H, $CH_2C\underline{H}_2NHSO_2$), 3.15 (br m, 4H, $NC\underline{H}_2COO$), 2.99 (s, 3H, $SO_2C\underline{H}_3$), 2.78 (br m, 6H, $NC\underline{H}_2CH_2NHSO_2$/cyclen-$C\underline{H}_2$), 2.50 (br m, 10H, cyclen-$C\underline{H}_2$), 1.35 (s, 18H, $COOC(C\underline{H}_3)_3$), 1.30 (s, 9H, $pyC(C\underline{H}_3)_3$); ^{13}C NMR (151 MHz, $CDCl_3$): δ = 172.1 ($\underline{C}OO^tBu$), 154.3 (C^2), 147.7 (C^6), 144.9 (C^5), 133.6 (C^4), 122.0 (C^3), 82.2 ($COO\underline{C}(CH_3)_3$), 58.6 ($N\underline{C}H_2py$), 56.7 ($N\underline{C}H_2COO$), 53.6 (cyclen-$\underline{C}H_2$), 53.4 (cyclen-$\underline{C}H_2$), 50.3 (br m, cyclen-$\underline{C}H_2$), 40.3 ($NCH_2C\underline{H}_2NHSO_2$), 38.7 ($SO_2\underline{C}H_3$/ $NC\underline{H}_2CH_2NHSO_2$), 33.5 ($py\underline{C}(CH_3)_3$), 30.9 ($pyC(\underline{C}H_3)_3$), 28.1 ($COOC(\underline{C}H_3)_3$); ESI/MS$^+$ m/z 670.0 $[M+H]^+$; HRMS Calcd for $C_{33}H_{61}N_6O_6S$ 669.4373. Found 669.4362.

97. 2,2'-(4-((5-tert-butylpyridin-2-yl)methyl)-10-(2-(methylsulfonamido)ethyl)-1,4,7,10-tetraazacyclododecane-1,7-diyl)diacetic acid (L^{13})

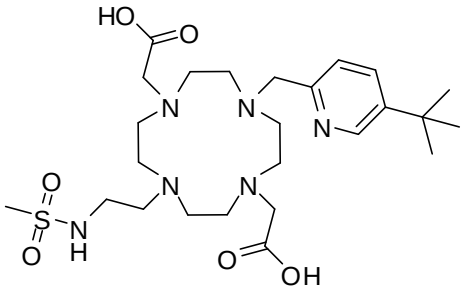

tert-Butyl 2,2'-(4-((5-*tert*-butylpyridin-2-yl)methyl)-10-(2-(methylsulfonamido)ethyl)-1,4,7,10-tetraazacyclododecane-1,7-diyl)diacetate (45 mg, 0.67 mmol) was dissolved in DCM (3 mL) with stirring. To this was added TFA (1 mL) and the mixture stirred at rt for 18 h. After this time, the solvent was removed under reduced pressure to give a yellow oil, which was repeatedly washed with DCM to yield a pale yellow oil (37 mg, 98 %). ^{1}H NMR (600 MHz, D_2O): δ = 8.63 (d, *J* = 2 Hz, 1H, H^6), 8.43 (dd, *J* = 8, 2 Hz, 1H, H^4), 7.87 (d, *J* = 8 Hz, 1H, H^3), 3.94 (s, 2H, NC$\underline{H}_2$py), 3.70 (br m, 2H, NC$\underline{H}_2$COO), 3.50 (br s, 2H, NC$\underline{H}_2$COO), 3.43 (br m, 4H, cyclen-C$\underline{H}_2$), 3.30 (br m, 6H, cyclen-C$\underline{H}_2$), 3.15 (m, 2H, $CH_2C\underline{H}_2NHSO_2$), 3.03 (br m, 2H, cyclen-C$\underline{H}_2$), 2.96 (m, 2H, NC$\underline{H}_2CH_2NHSO_2$), 2.94 (s, 3H, $SO_2C\underline{H}_3$), 2.79 (br m, 2H, cyclen-C$\underline{H}_2$), 2.72 (br m, 2H, cyclen-C$\underline{H}_2$), 1.22 (s, 9H, pyC(C$\underline{H}_3$)$_3$); ESI/MS$^+$ m/z 557.8 $[M+H]^+$.

98. [Dy.L^{11}]

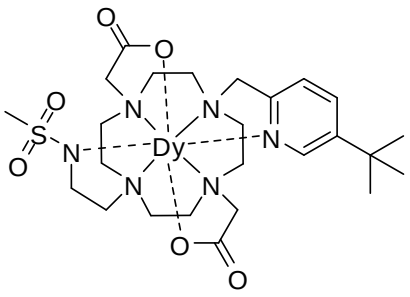

$Dy(III)Cl_3.6H_2O$ (8.5 mg, 0.0226 mmol) was added to a stirred solution of 2,2'-(4-((5-*tert*-butylpyridin-2-yl)methyl)-10-(2-(methylsulfonamido)ethyl)-1,4,7,10-tetraaza-cyclododecane-1,7-diyl)diacetic acid (10.5 mg, 0.0189 mmol) in water (2 mL) and the

pH adjusted to 5.5 using $NaOH_{(aq)}$. The reaction was left stirring at 50°C overnight. After cooling to rt, the pH was increased to 10 and precipitated metal hydroxide removed by centrifugation. The pH was lowered back to 5.5, before the solvent was removed under reduced pressure and the residue taken up into ethanol. Any remaining metal hydroxide precipitate and other insoluble material was again removed by centrifugation. The solvent was removed under reduced pressure to yield a white solid (13 mg, 97 %). ^{1}H NMR (400 MHz, D_2O, pD 6.5): δ = - 58.9 (^{t}Bu); ESI/MS$^+$ m/z 740.8 $[M-H+Na]^+$; HRMS Calcd for $C_{25}H_{41}{}^{160}DyN_6O_6SNa$ 736.1958. Found 736.1945.

99. [Tb.L^{11}]

An analogous procedure to that described for **[Dy.L^{11}]** was followed using 2,2'-(4-((5-*tert*-butylpyridin-2-yl)methyl)-10-(2-(methylsulfonamido)ethyl)-1,4,7,10-tetraaza-cyclododecane-1,7-diyl)diacetic acid (10.5 mg, 0.019 mmol) and Tb(III)$Cl_3.6H_2O$ (8.6 mg, 0.023 mmol) to give a white solid (12.7 mg, 94 %). ^{1}H NMR (400 MHz, D_2O, pD 6.5): δ = -55.8 (^{t}Bu); ESI/MS$^+$ m/z 735.8 $[M-H+Na]^+$; HRMS Calcd for $C_{25}H_{41}{}^{159}TbN_6O_6SNa$ 735.1960. Found 735.1951.

100. [Eu.L^{11}]

An analogous procedure to that described for **[Dy.L^{11}]** was followed using 2,2'-(4-((5-*tert*-butylpyridin-2-yl)methyl)-10-(2-(methylsulfonamido)ethyl)-1,4,7,10-tetraaza-cyclododecane-1,7-diyl)diacetic acid (3.7 mg, 6.58 µmol) and Eu(III)$Cl_3.6H_2O$ (3.1 mg, 8.56 µmol) to give a white solid (4.4 mg, 95 %). ESI/MS$^+$ m/z 707.2 $[M]^+$; HRMS Calcd for $C_{25}H_{42}{}^{151}EuN_6O_6S$ 705.2085. Found 705.2076.

101. [Gd.L^{11}]

An analogous procedure to that described for **[Dy.L^{11}]** was followed using 2,2'-(4-((5-*tert*-butylpyridin-2-yl)methyl)-10-(2-(methylsulfonamido)ethyl)-1,4,7,10-tetraaza-cyclododecane-1,7-diyl)diacetic acid (3.8 mg, 6.83 µmol) and Gd(III)$Cl_3.6H_2O$ (3.0 mg,

8.19 µmol) to give a white solid (4.6 mg, 98 %). ESI/MS^+ m/z 734.8 $[M-H+Na]^+$; HRMS Calcd for $C_{25}H_{41}{}^{154}TbN_6O_6SNa$ 730.1915. Found 730.1915.

102. [Tm.L^{11}]

An analogous procedure to that described for **[Dy.L^{11}]** was followed using 2,2'-(4-((5-*tert*-butylpyridin-2-yl)methyl)-10-(2-(methylsulfonamido)ethyl)-1,4,7,10-tetraaza-cyclododecane-1,7-diyl)diacetic acid (8.3 mg, 0.015 mmol) and Tm(III)$Cl_3.6H_2O$ (6.9 mg, 0.018 mmol) to give a white solid (10.5 mg, 97 %). ^{1}H NMR (400 MHz, D_2O, pD 6.5): δ = +44.3 (^{t}Bu); ESI/MS^+ m/z 745.8 $[M-H+Na]^+$; HRMS Calcd for $C_{25}H_{41}{}^{169}TbN_6O_6SNa$ 745.2048. Found 745.2066.

6.3 References

1. I. Stirling, G. Bruton, S. H. Calvert, and B. P. Clarke, 1985.

2. H. Gysling and M. Tsutsui, *Adv. Organomet. Chem.*, 1971, **9**, 361–395.

3. A. L. Van Geet, *Anal. Chem.*, 1968, **40**, 2227–2229.

4. D. S. Raiford, C. L. Fisk, and E. D. Becker, *Anal. Chem.*, 1979, **51**, 2050–2051.

5. A. Beeby, I. M. Clarkson, R. S. Dickins, S. Faulkner, D. Parker, L. Royle, A. S. de Sousa, J. A. G. Williams, and M. Woods, *J. Chem. Soc., Perkin Trans. 2*, 1999, 493–504.

6. O. V. Dolomanov, L. J. Bourhis, R. J. Gildea, J. A. K. Howard, and H. Puschmann, *J. Appl. Crystallogr.*, 2009, **42**, 339–341.

7. G. M. Sheldrick, *Acta Crystallogr., Sect. A: Found. Crystallogr.*, 2008, **64**, 112–122.

8. K. H. Chalmers, E. De Luca, N. H. M. Hogg, A. M. Kenwright, I. Kuprov, D. Parker, M. Botta, J. I. Wilson, and A. M. Blamire, *Chem. Eur. J.*, 2010, **16**, 134–148.

9. Z. Kovacs and A. D. Sherry, *J. Chem. Soc., Chem. Commun.*, 1995, 185–186.

10. Z. Kovacs and A. D. Sherry, *Synthesis-Stuttgart*, 1997, 759–763.

11. K. H. Chalmers, PhD Thesis, Durham University, 2011.

12. F. Cottet, M. Marull, O. Lefebvre, and M. Schlosser, *Eur. J. Org. Chem.*, 2003, 1559–1568.

13. S. Brandes, C. Gros, F. Denat, P. Pullumbi, and R. Guilard, *Bull. Soc. Chim. Fr.*, 1996, **133**, 65–73.

14. M. Woods, G. E. Kiefer, S. Bott, A. Castillo-Muzquiz, C. Eshelbrenner, L. Michaudet, K. McMillan, S. D. K. Mudigunda, D. Ogrin, G. Tircsó, S. Zhang, P. Zhao, and A. D. Sherry, *J. Am. Chem. Soc.*, 2004, **126**, 9248–9256.

15. O. Reany, T. Gunnlaugsson, and D. Parker, *J. Chem. Soc., Perkin Trans. 2*, 2000, 1819–1831.

Appendix: List of Complexes

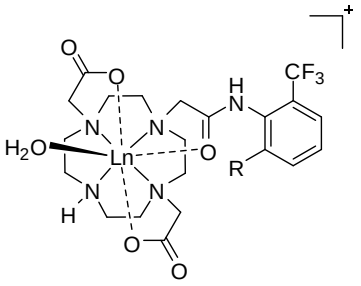

[Ln.L^1]$^+$; R=H
[Ln.L^2]$^+$; R=CN

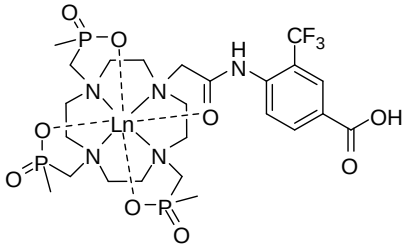

[Ln.L^3]

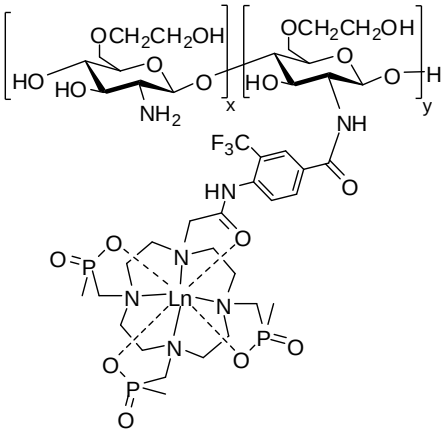

[Ln.L^3-chitosan]

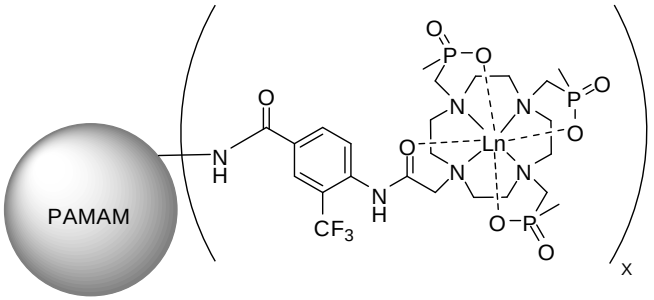

[PAMAM-(Ln.L^3)$_x$]

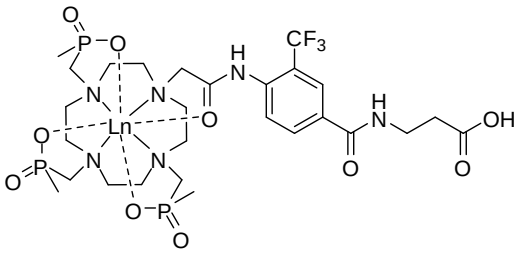

[Ln.L^3-βala]

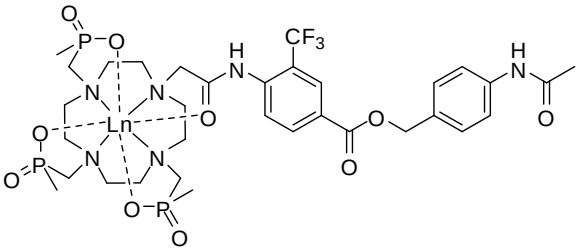

[Ln.L^4]

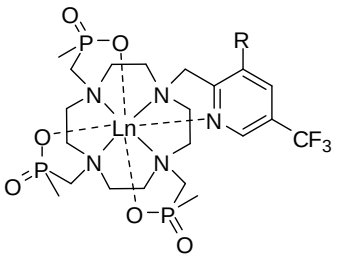

[Ln.L^{5}]; R=H
[Ln.L^{6}]; R=Cl

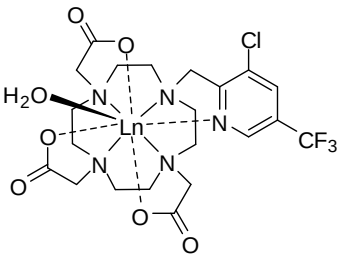

[Ln.L^{7}]

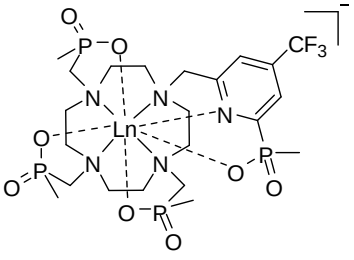

[Ln.L^{8}]$^{-}$

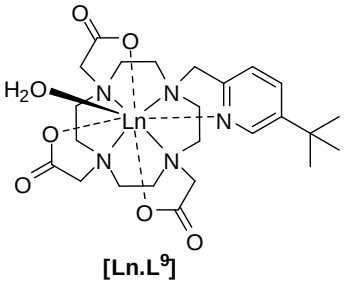

[Ln.L^{9}]

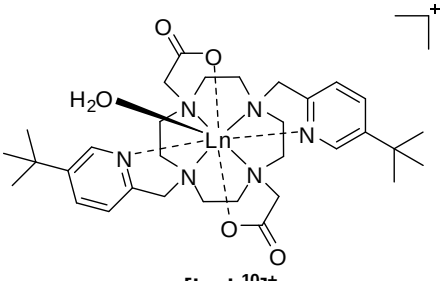

[Ln.L^{10}]$^{+}$

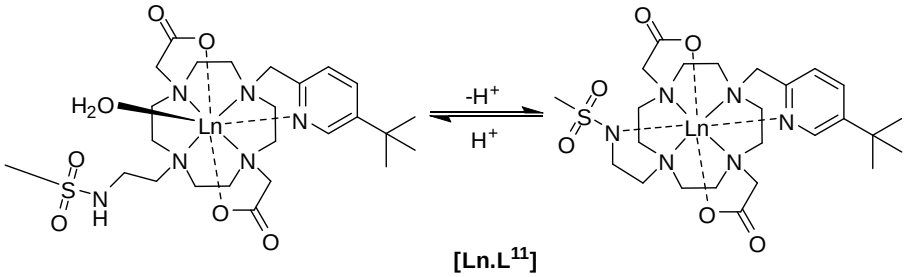

[Ln.L^{11}]